Monitoring biochemical reactions in stationary droplets

Etienne Fradet

École Polytechnique
Laboratoire d'Hydrodynamique

Thèse présentée pour obtenir le grade de

DOCTEUR DE L'ÉCOLE POLYTECHNIQUE

Spécialité : Mécanique

par

Etienne Fradet

Monitoring biochemical reactions in stationary droplets

Thèse soutenue le 21 novembre 2013 devant le jury composé de

Ludovic Jullien	rapporteur	ENS
Jean-Baptiste Salmon	rapporteur	Université de Bordeaux
Olivier Acher	examinateur	Horiba - Jobin Yvon
Andrew D. Griffiths	examinateur	ESPCI
Florian Hollfelder	examinateur	University of Cambridge
Charles N. Baroud	directeur de thèse	Ecole Polytechnique

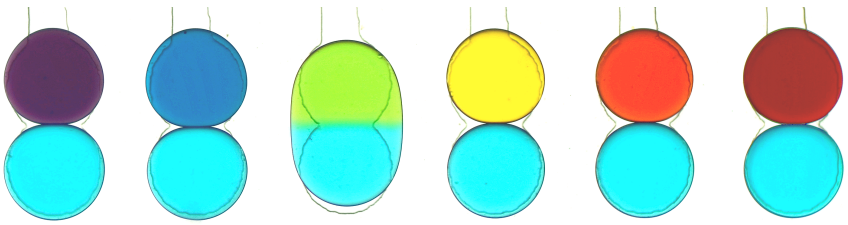

Monitoring biochemical reactions in stationary droplets

Etienne Fradet

Résumé

La microfluidique de gouttes - *i.e.* l'emploi de gouttelettes comme microréacteurs - offre de nombreux avantages pour l'étude des systèmes biologiques. Dans ce travail de thèse, nous présentons une nouvelle approche pour la production et la manipulation de gouttelettes au sein de microcanaux afin de suivre l'avancement de réactions biochimiques au cours du temps. Contrairement aux approches existantes, notre dispositif utilise des gradients de confinement afin de produire et guider une unique goutte vers son lieu de stockage. Ce faisant, deux gouttes de contenus différents peuvent être appariées et fusionnées afin de déclencher une réaction chimique. Les réactifs n'étant pas activement mélangés, un front de réaction se propage alors le long de la goutte fille duquel on peut extraire la cinétique de la réaction. Nous commençons par l'étude de réactions simples ayant lieu en une étape. Un modèle 1D de réaction-diffusion permet de représenter la dynamique du front de réaction ce qui est vérifié en confrontant les solutions de ce modèle, obtenues numériquement ou analytiquement, à des mesures effectuées en gouttes. Puis, nous nous intéressons au cas des réactions enzymatiques. Nous démontrons d'abord la parallélisation de notre technique d'appariement de gouttes afin de reproduire en microcanal différents tests enzymatiques usuellement effectués en plaque multipuits. Finalement, nous étudions le cas des réactions enzymatiques rapides à l'aide de notre modèle de réaction-diffusion. Là encore, la comparaison d'expériences tenues en gouttes et de prédiction issues de notre modèle nous permet d'extraire une mesure des paramètres cinétiques de la réaction mise en jeu.

Mots clefs: Goutte, microfluidique, gradient de confinement, laser, réaction-diffusion, raccordement asymptotique, enzyme

Abstract

Droplet microfluidics - *i.e.* the use of droplets as microreactors - offers significant advantages for the study of biological systems. In this work, we present a new platform for the production and manipulation of microfluidic droplets in view of measuring the evolution of biochemical reactions. Contrary to existing approaches, our device uses gradients of confinement to produce a single drop on demand and guide it to a pre-determined location. In this way, two nanoliter drops containing different reagents can be placed in contact and merged together in order to trigger a chemical reaction. Then, an analysis of the observed reaction front yields the reaction rate. We start with the case of one step reactions. We derive a one dimensional reaction-diffusion model for the reaction front and compare numerical and analytical solutions of our model to experiments held in our microsystem. Then, we turn our attention to the case of enzymatic reactions. First, we show how the device operation can be parallelized in order to react an initial sample with a range of compounds or concentrations and we perform standard well-mixed enzyme assays with our parallelized chip, thereby mimicking titer plate assays in droplets. Second, we build onto our reaction-diffusion model to predict the rate of fast enzymatic reactions held in our device. Again, numerical and analytical solutions of our model are compared to experiments done in droplets which yields measurements of the kinetic parameters of the reaction at play.

Key words: Droplet, microfluidics, gradient of confinement, laser, reaction-diffusion, asymptotics, enzyme

Remerciements

Décembre 2013. Avec l'année se termine aussi ma thèse qui n'aurait certainement pas vu le jour sans l'aide, les conseils et le soutien de toutes celles et ceux que je remercie ici.

Je pense d'abord à Charles, naturellement, qui dès notre première entrevue m'a communiqué son goût pour la science, les belles manips et (surtout) sa joie de vivre. C'est une grande chance d'avoir fait mes premiers pas de chercheur à tes côtés. Merci!

L'équipe microfluidique ensuite: Caro, toujours partante pour tenter une manip et m'aider en salle *grise*; Rémi bien sûr, qui a toujours su répondre à mes questions et m'a révélé tous les secrets des gradients de confinement; sans oublier Paul, Sungyon, Anette, Hatem, Nadia, Yonathan, Tanmay, Gabriel, Nicolas, Raphael, Magali, Clément, Sébastien et Cyprien avec qui c'est un réel plaisir de travailler tous les jours.

Vient le tour du LadHyX dont je remercie tous les membres pour la grande convivialité qui y règne. Je remercie Patrick Huerre, Jean-Marc Chomaz et Christophe Clanet pour m'avoir accueilli au LadHyX ces trois années durant. Un grand merci à Thérèse, Sandrine et Delphine qui gèrent l'essentiel des à-côtés administratifs de la vie des thésards, ainsi qu'à Dany, Tonio et Toai qui m'ont sauvé la vie plus d'une fois à l'atelier ou face à un PC refusant obstinément de fonctionner. Et il y a le foot, qui ne pourrait être ce grand défouloir hebdomadaire sans son équipe d'aficionados. Je me dois donc de remercier Bapt, Caro, Bénus, PB, Guillaume, Pascal, Clément, Rémi, Jon, Pierre, Cristobal, Diego, Loïc, Anders, Marine, Eunok, Manu, Gaëtan et Mathieu. Sans oublier Fabien, Nico, Miguel et Franz. Enfin, je tiens à remercier Sébastien et Xavier pour l'inestimable aide qu'ils m'ont apportée dans les parties numériques et théoriques de mon projet de thèse.

Une thèse ne se fait seul, mais en équipe, ce qui m'a mené à rendre visite à de nombreux laboratoires. Je remercie particulièrement l'équipe de David McGloin à Dundee, Big and Wee Craig en tête, pour m'avoir initié aux lasers et (surtout) au haggis. Je remercie également l'équipe de Florian Hollfelder à Cambridge qui m'a chaleureusement accueilli. Je pense notamment à Fabrice , Liisa et Chris. Et l'équipe du LOB enfin, dont l'aide ces trois années durant a été de toute première importance. Je pense particulièrement à Paul, Cédric, Marten, Antigoni, Rachid, Stéphane et Max.

Je remercie enfin mon jury de thèse. Mes rapporteurs d'abord, Ludovic Jullien et Jean-Baptiste Salmon, pour leur lecture approfondie de mon manuscrit; mes examinateurs ensuite, pour la belle discussion scientifique que nous avons eue le jour de la soutenance.

Pour finir, je remercie mes proches, mes parents, Marie-Lise, Jonathan et Thomas, et mes amis qui ont découvert la microfluidique à mes côtés à mesure que je les abreuvais d'histoires de gouttelettes (souvent) indisciplinées.

Contents

Introduction

Unravelling the complexity of biological systems often deals with massive screens against varying experimental conditions [1]. In this regard, the gold standard to perform a large number of assays is the microtiter plate which allows for independent reactions to be run in parallel [2]. The success of the plate relies heavily on several key assets. First, the wells of a plate are independent from each other so that different samples loaded in different wells do not interact. Second, the wells of a plate are accessible individually for pipetting at any time of an experiment. As a result, different compounds can be pipetted in different wells at will while promising candidates can be picked out of their well by reverse pipetting. Third, the wells of a plate are arranged in a 2D format which simplifies the observation of large data sets, makes multiplexed assays straightforward and allows for the parallelization and the automation of the labor intensive pipetting work to load the plate [3].

Over the last sixty years, tremendous work has been done to automate liquid handling and miniaturize wells in order to make high throughput compaigns more efficient, both by reducing time and cost and increasing information content [4]. As a result, the plate format passed from 1 to 6 to 96 up to 1536 wells per plates, bringing by the same token the volume of reagent per well from 200 μL down to 2 μL as shown on Fig. 1a)-c).

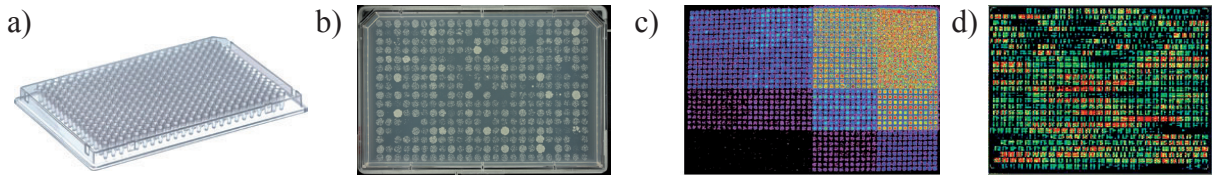

Figure 1: Different 2D arrays of microreactors used routinely in biology. a) 384 wells PCR plate from ThermoScientific [5]. b) 96 wells plate after screening [6]. c) 1536 wells plate after screening of luciferase secreted by Metridia. The Metridia substrate concentration is increased from left to right. Forskolin concentration (a promoter) is increased from bottom to top. [7] d) DNA chip [8].

However, further miniaturization of microtiter plates yields a poor control of the reagent concentration, mainly for two reasons. First, evaporation becomes significant below 1 μL of reagent per well as the surface-to-volume ratio is increased [9]. Second, conventional

pipettes have a good precision down to few hundreds of nL. In addition, reverse pipetting is compromised as the volume of reagent is decreased. Indeed, owing to surface tension, small droplets attach solid substrate tighter than larger drops. As a result, smaller drops resist extraction from the plate better which prevents from pipetting them out of their well [10].

To address these issues, different microtechniques mimicking the microtiter plate 2D format arose such as DNA chips shown on Fig. 1 d), thereby bringing the reactor volume down to few nL or pL while allowing for massive parallelization. Yet, the same level of control as when using plates has not been reached as most deposition techniques rely mostly on the chemical deposition on a solid substrate of predefined compounds against which a solution of the target compound is screened. In contrast to microtiter plates, these miniaturized chips thus lack versatility while requiring advanced deposition techniques.

Another approach to miniaturize microtiter plates with greater versatility consists in using tiny droplets as chemical vessels that can be combined at will to onset chemical reactions. This idea of compartmentalizing compounds in drops was first suggested by Lederberg [11], and later on by Tawkik and Griffiths [12]. Indeed, the content of a drop can be precisely controlled and is naturally isolated from the drop environement by the droplet interface, thereby making each droplet a microreactor similar to the well of a plate. Patterning a 2D area with different droplets is straightforward when using surface microfluidic manipulations, *i.e.* through electro-wetting [13, 14] or surface acoustic waves [15], or more classical droplet deposition techniques such as inkjet printing [16]. Nonetheless, like microtiter plates, these channels suffer from their *open* structure.

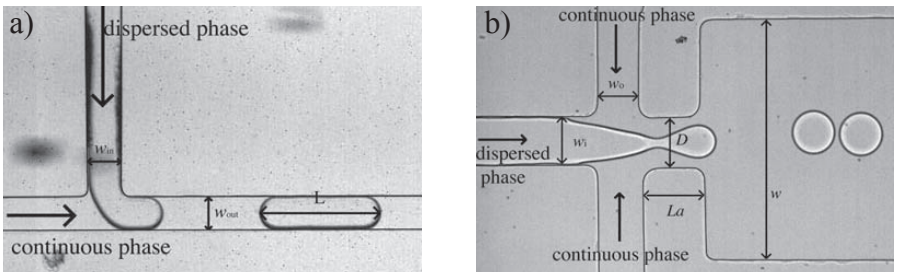

Figure 2: Standard droplet generation units. a) T-junction. b) Flow-focuser. From Baroud *et al.* [17].

Producing arrays of droplets in *closed* microchannels has proved more challenging mostly because individual droplets are not directly accessible in this geometry and hence must be produced and manipulated indirectly on chip. To this end, the most widely used methods to generate droplets in microfluidic devices, *i.e.* the T-junction [18] shown on Fig. 2 a) or the flow-focusing device [19] shown on Fig. 2 b), make use of a continuous flow of the carrier fluid to shear off the dispersed phase into droplets. Then, the constant mean

flow is readily available to transport and mix drops down the channel. However, instead of depositing independent drops at some prescribed location, these methods yield long trains of droplets in which hydrodynamic interactions couple the motion of the different drops [17]. Therefore combining a given drop with another or extracting it from the train cannot be achieved without dramatically affecting the rest of the train.

Instead of flowing the outer phase continuously, Dangla *et al.* [20] suggested recently to use local variations in the channel height to produce and transport droplets within microchannels. As a result, the outer flow can be used intermittently instead of continuously which yield a greater control on each individual droplet. My PhD work builds on this new approach to manipulate droplets in order to (i) selectively build arrays of droplets, thereby mimicking the titer plate, and (ii) study biochemical reactions within droplets when droplets have not been mixed by the outer flow. These two parts compose the four chapters of this manuscript which are described in more detail below.

In chapter 1, we start by reviewing the different approaches developed to use droplets as microreactors within microchannels. Then, we present the two techniques developed in the lab to manipulate droplets either passively using local changes in the channel height, or actively using a laser spot to push or merge drops. Finally, we discuss the different techniques available to produce droplets as well as their ease for large scale integration. This leads us to consider step or wedge junctions to produce drops instead of the more classic continuous flow based methods.

In chapter 2, we demonstrate the combination of the rails and anchors technique with the laser actuation to perform advanced operations on arrays of droplets. We start by presenting the microfabrication techniques and the optical setup we used over the last three years. Then we explain three different protocols to either selectively extract a drop from an array, selectively place a drop in an array and selectively trigger a chemical reaction in an array of paired droplets. These three operations show the great versatility and the robustness we achieve by combining our active and passive techniques to manipulate droplets. In the last section, we present an innovative approach to pair droplets on demand without the need to flow the outer phase. This allows us to build an array of six different pairs of droplets in which each droplet has been assigned to a trap. Finally, we study the mixing during and after the coalescence of two drops in our device. This allows us to build a general reaction-diffusion (RD) model to analyse chemical reactions taking place once two drops containing the reagents are merged in our device.

In chapter 3, we consider the case of one step reactions with initially separated reagents. The first section is a reminder of standard collision theory from which we derive the general second order rate law for bimolecular reactions. In the second section, we present experiments held in droplets from which we extract the reaction rate constant by directly fitting our experiments with our RD model. To get a better understanding of the physics at play, we then turn our attention to the theoretical treatment of our RD model with a

second order rate law. Following the work of Gálfi and Rácz [21] and Trevelyan *et al.* [22], we derive an analytical asymptotic solution of our RD problem in both the early and the large times limits. Finally, we perform experiments in droplets to which we compare our theoretical findings.

In chapter 4, we finally turn our attention to the case of enzyme catalyzed reactions. We start by recalling the standard Michaelis-Menten theory as well as the underlying assumptions. Next, we use our parallelized chip to replicate on chip standard enzymatic assays such as the measurement of steady state kinetic parameters or inhibition constants. We then study the case of fast enzymatic reactions which require a RD treatment when held in droplets within our merging device. Thus, the next section revisits the steady state approximation in RD which allows us to derive a model for steady state enzyme kinetics in RD. We finally compare the last model with experiments held in microchannel. As a benchmark, we start by comparing our RD model to experiments done in a T-shaped microchannel, and then use our RD model to extract the steady state parameters of a fast enzyme catalyzed reaction held in our merging device.

We conclude with some perspectives on the different results presented in this manuscript which should lead to further applications in the near future.

Chapter 1

A microfluidic toolbox for 2D droplet manipulation

In this chapter, the section 1.1 presents the different approaches proposed to use droplets as microreactors and to build arrays of droplets. The next two sections 1.2 and 1.3 present the microfluidic tools developed in our group to manipulate droplets. The first technique is completly passive and relies on local modulations in the channel height. The second technique is active and makes use of a laser to actuate water droplets. These two sections correspond mostly to the work of Rémi Dangla and Marìa Luisa Cordero respectively, on which my PhD is built. The last section 1.4 of this chapter discusses the different droplet production techniques, their ease for large scale integration, and their ability to produce addressable arrays of droplets.

1.1 Toward addressable arrays of droplets

The ideal array of droplets would contain a large (typically 1 million) and well organized set of droplets of controlled formulation. Several requirements, such as encapsulating compounds into droplets, or precisely manipulating drops, have to be met when aiming at this ideal platform for screening. Hereafter, we review the different existing approaches to use droplets as microreators, and to build arrays of droplets.

1.1.1 Droplets as microreactors

The first step of any chemical experiment consists in initiating the reaction by putting in contact the different reagents. Droplet microfluidics proved very successful to this end. When working with microdroplets, reagents have to be brought together in a single droplet. This has been performed either by flowing different streams of reagents at a droplet production site or by merging different droplets containing each reagent as shown on Fig. 1.1.

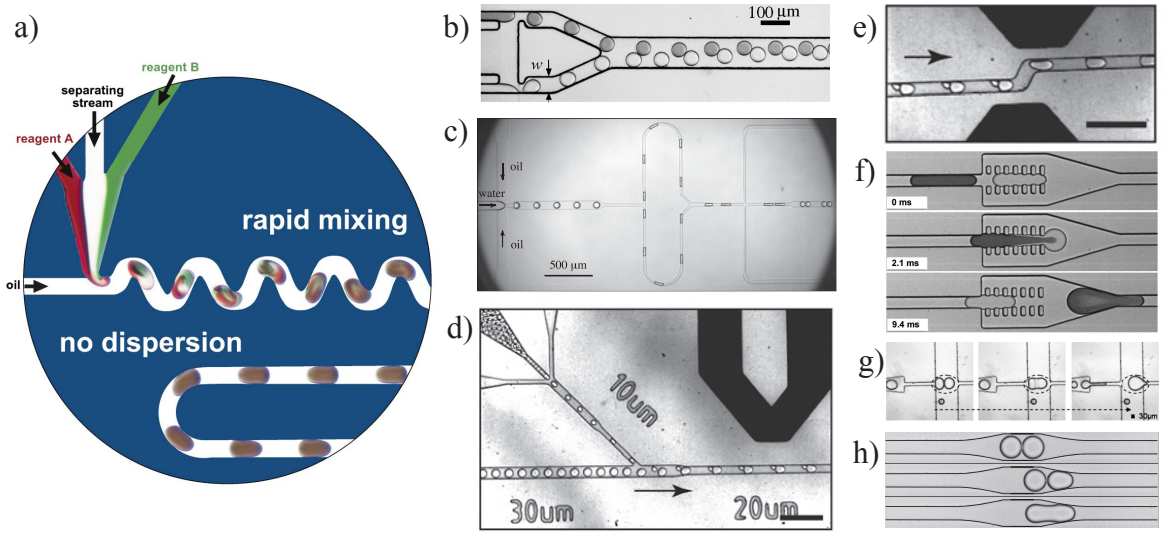

Figure 1.1: The two approaches used in droplet microfluidics to bring reagents in contact. a) Flowing to reagents at a droplet formation site. From Song *et al.* [23] b) Two trains of droplets exiting distinct nozzles are hydrodynamically synchronized. From Frenz *et al.* [24] c) Loop channel. From Brémond *et al.* [25]. d) Synchronization of droplet trains using an electrode. From Mazutis *et al.* [26] e) Electrocoalescence of touching drops. From Mazutis *et al.* [26] f) Pillar induced coalescence. From Niu *et al.* [27] g)-h) Separation driven coalescence. From Tan et al. [28] and Brémond *et al.* [25].

The first use of droplets as microreactors in closed microchannel chose the former option. Taking advantage of the laminar flows at play in microchannel, Song *et al.* [23] flowed reagents next to each other at a T-junction where a stream of oil sheared off the stream of reagents, thus producing a train of droplets containing the reacting mixture. These droplets were then pushed down a linear microchannel while their content was reacting as shown on Fig. 1.1 a). A key asset of this approach is the ability to vary the composition in droplets by adjusting the relative flow rates of the different reagents.

The second approach to use droplets as microreactors proceeds in two steps, namely droplet pairing and droplet merging. To these ends, different methods were proposed. Pairing was perform either by combining droplets of a single train or by synchronizing two coflowing trains of droplets. By controlling the hydrodynamic coupling between droplets alined in a train, Fuerstman *et al.* [29, 30] showed that a loop channel can split and rearrange spacings and orders between drops by having side arms of different lengths. Similarly, hydrodynamic couplings were used to synchronize two trains of droplets exiting distinct nozzles [31]. Frenz *et al.* [24, 32, 33] used a *ladder* channel to form a train of pairs of distinct droplets as shown on Fig. 1.1 b). On the other hand, active methods can also be used to delay one drop and allow the next coming drop to catch up. Mazutis *et al.* [26]

used an electrode to slow down each two droplet of a train in order to form pairs as shown on Fig. 1.1 d). Similarly, a focused laser can be used to block each two droplets as shown by Baroud *et al.* [34]. The second step of this approach consists in merging paired drops. Here again, different solutions have been proposed. For instance, Mazutis *et al.* [26] used electrodes, while Baroud *et al.* [34] used a laser, to actively merge pairs of droplets. Tan et al. [28] used widenings in the channel to passively slow down and merge consecutive droplets as shown on Fig. 1.1 g). Similarly, Niu *et al.* [27] used pillars to slow down adjacent droplets and induce their fusion as shown on Fig. 1.1 f). The physics behind this coalescence mechanism was furthermore explored by Brémond *et al.* [25] who showed that a separation of two touching droplets destabilizes their interface and leads to coalescence (Fig. 1.1 h)).

Although these different techniques to use droplets as microreactors received much attention, they impose severe limitations on the time window over which a reaction can be observed which limits their use in lab-on-a-chip applications.

The time window issue The time window over which one can observe a chemical reaction on chip is limited on both ends. On the one hand, the upper bound is given by the residence time of droplets on chip which is limited since droplets are constantly pushed by a carrier fluid. Thus, reaction slower than the droplets residence time on chip cannot be detected, or their monitoring is limited to end point measurements perform on another chip. On the other hand, the lower bound is defined by the time required to mix the reagents once they are encapsulated. Indeed, as reagents are initially separated, either in two different streams or two different droplets, they need some time to mix before the reaction can be monitored. As a result, reactions faster than this mixing time cannot be resolved. Song *et al.* [23] managed to bring the mixing time of their device down to a few ms, which is comparable to commercial stopped-flow devices used for fast kinetic studies. However, this performance was mostly achieved by injecting fluids faster as they report droplets speeds between 10 and 300 mm/s! Here again, real time measurements are not amenable on a single droplet, but rather require averages over many droplets, and the sample consumption is dramatically increased by the use of high injection flow rates. These two limits have strongly motivated the development of ways to hold droplets stationary against an outer flow in order to build arrays of drops. The next two subsections present the different passive trapping techniques developed in droplet microfluidic, the first group being built on *serial* microchannel while the second group is dedicated to *2D* microchannels.

1.1.2 Trapping droplets in serial microfluidics

The first arrays of droplets were built on meandering linear microchannels by rearraging a train of droplets in a 2D format. As the train was flowing along the track defined by the side walls of the microchannel, each of its wagons (*i.e.* its droplets) was parked one after the other on the side of the track, for example by pushing the drops into parallel

dead-end microchannels [35, 36, 37], by having side pockets in the channel [38] or into parallel corrugated channels. [39, 40]

Tan *et al.* [35] first described the basic unit to trap beads along linear microchannel. Later on Shi *et al.* [36] used the same approach to trap droplets. As shown on Fig. 1.2 a), Tan's traps consist of a dead-end surrounded by a bypass channel. This is a two states system in which the trajectory of a droplet across the trap depends on wether the trap is occupied or not. Dimensions of the trap are thus adjusted so that, when the dead-end is empty, its hydrodynamic resistance is lower than the bypass resistance, and conversely, when the trap is occupied, the dead-end resistance is larger than the bypass resistance. As a result, when a train of droplets enters this trap, the droplet at the front of the train enters the dead-end and plugs it, while the following drops bypass the trap. Fig 1.2 b) shows an example of array obtained by parallelizing Tan's traps.

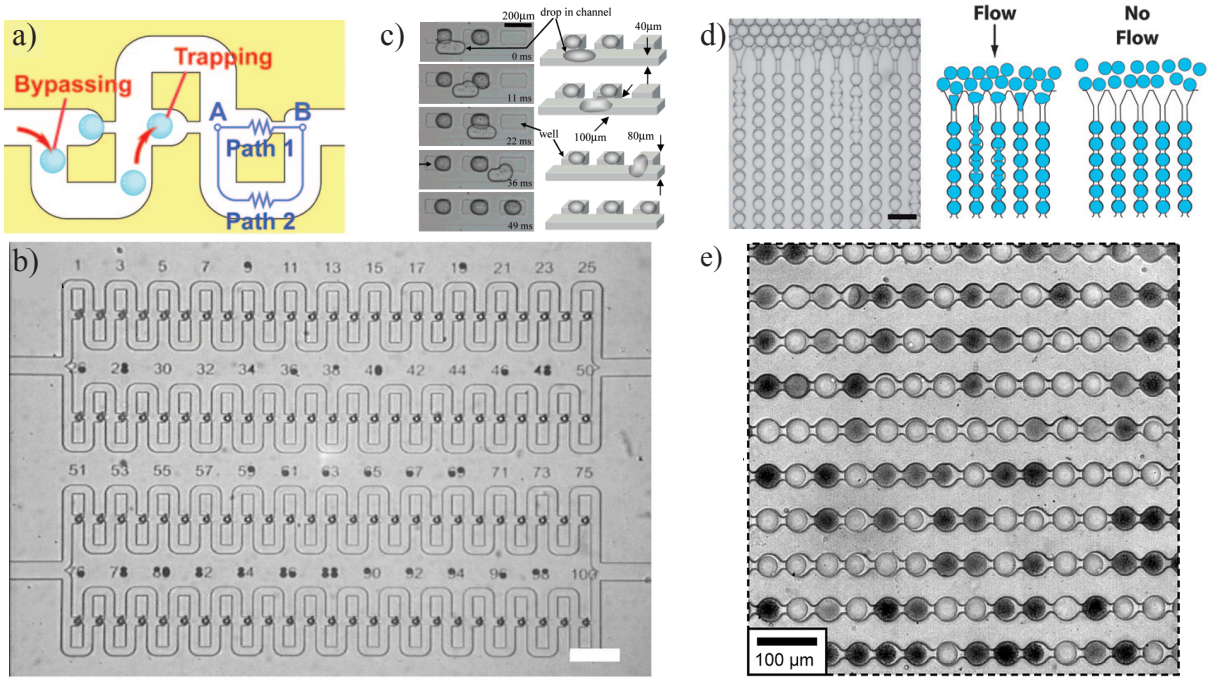

Figure 1.2: Different arrays of droplets built on serial microchannels. a) and b) Dead-end traps. From Tan *et al.* [35]. c) Side pockets. From Shim *et al.* [38] d). and e) Corrugated channels. From Schmitz *et al.* [39] and Edd *et al.* [40] respectively.

Similarly, droplets can be parked along a serial microchannel by using pocket of increased height placed aside the channel as shown on Fig. 1.2 b). Instead of playing on viscous effects, this makes use of capillary effects. Indeed, droplets enter into the side pockets because of their increased height which allows the drops to decrease their surface energy by releasing their confinement. In addition, once a droplet has entered into a

pocket, there is a capillary energy barrier to extract it from the pocket which prevents the drop from escaping from the trap. As a result, droplets are trapped as they pass by empty pockets which allow to store a complete train of droplets.

The last approach shown on Fig. 1.2 d) combines viscous and capillary effects. It consists of flowing a large group of droplets, initially in a wide reservoir, into corrugated microchannels placed in parallel. The large hydrodynamic resistance of the corrugations generates traffic jams at the entrance of the microchannels. This forces droplets to push one another into the corrugations. On the other hand, corrugations being wide pockets separated by tiny constrictions, droplets must squeeze in order to pass from one pocket to another. As a result, there is a capillary barrier for droplets to progress into these corrugations so that, as corrugated microchannel fill up, the back pressure required to push a whole train of droplet increases dramatically. In steady state, an intermittent motion of droplets advancing into the corrugations thus takes place.

These approaches have proven powerful to trap trains of droplets. Resulting arrays are also well organized when parking droplets aside of their track as the natural spatial indexation of trains of drops in serial microchannel is conserved. The indexation order is reversed though. The last approach, based on corrugated microchannels, yields randomly filled arrays, and hence requires a labeling method to identify each droplet in the array. When aiming at selectively releasing droplets from their trap, strong limitations are faced. Tan *et al.* managed to release beads from their trap by using a cavitation bubble induced by a laser local heating. Beads are then pushed out of their trap as the bubble is expanding. This procedure could be employed to untrap droplets from Tan's or Fraden's traps, but at the cost of severe damages on the drops content. In the case of Holze's traps, droplets are completely surrounded, either by the channel walls or by other drops, which prevents from any simple untrapping without affecting the rest of the train of droplets. All in all, the closed nature of these trapping techniques does not allow for simple extraction of droplet which limits their use for more advanced operations such as droplet pairing, and highlights the lack of addressability faced when working with serial microchannels.

The addressability issue The wells of a microtiter plates are addressable reactors as one can pipette in or from each of them individually at will. When aiming at mimicking the titer plate using droplets, the addressability issue is therefore twofolds: the trapping technique at play should allow to place droplets in a trap, and to extract droplets from a trap when needed. As discussed above, 1D microchannels fulfil the controlled filling of an array thanks to their natural spatial indexation. However, the extraction of a given trapped droplet is strongly limited by the lateral confinement on the drop. To this end, another approach to trap droplets consists of removing the side walls of the microchannel and work within wide microchannels.

1.1.3 2D arrays of droplets

In wide microchannels, droplets are not anymore guided by the side walls of the microchannel, but free to move in the plane of the microchannel. As a result, groups of droplets are not well organized trains, but rather herds without any spatial indexation. In these conditions, addressing a droplet per trap requires new tools for droplet guidance and trapping.

Most techniques used for droplet 2D manipulation were first developed to handle other objects such cells, plastic beads or gel particles. The first attempt to hold a cell stationary in a 2D microchannel consisted of placing obstacles on the droplet path as shown on Fig. 1.3 a). This has been later on used by Huebner *et al.* [41] to hold drops with a tapped obstacle which allows the outer phase to flow through when the trap is empty and forces the outer phase to flow around when a droplet is occupying the spot. The strength of this technique relies on its straightforward parallelization to built large arrays of stationary droplets as shown on Fig. 1.3 b), and its ability to trap several droplets side by side at the same location as shown on Fig. 1.3 c). These arrays were nonetheless randomly filled and chemical labelling of each droplet was required to identify drops. This becomes limiting when aiming at building arrays of paired droplets in order to perform a large number of different reactions on chip. As shown on Fig. 1.3 c), the random filling method lacks robustness as traps are not all filled the same way. In addition, the use of obstacles to stop droplets requires an outer flow for trapping to be efficient, and makes the extraction of a given drop from its trap difficult as the only way out is against the outer flow! As for serial microchannels, the close structure of these traps makes the extraction of droplets difficult.

Another approach consists in working with grooves instead of obstacles. This was first used for gel particles as shown on Fig. 1.3 d) where rigid particles have a fin sliding along a groove etched on the top surface of a microchannel. Abbyad *et al.* [42] suggested to transpose this method to deformable objects such as droplets. Indeed, while rigid obstacles act as repulsive regions that droplets cannot enter, indentations act as attractive regions where droplets preferably sit as they lower their surface energy at the indentation location. Guiding and trapping can therefore be achieved using grooves of various shapes. Parallelization of traps is also straightforward using standard lithography as shown on Fig. 1.3 e) and droplets are easily individually detached from their trap as droplets do not touch directly the channel surface. On the downside, the resulting arrays are randomly filled. Droplets can nonetheless be actively placed in these arrays as they can flow between traps and as they interact weakly with each other in wide microchannels.

Hereafter, we explain in more detail the mechanism which allows droplets to decrease their surface energy by sitting on indentations and look at two practical indentations, namely *anchors*, which are circular pockets to hold droplets stationary, and *rails*, which are linear grooves to guide droplets along their direction.

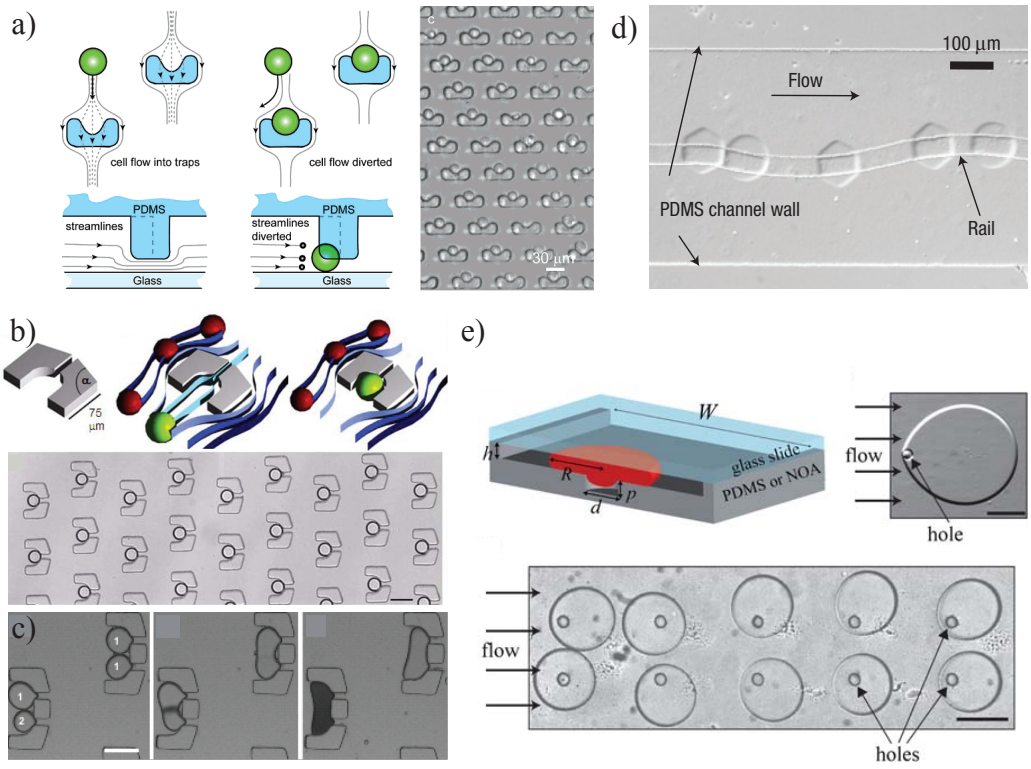

Figure 1.3: a) Obstacles to trap cells. From Di Carlo *et al.* [43]. b) Obstacles to hold a single drop per trap. Huebner *et al.* [41] c) Obstacle to hold two drop per trap. From Huebner *et al.* [44]. d) Groove etched on the top surface of a microchannel in order to guide particles of gel. From Chung *et al.* [45]. e) Circular indentation called *anchor* to hold a single drop per trap. From Abbyad *et al.* [42].

1.2 Gradients of confinement for passive droplet manipulation

Squeezed droplets can move spontaneously when they feel a change in confinement. The underlying driving force is then proportional to the local gradient of confinement experienced by the drop. In this section, we start by recalling the physics behind this phenomenon. Then, we shed some light on the mechanism through which indentations in the channel height can actuate droplets in a 2D microchannel.

1.2.1 Surface tension and the Young-Laplace equation

The first account that gradients of confinement can act mechanically on droplets dates back to 1710. At the time, Hauksbee [46], one of Newton's assistants, observed that a droplet of oil, squeezed between two glass plates forming a wedge, moves spontaneously to the thinnest part of the wedge as shown on Fig. 1.4. Hauksbee accounted for this observation

by assuming an attractive force of surfaces upon liquids, which increases as the distance between the plates decreases. The origin of this mysterious force has puzzled scientists for nearly a hundred years as it took 77 years for the concept of surface tension to emerge (Monge, 1787 [47]) and another 31 years for its mathematical translation, which explains Hauksbee's account, to be derived (Young, 1805 [48] and Laplace, 1808 [49]).

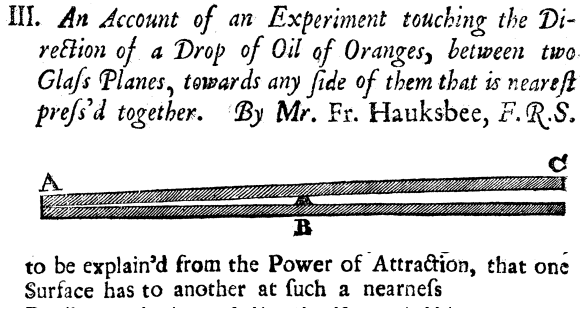
III. *An Account of an Experiment touching the Direction of a Drop of Oil of Oranges, between two Glaſs Planes, towards any ſide of them that is neareſt preſs'd together.* *By Mr.* Fr. Hauksbee, *F.R.S.*

to be explain'd from the Power of Attraction, that one Surface has to another at ſuch a nearneſs

Figure 1.4: Hauksbee's experiment and his explanation for the motion of a drop of oil of orange toward the thinnest side of the wedge. From Hauksbee [46].

Surface tension: Force point of view

Cohesion of matter is ensured by attractive interactions between the constitutive atoms or molecules. These cohesive interactions are a material property and thus change from one material to another. As a result, atoms or molecules near the interface between two phases feel different attractive forces from each phase, and can thus be pulled toward one side of the interface or the other. To account for this contrast in attraction localized at the interface, an interfacial tension, denoted γ, is introduced. This is a force per unit length (in N/m), analogous to a spring stiffness, which pulls the interface in every direction with a magnitude γ.

In the case of an interface separating non-miscible fluids, the interface can deform and thus curves into a rounded shape because of the difference of molecular attraction on each side of the interface. In static equilibrium, the sum of the forces acting upon a unit segment of interface must balance. As a result, the pressure forces pushing on each side of a unit segment ds of the interface must balance the tension forces acting at the edges of the segment as shown on Fig. 1.5 a). This yields the famous Young-Laplace equation:

$$\gamma\boldsymbol{\kappa} \;=\; p^{+} - p^{-} \tag{1.1}$$

where γ is the interfacial tension, $\boldsymbol{\kappa}$ is the mean interface curvature and $p^{\pm}$ are the pressures on either side of the interface.

Furthermore, any contrast of γ creates a flow along the interface from the low to the high surface tension region. This interfacial flow then entrains the surrounding fluids on

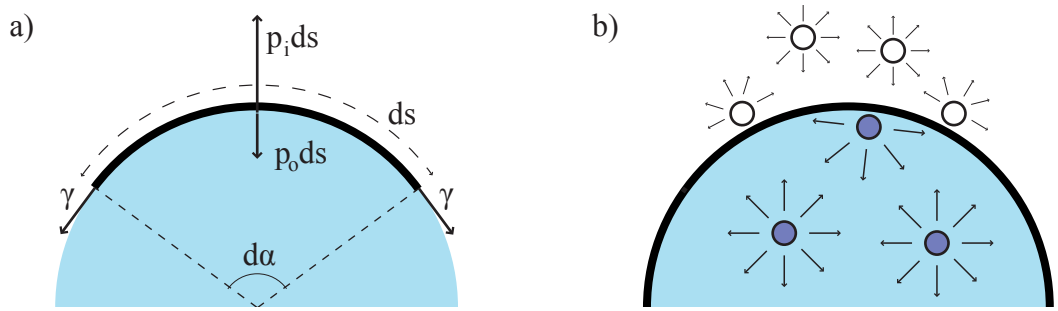

Figure 1.5: a) Force balance acting upon a unit segment ds of interface when there is no flow in the fluid phases. b) Molecular origin of surface tension. Molecules near the interface lacks neighbors to interact with and thus deposit part of their internal energy U at the interface. The deposited energy is the interfacial free energy E_γ.

both sides of the interfaces which generates shear stresses at the interface. A balance of the tangential stresses acting upon a unit segment of interface then yields:

$$\frac{\partial \gamma}{\partial \vec{n}} = \mu^+ \frac{\partial \vec{u}^+}{\partial \vec{n}} - \mu^- \frac{\partial \vec{u}^-}{\partial \vec{n}} \tag{1.2}$$

where $\vec{u}^\pm$ are the velocity vectors on either side of the interface, $\mu^\pm$ are the fluid viscosities on each side of the interface, $\vec{n}$ is the outer normal to the interface and $\frac{\partial}{\partial \vec{n}}$ is the gradient operator along the interface.

These two relations can be further combined to yield the generalized Young-Laplace equation:

$$\boldsymbol{\sigma}^+.\vec{n} - \boldsymbol{\sigma}^-.\vec{n} = \gamma \boldsymbol{\kappa} - \frac{\partial \gamma}{\partial \vec{n}} \tag{1.3}$$

where $\boldsymbol{\sigma}$ are the local stress tensors on either side of the interface.

Surface tension: Energy point of view

Equivalently, surface tension can be thought of as an energy per unit area (in J/m^2). The physical picture reads as follows. In the bulk of a liquid, molecules share some internal energy U with their neighbors. Near the interface, these molecules are unhappy as they lack neighbors to share their internal energy with and thus deposit some free energy at the interface as shown on Fig.1.5 b). As a result, the larger the interface surface area A, the larger the amount of energy deposited at the interface E_γ. The interfacial tension γ is then defined as the link between E_γ and A:

$$E_\gamma = \gamma A \tag{1.4}$$

More rigorously, the interfacial tension corresponds to the free energy that must be supplied to increase the area of an interface by one unit at fixed temperature T, fixed volume of the system V and fixed number of molecules in the system n [50]:

$$\gamma = \left.\frac{\partial E_\gamma}{\partial A}\right|_{(T,V,n)} \tag{1.5}$$

As a result, the state of any interface is characterized by its surface free energy E_γ. At equilibrium, E_γ reaches a minimum of the interface free energy landscape. Out of equilibrium, there is a potential force $\vec{F}_\gamma$ tending to restore the static equilibrium. As any potential force, $\vec{F}_\gamma$ is given by the local gradient of surface energy ∇E_γ:

$$\vec{F}_\gamma = -\vec{\nabla} E_\gamma \tag{1.6}$$

The next subsection makes use of $\vec{F}_\gamma$ to manipulate droplets in 2D microchannels.

1.2.2 A first experiment in a 2D microchannel

The basic 2D microchannel is a wide test section with a width w and a length l much larger than its height h as shown on Fig. 1.6. This channel geometry, essentially consisting of the thin gap between two parallel plates, is classic in the fluid mechanics literature and refered as a Hele-Shaw cell. Both single phase [51] and multi phase flows [52] have thus been studied in this geometry.

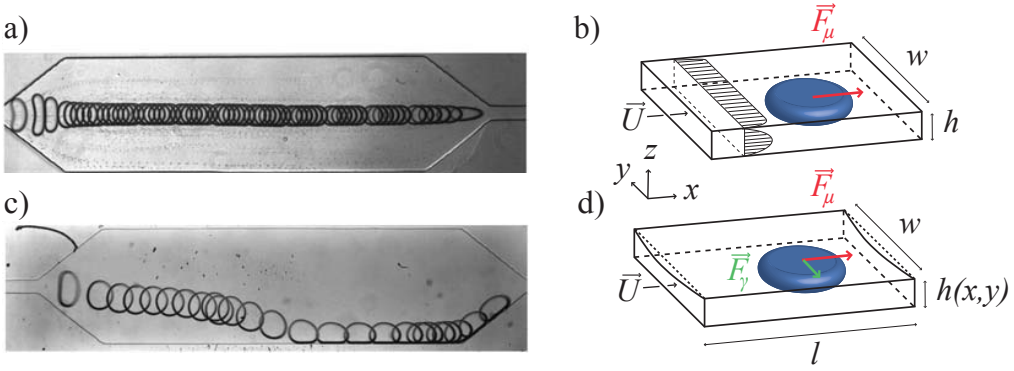

Figure 1.6: a) Superposed positions of a water droplet in paraffin oil at different time point. b) Cartoon of the corresponding situation. The droplet is squeezed between parallel plates and is only pushed by the outer drag $\vec{F}_\mu$. c) Superposed position of a water droplet in silicone oil V100 at different time point. b) Cartoon of the corresponding situation. The channel roof has deformed into a rounded shape which yields local slopes in the channel height exerting a force $\vec{F}_\gamma$ upon the droplet. From Dangla *et al.* [53]

In such a high aspect ratio microchannel, the laws of fluid motion reduce to the linear Darcy's law. The flow of the outer fluid applies a drag force $\vec{F}_\mu$ on the droplet through hydrodynamic drag. This force is always directed in the direction of motion of the outer fluid and its magnitude depends strongly on the droplet surface area, hence the droplet shape. In our experiments, we mostly consider droplets flattened between two flat plates. Then, the droplet shape is close to a cylinder of height h and in-plane radius $R \gg h$. The drag force on such drop is then known to scale as $F_\mu \sim \mu^{out} U^{out} R^2/h$, where μ^{out} and U^{out} are the outer fluid viscosity et velocity [54]. This scaling has been validated by asymptotic analyses of two limit cases: (i) the Hele-Shaw flow around a stationary inviscid bubble [55] and (ii) the Hele-Shaw flow around a rigid cylinder [56]. $\vec{F}_\mu$ therefore increases with the flow velocity and depends strongly on the size of the droplet.

As a result, droplets pushed down a Hele-Shaw cell by an outer flow are expected to follow the streamlines of the carrier fluid. This prediction was tested experimentally by Dangla *et al.* [53]. In the experiment shown on Fig.1.6 a) and c), the trajectory of a drop in a wide microchannel made of PDMS was measured for different pairs of fluids. Droplets were expected to flow straight from the inlet to the outlet, but was observed to depart from their predicted trajectory for few pairs of fluids as shown on Fig.1.6 c). Thus, instead of being simply pushed by the outer drag $\vec{F}_\mu$ along the outer flow, droplets were also experiencing a transverse force $\vec{F}_\gamma$. The origin of $\vec{F}_\gamma$ was further attributed to local deformations of the microchannel, which had swollen due to oil imbibition into PDMS. Indeed, instead of being pressed between parallel plates, droplets were rather squeezed in a wedge as shown on Fig. 1.6 d), where one side of the drop is more constrained than the other. This creates an imbalance in Laplace pressure across the droplets which pushes the drop toward the wider part of the wedge until the drop reaches the side wall of the microchannel.

The origin of $\vec{F}_\gamma$ can also be explained in terms of surface energy as droplets behave so as to minimize their surface energy. The surface energy of a droplet can be written as $E_\gamma = \gamma A$, where γ is the interfacial energy and A the surface area of the droplet. While γ can be considered as nearly constant over the course of the experiment, A varies significantly as the droplet changes its shape by moving along the wedge. Unconfined drops take a spherical shape in order to minimize their surface area, and hence their surface energy. On the other hand, droplets confined between the top and bottom walls of a 2D microchannel are constrained to flatten along the channel wall and can only curve away from these walls. Consequently, they adopt a pancake shape of much larger surface area, and thus seek for opportunity to decrease their surface area. As a result, when pressed in a wedge, droplets moves toward the wider part of wedge in order to be as spherical as allowed by the wedge top and bottom walls, thereby lowering their surface energy.

This first experiment shed some light on the ability of gradients of confinement to act on droplets in a 2D microchannel. Thanks to standard lithography or micro milling techniques, the height of a microchannel can be precisely controlled and one can thus taylor

the surface energy landscape of droplets in 2D microchannels in order to manipulate them passively.

1.2.3 Two patterns of interest: Rails and anchors

Two patterns of interest were studied: *Anchors* which refers to localized pockets of increased channel height and *rails* which are linear grooves etched on top of the base 2D microchannel.

In a first experiment, rails were shown to guide droplets along a prescribed path. As shown on Fig. 1.7 a), a droplet flowing down a 2D microchannel follows a sinuous rail which enables the droplet trajectory to have some angle with the outer drag $\vec{F}_\mu$. Rails define valleys of surface energy in which droplets are trapped. Consequently, as the outer drag pushes a drop out of the valley, the droplet experiences a restoring force $\vec{F}_\gamma$ due to its increase in surface area. In addition, $\vec{F}_\gamma$ has to be perpendicular to the rail direction as the gradient of the droplet surface energy is the largest along that direction. As a result, when the rail has some angle with the outer drag $\vec{F}_\mu$, the holding force $\vec{F}_\gamma$ balances a part $\vec{F}_\mu^{\perp}$ of the outer drag and a remaining unbalanced component $\vec{F}_\mu^{\parallel}$ of the outer drag propels droplets along the rail as shown on Fig. 1.7 b).

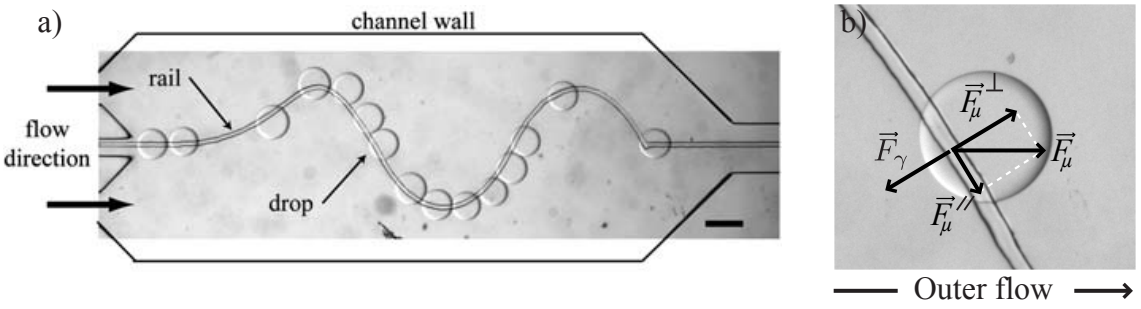

Figure 1.7: a) A proof of concept experiment. The channel height is 100 μm, the rail width and height are both 50 μm. The image shows a superposition of a droplet position at different time points to yields its trajectory. The droplet follows a sinuous rail. From Abbyad *et al.* [42] b) Force balance of a droplet on a rail.

In a second experiment, anchors were shown to hold droplets stationary against an outer flow as shown on Fig. 1.8 a). Similarly to rails, anchors are localized minima of surface energy and as such, there is an energy barrier to escape them. As a result, when an outer flow pushes a drop out of an anchor, the droplet experiences a restoring force tending to keep it in the anchor. Droplets can thus be held stationary against an outer flow. When the outer fluid velocity is increased, a drop in an anchor is deformed from its circular shape by the increased outer drag up to a critical outer velocity $U^\star$ at which point the drop cannot be held anymore and is unpinned by the outer flow [42]. Thus,

for given drop and channel geometries, we can measure the critical velocity $U^\star$ beyond which the outer drag overcomes the anchoring force ($F_\mu \geq F_\gamma$) in order to estimate F_γ. The holding force of an anchor was shown to range between 1 nN and 1000 nN for typical microchannel dimensions, and to not depend on the droplet size R, but only on the channel geometry [57].

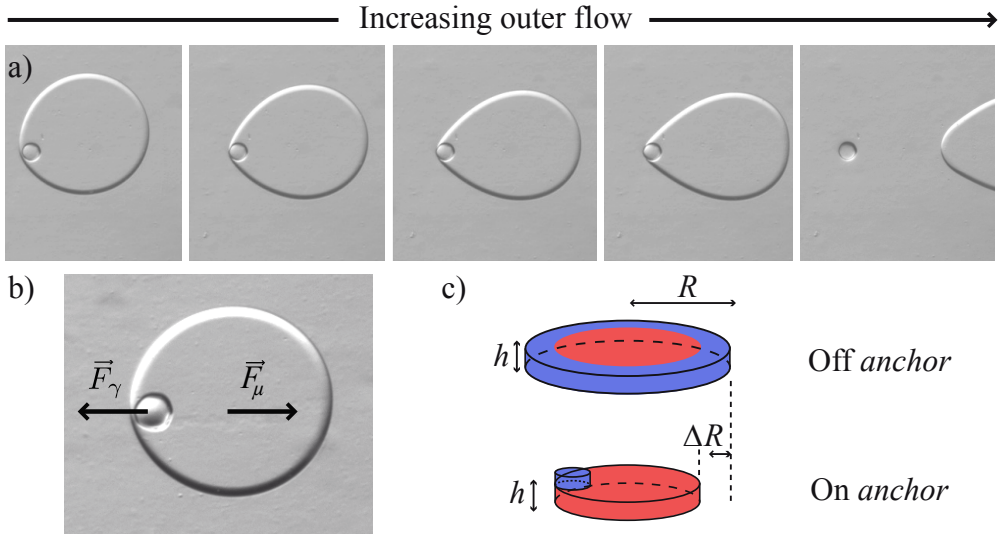

Figure 1.8: a) An anchor can hold a droplet against an outer flow up to a critical outer velocity $U^\star$. The channel height is 100 μm and the anchors diameter and height are both 50 μm. b) Force balance on a trapped droplet. c) Sketch of the change in surface area when a droplet sits on an anchor.

This result can be understood as follows. In a 2D microchannel, droplets are squeezed between the top and bottom walls of the channel and as such, drops adopt a pancake shape. In the plane of the microchannel, one can thus describe the drop by its radius R; in the case when $R \gg h$, the main contribution to the surface area is given by the top and bottom boundaries of the droplet and we can write $A \approx 2\pi R^2$, with a small correction due to the area around the drop in the vertical direction. As a result, a droplet sitting *off* anchor has a surface energy $E_\gamma \approx 2\pi\gamma R^2$. As a droplet enters an anchor, part of its volume is transferred into the anchor so that its in-plane radius has to shrink by ΔR as shown on Fig. 1.8 c). Consequently, both the droplet surface area and surface energy are lowered. A detailed study of the droplet geometry can be found in Dangla *et al.* [57] and yields an exact expression for the anchor holding force $\vec{F}_\gamma$.

An important regime concerns velocities that are slightly below the critical velocity. In this regime, the anchor strength is sufficient to hold one droplet stationary but not two, since the net drag force experienced by the touching pair increases while the anchoring force remains constant. Abbyad *et al.* [42] identified a range of velocities where drops enter

into a *buffering* mode, in which an incoming drop replaces the drop that was previously anchored. This buffering regime will be used in Chapter 2 to selectively place droplets in a large array of anchors.

The strength of this technique relies on its simplicity, its robustness, and its favorable scalings with the droplet size R which allow to consider massive parallelization and miniaturization. Droplets can be trapped and detached by playing on the outer phase flow, droplets can be guided to the side of a 2D microchannel and very large arrays of droplets can be created by straightforward parallelization. Nonetheless, the resulting arrays lack addressability as discussed in section 1.1.3: Arrays are randomly filled, and the extraction of a drop from an anchor using an increased outer flow will affect the surrounding trapped droplets. Consequently, the rails and anchors technique would greatly benefit from an active droplet manipulation technique on top of it in order to build large, addressable arrays of droplets. In the same way, interconnecting rails has proven challenging as the interconnection itself is a site of lower confinement where droplets preferably sit. As a result, interconnections between rails create traffic jams problems which can be solved by using an active droplet sorting method. More generally, active droplet manipulations add selectivity to the droplet operations amenable using the passive rails and anchor technique.

1.3 Active droplet manipulation using a laser

In this section, we discuss the different active techniques used to manipulate droplets in microchannel, and describe in more detail the actuation of droplets by a laser which is the active technique we have chosen in our experiments.

1.3.1 Available techniques

Most available techniques to actively handle droplets in a microfludic channel were first developed and used to handle microparticles such as functionalized plastic beads or cells. When working with such microparticles, a common problem consists of sorting a large population against a given criterion, say, the expression of a protein in a cell, or wether an antigene has bound to an antibody stuck on the surface of a bead or not. To this end, the gold standard is the FACS machine (Fluorescence Activated Cell Sorting). It originally dealt with diluting a cell solution and let it flow through a dripping faucet where cells were encapsulated into droplets as shown on Fig. 1.9 a).Then, droplets could be deviated from their trajectory by using an electric field. The full set up is shown on Fig. 1.9 b) and was first patented by Coulter in 1953. The throughput of this device can be massively increased by working in microchannel. Baret *et al.* [58] proposed such a use of microfluidics called FADS (Fluorescence Activated Droplet Sorter) as shown on Fig. 1.9 c).

From this push from the FACS application, many techniques were proposed to actively sort a train of droplets arriving at a T- or a Y-junction, some like electrodes being embeded

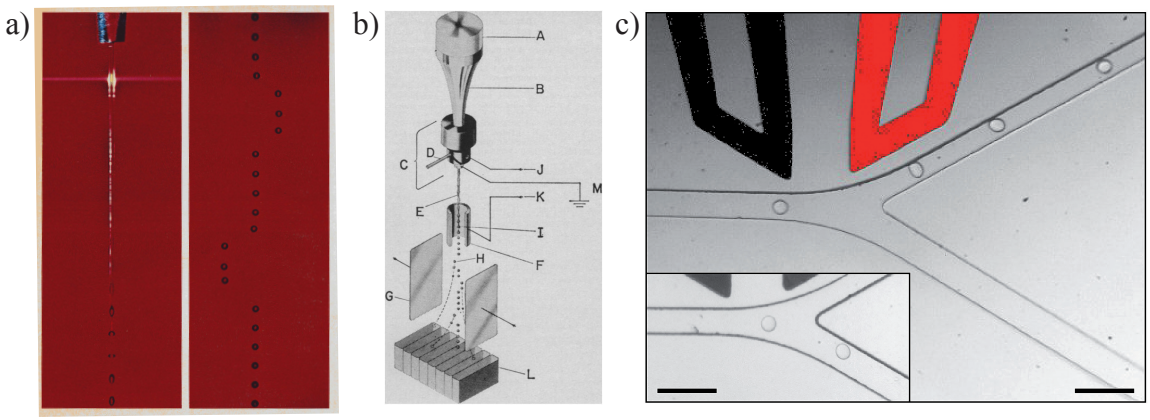

Figure 1.9: FACS machine. a) A dripping faucet produces droplets which can be deviated from their vertical trajectory by an electric field. From Herzenberg *et al.* [59]. b) Schematic of a cell sorter using electrodes. From Fulwyler *et al.* [60]. c) Cell sorter based on droplet microfluidics. A diluted solution of cells is emulsified into droplets. Each droplet contains at most one cell. Electrodes are used to separate empty droplets from the rest. Baret *et al.* [58].

on chip, other requiring extra equipment off chip to generate the outer stimulus.

To date, the most used active droplet manipulation technique makes use of electrodes embeded on chip as shown on Fig. 1.10 a). Here, the electric field generated by two oppositely charged electrodes was shown to deviate a droplet from its mean trajectory by charging oppositely the two sides of a drop surface, thereby creating an electric dipole sensitive to the outer electric field. Similarly, gradients of surface tension can be created by heating locally the droplet interface. This was achieved using a laser as shown on Fig. 1.10 b). Another way to sort trains of droplets can make use of magnetic fields when droplets are initially seeded with magnetic beads as shown on Fig. 1.10 c). Here, there is no surface tension gradients generated. Beads are simply held at a given location by the magnetic field and thus prevent the droplet from deviating from that location. Finally, surface acoustic waves were recently shown to achieve droplet sorting in a conventional PDMS microchannel. In this last example, the floor of a microchannel is mechanically attached to an oscillating piezoelectric transducer. Acoustic waves, with amplitudes in the nm range, thus propagate along the microchannel floor surface and pushes droplets along their direction as shown on Fig. 1.10 d).

The choice of one of these techniques among the rest is not obvious, each of them having pros and cons in their operation, and depends strongly upon the skills developed in a given lab. For instance, electrodes are not transparent and were thus placed around microchannels which limits the magnitude of the reachable electric field and becomes limiting when working with wide 2D microchannels. ITO electrodes were designed to this end [65] but

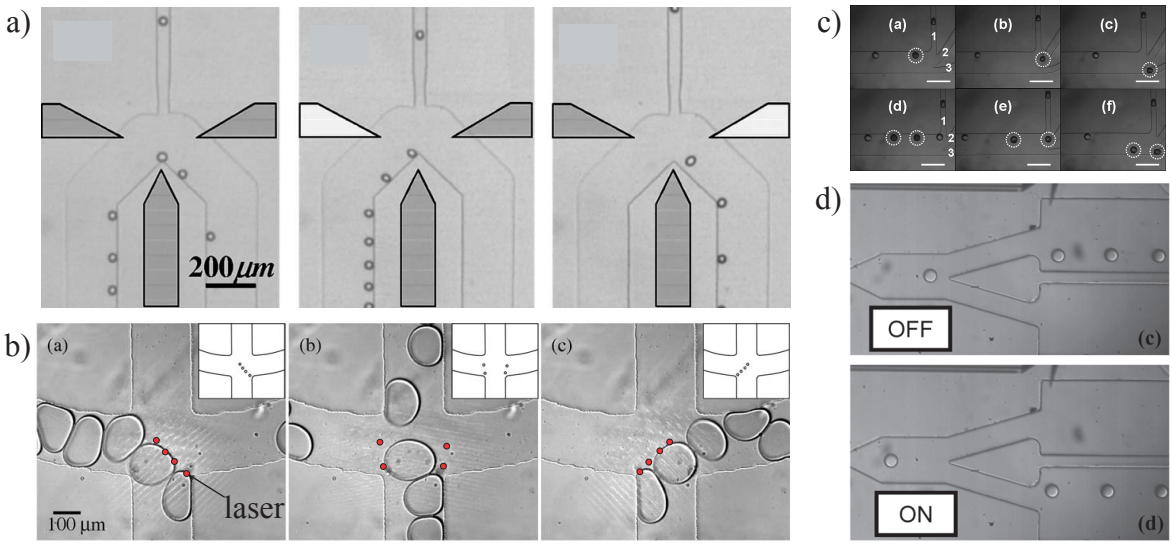

Figure 1.10: Active technique for droplets manipulation. a) Electrodes. From Ahn *et al.* [61]. b) Laser actuation. From Cordero *et al.* [62], c) Magnetic beads. From Zhang *et al.* [63]. d) Surface Acoustic Waves. From Franke *et al.* [64].

the microchannel fabrication gets much more complex. Similarly, magnetic beads limit the observation of droplets content and usually require large solenoids to be operated. Our lab having an expertise in droplet manipulation using lasers, we naturally opted for this solution which is explained in detail below.

1.3.2 Optical toolbox

To my knowledge, the idea of using a laser to actuate droplets through heat was first proposed by Kotz *et al.* [66]. A complete optical toolbox for droplet manipulation in microchannel was then developed by Baroud *et al.* [34], demonstrating complex operations such as sorting, pairing or merging droplets.

The local heating induced by a laser was first shown to block droplets pushed along a linear microchannel as shown on Fig. 1.11 a). Thus, the laser induces a net force which pushes the droplets away from the hot spot. This blocking force was then used to route droplets through a bifurcation as shown on Fig. 1.11 b), or to delay the droplet formation at a T-junction and thus perform a valve function as shown on Fig. 1.11. c). The laser was also shown to push droplets in 2D microchannels. Further applications were thus demonstrated. For instance, sorting droplets in wide microchannel was demonstrated as shown on Fig. 1.11 d). Lastly, droplets of a closed-pack train of droplets were merged by a static laser spot as the droplet-droplet interface was passing by as shown on Fig. 1.11 e).

The strength of this technique is therefore manifold. At the droplet level, a mobile

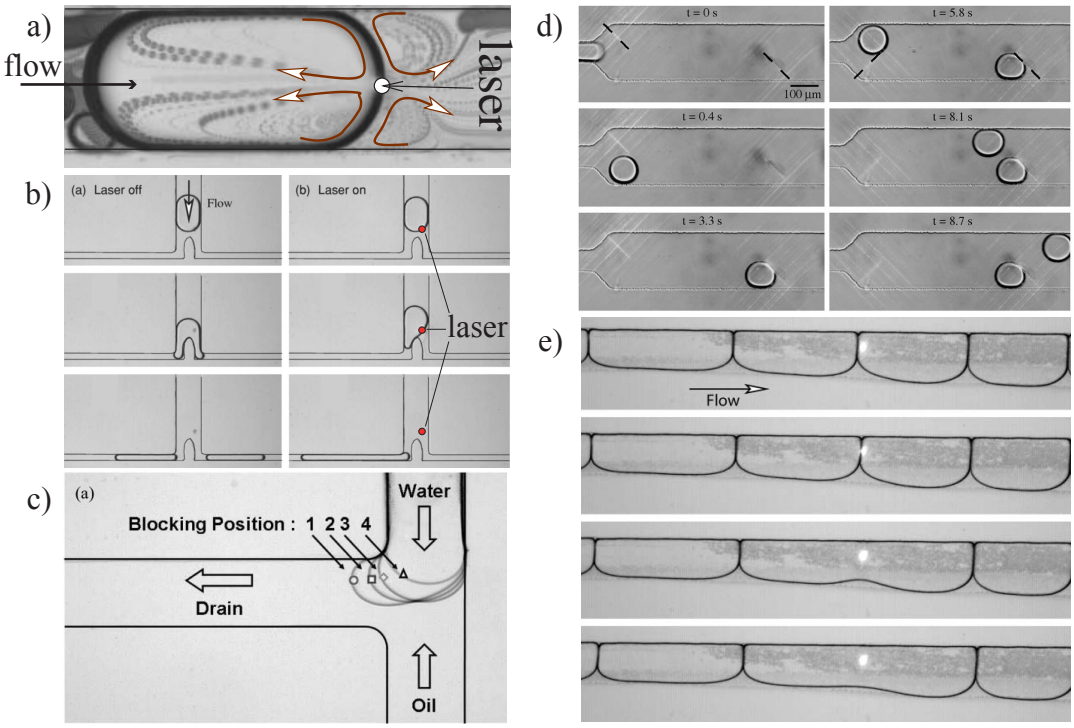

Figure 1.11: Optical toolbox. a) A droplet blocked by a laser spot. From Baroud *et al.* [67] b) Sorting droplets in a 1D microchannel. c) Valve. d) Sorting droplets in a 2D microchannel. e) Merging a train of drops. b) to e) are from Cordero *et al.* [62].

laser spot can push a drop in any direction and merge two droplets which demonstrates a great versatility. Parallelization is also amenable as holographic [68] or generalized phase contrast [69] methods allow to split a single laser beam into many independent spots. Lastly, an integrated version of this technique is already commercially available in any DVD writer. On the downside, high frequency actuation is limited by a heating time of a few ms needed to act upon droplets. In addition, the heating induced by the laser might have some effect on the droplet content. The stationary temperature field of a laser spot heating a 28 μm thick layer of water was measured. The temperature field was found to have a lorentzian shape centered on the laser spot, peaking at 80 °C and going back to the ambient on $\sim$20 μm [70]. However, the effect of this temperature field on the drop content has not been measured and is not obvious as it should take into account the fluid motion in the drop. Hereafter, we explain the physics behind the laser pushing force and we present a scenario for the laser induced coalescence of two drops.

1.3.3 Origin and magnitude of the laser force

The laser force $\vec{F_\lambda}$ was studied in detailed by Verneuil *et al.* [71] in a laterally confined microchannel. Their test section consists of a straight microchannel bypassed by a loop channel which droplets cannot access as pillars have been placed at the entrance and exit

of the loop as shown on Fig. 1.12 a). Thus, a droplet can be blocked in the test section by a laser spot, and the back pressure Δp (which yields $\vec{F_\lambda}$) that the droplet is experiencing can be estimated via the product of the outer oil flow rate Q and and the test section hydrodynamic resistance R^{hyd}:

$$\Delta p \;=\; R^{hyd}\, Q \tag{1.7}$$

The magnitude of $\vec{F_\lambda}$ was thus measured to be in the range 100-300 nN for a laser power of 100 mW and a channel height of 50 μm. Yet, the origin of $\vec{F_\lambda}$ is subtle. $\vec{F_\lambda}$ is a thermocapillay force induced by the Marangoni flows taking place inside and outside the droplet when it is heated by a laser spot. Verneuil *et al.* also observed that these surface flows were pointing toward the hot spot as sketched on Fig. 1.12 b). This is a key observation as it rules out classic thermocapillary explanation of $\vec{F_\lambda}$. Indeed, as surface tension is usually decreasing with increasing temperature, the local heating induced by the laser alone would create a local drop in surface tension so that the interface would be pulled away from the hot spot, thus creating a surface flow pointing away from the hot spot. This is not consistent with the first observation of Verneil *et al.*.

A second key observation is shown on Fig. 1.12 c). The white thread on that picture corresponds to micelles expelled from the interface after a laser pulse has heated the interface. This shows that, by heating up the interface, the laser spot depletes the interface of its surfactants. This second effect has thus to be taken into account in the explanation of the origin of $\vec{F_\lambda}$. As the surface tension of an interface is usually decreasing with increasing coverage of the interface by surfactant molecules, the local heating of the interface can increase the surface tension at the hot spot by dramatically decreasing the contamination of the interface at that location. Thereby, the interfacial flow points toward the hot spot which is in agreement with the experimental observation of Verneuil *et al.*. This is our understanding of $\vec{F_\lambda}$.

Next, PIV experiments, as shown on Fig. 1.12 d), allowed to resolve the different velocity scales in the different regions. Shear stresses acting upon the drop were shown to have two contributions of different magnitudes. On the one hand, the recirculation region near the hot spot was measured to have high fluid velocities but relatively low shear stresses as shear is mostly induced by the droplet curvature in that region. On the other hand, the thin films separating the droplet from the channel walls was measured to have relatively low velocities but high shear stresses mostly because of the thinness ($\sim$ 100 nm) of the films. As a result, the laser force $\vec{F_\lambda}$ is mostly due to shear stresses in the thin films separating a droplet from the channel walls which highlights the role of confinement in the origin of $\vec{F_\lambda}$ as shown on Fig 1.12 b). Droplets locally heated by a laser can thus be thought as pushing on the channel walls in order to escape the hot spot. Consequently, the more wall surface a droplet is in contact with, the more efficiently it can escape from the hot spot. The magnitude of the laser force has thus to increase with the confinement on the droplets.

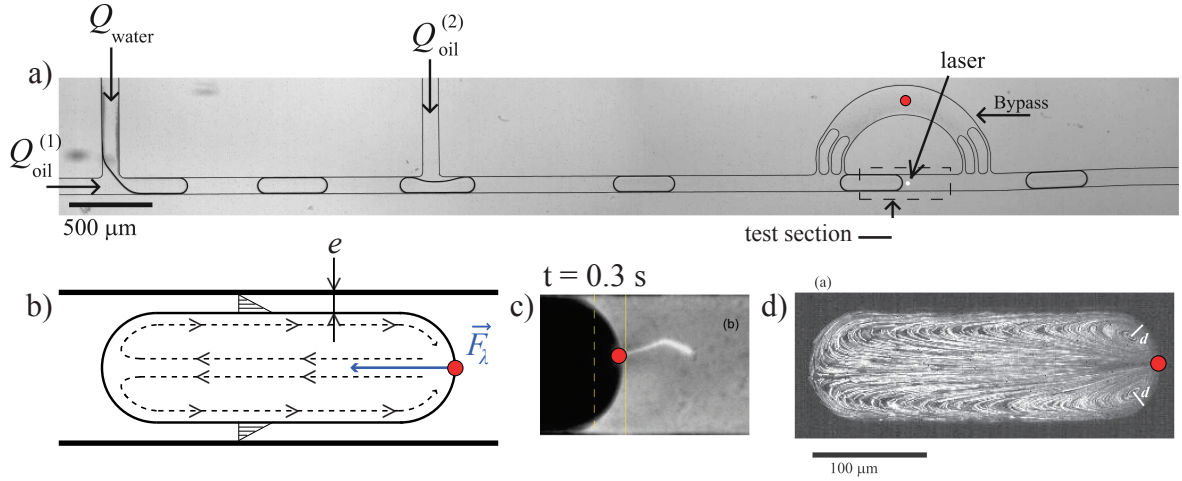

Figure 1.12: a) Test section. b) Sketch of the flow field pointing toward the hot spot, and the shear stresses in the lateral thin films. c) Ejected micelles when the laser heats up the interface. d) Flow field in a long droplet confined laterally. From Verneuil *et al.* [71].

In a 2D microchannel, the laser is therefore expected to push droplets to a lesser extent as in a 1D microchannel since the wall surface in contact with the drop is decreased. A rough estimate of 10 nN is obtained in Chapter 2 by comparing the laser push to the holding force of an anchor. A complete study of the origin and magnitude of the laser force in a 2D mircochannel is yet to be done.

1.3.4 A scenario for laser induced coalescence

The stabilization of droplets by surfactants in microfluidics has been extensively studied [72, 73]. As shown on Fig. 1.13, surfactants are bipolar molecules composed of a hydrophilic head and a lipophilic tail. At equilibrium, surfactant molecules adsorb onto the surface of drops which prevents droplets from directly touching each other. Droplets are thus separated by a thin film of the continuous phase that must drain for coalescence to take place. The commonly accepted stabilization mechanism of surfactant reads as follows. When the thin film separating the two drops drains, there is a flow between the drops (Black dashed arrows on Fig. 1.13) which decreases the surfactant surface concentration between the drops. As a result, there is gradient of surfactant concentration along the interface which creates Marangoni flows inside and outside the droplet. These flows counteract the film drainage by homogenizing the surfactant coverage of the droplets (Red solid arrows on Fig. 1.13) and hence yields an equilibrium thickness of the thin film between the drops.

By constantly depleting surfactants from the interface, the laser overcomes the stabilizing effect of Marangoni flows as it prevents from any homogenization of the surface

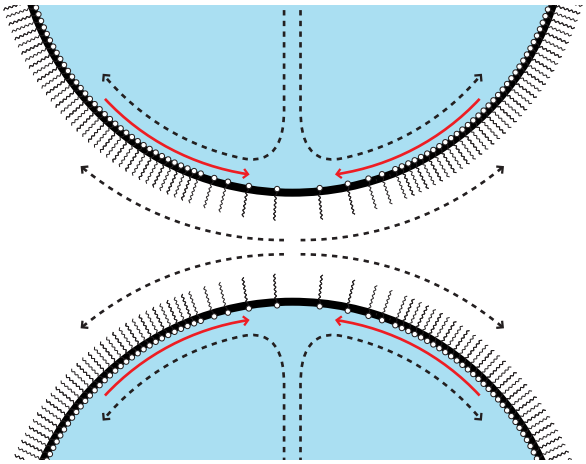

Figure 1.13: Equilibrium of the thin film of the continuous phase separating two droplets. A Marangoni flow (red solid arrows) counteracts the redistribution of surfactant molecules induced by the film drainage (black dashed arrows). [73].

coverage. As a result, the laser breaks the equilibrium of the thin film separating the drops and favors the drainage of the film, eventually leading to the coalescence of the drops. This scenario for the laser induced coalescence should however be confirmed by a complete experimental investigation as other scenarios involving electrostatic repulsions between surfactants molecules, steric effects or interface rigidification due to the surfactants molecules might have to be taken into account . Another key point is the mechanical effect of the contrast in surfactant along the interface. As mentioned in the last subsection, a local drop in the surfactant surface concentration yields a net force tending to push the drop away from the low surfactant region. As a result, when the laser is shined on a droplet-droplet interface, the two droplets are pushed away from each other by the laser force. Droplets need therefore to be held pressed against each other for the laser induced droplet fusion to operate robustly.

1.4 Droplet microfluidics without flow

Testing many different reactions on a single chip to perform multiplexed assays requires ways to bring the different sources of reagents on chip, and perform subsequent operations on these reagents such as dilution series, or combinatorial mixes. Thus, the successful approach to parallelize this set of operations requires each unit operation to be performed as simply as possible in order to keep the complexity of the assembled system as low as possible.

Different solutions exist using droplets which essentially consist in forming a train of droplets with varying formulations [74] and combine droplets of the train [75]. The large

scale parallelization of this serial workflow leads nonetheless to complications, mostly because of the flow of the carrier phase required to form and push the drops down the channel. Another approach consists in not flowing the outer phase. This allows to work with multiple droplet generation units connected to the same microfluidic device, hence yields a great versatility. On the downside, new ways of forming drops without the need to flow the outer phase have to be developed.

In this last section, we discuss the issue of large scale integration of droplet operations on chip in order to build large addressable arrays of droplets, thereby mimicking the microtiter plate format. To date, one of the major bottleneck remains the parallelization of flow based methods to form droplets. Instead, we present a flowless approach based on gradients of confinement which allows to produce droplet on a demand and in parallel.

1.4.1 Continuous flow methods for droplet production

Classic geometries

The amount of droplets produced on a single chip is defined as the product of the number of embeded droplet production units and the droplet generation frequency per unit. Most droplet based systems rely on generation of continuous streams of droplets in one of the three dominant geometries: T-junctions, flow-focusing devices, and coflow devices. A great deal of effort was done to generate droplets at high throughput, which was mostly achieved by injecting fluids faster. As a result, droplets produced in these geometries are generated at a high frequency and transported downstream at a high flow rate. However, the strong flow that advects drops also couples their motion hydrodynamically. Thus, when several droplet production units are connected to the same chip, complex collective behaviors arise from mechanical cross talks between the generators, resulting in either chaotic, quasi-periodic or synchronized regimes of droplet production [76]. The droplet generation frequency and the size of the produced droplet vary from one regime to another, and was shown to be controllable in synchronized regimes only. This highlights the sensitivity to small perturbations in injection rates of continuous flow methods to produce droplet.

An attempt to parallelize flow-focusers and T-junctions was performed by Nisisako *et al.* [77] who achieved to placed 128 injectors next to each other as shown on Fig. 1.14. They also report a high monodispersity but it is not clear what the effective range of injection rates keeps their device controllable [78]. Beyond the mechanical limitations of continuous flow methods toward parallelization, another limitation concerns the large scale integration of these droplets generation devices. Indeed, for each reagent inlet, these techniques require another inlet for the outer phase which limits the number of connecting points to the chip available to deliver different reagents.

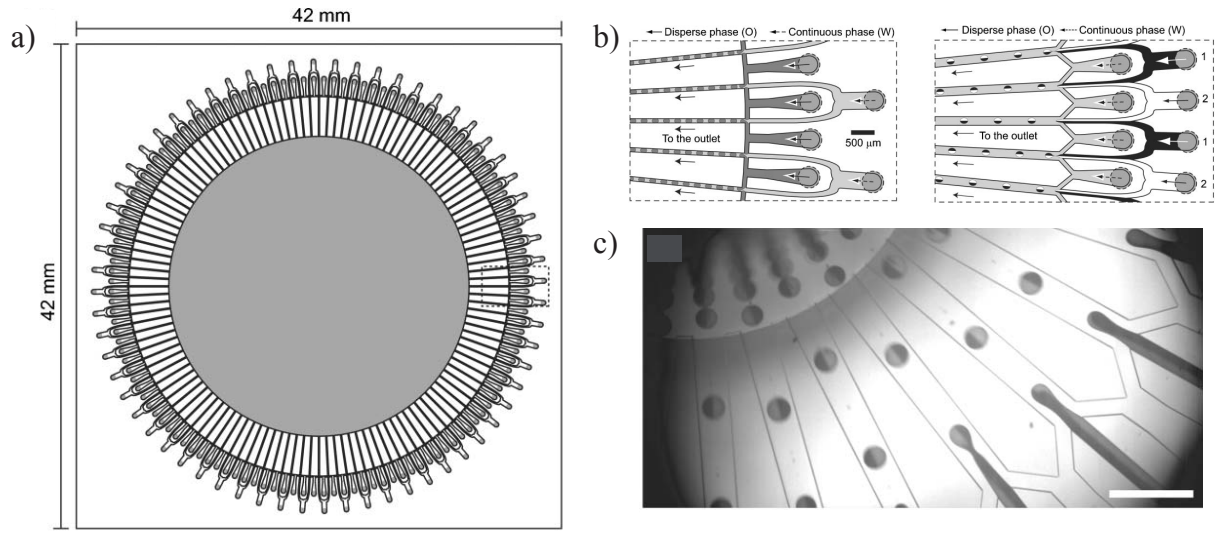

Figure 1.14: a) Continuous flow unit for droplet generation arranged along a circle. b) The device can be run in T-junction mode and in flow-focusing mode. c) Experimental picture in the FF mode. From Nisisako*et al.* [77]

Gradients of confinement for droplet production

To address these last limitation, another approach to design parallelized droplet generators consists in not flowing the outer phase when forming droplets. As a result, a single inlet for the outer phase is required, the rest of the connecting points to the chip being available for different dispersed phases. This has been achieved through an intelligent design of the channel geometry. Mimicking the step emulsification technique, Sugiura *et al.* designed a double steps junction able to produce droplet without the need to flow the outer phase. As shown on Fig. 1.15 a) and b), their device consists of a straight inlet channel connected to a large reservoir where the height of the channel has been slightly increased nearby the inlet channel, and greatly increased further downstream. Various geometry were tested later on, including the single step junction shown on Fig. 1.15 b).

The first step to operate this device consists in filling the microchannel with a fully wetting continuous phase. Next, the dispersed phase is injected through an inlet channel. As a thread initially flowing in an inlet channel, enters the large reservoir it expands into a cylindrical bulb as shown on Fig. 1.15 a) and b). For a given size of the bulb, the thread in the inlet channel necks, thereby forming a droplet. In Suguria's device shown on Fig. 1.15 a), the cylindrical bulb also meets a second step junction where it is allowed by the increased channel height to expand vertically, which promotes droplet formation. These devices were shown to produce ~ 1 droplet per second, which badly compares to the kHz rates of flow focusing devices. This low throughput is nonetheless compensate by a straightforward parallelization of the injectors which yields an overall throughput in the kHz range. In addition, this technique yields emulsions with a high monodispersity as

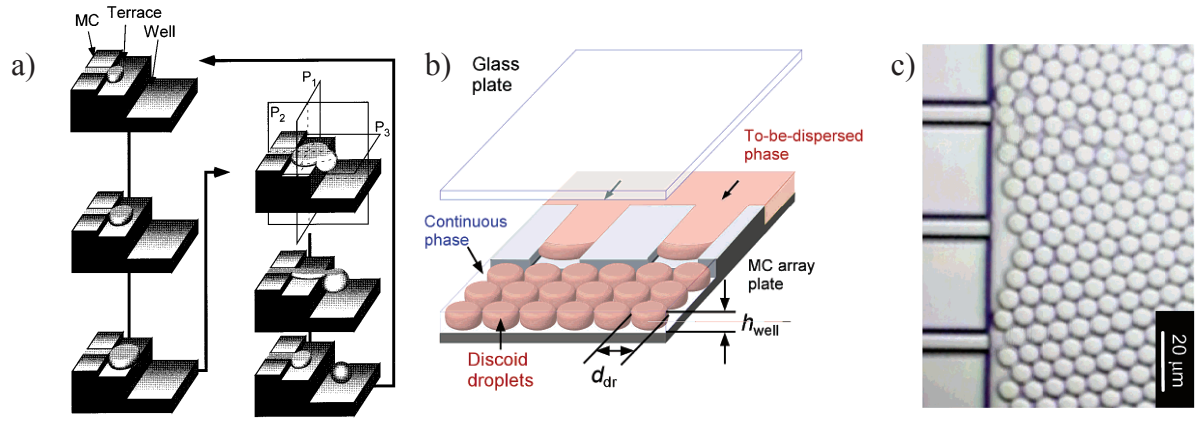

Figure 1.15: a) Two steps junction forming a terrace. From Sugiura *et al.* [79]. b) Single step junction. From Kobayashi *et al.* [80]. b) Large scale production of mono disperse droplets. From Kobayashi *et al.* [80]

shown on Fig. 1.15 c).

More recently, Dangla *et al.* [20] proposed another geometry to produce droplets with gradients of confinement as well as an explanation for the mechanism at play in the droplet formation process. As shown on Fig. 1.16 a), their device consists of a straight inlet channel connected to a large reservoir of inclined roof. As a non-wetting thread enters the reservoir, it expands radially into a cylindrical bulb shape while being pulled downstream by a potential force $\vec{F}_\gamma$ induced by the gradual release of vertical confinement. Here again, when the bulb reaches a critical size, the thread in the inlet necks and forms a drop. Then, this drop displaces spontaneously further downstream as it is squeezed in a wedge.

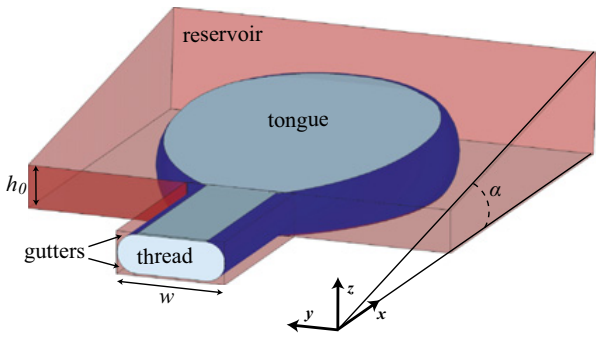

Figure 1.16: Wedge junction geometry. The thread expands into a bulb in the reservoir while being pulled by the gradient of confinement induced by the wedge.

The physical mechanism of droplet formation by deconfinement

Dangla *et al.* further pointed out three key observations: (i) Necking of the interface takes place in the inlet channel, (ii) there is no droplet formation in a flat reservoir, and (iii) droplets of finite size are produced, even at very low injection rates.

The observation (iii) led the authors to assume that the interface evolves in a quasi-static manner, *i.e.* that the interface around the thread and the bulb is at each instant in an equilibrium state. In this case, the Young-Laplace equation (1.1) imposes that the shape of the interface must be such that its mean curvature $\boldsymbol{\kappa}$ is constant over the entire interface, apart from the regions where it is pressed against a channel wall and forced to follow the wall geometry. Yet, the constraints on the interface differ in the inlet channel and in the reservoir. The mean curvature $\boldsymbol{\kappa}$ can be decomposed into a vertical component $\boldsymbol{\kappa}^{\perp}$, normal to the microchannel plane, and an in-plane component $\boldsymbol{\kappa}^{\parallel}$:

$$\boldsymbol{\kappa} \;=\; \boldsymbol{\kappa}^{\perp} + \boldsymbol{\kappa}^{\parallel} \tag{1.8}$$

In the reservoir, the curvature of the thread decreases as the thread expands into the reservoir for two reasons. First, the in-plane radius of the thread R increases as more fluid is injected as shown on Fig. 1.17 a). This leads the in-plane curvature $\boldsymbol{\kappa}^{\parallel} \sim 1/R$ to decrease. Second, the vertical confinement on the thread decreases as the thread propagates down the reservoir, hence the vertical curvature of the thread $\boldsymbol{\kappa}^{\perp} \sim 1/h$ decreases too.

In the inlet channel, the in-plane curvature of the thread is null at first (top picture of Fig. 1.17 a)), while the vertical curvature is fixed by the curved pieces of interface near the corners of the inlet channel cross section (top picture of Fig. 1.17 b)). As fluid is injected, the curvature of the downstream part of the thread decreases, thus forcing the upstream curvature to decrease because of the mechanical equilibrium at play. As a result, the interface in the inlet channel departs from the side walls of the channel in order to decrease its vertical curvature $\boldsymbol{\kappa}^{\perp}$. However, this holds true up to a criticial point at which the vertical radius of curvature reaches the channel half-height $h/2$: $\boldsymbol{\kappa}^{\perp} \sim 2/h$ (middle picture of Fig. 1.17 b)). At this point, no further release of vertical curvature is allowed by the channel geometry without leading to the unphysical situation shown on the bottom picture of Fig. 1.17 b).

As a result, the interface in the inlet channel has to bend inward to adopt a negative in-plane curvature $\boldsymbol{\kappa}^{\parallel} < 0$, and hence further decrease its mean curvature $\boldsymbol{\kappa}$ (middle picture of Fig. 1.17 a)). At this criticial point, the static equilibrium does not hold anymore, a pressure imbalance appears in the outer phase, creating a flow from the reservoir to the inlet channel, which promotes necking, and leads to droplet formation (bottom picture of Fig. 1.17 a)).

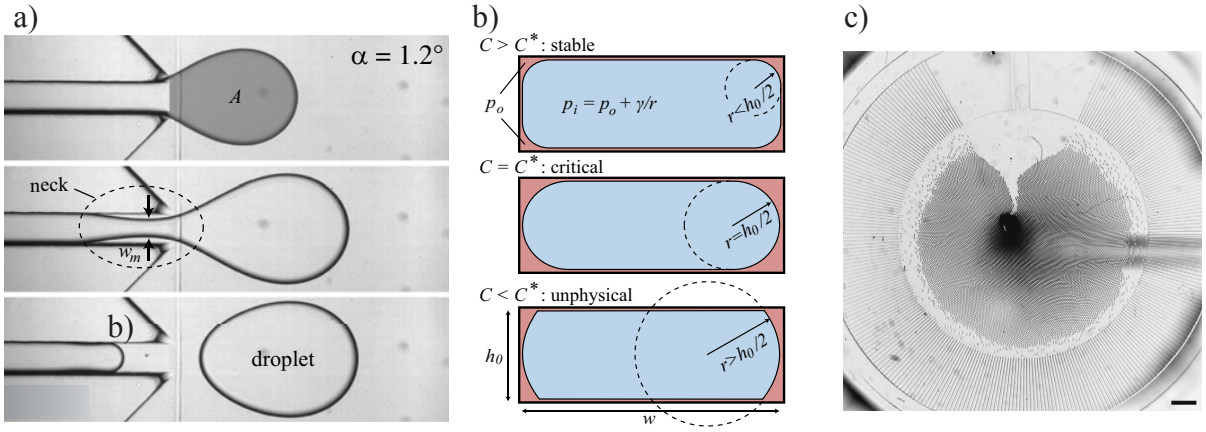

Figure 1.17: a) The three distinct steps of the droplet formation mechanism: (i) Inflation of the thread into a bulb, (ii) Necking in the inlet channel and (iii) Pinch off to form a drop. b) Cross section of the thread in the inlet channel for three value of the mean curvature $\boldsymbol{\kappa}$: *Top* High vertical curvature, the interface flattens against the side walls of the channel. *Middle* Critical vertical curvature. The interface is touching the side walls of the channel. It cannot decrease its vertical curvature any further without violating the non-wetting boundary condition. *Bottom* Below the critical vertical curvature. The interface presents a kink. This situation is not physical. c) Parallelization of wedge junctions along a circle. The reservoir is in the center, the inner phase is inject inward.From Dangla *et al.* [20].

To sum up, the sudden release in confinement in this channel geometry forces the interface in the inlet channel to depart from the side walls in order to conserve the quasi-static equilibrium of the interface. But as more fluid is injected in the reservoir, the thread is set out of equilibrium, leading to necking and droplet formation. We showed recently that the same arguments holds true to explain the droplet formation in the step junction geometries [81]. The corresponding paper is attached at the end of this manuscript in the appendix D.

Parallelization reveals the strong power of this technique. Indeed, droplet mass production was performed by dispersing one phase through many step/slope junctions placed in parallel (Fig 1.17 c)), achieving throughputs in the kHz range which compares favorably with flow-focusing devices. But this technique also allows us to design parallelized yet independent generators by connecting the different inlet channels to different sources of reagent. This opens the way to the massively parallelized on-demand droplet generation of droplet having different formulation. The control of the droplet generation is then performed actively as described below.

1.4.2 Toward on demand droplet formation in parallel

To form individual droplets on demand without the need to flow the outer phase, some other mechanism to produce enough shear on the water/oil interface is necesseray on top of a valve enabling to generate one drop at a time. Most suggested mechanism rely on active destabilization of the water/oil interface by different means. Recent examples include the use of programmable microinjectors, syringe pumps, piezoelectric actuators, high-voltage pulses, electrowetting on dielectrics and dielectrophoretic pressure [82]. However, none of this active technique to destabilize the water/oil interface has been integrated on a large scale.

Pneumatic valves and the tyranny of numbers

To my knowledge, the only valve that has been integrated on a large scale is the pneumatic valve from the Quake's group which allows each reactor to be addressed individually. In 2000, Unger *et al.* [83] from the Quake's group published a seminal paper showing how to fabricate microfluidic valves, and thus microfluidic transistors. Quake's valve can stop the flow of a liquid in a straight microchannel by locally collapsing the channel. The idea consists in superposing a perpendicular microchannel filled of air on top of the layer where the former microchannel sit as shown on Fig. 1.18 a). Then by increasing the air pressure in the top microchannel, the thin layer of PDMS separating the two layers deforms and obstructs the bottom microchannel. As the fabrication of these valves relies on soft lithography only, there are readily parallelizable as shown on Fig. 1.18 b). The increase in the on chip valves density is however limited by a connectivity issue as shown on Fig. 1.18 c). This is the *tyranny of numbers*: there is a practical limit to the complexity of macroscopically assembled systems [84]. Indeed, microchannels dedicated to reagents do not share the same outlet, but meet at crossing points were a pneumatic valve allow them to meet or not. As a result, each reagent is not associated to one inlet, but at least four, which strongly limits the large scale integration of this technique.

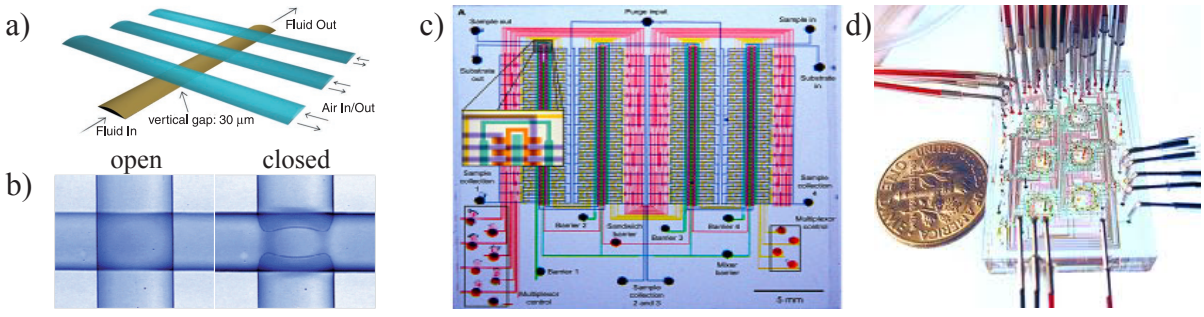

Figure 1.18: a) Quake's valves. From Unger *et al.* [83]. b) The two states of the valve. c) Large scale integration of Quake's valves. From Thorsen *et al.* [85]. d) Practical upper limit of Quake's valves integration.

This example highlights the fact that the level of complexity achievable through integration is limited by the level of complexity of the basic block to be assembled. In this regard, I believe that using droplets produced with a step or a wedge junction allows us to simplify the basic block, and hence to hope for microfluidic devices with a higher degree of integration in the near future.

Gradients of confinement for parallel formation of drops on demand

Indeed, gradients of confinement methods to produce droplets requires only one inlet channel per reagent. Then, controlling the formation of a drop on demand can be done off chip using a computer controlled pressure source for instance. This would allow us to bring on chip as many microreactors as the chip shown on Fig. 1.18 b) while keeping the complexity of the integrated chip very low, thereby ensuring its reliability and robustness.

First attempts to pair droplets on demand have been performed, by producing droplets using either steps [86] or wedge junctions [20] and a first parallelization of these junctions to produce droplet on demand is presented in the next chapter.

1.5 Discussion of Chapter 1

Droplet microfluidics has the potential to dramatically increase the throughput of current techniques for the study in parallel of many different chemical reactions. Large arrays of droplets have been built using both 1D and 2D microchannels, thereby allowing different conditions to be tested in parallel on a single chip. Arraying droplets in 1D microchannels was shown to produce well organized arrays of droplets thanks to the natural spatial indexation of trains of droplets. However, the closed structure of the trapping technique at play prevents from any subsequent operations on trapped droplets, such as dilution series or combination of droplets, which limits the applications of such 1D arrays.

On the other hand, 2D microchannels yields randomly filled arrays where droplets are still accessible for further operations. In addition, 2D microchannels solve an endemic issue related to 1D microchannel: *long range interactions*. Indeed, any failure occurring locally in a serial microchannel, be it a microfabrication defect or dust stuck in the channel, blocks the whole train of droplet flowing down the channel, and hence the whole device breaks down. In a 2D microchannel, local failures are bypassed and hence do not affect the rest of the chip which can thus continue to work despite some local failures. This makes 2D microchannels much more robust and sound blocks onto which more complex system can be assembled.

Active techniques are nonetheless required to organize spatially arrays in 2D microchannels. Amongst the different available techniques, we choose the laser actuation and showed that a laser hot spot can push a droplet and merge two droplets. Finally, we have pre-

sented the issue related to the large scale integration of many different reactions on chip. Conventional continuous flow methods to produce droplets cannot be simply parallelized which limits their use in operations involving many different species. Instead, we propose a droplet generation device which does not need the outer phase to be flowed. The parallelization is then straightforward and yields a high throughput droplet production, while as injectors are independent, different reagents can be simply brought on chip.

In the next chapter, we demonstrate the combination of our passive droplet trapping technique with the active laser actuation. We start by building spatially organized arrays of droplets in 2D microchannels using continuous flow methods for droplet generation. Then, we turn our attention to microchannels being operated without a mean flow and we present an innovative device to form on demand six different pairs of droplets in parallel, and use it to study chemical kinetics under varying conditions.

Chapter 2

Combining gradients of confinement with laser forcing

The current challenge is to pattern a 2D area with a heterogeneous droplet population, either by selectively placing a drop at a desired location, selectively extracting a drop, or selectively initiating a chemical reaction. To date, none of the methods for arraying drops, as explained in Chapter 1, allows for such a controlled operation to organize spatially a 2D array of droplets. Instead, random filling is used in most cases. While random distributions of drops can yield useful information in the case of two droplet species [87], it quickly becomes limiting when there are many species to be studied simultaneously.

In this chapter, we demonstrate how the controlled filling, extraction, or reactions can be performed in a 2D format by combining the rails and anchors approach with the selective manipulation through laser-induced local heating [67, 88, 62]. The rails and anchors provide a passive, robust and simple 2D guidance and trapping of drops, while the mobile laser spot adds an intelligent and versatile selectivity. This chapter contains most of the microchannels designs and protocols of operation I did during my PhD.

We start with the materials and methods in section 2.1 where our microfabrication technique and our optical set up are presented. In section 2.2 we present three experiments where we selectively build spatially organized arrays of distinct droplets using continuous flow droplet generation units. These demonstrations deal with selectively extracting a drop from an array, selectively filling an array with a controlled drop population by showing how to build an array of drops which displays a gradient of concentration, and selectively triggering local reactions in an array of paired droplets. In section 2.3, I demonstrate the use of gradients of confinement to produce and pair droplets on demand in a 2D microchannel which allows to passively address a droplet to a trap in a 2D microchannel. In addition, parallelization of the basic storage unit is presented. Lastly, in section 2.4, we present our approach to monitor chemical reactions in our merging chamber.

These results were published in Lab-on-a-Chip, the first two sections 2.1 and 2.3 in [89], and the next two sections 2.3 and 2.4 in [90]. The corresponding manuscripts are attached in appendix D.

2.1 Materials and methods

2.1.1 Microfluidic device fabrication

All experiments were conducted in PDMS microchannels sealed onto glass slides by plasma bonding. The fabrication procedure relies on dry film photoresist soft lithography techniques [91, 92] which enable rapid prototyping of multi-level structures. The multilayer masters were etched in stacks of Eternal Laminar E8013 and Eternal Laminar E8020 negative films (of thickness 15 μm, 35 μm and 50 μm respectively) depending on the desired thickness of the main channel and patterns. The successive steps were the following: (i) photoresist layers were successively laminated onto a clean glass slide using a PEAK Photo Laminator (PS320) at a temperature T = 100 °C until the desired height h of the main channel was reached, (ii) The photoresist stack was exposed to UV (Hamamatsu Lightingcure LC8) through a photomask of the base channel (comprising a test section, droplet generation devices and entrance and exit channels), (iii) Additional photoresist layers were laminated on top of the exposed stack until the desired depth of the patterns (anchor holes and/or rails) was reached, (iv) The stack of photoresist films was exposed again to UV, through the second photomask featuring only the patterns to be added onto the base channel. Finally, the full structure was developed by immersion in an aqueous bath of carbonate potassium at 1% mass concentration. These four steps are summarized on Fig. 2.1.

Liquid PDMS (Dow Corning Sylgard 184), prepared with a 1:10 ratio of curing agent, was poured onto the master and cured 2 h at 70 °C. The PDMS slab containing the channel footprint was then cut off and sealed onto a glass slide by plasma bonding. Furthermore, in order to render the internal channel surface hydrophobic, a surface treatment was applied. A dilute solution of 1H,1H,2H,2H-perfluorodecyltrichlorosilane (Sigma-Aldrich) in FC40 oil (3M Fluorinert) (20 μL in 1 mL of FC40) was flowed through the microchannel for approximately 5 min. The channel was then rinsed with pure FC40 to remove the residue chemicals remaining in the bulk.

2.1.2 Chip general design and operation

The common architecture of the microfluidic chip was a base channel with a blank test section onto which rail and anchor patterns were etched. The base channel consisted of one or two droplet generation devices discharging into a wide main test section. The system then emptied into a single outlet channel. The height of the base channel h was either 100 μm for the channels of section 2.2 or 150 μm for the channels of section 2.3.

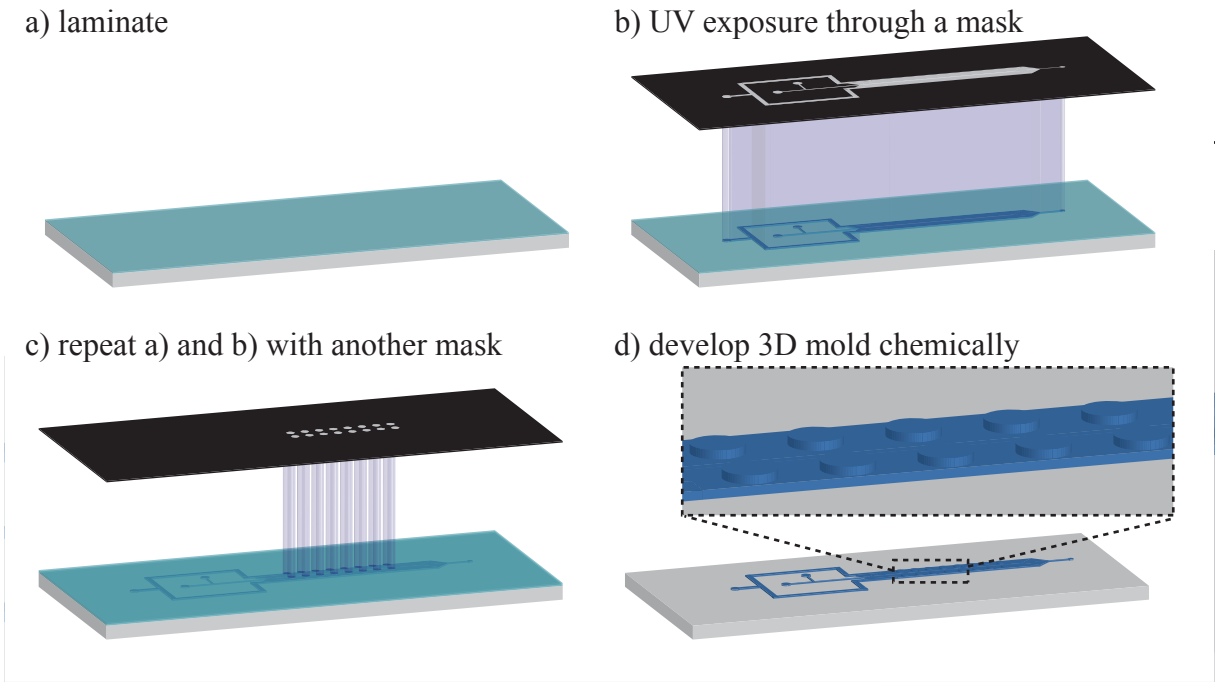

Figure 2.1: Dry film soft lithography main steps to texture the roof of a microchannel. Here a series of pillars is created on top of the mold of a base channel.

Channels upstream of the test section had widths ranging from 100 to 200 μm. The test section was a rectangle a few mm long on each sides. Various patterns of rails and anchors could then be added onto the base test section depending on the desired applications.

Throughout the study, the continuous phase was FC40 oil (3M Fluorinert) of viscosity $\mu^{\text{out}} = 4.1$ cP containing fluorinated surfactants for both emulsion stabilization and improvement of the wetting conditions. Experiments described in sections 2.2.1 and 2.2.2 used a Krytox (Dupont) ammonium salt, at 0.5 % mass concentration, while those in sections 2.2.3 and 2.3 used a PEG-based surfactant at mass concentrations between 0.01 % and 1% [93]. The interfacial tension γ between a pure water drop and the FC40 solution was measured to be 22 mN/m. We observed however that the contents of the drops, such as the chemicals of sections 2.2.3 and 2.3 or the fluorescent beads, could have an impact and reduce this value in some cases.

A system of computer controlled syringe pumps (Cetoni neMESYS) was used to control the different flow rates of oil and aqueous solutions in real time.

2.1.3 Optical setup and laser operation

The optical arrangement employed for droplet manipulation makes use of a 1480 nm continuous wave infrared laser source (Fitel Furukawa FOL1424) and a commercial inverted

microscope system (Nikon TE2000) equipped with epifluorescent illumination (Exfo X-cite 6210C). A pair of galvanometric mirrors (Cambridge Technologies 6210H) permits beam positioning in the microchannels. Following the galvanometric mirrors, the laser beam is both expanded appropriately to overfill the back aperture of the microscope objective and relayed to the back aperture of the objective by a 4f conjugate lens system and an appropriate dichroic mirror (OCTAX) as shown on Fig. 2.2.

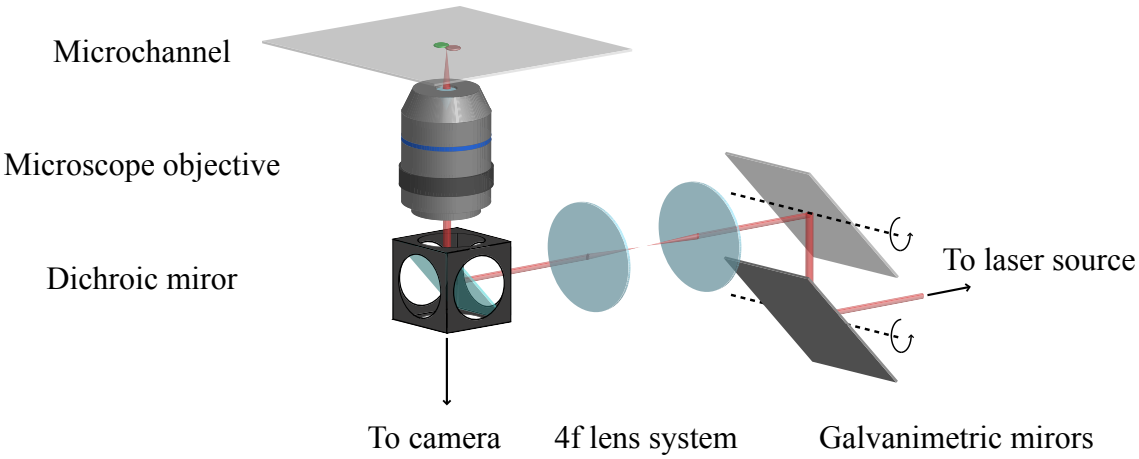

Figure 2.2: Optical setup used to image and shine a laser focused in the plane of the microchannel.

The laser power was measured to be up to 200 mW in the focal plane of the microscope objective. The described system provided an approximately diffraction limited spot at the focal plane with beam waist in the μm range [70]. Position of the laser spot can be controlled by a mouse click using in-house Labview programs. Finally, imaging of the microscope field of view is ensured by different cameras (Photron Fastcam 1024 PCI, Spot camera, Nikon D70). Whilst the laser spot wavelength was outside the range of both cameras, the spot location was visible as a dark shadow on the computer screen. We think this is due to a local lens effect of the laser which slightly deforms PDMS in the neighborhood of the hot spot.

2.2 Building spatially organized 2D arrays of droplets

In this section, we demonstrate the combination of rails and anchors with laser forcing to selectively build 2D arrays of droplets. To this end, we performed three different experiments as examples of combination. It deals with selectively extracting particular droplets from a large array of droplets, selectively placing a droplet in an array and selectively triggering a chemical reaction in an array of paired droplets. These three examples are all based on continuous flow methods to generate drops.

2.2.1 Extracting a drop from an array of holes

Droplets have been early on proposed as vessels to encapsulate single biological compounds such as enzymes, cells [94], subcelular organelles [95] or DNA strands [96]. The classic approach consists in emulsifying a very diluted solution of these compounds which results in a Poissonian distribution of the droplet filling: Most droplets are empty while some contain a single compound only. The next step of the assay then consists in sorting the empty drops from the filled ones which is often done on another chip. Another approach allows us to perform the last two operations on a single chip. It consists in building an array of droplets, and extract from the array the filled droplets only. Hereafter we present a chip to do so.

Chip design

We want to use the laser spot to unpin a given droplet from an array of droplets. To this end, the laser force $\vec{F_\lambda}$ must overcome the anchoring force $\vec{F_\gamma}$. In a laterally confined channel, the magnitude of $\vec{F_\lambda}$ was measured to be around 100 nN [71], and we expect it to be smaller, without having measured any proper estimate, in a laterally unconfined channel as discussed in Chapter 1. To be on the safe side, we thus design anchors as weak as allowed by our microfabrication technique in order to satisfy the criterion $F_\lambda \geq F_\gamma$. As a result, the test section is a 10×3 mm rectangle, 100 μm high, on top of which a square lattice of anchors is etched as shown on Fig. 2.3. Anchors are 50 μm in diameter and 50 μm in depth.

Figure 2.3: Chip geometry. The diameter of the anchor is 50 μm and is not to scale on this sketch.

An estimate of F_γ can then be calculated. Indeed, a detailed study of the droplet geometry, taking into account the droplet spherical cap in the anchor as shown on Fig. 2.4, yields the following anchoring strength [57] in the case of a pancake droplet with an in-plane radius R much larger than the anchor diameter $d \ll R$:

$$F_\gamma \approx \gamma h \frac{\pi}{2} S(b) \tag{2.1a}$$

$$\text{with } S(b) = \frac{b}{2} - \frac{4}{3b}\left(1 - \left(1 - \frac{b^2}{4}\right)^{3/2}\right) \text{ the drop shape function} \tag{2.1b}$$

$$\text{and } b = \frac{d}{h} \text{ the anchor ratio} \tag{2.1c}$$

From the equation (2.1a), we estimate $F_\gamma = 14$ nN with $\gamma = 22$ mN/m, $h = 100$ μm and $d = 50$ μm. Nonetheless, the laser was found to not be able to detach droplets from their anchors. Therefore, an upper bound of the laser force in a 2D microchannel was found to be $\sim$10 nN.

To overcome this issue, we imposed a weak flow of the outer phase, which adds a drag force $\vec{F_\mu}$ on top of the laser force $\vec{F_\lambda}$ to the total unpinning force. We estimate $\vec{F_\mu}$ by the drag force of a plug flow acting on a rigid cylinder placed a Hele-Shaw cell which is known to be [56]:

$$\vec{F_\mu} = 24\pi\mu^{\text{out}}\frac{\vec{U}^{\text{out}}R^2}{h} \tag{2.2}$$

where μ^{out} and $\vec{U}^{\text{out}}$ are the viscosity and the velocity of the outer phase. This yields $F_\mu = 3$ nN with $w = 3$ mm, $h = 100$ μm, $\mu^{\text{out}} = 4.1$ mPa.s and $U^{\text{out}} = 95$ μm/s (corresponding to a flow rate of $Q_0 = 2$ μL/min).

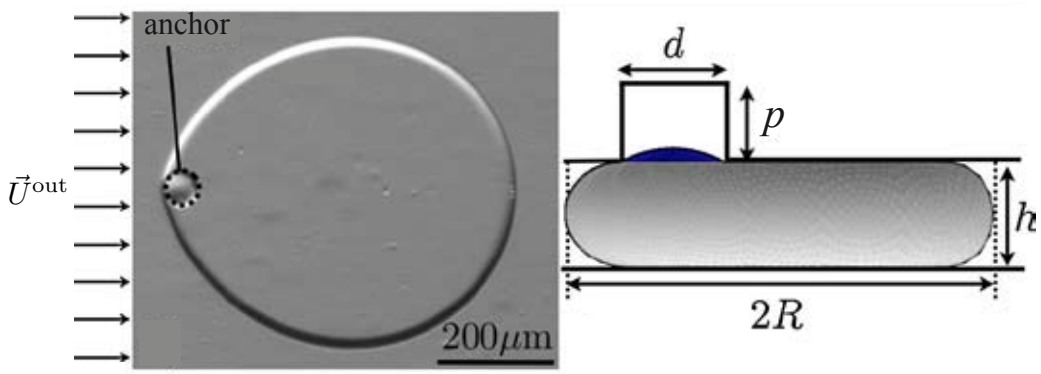

Figure 2.4: Anchor geometry. Left-hand- side: Top-down view obtained from experiments. Right-hand side: Side view obtained with Surface Evolver. From Dangla *et al.* [57].

As a result, anchors can hold two droplets (as $F_\gamma \geq 2F_\mu$) which allows free droplets to bump onto trapped droplets without detaching them. Furthermore, this confirms our estimate of F_λ as a laser push was able to detach droplets with this weak flow.

Chip operation

An example of implementation is shown on Fig. 2.5. In this experiment, drops are initially formed in a flow focusing geometry and flowed into the test section, which is patterned with a square lattice of anchors. Some drops become anchored at the hole positions, filling the lattice in a random fashion. The water flow is then stopped and the oil flow rate is held constant at $Q_0 = 2$ μL/min.

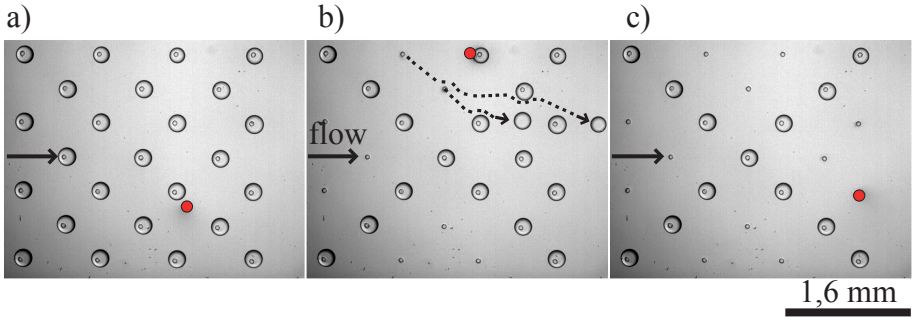

Figure 2.5: Selectively extracting drops. a) The array of holes is initially filled with water drops. b) The laser (red dot) is focused on the water-oil interface, pushing the drops out of the anchor. c) An X is patterned with the remaining droplets.

Once the lattice is filled (Fig. 2.5 a)), the laser spot is selectively positioned within the test section. If the laser is focused inside the droplet, it can remove it from the anchor. This allows the user to select a position on the computer screen and to remove the corresponding drop at that particular position. The oil flow rate then transports the drop away from the array and out of the microchannel as shown on Fig. 2.5 b). Fig. 2.5 c) shows an X pattern formed using this method.

This device can be operated in two different regimes. In the current regime, small anchors and a weak oil flow rate are used, therefore requiring a high laser power ($P_{\text{laser}} = 200$ mW) to remove the drops. Alternatively, lower laser powers can be used by increasing the flow rate to work closer to the critical anchoring velocity. In that case however, extracted drops interact with their neighbours and can lead to a buffering mode, in which drops downstream of the extracted drop also get unpinned. Rails could then be used to guide detached droplets between trapped ones and avoid the unwanted downstream detachments.

2.2.2 Selectively filling an array

Here, the ability to sort and subsequently fill a two-dimensional array with droplets of a uniform size is presented. The methodology is again based upon the combination of rails and anchors of different strengths, with a highly localised laser induced forcing for derailing the drops. By superposing anchors onto rails, droplets may be guided directly to the anchor sites where they become trapped on these storage rails. The presented method involves first selectively filling these storage rails and then allowing the droplets to assemble into the desired array by entering into a buffering mode through an increase of the carrier oil flow rate.

Chip design

To construct an array of droplets, we use a chip test section composed of 6 rails, each of which is periodically superposed with 16 anchor sites, producing a 96 drop array, thus mimicking the 96 wells plate format. The rail sorting portion of this test section is shown in Fig. 2.6 a) which demonstrates active switching of droplets between rails, achieved by employing laser induced forces as described in Chapter 1. In the absence of the laser, droplets are guided along the central rail to the exit of the chip by default. The selective derailing operation is demonstrated in Fig 2.7. To fill the array, rails are filled in sequence, row by row, beginning with the right most junction to the left most junction. Any order can be used however, even working on a drop-by-drop basis.

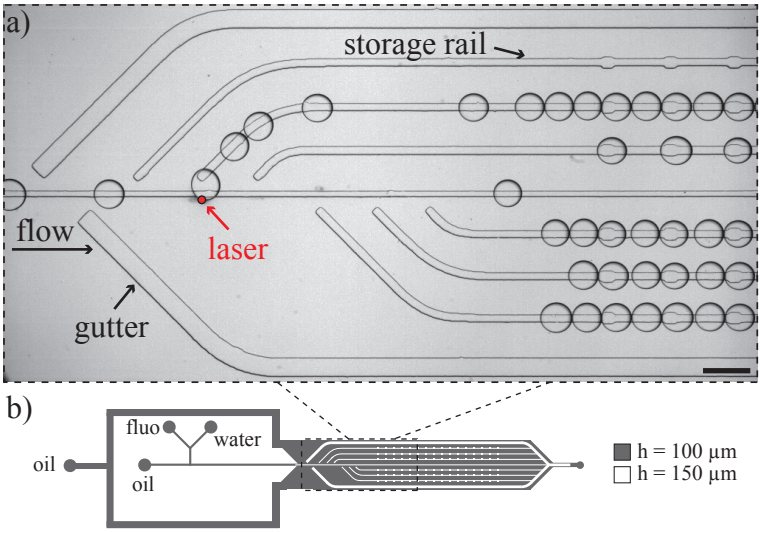

Figure 2.6: Test region (20 × 4.5 mm, $h = 100$ μm) for building an array of droplets. All rails are 50 μm deep. The central default rail is 50 μm wide. The side gutter rails used to filter out large droplets are 200 μm wide. The 6 storage rails are 75 μm wide and the anchor sites superimposed on these rails are 120 μm squares. The image shows the fifth rail being filled. b) A schematic of the complete chip design illustrates the droplet formation portions of the chip relative to the test region. The scale bar is 600 μm.

Selective filling of the array, in addition to anchoring the drops in place, depends upon several key design features which are highly sensitive to droplet size. Consequently, the device geometry is constructed specifically for a given droplet size. For this experiment the chips (shown in Fig. 2.6 b)) are designed for droplets of a 150 μm radius.

The first of these features is designed to ensure that all droplets placed on the array are of the same size. Such steps are necessary, as droplet monodispersity is not guaranteed for transient stages of droplet production, nor for all flow rates. Droplets are only placed in the array when the laser is used to direct them there. Furthermore, droplets below the

size of interest cannot be derailed from the central rail, due to the limit on the maximum deflection achievable with the employed laser power. Small droplets are therefore guided out of the chip and never reach the storage rails. To ensure droplets of a size larger than those under study are also eliminated, two side gutters are placed upstream and redirect large droplets along the side of the test section. Therefore, large droplets are prevented from entering the array portion of the chip as the gutter rails provide an energetically favorable alternative route. These features ensure that only droplets of the desired size are available for active laser forcing onto the array rails.

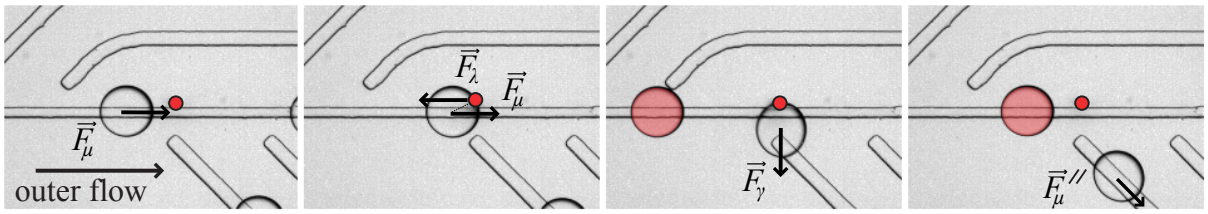

Figure 2.7: Switching rails. The laser, placed slightly off the central rail, blocks a droplet in front of a storage rail. The droplet turns around the laser spot and meets the storage rail which attracts droplets as it is wider than the central rail.

The remaining features are concerned with filling the storage rails. Once a droplet passes the two side gutters, it enters the rail switching area and is available for sorting into the storage rails containing square anchor sites. As can be seen in Fig. 2.7, the storage rails have been designed to be wider than the central guide rail and there is a gap between the storage rails and the central default rail. This intentional gap is to avoid junction sites, where the local width reaches a maximum value. This leads to junctions behaving as anchor sites from which drops cannot be removed. Upon deflection by the laser, the droplet sees the wider side rail as an energetically favorable route and leaves the default rail as illustrated in Fig. 2.7.

Once sorted onto the storage rails, the droplet encounters anchor sites and becomes trapped. The dimensions of the anchors have been chosen for the given droplet radii so that they may hold one droplet parked stationary against the mean flow. However, the anchor site is intentionally too weak to hold multiple droplets stationary: $F_\mu < F_\gamma < 2F_\mu$. Consequently, under the correct external flow conditions the droplets will enter into a buffering regime. It is noteworthy that whilst the storage rails are being filled with droplets, the apparent channel cross section available for the oil to flow through decreases due to the stationary droplets. Such a reduction causes an increase in the velocity that must be taken into account when filling the anchor sites, to prevent all the droplets from being swept out of the array. Therefore, the entrainment oil flow rate Q_e is reduced from 40 to 20 μL/min during the filling period as the storage rails become populated, while the small oil (Q_o) and water (Q_w) flow rates are maintained at a steady 0.5 μL/min and 0.18 μL/min respectively. This ensures that all rails are completely filled with monodisperse droplets during the filling

procedure. Once this procedure is completed, the entrainment flow rate Q_e is increased slowly to 70 μL/min to initiate the desired droplet buffering regime (Fig. 2.8). Under these conditions arrays of 96 droplets may be constructed in a controlled manner at a rate of approximately 1 min per rail for droplet sorting and a further minute for droplet buffering into a complete array.

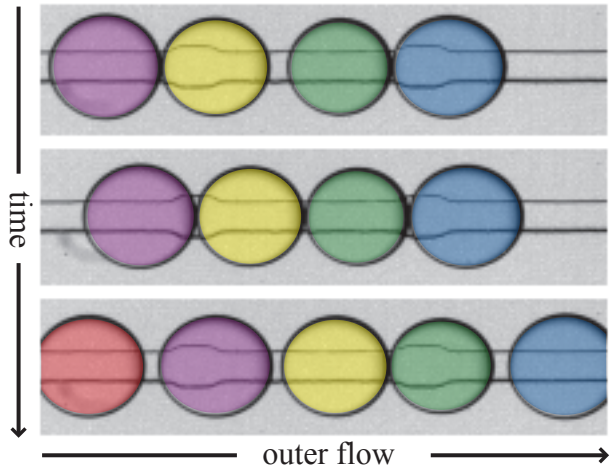

Figure 2.8: Buffering mode. The anchoring force of each anchor is large enough to hold one droplet by not two. As a result, each incoming droplet on the storage rail takes the place of the first trap droplet it meets, and by a domino effect, the whole set of trapped droplet shift one trap downstream. Once the storage rails are filled the entrainment flow rate Q_e is increased to initiate a buffering mode whereby the droplets self arrange into an array of one droplet trapped at each anchor site.

Whilst maintaining the droplet size for a given chip design, this methodology may be extended to droplets of varying composition. An example of such a controlled filling appears in Fig. 2.9, where an array of 96 anchored droplets with an increasing concentration of fluorescent beads is shown. In the chip used here, a mixer was positioned before the T-junction used for droplet formation, allowing the composition of the droplets to be altered in time. To modify the composition of the droplets, a stream of pure water is mixed with a concentrated bead solution in pure water (0.4 % by volume). For the various rails of the array, the ratio of pure water to bead solution is altered by varying the relative flow rates whilst maintaining an overall flow rate of 0.18 μL/min for the mixture. This ensures that the droplets are of uniform size. For the top rail, droplets are composed entirely of pure water and the flow rate of the bead solution is set to zero. For each row, moving down the array, the flow rate of the bead solution is increased in 0.005 μL/min increments whilst the water rate is decreased by the same amount.

Chip operation

The filling protocol begins with the top rail, which is filled with droplets containing pure water. The laser is then removed, causing all droplets to follow the default central path to the drain. The droplet composition is then altered to the concentration required for the next rail and allowed to reach a steady state before filling of that rail commences. To do so we translate the laser to the correct position for the new rail and direct droplets into the storage rail. Once the rail is filled with droplets, the laser is again removed and the droplet composition altered. The remaining storage rails are filled in this stepwise manner, changing the droplet formation specifically for each rail and using the laser to position the droplets onto the rails.

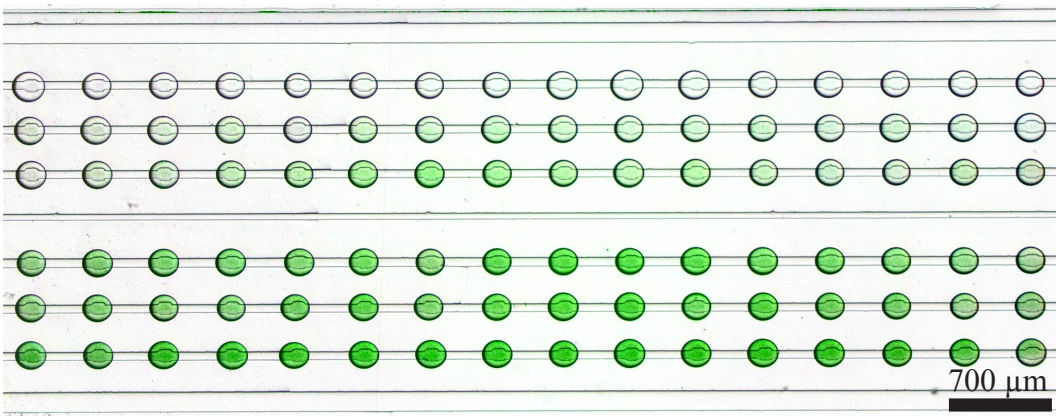

Figure 2.9: A superposition of bright-field and fluorescent images of a 96 anchor array. The droplet composition has been altered from pure water to a solution of water and green fluorescent beads to create a gradient. The droplet volume is 7 nL each.

2.2.3 Controlled initiation of chemical reactions at anchor sites

Our demonstration of the power of the technique is to carry out the loading of two droplets into the anchor sites and then use laser induced merging of droplets to enable controlled chemical reactions within selected droplet pairs. This can be done at a location predefined by the anchor position and it indicates the potential of this method as an analysis and assaying tool.

Chip design

We make use of an array of anchors in the chip test section. A key point here is that the anchor holes are designed to be twice as wide as the droplet diameters, so that each can accommodate two droplets. In this situation, where the holes are larger than the droplets, an outer flow rate of 80 μL/min removes one drop per trap while in the experiment presented in the last subsection, an outer flow rate of 10 μL/min detaches all the drops.

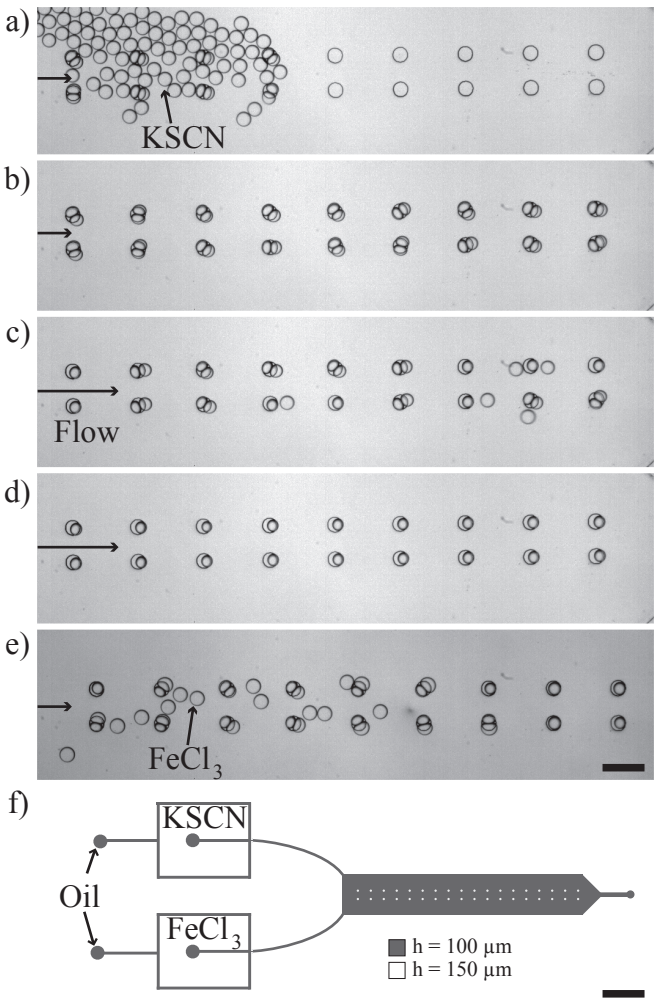

Figure 2.10: a) and b) Filling first species into anchor holes. c) and d) Emptying one droplet from each trap to leave one drop per anchor site. e) Bringing in the second species droplets to anchor holes. The scale bar is 400 μm. f) Schematic of channel used, illustrating dual inlets for the two different chemical species. The test section (containing the anchors) is 100 μm high, 1 cm long and 3 mm wide. The anchor holes have a height of 50 μm and a diameter of 200 μm. The scale bar is 3 mm.

Chip operation

To initiate a chemical reaction we must load droplets with different contents into each hole site. We choose droplets with $FeCl_3$ and KSCN, which react to form a colored liquid from two colorless ones. We begin by generating one species of droplets from the top flow focusing junction and fill the anchor sites (Q_o^{top}=7 μL/min, Q_w^{top}=0.1 μL/min). Initially, this leads to two droplets occupying each anchor site, since the holes are twice as big as the droplets (Fig. 2.10 a) and b)). We then increase the oil flow rate (Q_o^{top}=80 μL/min, Q_w^{top}=0 μL/min) to wash out one of each pair, thus leaving one droplet per site (Fig. 2.10 c)

and d). We then introduce droplets containing the second species from the bottom flow focusing device (Fig. 2.10 e)). Here lower flow rates than for the first droplets are used to prevent accidentally knocking any further droplet out of the holes: Q_o^{bottom}=5 μL/min, Q_w^{bottom}=0.05 μL/min. A loaded array, with two droplets per trap site, each with different contents, is shown in Fig. 2.11 a).

Having established the ability to fill the holes with droplets we can then use laser induced droplet merging to start the chemical reaction. With the control we have over the positioning of the laser this means that we can target a specified droplet pair in the array. The power used is 200 mW, and a dwell time at the droplet interface of 100 ms is required before any fusion takes place when laser position is well placed.

The process of laser initiated droplet merging is shown in Fig. 2.11 b), where we choose to react the droplets such that they form a W pattern. The track of the laser is shown by the solid and dashed lines in Fig. 2.11 b), which correspond to a time t = 117 ms after the merging of the drops at the top-center location. Fig. 2.11 c) shows the final state where only the droplets illuminated by the laser have undergone the reaction.

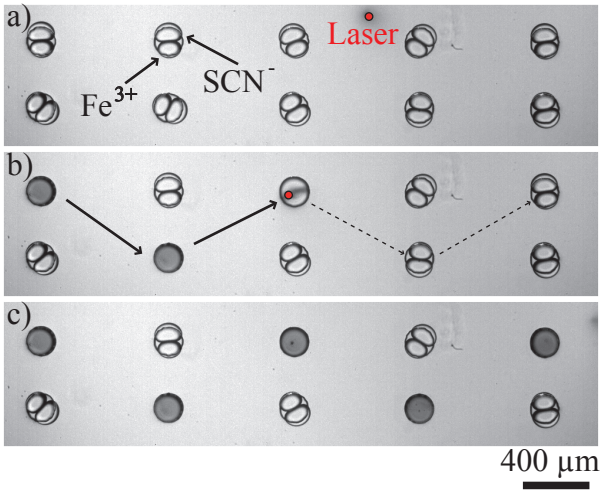

Figure 2.11: Laser induced merging of droplets in anchor sites. a) Filled droplet array. Laser spot is shown as a red dot. b) The laser is scanned in the pattern shown. As it stops on the droplet-droplet interface it initiates fusion and a chemical reaction takes place. The solid line shows where the beam has been, the dashed line its future path. c) The laser completes its path leaving 5 anchor points with a reaction product and all other droplets undisturbed.

2.3 Pairing droplets on demand using gradients of confinement

The approach to pair droplets presented in the last section allows us to study many reactions simultaneously on chip and can be massively parallelized. However, it becomes limiting when working with many species. Limitations are twofolds. First, the use of a continuous flow method to produce droplets prevents from connecting many droplet generation units to the device and hence limits the number of species that can be combined on chip. Second, the array that is produced is not spatially organized when working with more than two droplet populations. As a result, a labelling method is required to identify drops which again is limiting when the number of species or the number of droplet formulations is increased.

In this section, we address these limitations by adopting a new approach to pair droplets. We use gradients of confinement to produce, propel and trap droplets which allows us to not flow the outer phase. This has two major consequences. First, many inlets for reagents can be connected to the same chip without extra syringes for the outer phase and without hydrodynamic couplings between these inlets. Second, droplets can be produced at will by controlling the injection of the reagents. Then, rails can be used to connect each inlet to a given storage site. This ensures that our chip can assign a given droplet to a given trap to yield a spatially organized array of distinct pairs of droplets once traps have been placed in parallel. We start by presenting the basic merging chamber to pair two droplets on demand, and its parallelization in a second time.

2.3.1 Merging chamber geometry and operation

The device consists of a square test section connected to four inlet channels of smaller width and height, two for oil and two for aqueous solutions, as shown on Fig. 2.12 a). In addition, a goggle-like pattern, of larger height, is etched on top of the test section. This multi-level structure (Fig. 2.12 b) is micro-fabricated using multi-layer dry film soft lithography without the need for a mask aligner, since it relies on superposing millimeter-scale structures. The geometry provides the three operations that must be performed on the drops: their production, propulsion and pairing.

During operation, the device is first filled with a fully wetting oil used as the continuous phase and the oil is kept stationary for the rest of the experiment. By pushing the aqueous solutions past the step into the test section, a drop detaches when it reaches a well-calibrated size, a technique known as step emulsification [79]. The drop size is determined by the height of the step and, to a lesser extent, the injection rate of the dispersed phase [81]. As a result, injecting the aqueous solution past the step allows the production, on demand, of a single droplet of desired volume.

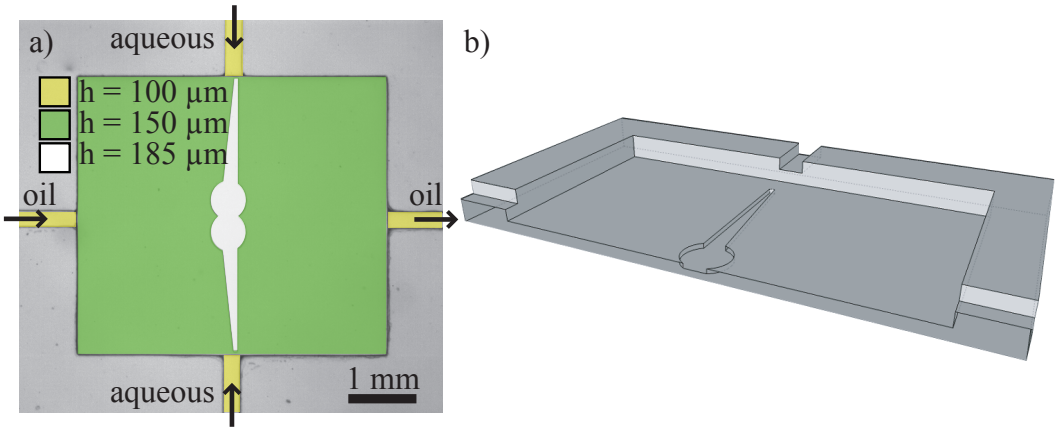

Figure 2.12: a) Top-dow view of the test section. It consists of three regions of different heights h: Four inlet channels in yellow, the test section in green, and the goggle pattern in white. b) Perspective view of the reaction chamber with the different changes in channel height.

In the experiments reported here, the drops that detach are large enough to remain squeezed between the top and bottom walls and this vertical confinement makes the drops sensitive to channel height modulations [42, 20]. Indeed, confined droplets have a larger surface energy than spherical unconstrained drops of identical volume. Since droplets tend to minimize their surface energy, they migrate towards regions of reduced confinement. Consequently, the V-shaped grooves in our device, corresponding to the arms of the goggle, passively propel droplets toward the center of the test section by gradually releasing their confinement. Finally, droplets coming from the two inlet channels are held against each other in adjacent anchors in the center of the test region. The shape of the anchors ensures that the two drops are touching.

Typical device operation is shown in Fig. 2.13. The device is first filled with a mixture of perfluorinated oil (FC40, 3M Fluorinated) and a PEG based fluoro-surfactant [72] at 0.1 % (w:w). Next, a solution of $FeCl_3$ at 0.27 M, denoted A, is injected from the bottom injection channel. A drop detaches and comes to a rest in the central trap, after which a drop of KSCN at 0.8 M, denoted B, is generated in the same way from the top injection channel (Fig. 2.13 a) and b)). The drop pair does not merge, due to the presence of the surfactant (Fig. 2.13 c)). However, a laser pulse on the touching interfaces triggers their fusion, which is initiated after the laser has already been removed, and the fused drop quickly relaxes to the final oblong shape which is imposed by the anchors. The reaction starts immediately after fusion and a reactive front propagates in the fused droplet, as shown in Fig. 2.13 d) and e), until the reagents have been used up. Finally, once the reaction is completed, a transverse oil flux is used to remove the drop and reset the test section for another experiment.

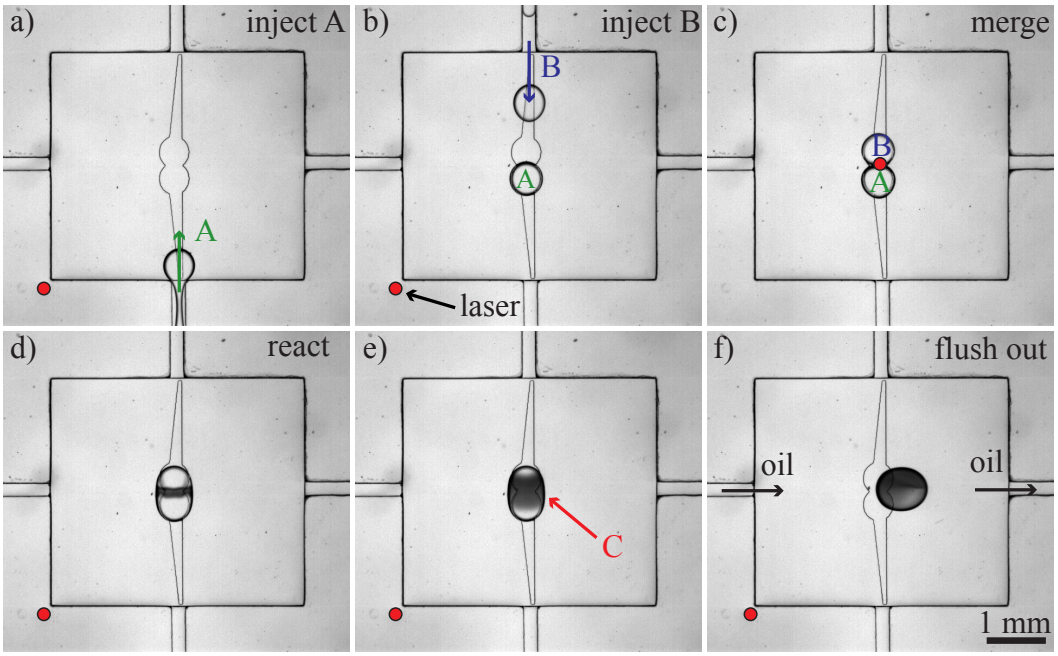

Figure 2.13: Channel operation for a test reaction between Fe^{3+} and SCN^{-}. a) and b) Reagents are injected at 0.5 μL/min and paired at the center of the chamber. c) A 200 ms long laser pulse in placed on the droplet-droplet interface and removed. d) to f) Coalescence starts which triggers the chemical reaction. Once the reaction is completed a transverse flush of oil empties the chamber.

2.3.2 Parallelization

Chip design

This workflow is readily parallelizable which allows us to test different conditions on the same device. Such a design is shown on Fig. 2.14 a), where the rails and anchors pattern presented in the last subsection has been reproduced in order to allow six independent conditions to be tested on a single chip. An extra inlet is dedicated to the counterpart reagent of the reaction to be tested. Each inlet is connected to the main rectangular channel by a step junction. Crucially, the droplet size is mostly defined by the ratio e:

$$e = \Delta h/h \tag{2.3}$$

with Δh the height of the step junction and h the height of the inlet channel. Here, we fixed $e = 0.5$ which led us to use 5 different heights in the channel design as shown on Fig. 2.14 b). The inlet labeled B on Fig. 2.14 a) has an inlet channel 65 μm high and a step height of 35 μm which yields $e = 0.54$, while the inlets labeled A1 to A6 have inlet channel 100 μm high and a step 50 μm high which yields $e = 0.5$. These different heights were chosen according to the available thicknesses of the photoresist in the lab (15, 35 and 50 μm).

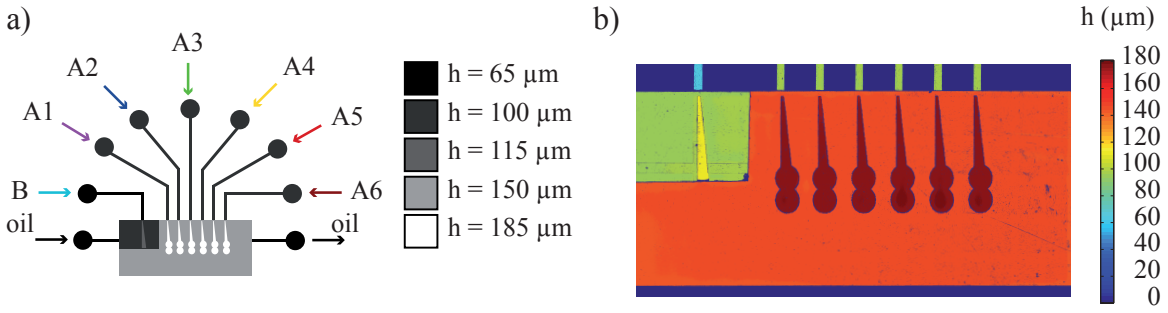

Figure 2.14: A parallelized chip that can test six independent reactions. a) A sketch of the chip that shows the different inlets and the different channel heights. b) Map of the different channel heights measured using an optical profilometer Zygo NewView 7100.

Chip operation

The chip operation is depicted on Fig. 2.15. In this parallel chip, the top row of traps is filled with a single drop of each of the six independent reagents, which originate from different syringes outside the chip as shown on Fig. 2.15 a). Once those positions are occupied, a bunch of droplets is produced at the remaining inlet on the left hand side in order to bring droplets containing the counterpart reagent as shown on Fig. 2.15 b). When the desired amount of droplets is generated, the droplet production is stopped and a gentle flow of oil pushes the droplets toward the empty trapping sites (Fig. 2.15 c)). It is also possible to use the laser to guide individual droplets into the desired anchors or to prevent some unwanted droplets from entering a trap. This leads to all six positions being occupied by six different pairs of drops as shown on Fig. 2.15 d). This is illustrated on Fig. 2.16 a) where an array of distinct pairs of colored droplet has been built following this procedure. Independent reactions can again be triggered when desired by the laser as shown on Fig. 2.16 b).

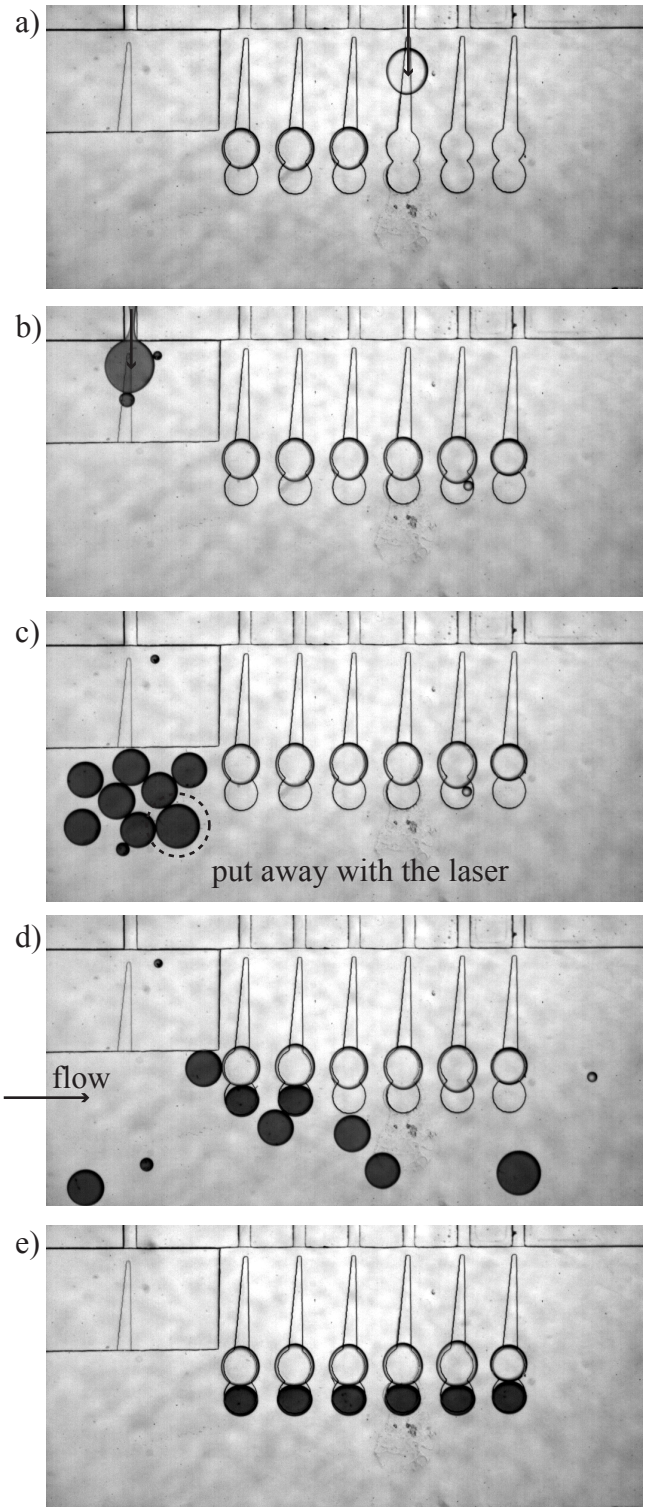

Figure 2.15: a) The 6 central inlets produced one drop each. b) The inlet on the left hand side produces several drops to fill the empty traps. c) Undesired droplets are pushed away using the laser. d) An outer flow of oil pushes the droplets in the unoccupied traps. e) An array of 6 distinct drops is obtained.

Figure 2.16: a) Array of six distinct pairs of droplets. b) A droplet pair has been merged on demand using a laser pulse.

Further parallelization

This level of parallelization is well suited for few applications like Michaelis-Menten assays, or enzyme inhibition studies which requires few tens of concentrations to be tested. These two examples are shown in Chapter 4. These dose response assays could nonetheless be greatly simplified by adding a dilution device on chip, which has been done for continuous flow methods to produce droplets [97], but not for methods based on gradients of confinement. Further parallelization is also highly desirable when aiming at combinatorial studies or screening of libraries of compounds.

2.4 Monitoring reactive fronts in paired droplets

In the last section, we showed that our merging chamber allows us to pair on demand two drops and hold them against each other without the need to flow the outer phase. As a result, droplets are not actively mixed by any outer flow and a reactive front forms and propagates across the daughter droplet when the droplets contain reacting species. In this section we derive a reaction-diffusion model to represent the dynamics of product formation in our device.

2.4.1 Approach and motivations

To mix or not to mix?

The natural way of studying a chemical reaction consists in first mixing the reacting mixture, and subsequently monitoring the product formation (or the consumption of the reagents) over time. The mixing step is therefore key as its duration sets a *dead* time of the device in use before which the chemical reaction cannot be resolved.

The mixing process of two soluble liquids proceeds in two independent mechanisms. On one hand, flows can break up the liquids into clumps which are intermingled, while on the other hand, molecular diffusion occurs at the boundary of these clumps [98]. Molecular diffusion is spontaneous and ultimately homogenizes any non-uniform mixture, but relatively slowly. As a result, the ability of the flows to reduce the size of the clumps in order to enhance the homogenization through diffusion is crucial when aiming at an efficient mixing.

The Reynolds number of a flow compares the relative influence of inertial to viscous effects on the flow dynamics. It is defined by $Re = UL/\nu$, with U and L characteristic velocity and length scales, and ν the kinematic viscosity of the fluid at play. In microchannels, the Reynolds number is usually small compared to one: $Re \ll 1$. As a result, flows are laminar and cannot break clumps of liquids into smaller clumps like their turbulent ($Re \gg 1$) counterparts do. Mixing is thus mostly ensured by diffusion in microfluidic devices. A great deal of effort has nonetheless been done to achieve fast mixing in microsystems. In single phase systems, corrugations in the channel geometry were shown to induce chaotic advection, and achieve good mixing [99]. In two phases flows, recirculations inside drops were used to induce a series of stretching and folding events of the drop content which also allows fast mixing [100]. Anyhow, the mixing rate of these methods relies mostly on a fast injection rate of the reagents which is not desirable when aiming at saving reagent, or performing reactions in parallel.

Another approach suggested by Kamholz *et al.* [101] takes advantage of the poor efficiency of mixing at small scales, and proposes to not mix the reagents actively. Instead, reagents are initially kept separated and the transport mechanism that brings the reagents together is taken into account in the modelling of the product formation. As shown on Fig. 2.17 a), the device proposed by Kalmholz *et al.* consists of a T-junction, where each solution of reagent is flown from one arm of the T. Thus, reagents are advected down the channel by two coflowing streams while being allowed to meet through cross diffusion. As a result, a stationary reaction-diffusion pattern takes place in the body of the T.

Our approach, first suggested by Huebner *et al.* [44] brings the later workflow into droplets. The idea is to trap two droplets containing different reagents next to each other, merge them and follow the evolution of the reactive front taking place along the daughter droplet, labeled x on Fig. 2.17 b), and over time. The resulting space-time diagram shown on Fig. 2.17 c) is analogous to the one we would have obtained with a T-shaped channel. As a result, we expect to be able to extract kinetic parameters of the reaction at play by using a reaction-diffusion model.

Motivations

This approach has many advantages. First, the use of droplets allows us to test many different reactions on a single chip and improves greatly the sample consumption compared to continuous flow methods like the T-sensor. Second, as there is no mixing step in our

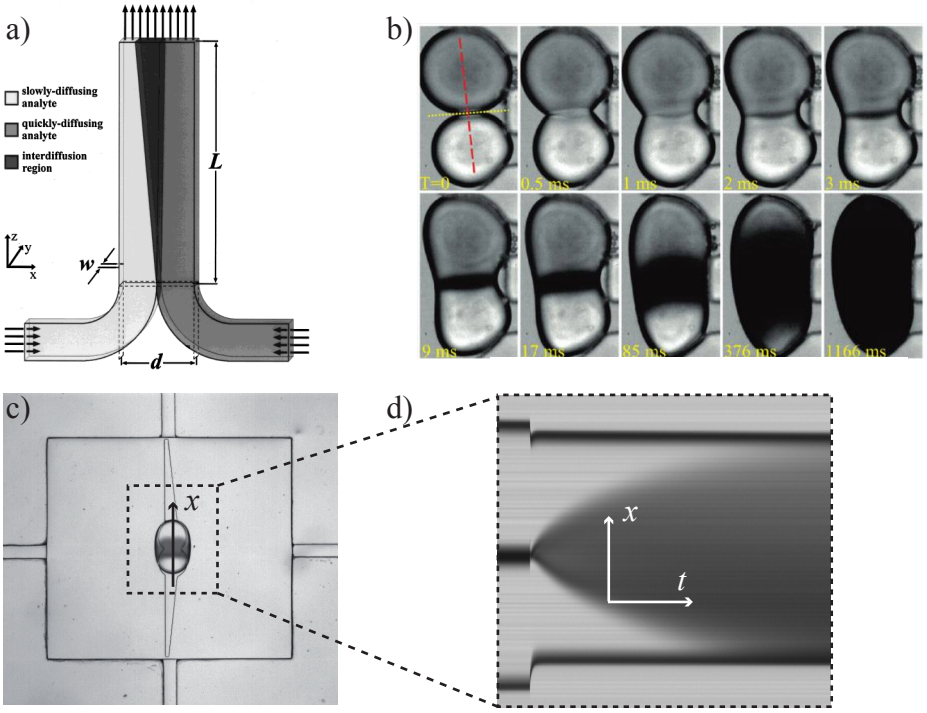

Figure 2.17: a) T-junctions. In co-flowing streams, reagents meet through cross diffusion and a stationary pattern takes place from which the reaction kinetic parameters can be extracted. From Kamholz *et al.* [101]. b) Front propagation in Huebner's device. From Huebner *et al.* [44]. c) The gray levels are read along the daughter droplet labeled x and over time t. d) The resulting space-time diagram is analogous to the one we would have obtained with a T-shaped channel.

workflow, the associated dead time vanishes. When compared to the T-sensor shown on Fig. 2.17 a), this methods has also a much better defined starting point of the chemical reaction as the first instant of the experiments are defined by the droplet coalescence event. A difference distinguishing the T-sensor from our droplet based methods concerns the time required to perform an experiment. When using a T-sensor, one has to wait for the reaction-diffusion pattern to reach its steady state which can last several minutes. In the droplet based approach, product formation is monitored over space and time which drastically shortens the time required for the experiment to be done. On the other hand, the time resolution cannot be set at will when using droplets, while one can do so by increasing the injection rates when using a T-sensor. The complete passivity of the droplet based approach is nonetheless a clear advantage when aiming at large scale integration.

2.4.2 Processing steps

As shown in the section 2.17 b), a chemical front propagates across the daughter droplet once two droplets containing different chemicals are merged in our device. In order to

extract reaction rates from the dynamics of this chemical front, we need in the first place to define an observable that we can extract from our recordings. Secondly, we need to derive a model for the evolution of that observable. This last step will be done in the next chapters 3 and 4 for two classes of reactions, namely one step reactions and enzyme catalyzed reactions.

Extracting concentration maps

Our raw data are the local depth averaged intensities extracted at each time point from a picture of the field of view of the merging chamber as shown on Fig. 2.18 a). The first step of the analysis consists in converting these intensity maps into concentration maps of the absorbing species as shown on Fig. 2.18 b). This is usually done via a calibration curve as shown on Fig. 2.18 c). When working in absorbance however, the conversion of intensities into concentrations can be directly done via Beer's law which relates the local absorbance A to the local concentration of the absorbing species, denoted P (in mol/m^3) as it is commonly the product of a reaction:

$$A = \epsilon h P \qquad \text{with} \quad A \;=\; -\log_{10}\left(\frac{I}{I_0}\right) \tag{2.4}$$

with ϵ the molar extinction coefficient (in M^{-1}m^{-1}) of the absorbing species, h (in m) the optical path length of light which corresponds to the channel height here and I_0 the background intensity.

In fluorescence, this would have been done via a calibration curve, usually linear, that relates the fluorescent intensity I to the local concentration of fluorophore denoted P:

$$\alpha\frac{I}{I_0} \;=\; P \qquad \text{with } \alpha \text{ a calibration coefficient} \tag{2.5}$$

In both cases, the background intensity I_0 is key for the conversion of intensities into concentrations. As shown on Fig. 2.18 a) and b), the background intensity varies over the field of view because of the reflexions of light on the indentations etched on the top surface of the channel, or because of inhomogeneity in the illumination... As a result, the background substraction should be done pixel by pixel. However, as drops change shape during coalescence, the artefacts induced by their interface varies too, which makes the background intensity I_0 change over time. As the chemical reaction might have started, we cannot take the initial picture as a reference. Instead, we hold I_0 constant and define it as the maximum intensity inside the daughter droplet on the first frame after the start of droplets coalescence. The conversion of gray levels into concentrations is then done either using a calibration curve obtained beforehand as shown on Fig. 2.18 c), or directly using

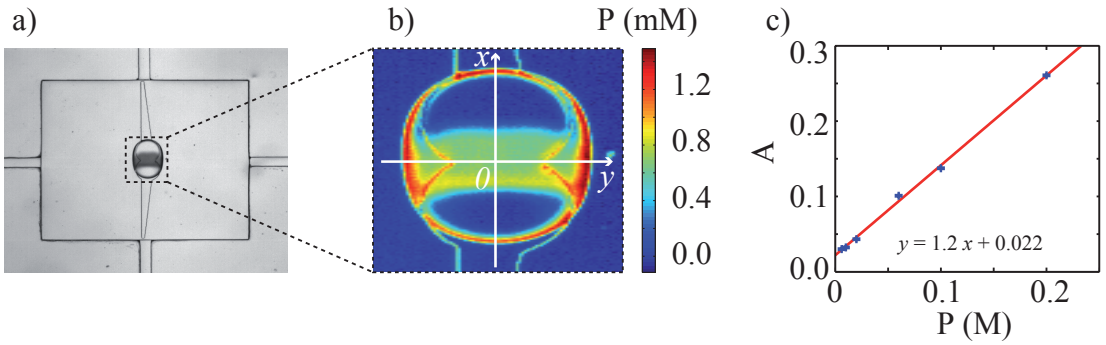

Figure 2.18: Gray level conversion. a) Raw picture from the experimental movie at $t = 2.5$ s. b) Extracted map of the concentration of $FeCl_3^{2+}$ (denoted P). This is obtained by taking -log of the raw picture, adding $\log(I_0)$ to each pixel and multiplying by a calibration coefficient. c) Calibration curves of the absorbance A against the product concentration$P$ which yields the calibration coefficient.

the equation (2.4) when ϵ is known.

It is also noteworthy that the local intensities extracted from the experimental movies are related to the depth averaged concentration of the absorbing species. As a result, we will not consider any vertical variation of the concentration fields, which is reasonable owing to the relative small height of the the channel compared to in-plane length scales.

Building space-time diagrams

Next, we need to define a spatial window in which product formation can be observed. The position of a pixel is located by its x and y coordinates as defined on Fig. 2.18 b), the x direction being along the daughter droplet, the y direction across the daughter droplet, and the origin $(0, 0)$ in the middle of the daughter droplet. As shown on Fig. 2.19 a), the droplet interface and the indentation etched on the channel surface introduce artifacts which must not be taken into account.

Measurements of the product concentration along the x and y directions shows that the product distribution $P(x, y, t)$ does not depend on y, but on x only. Indeed, the product distribution shows no variation when we measure it along the x direction at different y locations. Fig. 2.19 b) shows three product profiles centered on the daughter central line and 45 μm from each other. Far enough from the droplet boundaries, these profiles superpose very well. Their variation, defined as the ratio of their standard deviation to their mean value, was found to be 2 %. On the other hand, the product distribution shows large variations when measured along the y direction at different x positions. As a result, we will focus on the product profiles along the x direction only, and define our product profile $P(x, t)$ as the average of the product concentrations along 10 lines of pixels centered on the central line of the daughter droplet, *i.e.* a 90 μm wide box in the middle of the daughter

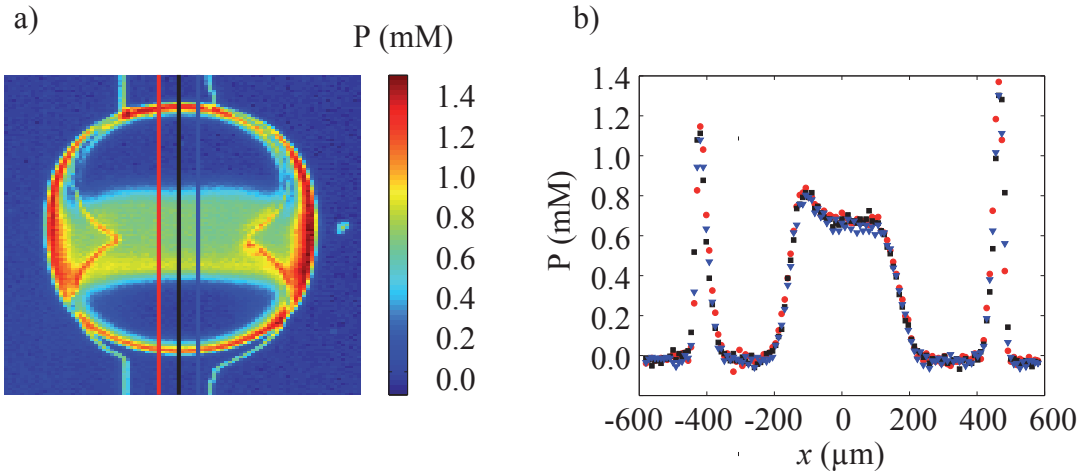

Figure 2.19: a) Three parallel lines along the daughter droplet along which the product concentration is measured. b) The corresponding product distributions, color by color. The variation of these three product distributions is 2 %.

droplet. This enhances the signal to noise ratio by averaging out potential noise.

This procedure can be routinely applied on each frame of an experimental movie yielding a product profile along the x axis at each time point t. Fig. 2.20 a) shows the resulting space-time diagram showing the time evolution of the product distribution along both x and t. Similarly, we extract the product concentration along the y axis at $x = 0$ and at each time point. The resulting space-time diagram is shown on Fig. 2.20 b). One can see that the product is well mixed along that direction.

Modelling the spatio-temporal pattern

The last step of the data processing consists in comparing the experimental spatio-temporal pattern shown on Fig. 2.20 a) with the solution of a model for the dispersion of product over space and time. This model consists of the conservation equations for the different species taking part in the chemical reaction. When considering the product P of the reaction, in general terms, its conservation reads as:

$$\frac{\partial P}{\partial t} + \underbrace{\vec{u}.\vec{\nabla}P}_{\text{Advection}} = \underbrace{D_P \nabla^2 P}_{\text{Diffusion}} + \underbrace{R}_{\text{Reaction}} \tag{2.6}$$

where $\vec{u} = (u, v)$ is the local depth averaged velocity field, D_P is the diffusion coefficient of P, and R is a source term due to the chemical reaction that we aim at identifying. As we showed that P is well mixed along the y direction, its derivatives with respect to y must vanish. In addition, P being a depth averaged concentration, it does not depend on z.

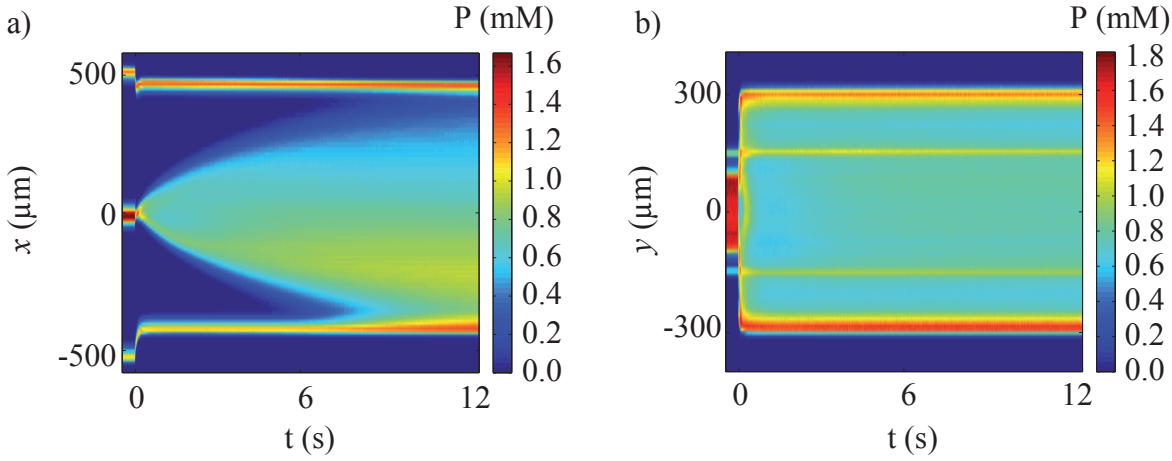

Figure 2.20: Space-time diagrams along x and y. a) Along the x axis. Average of 10 lines of pixels along the daughter droplet which makes an average over 90 μm. b) Along the y axis at $x = 0$. There product is well-mixed along this direction.

This simplifies the equation (2.6) into:

$$\frac{\partial P}{\partial t} + u\frac{\partial P}{\partial x} = D_P\frac{\partial^2 P}{\partial x^2} + R \tag{2.7}$$

The next subsections are concerned with identifying the effective transport mechanism along the x axis. The identification of the source term R will be done in the next two chapters 3 and 4 for two different types of reactions. We thus fix:

$$R = 0 \quad \text{in the rest of this chapter}$$

2.4.3 Flow and mixing in merging drops

Flow field in the daughter droplet

The equation (2.7) reduces to a 1D advection-diffusion equation when R is set to zero. The non-dimensional number that compares advection and diffusion is the Péclet number Pe defined as $Pe = Ul/D$ with U a velocity scale, l a length scale, and D the diffusion coefficient. Hereafter, we look for estimates of U and l in order to show which is the dominant transport mechanism at play.

Flows in the daughter droplets are mostly due to the strong deformations that the droplet interface undergoes during coalescence. Working with droplets of the same size simplifies greatly the possible deformations of the interface by making the problem symmetric. By doing so, we expect the flow in one drop to be the mirror image of the flow in the other drop. As a result, we also expect a stagnation point in the middle of the daughter

droplet. This is the Curie's principle applying for linear problems:

"Lorsque certaines causes produisent certains effets, les éléments de symétrie des causes doivent se retrouver dans les effets produits" – Pierre Curie [102]

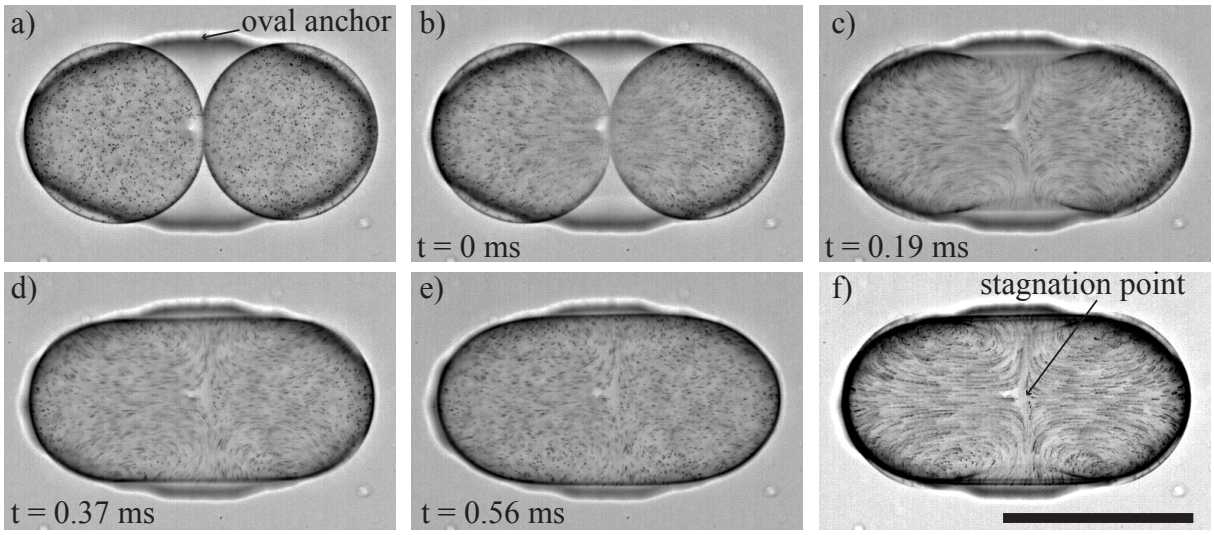

Figure 2.21: Snapshots of two coalescing droplets seeded with plastic beads. a) Initial state. b) to e) Coalescence. f) Superposition of the pictures c) to e) which reveals the stagnation point in the middle of the daughter droplet. Scale bar is 100 μm.

This is verified by seeding droplets with plastic beads as shown on Fig. 2.21 f) where the superposition of frames at different time points reveals the streamlines of the flow at play. This is a stagnation point flow with the stagnation point at the middle of the daughter droplet. The velocity at the stagnation point is therefore zero, and it increases with the distance from the stagnation point to reach its maximum value at the droplet interface. As a result, we expect diffusion to dominate advection in the neighborhood of the stagnation point, and advection to be dominant near the droplet interface. Along the x axis, there must be a central region where $Pe < 1$, sandwiched between two regions where $Pe > 1$ as shown on Fig. 2.22.

The Péclet number needs to be defined locally as the velocity scale U changes greatly with the distance from the stagnation point l. For a symmetric four-roll mill flow of strain E, the velocity scales linearly with the distance from the stagnation point:

$$U \sim El \tag{2.8}$$

In our device, the deformation of the droplet interface drives the flow. As a result, the strain of the flow E can be estimated by:

$$E \sim U_\infty / R \tag{2.9}$$

with U_∞ the velocity scale of the droplet interface and R the droplet radius. The Péclet number $Pe = Ul/D$ is then:

$$Pe = \frac{El^2}{D} \tag{2.10}$$

and the size l of the diffusion-dominated region scales like:

$$l(t) \;=\; \sqrt{Pe\frac{DR}{U_\infty(t)}} \tag{2.11}$$

By assigning a given value to Pe, the equation (2.11) allows us to quantify the size l of the box in which diffusion dominates advection to order $\mathcal{O}(Pe)$.

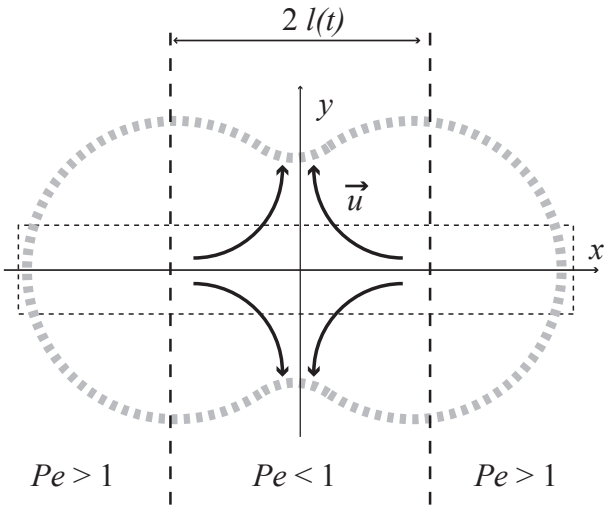

Figure 2.22: Péclet number along the x axis. A $Pe < 1$ near the stagnation point is sandwiched between two $Pe > 1$ regions.

The deformations along the x and y axes, denoted δ_x and δ_y as defined on Fig. 2.23 a), were monitored in order to measure the interface velocity scale. These deformations are shown on Fig. 2.23 b) and c). These deformations are bi-exponentials which is a signature of the two phases of the coalescence process: (i) A rapid unzipping of the interface followed by (ii) a slower viscous relaxation. From these plots, we can thus extract two time scales for the dynamics of both δ_x and δ_y:

Unzipping phase : This phase lasts ~ 0.5 ms. δ_x varies over 22 μm and δ_y over 250 μm, roughly a droplet radius. Velocity scales are thus $u \sim 44$ mm/s and $v \sim 500$ mm/s.

Viscous relaxation phase : This phase lasts ~ 50 ms. δ_x varies over 8 μm and δ_y over 25 μm. Velocity scales are thus $u \sim 160$ μm/s and $v \sim 500$ μm/s.

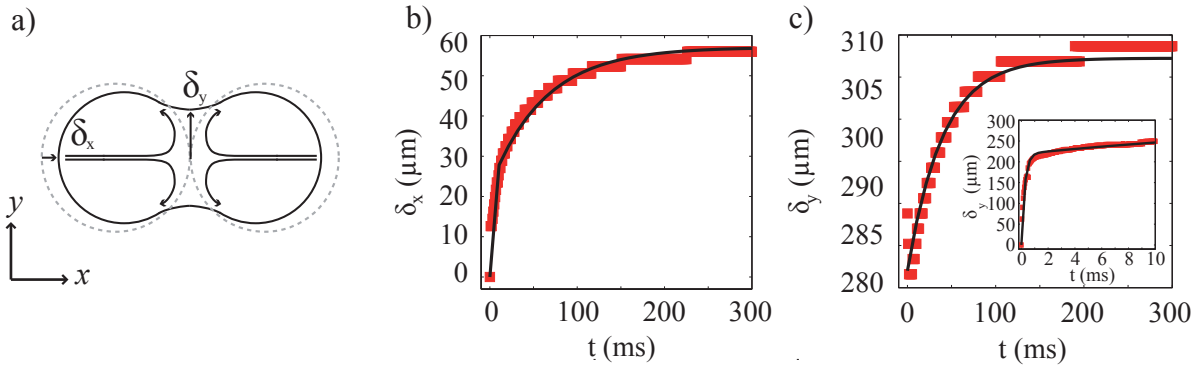

Figure 2.23: a) Sketch of the flow field inside the daughter droplet as it deforms. b) Droplet deformation along the x axis. Solid line: $y = 22 \times (1 - e^{-t/0.5}) + 8 \times (1 - e^{-t/50})$. c) Droplet deformation along the y axis. Solid line: $y = 282 + 25 \times (1 - e^{-t/50})$. Inlet: Zoom in the first 10 ms. Solid line: $y = 219 \times (1 - e^{-t/0.25}) + 95 \times (1 - e^{-t/33})$.

From these measurements, the equation (2.11) yields the size $l(t)$ of the box around the stagnation point in which diffusion dominates advection to order $\mathcal{O}(Pe)$. As shown on Fig. 2.24, l increases over time because of the global deceleration of the interface, and overcomes the droplet size in ∼300 ms for $Pe = 0.1$. As a result, we can neglect any flow in the drop 300 ms after fusion has started. We can also compare l with the typical diffusive length scale $\sqrt{4Dt}$ of the mixing layer that forms between the contents of the two drops. As shown on Fig. 2.24, l does not overcome $\sqrt{4Dt}$ for $Pe = 0.1$ which shows that the flow inside the drops does not affect the mixing layer to that order. On the other hand, l does overcome $\sqrt{4Dt}$ for $Pe = 0.01$ at $t = 150$ ms. This shows that small effects on the mixing layer due to the flow inside the drops are expected up to $t = 150$ ms, after what diffusion dominates.

As a result, even if there is a flow in the droplet during the viscous relaxation phase, up to 300 ms after the fusion has started, the dominant transport mechanism in the mixing layer is diffusion, with some $\mathcal{O}(10^{-2})$ corrections for $t \leq 150$ ms.

Mixing of the drops content

The four-roll mill flow in the middle of the daughter droplet ensures that the contents of the drops remain separated after fusion, even during the flow period. This is verified by merging a pure water drop with a drop containing the dark blue 2,6-dichlorophenolindophenol (DCPIP) as shown on Fig 2.25. Indeed, the front separating the dyed water from the pure water remains straight throughout the experiment, with only diffusive transport acting to smooth the initially sharp separation. Furthermore, a sequence of regimes, all well separated in time, takes place. The initial flow has been measured to affect the mixing layer up to 150 ms. Next, the drop contents mix through diffusion until the diffusive front reaches the drop edge at $t = 50$ s. Finally, at large times, the drop content is well mixed

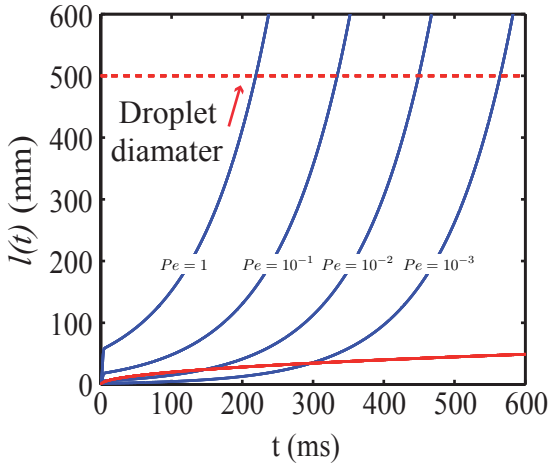

Figure 2.24: *Solid blue:* The size l of the $Pe < 1$ region is estimated via $l(t) = \sqrt{PeRD/\delta_x}$ for various values of Pe. The other parameters are $R = 500$ μm, $D = 10^9$ m^2/s and $\delta_x = 22 \times (1 - e^{-t/0.5}) + 8 \times (1 - e^{-t/50})$ with δ_x in μm and t in ms. *Solid red:* Diffusive length scale $\sqrt{4Dt}$.

and transport will not anymore affect the dynamics of the chemical reaction taking place inside the daughter droplet.

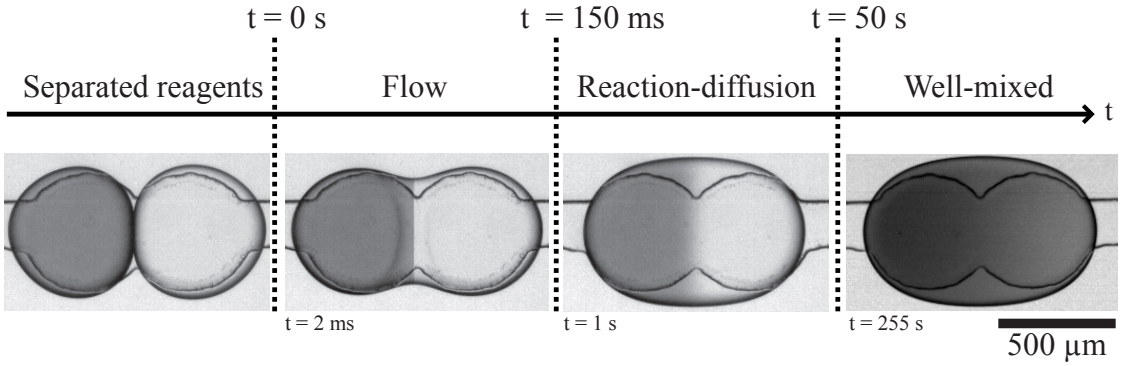

Figure 2.25: Different periods during the coalescence of two drops in our merging chamber. a) A drop of DCPIP (denoted B) at 6 mM and a drop of pure water are paired up and merged. b)-c) At early times $t \ll 150$ ms, a straight front forms between the drop contents. d) For 150 ms$< t <$50 s, the content of the drops meet through diffusion even if the interface deforms slowly. e) At large times $t \gg 50$ s, the drop contents are well-mixed.

Having identified that diffusion dominates advection, and that the reagents are initially well separated, we can build a model for the front propagation based on a diffusion equation.

Denoting B the concentration of DCPIP along the x axis, the conservation of DCPIP reads as:

$$\frac{\partial B}{\partial t} = D_B \frac{\partial^2 B}{\partial x^2} \tag{2.12a}$$

$$\text{with} \quad B = \hat{H}(x \leq 0) \quad \text{at } t = 0 \tag{2.12b}$$

$$\text{and} \quad \frac{\partial B}{\partial x} = 0 \quad \text{at } x = \pm L \tag{2.12c}$$

where $\hat{H}$ is the Heaviside function. This yields:

$$B(x,t) = \frac{B_0}{2} \operatorname{erfc}\left(\frac{x}{\sqrt{4D_B t}}\right) \tag{2.13}$$

in the limit where L is much larger than the diffusive length scale $\sqrt{4D_B t}$. This prediction (2.13) is verified by mesuring the gray levels along the x axis as defined on Fig. 2.26 a). The diffusion coefficient can be extracted from a quantitative analysis of the width of the front, by fitting the concentration profile of DCPIP with an error function $y(x,t) = 0.5 \operatorname{erfc}(x/\sigma(t))$, where $\sigma(t)$ is the time dependent width of the error function (Fig. 2.26 b)). The evolution of σ with time is shown on Fig 2.26 c). These data are well described by the function $\sigma(t) = \sqrt{4D_B t}$, which yields $D_B = 1.1 \times 10^{-9}$ m^2/s in agreement with published values [103]. Besides, as shown on the inlet of Fig. 2.26 c), a difference between the experiment and the model is observed during the first hundreds of ms which is in agreement with our estimation that the flow inside the drop has $\mathcal{O}(10^{-2})$ effects up to 150 ms after fusion has started.

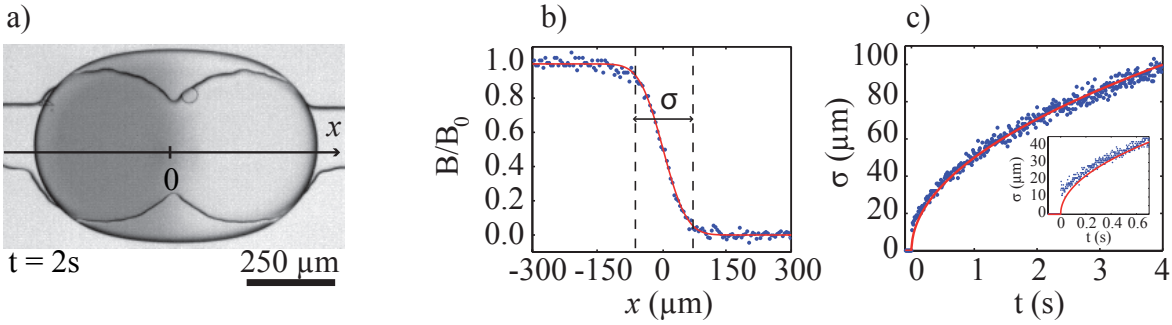

Figure 2.26: a) Diffusive front along the daughter droplet. b) Blue dots: Distribution of dye along the x direction, 720 ms after fusion starts. Red curve: $y = 0.5 \operatorname{erfc}(x/\sigma)$, where $\sigma = 60$ μm is the width of the error function. c) Blue dots: Measurements of σ extracted from the fit shown in b) performed at different time points. Red curve: $y = \sqrt{4D_B t}$, where $D_B = 1.1 \times 10^{-9}$ m^2/s is a fitting parameter. Inset: Zoom on the first 600 ms. The starting point t=0 s corresponds to the start of the droplets fusion.

2.4.4 Toward the study of chemical reactions

The next step of our approach consists in adding reacting species in the droplets. Having established that transport is purely diffusive along the daughter droplet, we will identify the reaction source term R by measuring concentrations along the daughter droplet and comparing them to the solution of the following 1D reaction-diffusion model:

$$\frac{\partial P}{\partial t} = D_P \frac{\partial^2 P}{\partial x^2} + R \tag{2.14}$$

with the reagents being initially touching Heaviside functions, and no-flux boundary conditions being applied at the edge of the daughter droplet.

2.5 Discussion of Chapter 2

In this chapter, we have presented two different ways to combine the passive droplet manipulation technique based on gradients of confinement with the active technique based on laser actuation in order to build spatially organized arrays of droplets, or of pairs of droplets. The first way uses a continuous flow of oil to generate and push droplets downstream, while the second way does not need a flow of the outer phase to operate. Instead, it uses gradients of confinement to generate and propel droplets. Both the gradients of confinement and the laser based techniques are highly scalable, independent of the microchannel material and rely on very simple microfabrication: The rails and anchors are produced using lithographic techniques and can easily be densified over wide areas. The design of the test section is nearly common to all of the devices, which only differ in the pattern of rails and anchors that are designed for a specific application. This further simplifies the fabrication in large quantities for commercial applications. As for the optical heating, any number of operations can be performed with single beam by simply scanning the laser focus or by using holographic techniques to split one beam into a complex pattern [68]. The tight focus of the laser allows manipulation of individual droplets, even in very dense arrays, providing a clear advantage over electrical or acoustic methods.

In the first approach using a continuous flow of oil, droplets are constantly pushed by the outer flow and can be deviated from their mean trajectory by using a rail or a laser push, or unpinned from an anchor using the laser or paired in a single anchor and merged using the laser. This has been used to demonstrate the first devices that allow a selective patterning of a 2D array with microfluidic droplets. We have illustrated it either by selectively filling or emptying the array, or by triggering a chemical reaction on demand.

The throughput of the devices presented in section 2.2 is appropriate for many applications that require a high level of control, since all of the experiments presented here lasted less than a few minutes using purely manual control of the flow rate and the laser position. This duration can be further reduced by using an automated time-sharing of the laser heating, which can produce many operations simultaneously, or by optimizating

the device designs. In the case of the droplet extraction for instance, a different pattern of anchors or the addition of gutter rails would allow the device to function at higher oil velocity, therefore allowing much faster sorting of the drops. Increasing the throughput in the case of the array filling depends on the ability to derail rapidly moving drops. This will be realizable by improving the tolerance on the microfabrication process, which would allow the distance between the side rails and the central rail to be better calibrated for the drop sizes. By optimizing this distance, drops can be derailed with a minimal deflection, which would allow us to work at higher flow rates.

In the second approach presented in section 2.3, there is no need to flow the outer phase to produce, propel and store droplets. Gradients of confinement are used instead. This allows us to connect many different sources of reagents to the same chip without adding extra syringes for the outer phase, as well as avoiding hydrodynamic couplings between the droplet generation units. The fluids are mostly stationary but can be injected sequentially. Combinatorial assays can thus be obtained by pairing droplets that originate from many different inlets through a preprogrammed sequence of operations. In practice, a few μL of sample are sufficient to run a series of reactions with different substrates in a few minutes. This performance yields significant gains in cost and time, motivating the use of such a device in the screening of molecular interactions or for measuring the kinetics of precious enzymes.

Finally, future work will have to investigate the effect of the laser heating on the contents of the droplets (using GFP for instance [104]), as well as ways to minimize these effects such as pulsing the laser source. While we expect that the heating can damage some proteins or sensitive biological material, it should still allow DNA or chemical manipulation without any significant artifacts.

Chapter 3

One step reactions

The next step of our work is to extract chemical information from the concentration fields in the drops once they have been merged. As explained in Chapter 2, our approach consists in comparing experimental profiles with the solutions of a 1D reaction-diffusion (RD), the dynamics of which depending strongly on the source term R at play. In this chapter, we study the case of bimolecular reactions following a one step chemical mechanism:

$$\mathrm{A} + \mathrm{B} \xrightarrow{k} \mathrm{C} \tag{3.1}$$

where A and B refer to the reagents, and C refers to the product of the reaction. Once a model for R has been chosen, the RD model includes the reaction rate constant k as a free parameter. As a result, solving the RD model for different reaction rate constants yields the value of k which makes the experimental and theoretical concentration maps fit best.

We start by recalling some basics of chemical kinetic theory in the case of well-mixed reagents to derive an expression for R in section 3.1. This allows us to derive a RD model for one step reactions. In section 3.2, we monitor the time course of a one step reaction in droplets with our merging device. By comparing the experimental space-time concentration maps we obtain to direct numerical simulations of our RD model, we can extract the rate constant k of the reaction at play. This procedure yields values of k in agreement with measurements performed in a commercial stopped-flow machine. Then, we turn our attention to the theoretical study of our reaction-diffusion problem in section 3.3. Two asymptotic regimes are identified, as well as characteristic time scales defining the transition from a reaction-controlled to a diffusion-controlled regime which are studied in section 3.4. This theoretical study is performed under the strong assumption that reagents have the same diffusion coefficient which makes the analytical treatment amenable. In section 3.5, we finally compare our theoretical predictions to experiments in the case where the reagents A and B are in equimolar proportions. The transition time between the reaction-controlled and the diffusion-controlled regimes is thus measured experimentally by monitoring the space averaged concentration of the reagent B.

3.1 Well-mixed case

In this section, we start by presenting collision rate theory in order to derive an expression for the reaction rate R. Then, we turn our attention to the experimental techniques used to study fast bimolecular reactions such as (3.1) in a well mixed tank, as well as models to extract the reaction rate constant from experimental time courses.

3.1.1 Reaction rate theory of bimolecular reactions

Reaction rate

Bimolecular reactions proceed in two steps: (i) A and B molecules have to meet in the reacting mixture and (ii) chemical bonds are created and/or broken up by the chemical transformation. The global rate R of these reactions have thus to take into account the rate of the two steps of the reaction process. As a result, one can generally write [105, 106]:

$$R = \underbrace{\text{Collision frequency}}_{\text{Transport}} \times \underbrace{\text{Collision efficiency}}_{\text{Chemistry}} \tag{3.2}$$

Consequently, R takes different forms depending on wether the collision frequency, or the collision efficiency limits the progress of the reaction. Indeed, in the case of perfectly efficient reactions, when A and B molecules react faster than their diffusive rate toward each other, R is a measure of the diffusion of A and B molecules toward each other. This is the case of *diffusion-limited* reactions [107]. On the other hand, in the case of inefficient reactions, A and B molecules have to collide many times before any chemical transformation takes place. Then, R is a measure of the collision efficiency, an hence the chemical transformation at play at the molecular level. Here after, we focus on that later case.

Collision theory

Let's consider that A and B molecules are hard spheres, of cross sections σ_A and σ_B, as shown on Fig 3.1 a). As a A molecule moves with a speed v in a solution containing B molecules at a concentration B, it collides with all the B molecules in a volume $(\sigma_A + \sigma_B)v$ in a unit time. When A molecules are present with a concentration A, this repeats A times [106]. The collision frequency f_{AB} is therefore given by:

$$f_{AB} = v(\sigma_A + \sigma_B)\ AB \tag{3.3}$$

Besides, we can call p the collision efficiency which corresponds to the number of unsuccessful collisions that A and B molecules have to undergo before they actually react. As a result, one can write from (3.2):

$$R = kAB \tag{3.4}$$

where k is the reaction rate constant defined as:

$$k = pv(\sigma_A + \sigma_B) \tag{3.5}$$

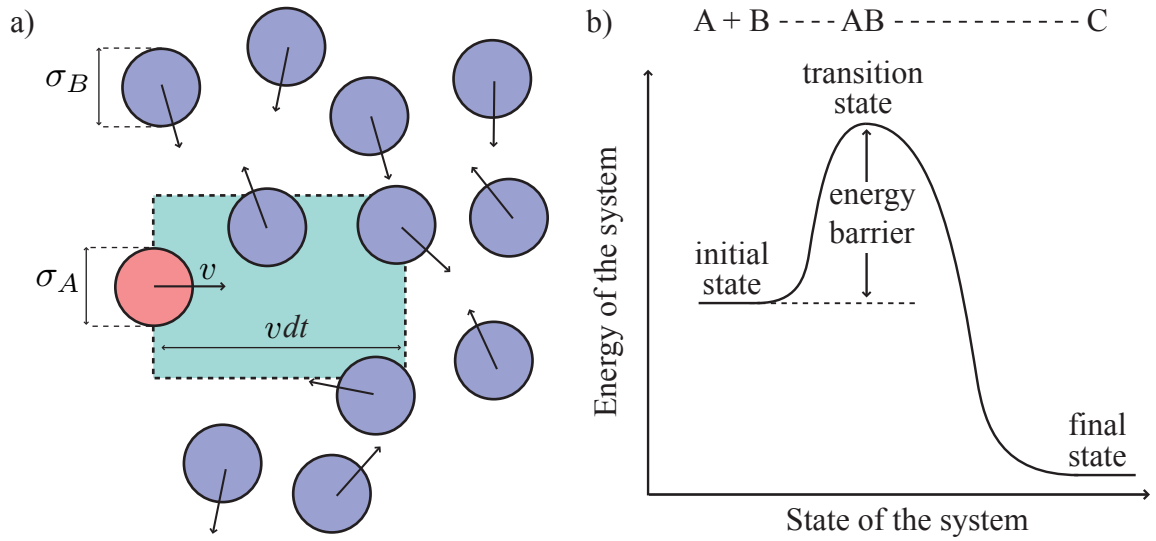

Figure 3.1: a) Collision theory. A particle A (red) travels through a population of particles B (blue), thereby colliding all particles B present in the area it sweeps (green). From Connors *et al.* [106]. b) Transition state theory. A chemical reaction takes place if the incoming particles A and B hold enough energy to overcome the energy barrier to form the pair AB. From Berry *et al.* [108].

The expression (3.4) of R was first demonstrated empirically based on the law of mass action by Waage and Gulberg [109]. However, no insight into the changes at the molecular level were accessible from the measure of k. Here, collision theory shows that k contains informations about both the geometry of the molecules A and B (via σ_A and σ_B), and the chemical reaction energetics via p. The inefficiency of a chemical reaction is indeed due to a barrier of energy which separates the initial and final states of the reacting system as shown on Fig. 3.1 b). Colliding molecules A and B have thus to hold enough energy in order to overcome the barrier and react. This barrier can be seen as the cost to change the initial conformation of the encounters A and B in order to pair them and form a transition state AB. As such, the height of the energy barrier gives a picture of the transition state through which the reacting system passes, and is thus key in the understanding of the molecular mechanisms underlying the overall $\mathrm{A} + \mathrm{B} \rightarrow \mathrm{C}$ reaction scheme. Experimentally, the energy barrier is obtained via Arrhenius law by measuring the reaction rate constant k.

The rate equation (3.4) allows us to build theoretical models for the time evolution of the concentrations of A, B and C. Measurements of k are thus performed by fitting

theoretical predictions onto experimental time courses of either A, B or C. In the next subsections 3.1.2 and 3.1.3, we present the well-mixed model describing the time evolution of A, B and C, and the experimental methods used to study fast reactions.

3.1.2 Transient dynamics

When the reagents A and B are initially well-mixed at a concentration A_0 and B_0 respectively, with no product C being formed initially, the time evolution of the concentrations A, B and C is readily obtained by a mass balance:

$$\frac{dA}{dt} = -kAB \qquad \text{with} \quad A(0) = A_0 \tag{3.6a}$$

$$\frac{dB}{dt} = -kAB \qquad \text{with} \quad B(0) = B_0 \tag{3.6b}$$

$$\frac{dC}{dt} = +kAB \qquad \text{with} \quad C(0) = 0 \tag{3.6c}$$

This set of equations (3.6a)-(3.6c) is readily solvable, either analytically or numerically. Furthermore, it shows that the initial stock of A molecules is consumed over a time scale $1/kB_0$, while the initial stock of B molecules is consumed within a time scale $1/kA_0$. These time scales are thus of the same order when $A_0 \approx B_0$ and very different from each other when A (resp. B) is in excess compared to B (resp. A). However, as the reagents are well-mixed, the reaction cannot proceed after the limiting reagent has been completely consumed. As a result, the *half-life* of the reaction $t_{1/2}$ is solely given by the initial concentration of the limiting reagent in both cases, and defined as the time after which one half of the initial amount of the limiting reagent is consumed, :

$$t_{1/2} = \frac{1}{kA_0} \quad \text{when } A_0 = B_0 \qquad \text{or} \qquad \frac{\ln(2)}{kA_0} \quad \text{when } A_0 \gg B_0 \tag{3.7}$$

Amongst the two available time scales $1/kA_0$ and $1/kB_0$, the actual time scale for product formation is thus the shortest. This is a strong constraint when aiming at resolving fast reactions which have rate constants up to 10^9 $\mathrm{M^{-1}s^{-1}}$ [105]. The half-life of these very fast reactions is then usually brought down by working with very dilute solutions of reagents, the detection of which becoming limiting... Indeed, there is always a tradeoff between the time resolution required, the limit of detection at play, and the sample consumption in the design of a chemical kinetic experiment. This compromise sets the required working concentrations of each reagent, but is not always achievable. To address this issue, different techniques have been developed to resolve different time scales. This is presented in the next subsection.

3.1.3 Experimental techniques for fast kinetics

A bit of history and flow methods

Until the 1920's, chemical and biochemical reactions were studied in the test tube with stopwatches on time scales of seconds or minutes [110]. In 1922, Hartridge and Roughton reduced the observable half-times to milliseconds [111] as they were aiming at resolving oxygen binding to haemoglobin. Their device shown on Fig. 3.2 a) consisted of two syringes, containing either A or B, that were connected to a capillary tube. Reagents were then injected quickly through the tube to onset rapid mixing through turbulence. The progress of the reaction could then be read along the tube, instead of over time, thanks to the space-time similarity induced by the flow. The time resolution in this approach can be set at will by adjusting the injection rates of the reagents. The limiting part became the sample consumption.

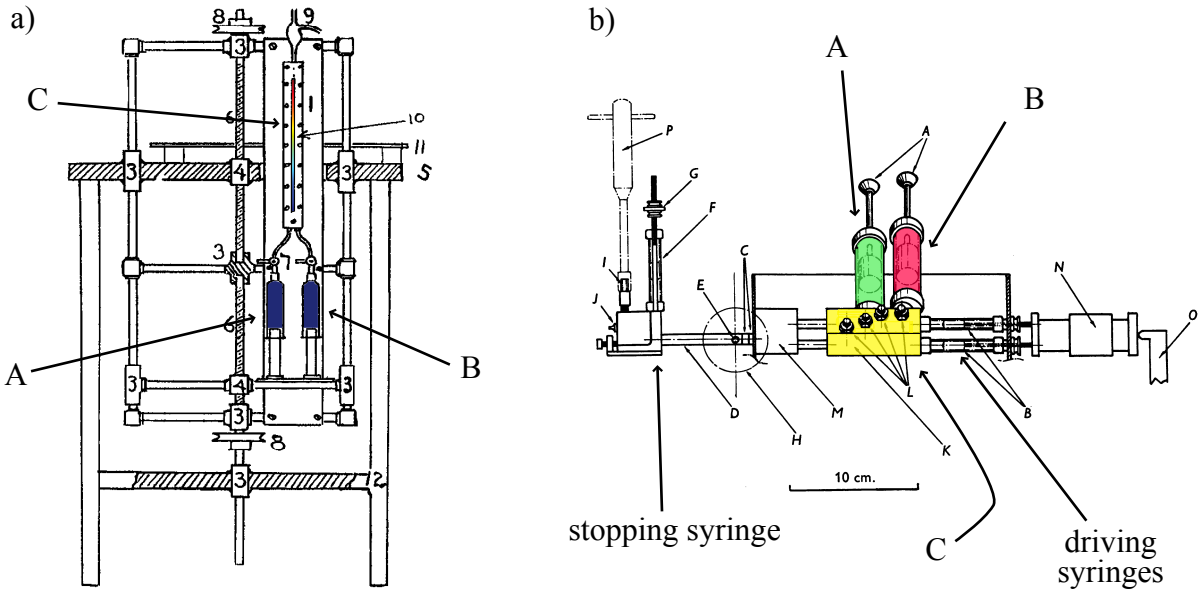

Figure 3.2: a) Continuous-flow device. Diagram from Dubois *et al.* [112]. b) Stopped-flow device. From Gibson *et al.* [113]. False colors are superposed.

Chance *et al.* [114] added fluid economy to the device of Hartridge and Roughton by stopping the flow just after injection of the reagents. This was achieved by placing an extra stopping syringe at the output of the capillary tube as shown on Fig. 3.2 b). The mixing time of this stopped-flow machine is then of a few ms, and the reaction is monitored over time.

Relaxation methods

Much faster time scales were later on resolved by Eigen *et al.* [115] using a completely different approach. Instead of monitoring the progress of a reaction after triggering its ignition, Eigen suggested to destabilize a chemical system in equilibrium and monitor the transient over which it recovers equilibrium. Various destabilization techniques were developed as shown on Fig. 3.3, the more widely used being the temperature jump. In these methods, a chemical equilibrium is forced by a sudden rise in temperature which leads the composition of the reacting mixture to change. This change is then monitored yielding resolution time scales down to a few μs.

The application of this method to biological compounds, such as enzymes, is nonetheless limited, mostly because these reactions usually have very small or very large equilibrium constants so that is not possible to produce significant perturbations on the equilibrium [116]. The gold standard to monitor fast biochemical reactions, *i.e.* enzyme catalyzed reactions or protein folding, thus remains the stopped-flow device, with an internal dead time in the ms range.

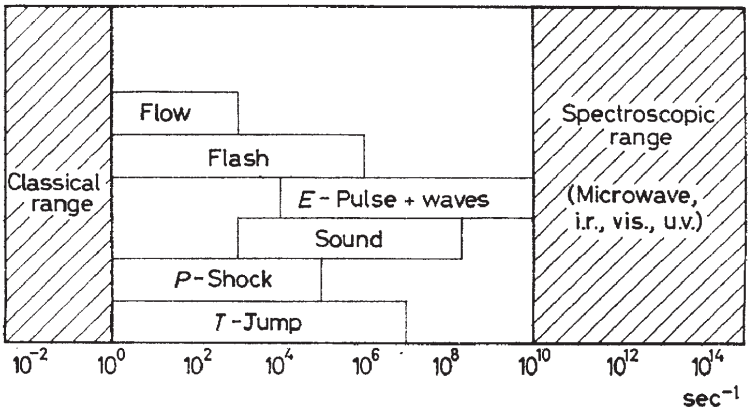

Figure 3.3: Time resolution of different fast kinetics methods. Apart from the *Flow* box, which refers to stopped-flow devices, the other boxes refer to relaxation methods with various excitation means. From Eigen *et al.* [115]

Our method based on droplet microfluidics

Like the stopped-flow machine, our merging chamber presented in the last chapter allows us to precisely trigger a chemical reaction and follow over time the evolution of the chemical reaction. As a result, this is a transient based method. However, the dynamics of product formation is not given by the chemical reaction only, but is also affected by the diffusion of the reagents which are initially kept in two distinct droplets. Thus, the product concentration varies over both space and time and has to be modeled by a reaction-diffusion equation.

In the next section, we study the same bimolecular reaction under the same conditions in both a stopped-flow machine and our reaction chamber. This allows us to compare measurements of the reaction rate constant using each technique.

3.2 Monitoring fast reactions in droplets

In this section, we use our merging chamber to monitor a fast chemical reaction with a one step reaction scheme such as (3.1). We start by performing a reference measurement of the reaction rate constant k using a stopped-flow machine. Next we study the same reaction in the same condition in droplets using our merging device. The reaction rate constant k is then measured by comparing our measurements to numerical solutions of our reaction-diffusion model. Lastly, we compare the measurements of the reaction rate constant k obtained using both techniques.

3.2.1 Experiments

We have chosen to study the reduction of the dark blue 2,6-dichlorophenolindophenol (DCPIP) into a colorless molecule by L-ascorbic acid (also colorless). We use the shorthand notation A for L-ascorbic acid, B for DCPIP and C for the reaction product. This reaction is known to have an overall one step mechanism [117] and is commonly used to measure the dead-time of stopped-flow devices as its rate constant k varies from 10^2 $M^{-1}s^{-1}$ at neutral pH up to 10^5 $M^{-1}s^{-1}$ at both acidic and basic pH.

A test reaction was performed in droplets at pH = 2 in the aim of reaching very fast reaction rates, but it led to precipitations of the product. No test reactions was done at alkaline pH. To avoid any complications on the droplet microfluidic side related to harsh pH conditions, we decided to work around neutral pH and fixed the pH at 6.

Reference measurement of k with a stopped-flow machine

Along with Paul Abbyad and Marten Vos, we first performed stopped-flow experiments to have a reference measurement of k. To this end, we fixed $B_0 = 0.6$ mM and varied A_0 from 10 mM up to 100 mM in order to follow the procedure of Matusmura *et al.* [118] at pH = 6. In these conditions, $A_0 \gg B_0$ so that A is nearly not consumed during the experiment. As a result, the concentration of A molecules is constant $A(t) \approx A_0$ at all times, and the concentration of B molecules has to decay exponentially $B(t) \approx B_0 e^{-k_{\text{obs}}t}$ with the observed rate k_{obs} being defined as $k_{\text{obs}} = kA_0$. As shown on Fig. 3.4 a), the stopped-flow traces we obtained are indeed exponentially decaying. From this traces, we obtain k_{obs} for five different values of A_0 as shown on Fig. 3.4 b). A linear fit of k_{obs} with A_0 then yields $k = 87 \pm 1.2$ $M^{-1}s^{-1}$.

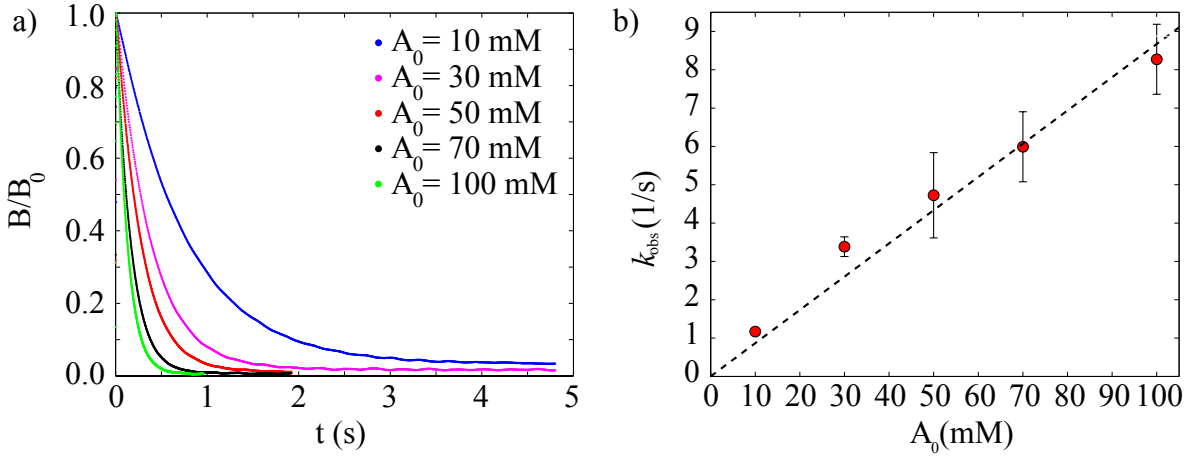

Figure 3.4: a) Stopped-flow traces for different values of the initial concentration of A. The initial concentration of B molecules is kept constant $B_0 = 0.6$ mM. The pH is 6. The stopped-flow device was from Biologic Instruments. b) Measurements of k_{obs} against A_0 to yield k. Error bars correspond to the standard deviation of three repeats.

Experiments in droplets

Next, we used the same solutions of reagents in droplets, on the same day to make sure that our solutions remain fresh. The experiment consists in injecting the solutions of A and B in our merging device to make two droplets of A and B trapped next to each other as shown on Fig. 3.5 a) and b). The next steps of the device operation consist in merging the drops with a laser pulse placed on the touching interfaces (Fig. 3.5 c)), recording the chemical reaction taking place and lasty, emptying the chamber with a transverse flush of oil (Fig. 3.5 d)). The bottom row of Fig. 3.5 shows closed up pictures of the reaction front taking place in the daughter droplets once A and B are allowed to mix. Droplet fusion is initiated after the laser has been removed (Fig. 3.5 f)), the fused drop quickly relaxes to the final oblong shape imposed by the anchors and the reagents remain well separated in the first instant after fusion (Fig. 3.5 e) and f)). A reactive front propagates in the fused droplet, as shown in Fig. 3.5 e) to k), until the limiting reagent has been exhausted.

As the distribution of DCPIP is fairly homogeneous across the daughter droplet (y axis on Fig. 3.6 a)) and propagates along the daughter droplet (x axis on Fig. 3.6 a)), we monitor it along the daughter droplet only by following the procedure detailed in Chapter 2. Thus, we obtain space-time concentration maps of DCPIP along the daughter drop as shown on Fig. 3.6 b). As one can see, the front propagates toward the B rich region and accelerates as A_0 is increased.

These two observations can be understood as follows. A and B mix and react near the front location as they are initially kept separated in two different drops. As $A_0 \gg B_0$, B is the first reagent to be exhausted where A and B meet. On the other hand, the excess of A is not much affected by the chemical reaction, and hence is essentially diffusing freely toward the B rich region where it consumes all the B molecules standing on its way. As a

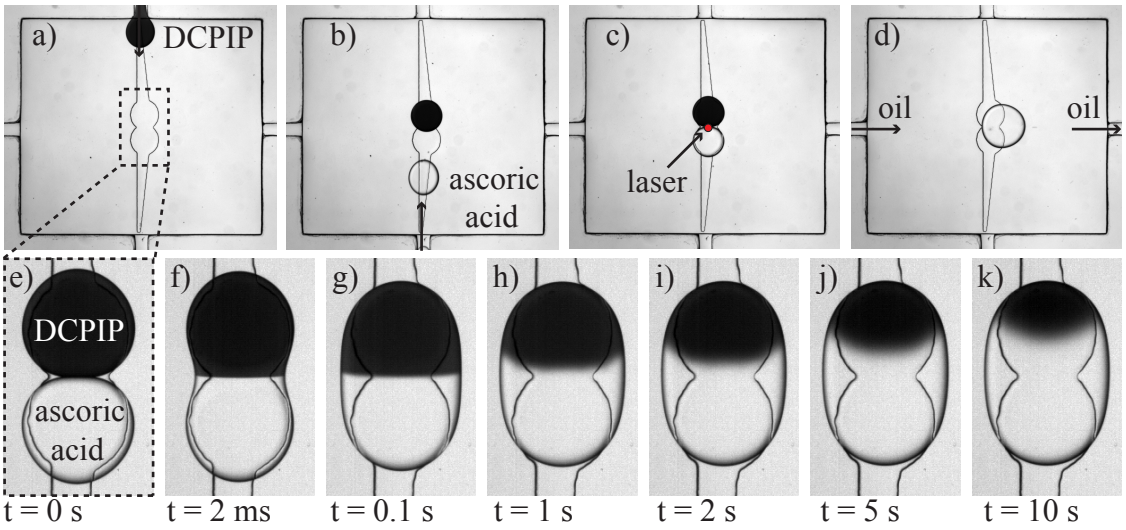

Figure 3.5: Test experiment with $A_0 = 100$ mM and $B_0 = 6$ mM. *Top row:* Device operation. a) - b) Injection of reagents. c) Laser pulse to merge the drops. d) Oil flush to empty the chamber. *Bottom row:* Reactive Front. e) Initial pair of droplets. f) - g) Quick relaxation of the droplet interface. h) - k) Reactive front propagation along the daughter drop.

result, the reaction front displaces toward the B rich region. Secondly, the time scale on which B molecules are consumed has to be defined locally by $1/kA(x,t)$. Nonetheless, the larger A_0, the larger $A(x,t)$ for all x and t, and hence the faster B molecules are consumed at each x position. As a result, the larger A_0 the faster the front propagates.

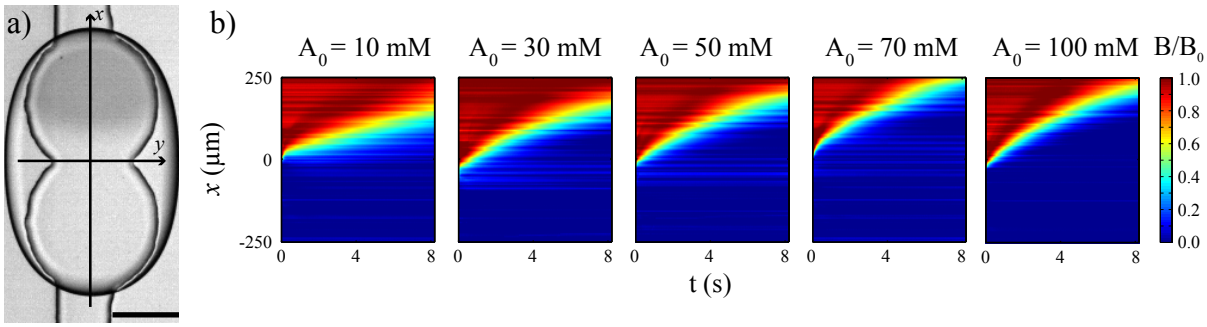

Figure 3.6: a) Kinetic experiment at working concentrations $A_0 = 100$ mM and $B_0 = 0.6$ mM. The directions along and across the drop are labeled x and y respectively. b) Space-time diagrams at fixed $B_0 = 0.6$ mM and A_0 varied from 10 mM up to 100 mM.

The next subsection is concerned with the derivation of a mathematical model for the space-time evolution of the concentrations of both A and B, which will allow us to quantitatively describe the propagation of the front.

3.2.2 RD model with initially separated reagents

We consider a one step reaction A + B $\rightarrow$ C held in our droplet system, and focus on modeling the distribution of A, B and C along the daughter droplet which we label by the coordinate x. We denote these distributions $A(x,t)$, $B(x,t)$ and $C(x,t)$ respectively.

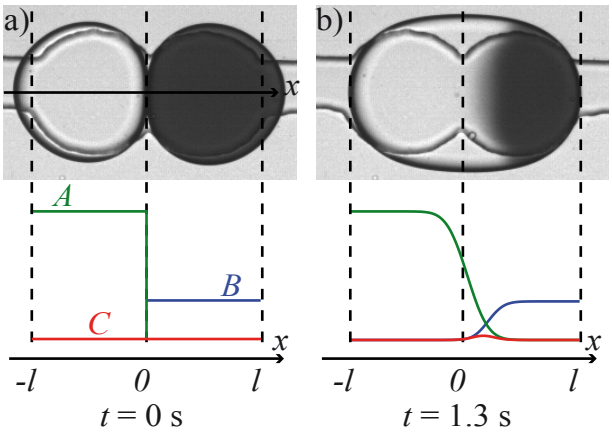

Figure 3.7: a) Initial conditions. The touching droplets are modeled with two touching Heaviside functions. b) Concentration profiles of A, B and C along the daughter droplet at a fixed time point $t = 1.3$ s. The initial concentration are $A_0 = 100$ mM and $B_0 = 6$ mM in this experiment. The size of the domain is $l = 500$ μm.

We model the two touching droplets by two touching 1D reservoirs of the reacting species A and B, A being on the left hand side and B on the right hand side as shown on Fig. 3.7 a). These reservoirs being placed next to each other, we model the initial distributions of A and B by two touching step functions, C being not formed initially. Hence the initial conditions on A, B and C read as:

$$A = A_0\ \hat{H}(x \leq 0) \qquad B = B_0\ \hat{H}(x \geq 0) \qquad C = 0 \tag{3.8}$$

with $\hat{H}$ the Heaviside function.

For $t > 0$, A and B are allowed to diffuse toward each other, and react with a second order rate law $R(x,t) = kA(x,t)B(x,t)$ at all positions x and times t, k being the reaction rate constant. As a result, the mass balances of A, B and C read as:

$$\frac{\partial A}{\partial t} = D_A \frac{\partial^2 A}{\partial x^2} - kAB \tag{3.9a}$$

$$\frac{\partial B}{\partial t} = D_B \frac{\partial^2 B}{\partial x^2} - kAB \tag{3.9b}$$

$$\frac{\partial C}{\partial t} = D_C \frac{\partial^2 C}{\partial x^2} + kAB \tag{3.9c}$$

where D_A, D_B and D_C are the diffusion coefficient of A, B and C.

Finally, our domain is bounded by the interface of the daughter droplet which is non-permeable. Hence we apply no-flux boundary conditions at the edges of the domain $x = \pm\, l$:

$$\frac{\partial A}{\partial x} = \frac{\partial B}{\partial x} = \frac{\partial C}{\partial x} = 0 \quad \text{at } x = \pm\, l \tag{3.10}$$

Thus, we have derived a model for A, B and C which depends on four free parameters: The rate constant k and the 3 diffusion coefficients D_A, D_B and D_C. B being colorful we were able to measure its diffusion coefficient $D_B = 1.1{\times}10^{-9}$ m^2/s by merging a droplet of DCPIP at 6 mM with a droplet of pure water as described in Chapter 2. On the other hand, A and C being colorless, we are not able to measure their diffusion coefficients using bright field images. Instead, we assume them to be $D_A = (M_B/M_A)^{1/3} D_B$ and $D_C = (M_B/M_C)^{1/3} D_B$ where M_A, M_B and M_C are the molar weights of A, B and C. These relations are derived from the Stokes-Einstein equation. Indeed, in his theory of Brownian motion, Einstein [119] relates the diffusion coefficient D of a spherical solute to its radius R provinding that solvent molecules are small compared to solute ones. Then, Einstein shows that $D = kT/6\pi\mu R$, with μ the solvent viscosity, k_B the Boltzmann constant, and T the temperature. As a result, $D_A/D_C = R_C/R_A$, which leads to $D_A/D_C = (M_C/M_A)^{1/3}$ when A and C are assumed to be homogeneous spheres.

By doing so, we are left with a model for A, B and C which has only one free parameter, the reaction rate constant k, on which we can fit. We can thus solve numerically the set of equations (3.9a)-(3.9c) for different values of k, and look for the value of k for which our experimental and simulated profiles of B fit best. Through this fitting procedure, we obtain a measurement of k.

3.2.3 Extracting the reaction rate constant from space-time diagrams

As discussed above, our RD model allows us to fit the reaction rate constant k, and hence to extract a measure of k from our data. Here, we start by presenting a local fitting procedure consisting in fitting on the whole space-time diagrams, hence on the local concentration fields $B(x,t)$. Then, we turn our attention to a global fitting procedure consisting in fitting

on the space-averaged concentration of B, denoted $\overline{B}(t)$. The reasons for looking at $\overline{B}(t)$ instead of $B(x,t)$ are twofolds. First, $\overline{B}(t)$ depends on time only which makes it easier to follow when compared to $B(x,t)$ which depends on both x and t. Second, monitoring $\overline{B}(t)$ requires to allocate a few pixels to record the fusion of one pair of droplets, while resolving spatially $B(x,t)$ requires to allocate few hundreds of pixels. This is a key advantage when working with dense arrays of pairs of droplets. In the current situation sketched on Fig. 3.8 a), our chip can store six pairs of droplets at most, and many pixels are available to resolve locally $B(x,t)$ in each pair of droplets. When aiming at increasing the number of pairs of droplets on chip by further miniaturization and parallelization as shown on Fig. 3.8 b), this is not the case anymore. There are only few pixels left to monitor each pair of droplets and $\overline{B}(t)$ only is readable in this situation.

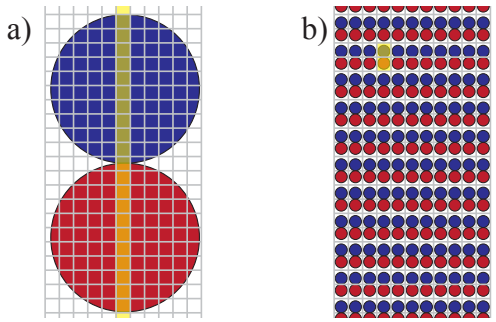

Figure 3.8: a) Sketch of the current situation. Many pixels are allocated to monitor a pair of droplets. We can resolve the gray levels along the pair of droplet (light yellow area). b) Sketch of a future miniaturization/parallelization of our pairing technique. Few pixels are allocated to register one pair of droplets (light yellow area).

Lastly, we study the dependency of the last two fitting procedures with the time window on which we fit.

Local fitting procedure

We used the Matlab routine `pdepe` to solve iteratively the set of equations (3.9a)-(3.9c) with the prescribed initial and boundary condition (3.8) and (3.10) respectively, for different values of the reaction rate constant k. The size of the numerical domain is given by the droplet size so that -500 $\leq x \leq$ 500 μm. The time window was fixed to 2 s so that computation are done for $0 \leq t \leq 2$ s. The remaining free parameter is the rate constant k. From our reference measurement, we expect k_{obs} between 1 s^{-1} and 10 s^{-1} which gives us a range of values of k to scan for each values of A_0.

At each iteration on k, we compare our simulated space-time diagram $B^{\text{sim}}(x,t)$ to our

experimental space-time diagram $B^{\text{exp}}(x,t)$ by calculating the error we make:

$$\text{error} \quad = \quad \frac{||B^{\text{sim}}(x,t) - B^{\text{exp}}(x,t)||}{||B^{\text{sim}}(x,t)||} \tag{3.11}$$

Once all the range of values of k has been scanned, we obtain the error as a function of the reaction rate constant k, or equivalently, as a function of the observed rate k_{obs}. As shown on Fig. 3.9, the error is a U shaped function with a minimum $k^{\star}_{\text{obs}}$, which we take as a measurement of k_{obs}. The error distribution has also a given width from which we extract the confidence interval on our measurement. The confidence interval Δk_{obs} is defined as the interval around $k^{\star}_{\text{obs}}$ in which the error varies between its best fit value $R^{\star}$ and 1.01 $R^{\star}$.

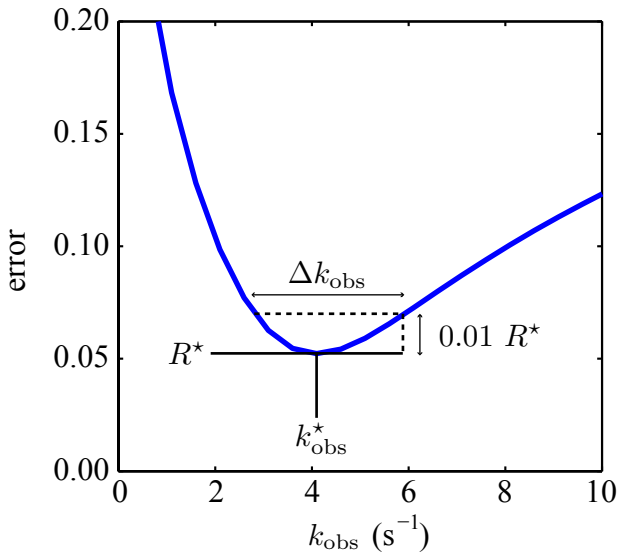

Figure 3.9: error against k_{obs} for $A_0 = 50$ mM and $B_0 = 0.6$ mM. Our measurement of k_{obs} is the minimum value $k^{\star}_{\text{obs}}$. The confidence interval on our measurement is Δk_{obs} and defined by taking the value of k_{obs} at which the error increases by 1% from its minimum value $R^{\star}$.

This procedure yields experimental and simulated space-time diagrams in good agreement as shown on Fig. 3.10. Here, the experimental space-time diagram of B is shown in the case $A_0 = 100$ mM and $B_0 = 0.6$ mM (Fig. 3.10 a)) as well as the corresponding best fit (Fig. 3.10 b)) obtained for $k_{\text{obs}} = 3.80 \pm 0.67$ s^{-1}, and a superposition of the profiles of B at different time points (Fig. 3.10 c)).

We performed this fitting procedure for our set of experiments at different A_0 (10, 30 50 70 100 mM respectively), which yields five measurements of k_{obs}, and hence $k = 82.8 \pm 0.5$ $\text{M}^{-1}\text{s}^{-1}$.

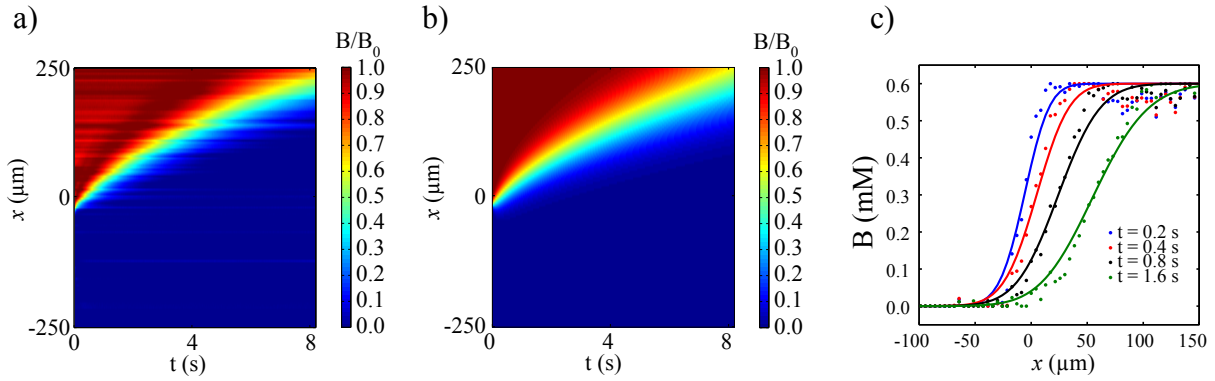

Figure 3.10: a) Experimental space-time diagram of B for $A_0 = 100$ mM and $B_0 = 0.6$ mM. b) Corresponding best fit space-time diagram. c) Superposition of the profiles of B at different time points.

Global fitting procedure

The space-averaged concentration of B is defined as:

$$\overline{B}(t) = \frac{1}{2l}\int_{-l}^{l} B(x,t)dx \tag{3.12}$$

Instead of looking for the local error, here we look for the error between the simulated and the experimental mean concentration of B, denoted $\overline{B}^{\text{sim}}(t)$ and $\overline{B}^{\text{exp}}(t)$ respectively. This error is defined as:

$$\text{error} = \frac{||\overline{B}^{\text{sim}}(t) - \overline{B}^{\text{exp}}(t)||}{||\overline{B}^{\text{sim}}(t)||} \tag{3.13}$$

Again, we solve iteratively the local problem (3.9a)-(3.9c) for different values of k and calculate the global error (3.13) at each iteration. The error is again a U shaped function from which we extract the minimum and the width as measurement of k_{obs} and the confidence interval Δk_{obs} on our measurement. As shown on Fig. 3.11, this procedure yields time courses in good agreement with our experimental space-averaged concentrations of B for different values of the initial concentration of A.

With our global fitting procedure, we obtain again five different measurements of k_{obs}. Taking the mean and the standard deviation of these five measurements yields $k_{\text{obs}} = 79.7 \pm 1.4\ \text{s}^{-1}$. Lastly, we compared our measurements of k_{obs} at different A_0 using our two fitting procedures and our stopped-flow measurements. As shown on Fig. 3.12, the three techniques yield measurements in good agreement which validates our RD model to represent the reactive front at play in the drops, and also demonstrate that our RD approach is sound in order to extract reaction rates from kinetic experiments held in our merging device.

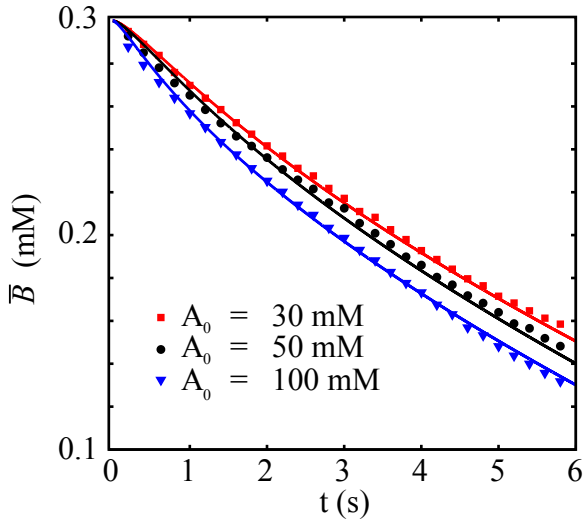

Figure 3.11: Time evolution of the space-averaged concentration of B (denoted $\overline{B}$) for three different values of A_0. The solid lines are the best fits obtained from the RD model.

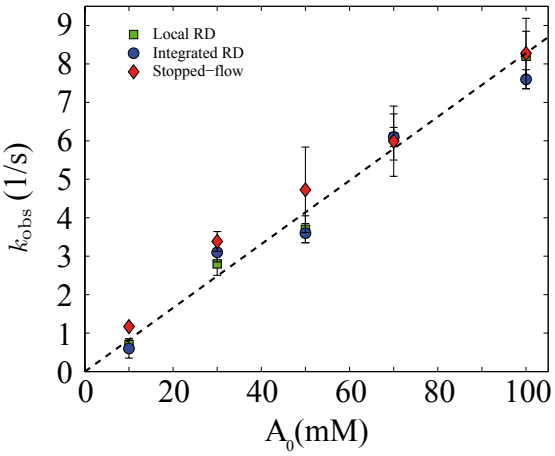

Figure 3.12: Comparison between on-chip measurements of k, obtained from spatial and integrated fits, with measurements of $k_{\text{obs}} = kA_0$ performed in a stopped-flow spectrometer. $B_0 = 0.6$ mM for all experiments. The error bars on the stopped-flow measurement correspond to variations between 3 different runs. The error bars on the RD measurements correspond to the selectivity of the different fitting procedures by taking the value of k_{obs} at which the residue increases by 1% from the miminum value.

Varying the time window for fitting

In both the local and integral fitting protocols, k is obtained by finding the minimum of the residual error between the simulations and the experiments. The selectivity of these measurements is then evaluated by measuring the confidence interval Δk_{obs}. When varying the ending point t_{end} of the time window, so that the fits are performed for $0 \leq t \leq t_{\text{end}}$, we find that a reliable measure of k can be obtained for time windows larger than around 1 s, independently of k_{obs}, and that the selectivity improves for longer windows. As shown on Fig. 3.13 in the case $A_0 = 50$ mM and $B_0 = 0.6$ mM, the error selects more and more a given value of k_{obs} as the time window t_{end} is increased, for both the local and the global fitting protocols.

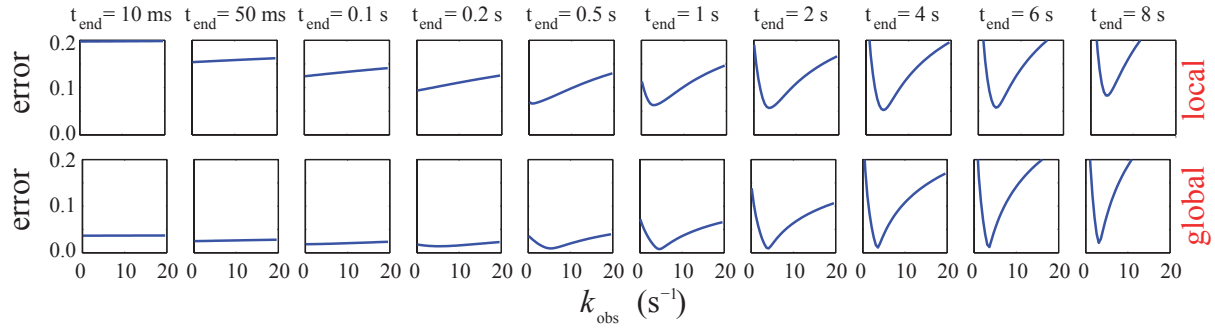

Figure 3.13: Errors against k_{obs} for increasing value of the ending time point t_{end} and for our two fitting procedures. This is the case $A_0 = 50$ mM and $B_0 = 0.6$ mM. *Top row:* Local fitting procedure. *Bottom row:* Global fitting procedure.

With $A_0 = 50$ mM, $B_0 = 0.6$ mM and $k = 80$ M^{-1}s^{-1}, we can also calculate the time scale k_{obs}^{-1}, or equivalently $1/kA_0$, over which B molecules are consumed: $k_{\text{obs}}^{-1} \approx 250$ ms, as well as the time scale over which A molecules are consumed: $1/kB_0 \approx 20$ s. As a result, Fig. 3.13 also shows that chemical information can be extracted from the RD front at times $t \gg k_{\text{obs}}^{-1}$. This contrasts strongly with well-mixed methods for which chemical information is no more available at times $t \gg k_{\text{obs}}^{-1}$.

Indeed, in a well-mixed tank, the reaction stops once the limiting reagent B is completely exhausted. This takes place on a time scale k_{obs}^{-1}. The slow time scale $1/kB_0$ is thus never reached. On the other hand, when the reagents are initially kept separated, not all the fresh B molecules are exhausted on the time scale k_{obs}^{-1}, but only the B molecules near the interface separating the A rich and the B rich regions. As a result, there are fresh B molecules left at times $t \gg k_{\text{obs}}^{-1}$ for the reaction to carry on. Consequently, we expect chemical information to be available up to $t \sim 1/kB_0$ after what time the initial excess of A molecules near the front location is completely exhausted.

So while techniques that rely on mixing the species must monitor the reaction on the

fast time scale $1/kA_0$, the RD based measurement relies on long observations up to the slow time scale $1/kB_0$, which makes it ideal to study fast kinetics. Indeed, methods such as the stopped-flow that need to mix the reagents have an endemic dead time of a few ms, before which reactions cannot be monitored. Resolving the fast time scale $1/kA_0$ is therefore a strong limitations when aiming at large k. Conversely, our approach does not suffer from any dead time induced by mixing as there is no active mixing involved, and it allows the reaction to be monitored up the slow time scale $1/kB_0$ which makes large k more easily accessible.

In the next section, we use asymptotic analyses to confirm theoretically these experimental observations and by the same token, to have a better understanding of the physics underlying the different asymptotic regimes.

3.3 Asymptotics in the case of equally diffusing species

From a theoretical point of view, the reaction-diffusion problem of two species A and B reacting via the second order scheme A + B $\rightarrow$ C, while being initally separated has attracted much interest since the pioneer work of Gálfi and Rácz [21]. The reasons for this excitement are twofolds. First, this system can sustain a reaction front, *i.e.* a spatially localized region with non-zero production rate $R(x,t) = kA(x,t)B(x,t)$, since the two reactants are initially separated in space. Such fronts are ubiquitous in the pattern formation process [120, 121]. In addition, the front results here from the particular choice of the initial conditions, which contrasts strongly with another class of RD front resulting from the interplay between autocatalysis and diffusion [122]. Second, the dynamics of this front presents two distinct asymptotic regimes, in which the product formation is either driven by the chemical reaction, or by the diffusion of the reagents toward the front.

In this section, we study the concentration fields of A, B and C for varying initial concentrations of A and B. Following Gálfi and Rácz [21], we focus on the case of equally diffusing species. We thus consider that A, B and C have the same diffusion coefficient D:

$$D \quad = \quad D_A \quad = \quad D_B \quad = \quad D_C \tag{3.14}$$

We start by directly solving numerically our RD model for different values of the concentration ratio $\hat{\phi} = B_0/A_0$. Then, we use asymptotic analyses to identitify two different regimes in the product formation rate. We derive analytical solutions for the concentration fields A, B and C in these two asymptotic regimes and compare our analytical results to DNS. The transition time to pass from one regime to other is discussed in the next section.

3.3.1 Dimensionless formulation

We first need to write the dimensional problem (3.9a)-(3.9c) in a dimensionless form. Indeed, in dimensional form, the RD problem presents 5 independent parameters: The

diffusion coefficient D, the initial concentrations of the reagents A_0 and B_0, the reaction rate k and the size of the domain l. Making the equations (3.9a)-(3.9c) dimensionless brings the number of free parameters down to 2, namely the concentration ratio $\hat{\phi} = B_0/A_0$ and the Damköhler number $Da = kA_0l^2/D$. This simplifies both the numerical and the analytical treatment of our RD problem. We use the same rules as Gálfi and Rácz [21] for non dimensionalization and note all the dimensionless quantities with a hat. Furthermore, a nomenclature is attached at the end of this chapter.

Concentrations

We choose to count the concentrations A, B et C in units of A_0 and thus we define the dimensionless concentrations $\hat{a}$, $\hat{b}$ et $\hat{c}$ as:

$$\hat{a} = \frac{A}{A_0} \qquad \hat{b} = \frac{B}{A_0} \qquad \hat{c} = \frac{C}{A_0} \tag{3.15}$$

The choice of A as a reference is arbitrary but does not matter as A and B have equivalent role in the chemical scheme (3.1). In the rest of this chapter, the initial concentration of A is assumed to be larger than that of B so that B is always the limiting reagent:

$$B_0 \leq A_0 \quad \text{or equivalently} \quad \hat{\phi} \leq 1 \quad \text{in the rest of this chapter}$$

Time scale

The dynamics of the system of equations (3.9a)-(3.9c) is driven by the forcing R from the chemical reaction. When B is the limiting reagent, the time scale τ associated to that forcing is:

$$\tau = \frac{1}{kA_0} \tag{3.16}$$

from which we can define a dimensionless time variable $\hat{t}$:

$$\hat{t} = \frac{t}{\tau} \tag{3.17}$$

Length scale

While the front has not reached the edges of the domain $x = \pm\, l$, the size of the domain l does not influence the dynamics of the front. As a result, there is no inner length scale available to make the space coordinate x dimensionless. The remaining length scale is the diffusive length scale based on τ. Thus the dimensionless space coordinate $\hat{x}$ reads as:

$$\hat{x} \;=\; \frac{x}{\sqrt{D\tau}} \tag{3.18}$$

Besides, this nondimensionalization can be done at each time t using the time-dependent length scale $\sqrt{Dt}$. This shows that the concentration profiles $\hat{a}$, $\hat{b}$ and $\hat{c}$ are expected to be self-similar [123]. Here, we choose the self-similar space coordinate $\hat{\eta}$:

$$\hat{\eta} \;=\; \frac{x}{\sqrt{4Dt}} \;=\; \frac{\hat{x}}{\sqrt{4\hat{t}}} \tag{3.19}$$

We will show explicitly self-similar solutions of $\hat{a}$, $\hat{b}$ and $\hat{c}$ in the next subsections 3.3.3 and 3.3.4.

Conservation laws

Then, the mass balances (3.9a)-(3.9c) become:

$$\frac{\partial \hat{a}}{\partial \hat{t}} \;=\; \frac{\partial^2 \hat{a}}{\partial \hat{x}^2} \;-\; \hat{a}\hat{b} \tag{3.20a}$$

$$\frac{\partial \hat{b}}{\partial \hat{t}} \;=\; \frac{\partial^2 \hat{b}}{\partial \hat{x}^2} \;-\; \hat{a}\hat{b} \tag{3.20b}$$

$$\frac{\partial \hat{c}}{\partial \hat{t}} \;=\; \frac{\partial^2 \hat{c}}{\partial \hat{x}^2} \;+\; \hat{a}\hat{b} \tag{3.20c}$$

Initial conditions

Similarly, the initial conditions become:

$$\hat{a} = \hat{H}(\hat{x} \leq 0) \qquad \hat{b} = \hat{\phi}\ \hat{H}(\hat{x} \geq 0) \qquad \hat{c} = 0 \tag{3.21}$$

with $\hat{\phi}$ the ratio of the initial concentrations of the reagents:

$$\hat{\phi} \;=\; \frac{B_0}{A_0} \tag{3.22}$$

Boundary conditions

Finally, the boundary conditions become:

$$\frac{\partial \hat{a}}{\partial \hat{x}} = \frac{\partial \hat{b}}{\partial \hat{x}} = \frac{\partial \hat{c}}{\partial \hat{x}} = 0 \quad \text{at } \hat{x} = \pm\ \sqrt{\mathrm{Da}} \tag{3.23}$$

where we define the Damköhler number Da based on l and D by:

$$\mathrm{Da} \;=\; \frac{kA_0 l^2}{D} \tag{3.24}$$

Dimensionless parameters $\hat{\phi}$ and Da

Through non-dimensionalization, 2 dimensionless parameters driving the dynamics of the fields $\hat{a}$, $\hat{b}$, $\hat{c}$ arose:

(i) $\hat{\phi}$: The ratio of the initial concentrations
(ii) Da: The ratio of the reaction to the diffusive time scales

Among these 2 parameters, the reaction rate k takes part only in the Damköhler number Da. As Da sets the position at which the boundary conditions on $\hat{a}$, $\hat{b}$, $\hat{c}$ are applied, it can be seen as a stretching parameter which pulls apart the boundaries of the domain when $\mathrm{Da} \gg 1$, and brings them close from each other when $\mathrm{Da} \ll 1$. As a result, the reaction front reaches the boundaries of the domain quickly when $\mathrm{Da} \ll 1$. This corresponds to a regime in which the reagents A and B first diffuse through the whole domain, mix well, and react in a second phase. This is the case of very slow reactions, or equivalently, the case of very small domains. Conversely, very fast reactions yield high values of Da . In the case $\mathrm{Da} \gg 1$, the reaction front propagates during a long period of time in a quasi-infinite domain. The boundaries do not play any role in the dynamics of the reaction front and we can thus set Da to infinity. Then, our dimensionless RD model reduces to a one parameter problem whose dynamics does not depend on k, and will therefore apply for all values of k.

Setting Da to unity yields a critical observed rate constant $k^{\star}_{\mathrm{obs}} = D/l^2$ below which the well-mixed regime takes place, and above which a reaction front needs to be taken into account. In our set up, we have $l = 500$ μm and $D = 1.1{\times}10^{-9}$ m^2/s which yields $k^{\star}_{\mathrm{obs}} = 4.4\ 10^{-3}$ M^{-1}s^{-1}. Hereafter, we place ourselves in the RD regime and focus on fast reactions: $k_{\mathrm{obs}} > k^{\star}_{\mathrm{obs}}$. As a result, we will consider an infinite domain $\mathrm{Da} \to \infty$.

It should be also noted that when the species A, B and C have different diffusion coefficients, the ratio of these coefficients has some effect on the species distribution, in both the early times [124] and the large times [125] asymptotic regimes but does not change the scalings with time of $\hat{a}$, $\hat{b}$ and $\hat{c}$ in these asymptotic regimes.

3.3.2 Direct numerical simulation

To simulate a quasi-infinite domain, we used a non-uniform mesh with a high point density near the front location, and a looser point density at the edges of the domain. As a result, the reaction front is not affected by the boundary conditions applied far away from the front. The details of the finite differences code we wrote are explained in appendix B.1.

Simulations of $\hat{a}$, $\hat{b}$ and $\hat{c}$ for two values of $\hat{\phi}$, namely 0.1 and 1, are shown on Fig. 3.14. Two different phases can be noted. In the first instants ($\hat{t} = 0.1$, 0.25, 0.5, 1 and 5), the distributions of $\hat{a}$ and $\hat{b}$ overlap and the distribution of the product $\hat{c}$ increases in amplitude in this overlapping region. Conversely, in the last instants ($\hat{t} = 100$, 500 and

1000), the distributions of $\hat{a}$ and $\hat{b}$ do not overlap anymore, except near a tiny region, and the distribution of the product $\hat{c}$ stops increasing in amplitude.

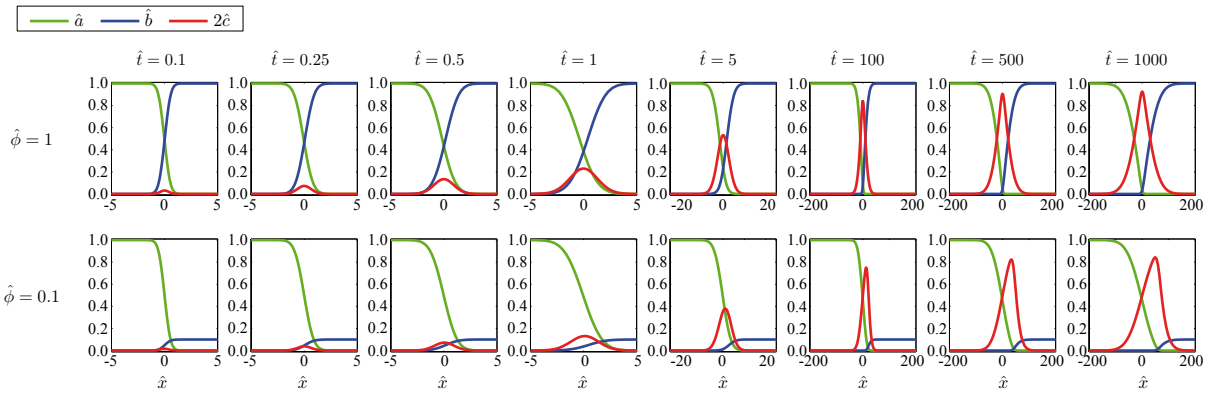

Figure 3.14: Distributions of $\hat{a}$, $\hat{b}$ and $2\hat{c}$ at different time points. The product distribution is multiplied by 2 for display purposes. The domain size is -1000< $\hat{x}$ <1000. *Top row:* Case $\hat{\phi} = 1$. *Bottom row:* Case $\hat{\phi} = 0.1$.

These first simulations highlight two different situations arising at different times. At early times, a *reaction-controlled* regime takes place in which the reagents $\hat{a}$ and $\hat{b}$ are not much affected by the chemical reaction, while the product formation is driven by the chemical reaction. At large times, a *diffusion-controlled* regime takes place in which the reagents $\hat{a}$ and $\hat{b}$ have been completely depleted near the interface separating the two reservoirs of fresh reagent, while the product formation is not driven by the chemical reaction anymore, but by the diffusive fluxes of fresh reagents toward the reaction zone instead. As a result, the front does not move when it is similarly fed from each side as shown on the top row of Fig. 3.14) in the case $\hat{\phi} = 1$, and the front moves toward the region with the weakest diffusive flux, hence toward the reservoir of B when $\hat{\phi} \leq 1$ as shown on the bottom row of Fig. 3.14. In the next subsections, we derive asymptotic solutions for the concentration fields $\hat{a}$, $\hat{b}$ and $\hat{c}$ in these two asymptotic regimes and study the transition times from one regime to the other.

3.3.3 Early times asymptotic solutions

The early times asymptotic solutions of the problem (3.20a)-(3.20c) was first suggested by Taitelbaum *et al.* [124] and later on by Trevelyan *et al.* [22]. Hereafter, we expand each function $\hat{a}$, $\hat{b}$ and $\hat{c}$ in powers of $\hat{t}$, and look for their leading order term in the limit $\hat{t} \to 0$.

In addition, we look for $\hat{a}$, $\hat{b}$ and $\hat{c}$ as self-similar solutions of the variable $\hat{\eta} = \hat{x}/\sqrt{4\hat{t}}$. Hence we look for $\hat{a}$, $\hat{b}$ and $\hat{c}$ as functions of $\hat{\eta}$ and $\hat{t}$, instead of functions of $\hat{x}$ and $\hat{t}$. We

thus expand $\hat{a}$, $\hat{b}$ and $\hat{c}$ for small $\hat{t}$ such that:

$$\hat{a}(\hat{x},\hat{t}) = \hat{\mathbf{a}}_0(\hat{\eta}) + \hat{t}\,\hat{\mathbf{a}}_1(\hat{\eta}) + t^2\,\hat{\mathbf{a}}_2(\hat{\eta}) + ... \quad (3.25a)$$

$$\hat{b}(\hat{x},\hat{t}) = \hat{\mathbf{b}}_0(\hat{\eta}) + \hat{t}\,\hat{\mathbf{b}}_1(\hat{\eta}) + t^2\,\hat{\mathbf{b}}_2(\hat{\eta}) + ... \quad (3.25b)$$

$$\hat{c}(\hat{x},\hat{t}) = \hat{\mathbf{c}}_0(\hat{\eta}) + \hat{t}\,\hat{\mathbf{c}}_1(\hat{\eta}) + t^2\,\hat{\mathbf{c}}_2(\hat{\eta}) + ... \quad (3.25c)$$

Injecting these expansions into the RD equations (3.20a)-(3.20c) then yields the following ODEs for $\hat{\mathbf{a}}_0$, $\hat{\mathbf{b}}_0$ and $\hat{\mathbf{c}}_0$:

$$-2\hat{\eta}\hat{\mathbf{a}}_0' = \hat{\mathbf{a}}_0'' \qquad -2\hat{\eta}\hat{\mathbf{b}}_0' = \hat{\mathbf{b}}_0'' \qquad -2\hat{\eta}\hat{\mathbf{c}}_0' = \hat{\mathbf{c}}_0'' \quad (3.26)$$

which integrates into:

$$\hat{\mathbf{a}}_0(\hat{\eta}) = \frac{1}{2}\mathrm{erfc}(\hat{\eta}) \qquad \hat{\mathbf{b}}_0(\hat{\eta}) = \frac{\hat{\phi}}{2}\mathrm{erfc}(-\hat{\eta}) \qquad \hat{\mathbf{c}}_0(\hat{\eta}) = 0 \quad (3.27)$$

after having taken into account the initial and boundary conditions (3.21) and (3.23). Hence, $\hat{a}$ and $\hat{b}$ are $\mathcal{O}(\hat{t}^0)$ functions of $\hat{t}$ while we need to look for the order $\mathcal{O}(\hat{t}^1)$ function in the expansion of $\hat{c}$. This function $\hat{\mathbf{c}}_1$ is the solution of:

$$4\hat{\mathbf{c}}_1 - 2\hat{\mathbf{c}}_1' = \hat{\mathbf{c}}_1'' + 4\hat{\mathbf{a}}_0\hat{\mathbf{b}}_0 \quad (3.28)$$

which, thanks to the source term $\hat{\mathbf{a}}_0\hat{\mathbf{b}}_0$, is a non-zero function. The equation (3.28) can then be integrated numerically using Broyden's method (detailed in appendix B.2).

As shown on Fig. 3.15, the distributions of $\hat{a}$, $\hat{b}$ and $\hat{c}$ are indeed self-similar since each of these distributions at different time points (Fig. 3.15 a) and c)) collapses on a single curve (Fig. 3.15 b) and d)) when plotted against $\hat{\eta}$. In addition, the leading order solutions $\hat{\mathbf{a}}_\mathbf{0}$, $\hat{\mathbf{b}}_\mathbf{0}$ and $\hat{\mathbf{c}}_\mathbf{1}$ (solid black lines on Fig. 3.15 b) and d)) correspond very well to the distributions obtained via the DNS which confirms our early time asymptotic solutions.

3.3.4 Large times asymptotic solutions

The large times limit $\hat{t} \gg 1$ has been first studied by Gàlfi and Ràcz. [21]. At large times, all the fresh reagents initially near the reaction front have been consumed. As a result, fresh reagents need to diffuse from their reservoir to the reaction zone in order to react. This has two consequences:

1. The size of the reaction zone $\hat{w}_f$ is much smaller than the diffusive length $\hat{W}_d$ over which fresh reagents have to diffuse to reach the reaction zone.

2. The product formation is limited by the diffusive supply of fresh reagents so that, per unit time, all the fresh reagents that reach the reaction zone are converted in product by the chemical reaction.

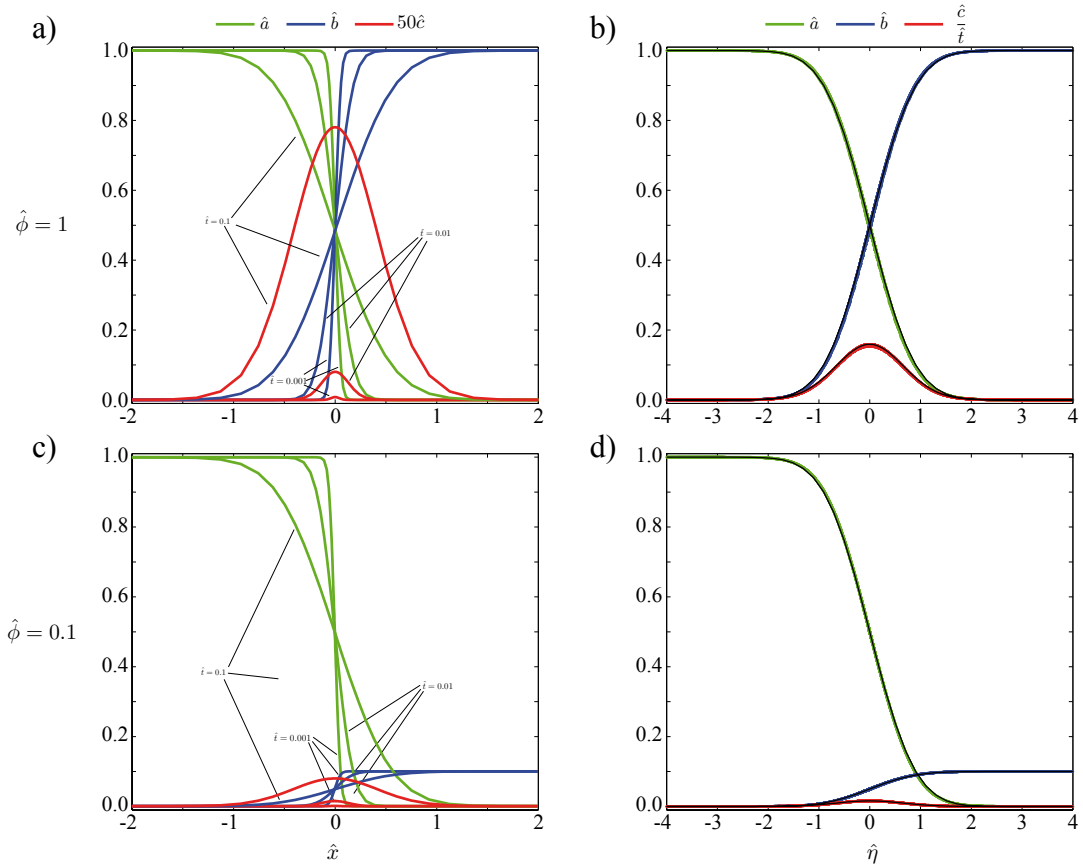

Figure 3.15: a) Profiles of $\hat{a}$ (green), $\hat{b}$ (blue) and $\hat{c}$ (red) at times $\hat{t} = 0.001$, 0.01 and 0.1 obtained numerically when $\hat{\phi} = 1$. b) Superposition of the profiles of $\hat{a}$, $\hat{b}$ and $\hat{c}/\hat{t}$ obtained numerically for $0.001 < \hat{t} < 0.1$ when $\hat{\phi} = 1$. Solid line: $\mathbf{\hat{a}_0}$, $\mathbf{\hat{b}_0}$ and $\mathbf{\hat{c}_1}$ when $\hat{\phi} = 1$. c) and d) Case $\hat{\phi} = 0.1$ with the same plots as a) and b).

This is a boundary layer problem for which two regions with different scale invariances have to be considered:

1. The *depletion zone* where the species purely diffuse toward the reaction zone. Diffusive fluxes thus balance time variations of the species in this region. This is the outer layer.

2. The *reaction zone*, where the reaction takes place. Diffusive fluxes balance the reaction consumption/production in this region. This is the inner layer.

Here we consider the depletion zone only as it sets the profiles of $\hat{a}$, $\hat{b}$ and $\hat{c}$ that we observe experimentally. A detailed study of the reaction front requires to solve the inner problem. This is done in the next section.

As we consider the case of equally diffusing species, we can perform linear combinations of the equations (3.20a)-(3.20c). This yields the relations:

$$\text{(3.20a) } - \text{ (3.20b) yields: } \quad \hat{a}(\hat{x},\hat{t}) - \hat{b}(\hat{x},\hat{t}) = \frac{1}{2}\text{erfc}(\hat{\eta}) - \frac{\hat{\phi}}{2}\text{erfc}(-\hat{\eta}) \tag{3.29a}$$

$$\text{(3.20a) } + \text{ (3.20c) yields: } \quad \hat{a}(\hat{x},\hat{t}) + \hat{c}(\hat{x},\hat{t}) = \frac{1}{2}\text{erfc}(\hat{\eta}) \tag{3.29b}$$

$$\text{(3.20c) } + \text{ (3.20b) yields: } \quad \hat{c}(\hat{x},\hat{t}) + \hat{b}(\hat{x},\hat{t}) = + \frac{\hat{\phi}}{2}\text{erfc}(-\hat{\eta}) \tag{3.29c}$$

since $\hat{a}-\hat{b}$, $\hat{a}-\hat{c}$ and $\hat{c}-\hat{b}$ all follow a diffusion equation. As a result, we can deduce $\hat{c}(\hat{x},\hat{t})$ from $\hat{a}(\hat{x},\hat{t})$ and $\hat{b}(\hat{x},\hat{t})$ via (3.29b) and (3.29c). We can thus solve for $\hat{a}(\hat{x},\hat{t})$ and $\hat{b}(\hat{x},\hat{t})$ only.

Scalings of the depletion zone

There is no chemical reaction in this layer. As a result, we expect all the species to be purely diffusive and to have amplitudes which do not vary over time:

$$\hat{W}_d \sim \hat{t}^{1/2} \qquad \hat{a} \sim \hat{t}^0 \qquad \hat{b} \sim \hat{t}^0 \qquad \hat{c} \sim \hat{t}^0 \tag{3.30}$$

As the length scale of the depletion layer $\hat{W}_d \sim \hat{t}^{1/2}$ is diffusive, we can look for $\hat{a}$, $\hat{b}$ and $\hat{c}$ as self-similar functions of the variable $\hat{\eta}$.

Similarity solutions in the depletion zone The scaling analysis invites us to look for:

$$\hat{a}(\hat{x},\hat{t}) = \hat{\mathbf{a}}^{\mathbf{out}}(\hat{\eta}), \qquad \hat{b}(\hat{x},\hat{t}) = \hat{\mathbf{b}}^{\mathbf{out}}(\hat{\eta}), \qquad \hat{c}(\hat{x},\hat{t}) = \hat{\mathbf{c}}^{\mathbf{out}}(\hat{\eta}) \tag{3.31}$$

As we assume that there is no reaction in the depletion zone, the conservation equations of $\hat{a}$ and $\hat{b}$ in this layer are obtained from (3.20a)-(3.20c) by dropping the reaction term $\hat{a}\hat{b}$. No flux boundary conditions away from the reaction zone can also be applied. At the reaction front $\hat{x} = \hat{x}_f(\hat{t})$, $\hat{a}$ and $\hat{b}$ must vanish. Indeed, if $\hat{a}$ and $\hat{b}$ were non zero at the front location, A and B would be reacting in the depletion zone, which cannot be allowed. As a result, the equations to be solved are:

$$\text{for } \hat{x} \le \hat{x}_f: \quad \frac{\partial \hat{a}}{\partial \hat{t}} = \frac{\partial^2 \hat{a}}{\partial \hat{x}^2} \qquad \hat{a}(\hat{x},\hat{t}) \underset{-\infty}{\to} 1 \qquad \hat{a}(\hat{x}_f(\hat{t}),\hat{t}) = 0 \tag{3.32a}$$

$$\text{for } \hat{x} \ge \hat{x}_f: \quad \frac{\partial \hat{b}}{\partial \hat{t}} = \frac{\partial^2 \hat{b}}{\partial \hat{x}^2} \qquad \hat{b}(\hat{x},\hat{t}) \underset{+\infty}{\to} \hat{\phi} \qquad \hat{b}(\hat{x}_f(\hat{t}),\hat{t}) = 0 \tag{3.32b}$$

Injecting solutions of the form (3.31) into the he equations (3.32a)-(3.32b) yields $\hat{\mathbf{a}}^{\mathbf{out}}$ and $\hat{\mathbf{b}}^{\mathbf{out}}$ from which we obtain $\hat{\mathbf{c}}^{\mathbf{out}}$ via (3.29b) and (3.29c):

$$\hat{\mathbf{a}}^{\mathbf{out}}(\hat{\eta}) = 1 - \frac{\mathrm{erfc}\,(-\hat{\eta})}{\mathrm{erfc}\,(-\hat{\eta}_f)} \quad \text{for } \hat{\eta} \le \hat{\eta}_f \quad \text{and} \quad 0 \quad \text{for } \hat{\eta} \ge \hat{\eta}_f \tag{3.33a}$$

$$\hat{\mathbf{b}}^{\mathbf{out}}(\hat{\eta}) = 0 \quad \text{for } \hat{\eta} \le \hat{\eta}_f \quad \text{and} \quad \hat{\phi}\left(1 - \frac{\mathrm{erfc}\,(\hat{\eta})}{\mathrm{erfc}\,(\hat{\eta}_f)}\right) \quad \text{for } \hat{\eta} \ge \hat{\eta}_f \tag{3.33b}$$

$$\hat{\mathbf{c}}^{\mathbf{out}}(\hat{\eta}) = \frac{\hat{\phi}}{2}\mathrm{erfc}\,(-\hat{\eta}) \quad \text{for } \hat{\eta} \le \hat{\eta}_f \quad \text{and} \quad \frac{1}{2}\mathrm{erfc}\,(\hat{\eta}) \quad \text{for } \hat{\eta} \ge \hat{\eta}_f \tag{3.33c}$$

The last unknown is the position of the front $\hat{x}_f$, or equivalently $\hat{\eta}_f = \hat{x}_f/\sqrt{4\hat{t}}$. As there is no reaction in the depletion zone, all the species reaching the reaction front are consumed at the reaction front. As a result, the diffusive fluxes of A and B must balance at $\hat{x} = \hat{x}_f$ which defines the front location:

$$-\frac{\partial \hat{a}}{\partial \hat{x}}\Big|_{\hat{x}_f} = \frac{\partial \hat{b}}{\partial \hat{x}}\Big|_{\hat{x}_f} \tag{3.34}$$

This yields:

$$\hat{\eta}_f = \mathrm{erf}^{-1}\left(\frac{1-\hat{\phi}}{1+\hat{\phi}}\right) \tag{3.35}$$

These asymptotic solutions (3.33a)-(3.33c) are compared to DNS on Fig. 3.16 for $\hat{\phi} =$ 0.1 and 1. Here again the distributions of $\hat{a}$, $\hat{b}$ and $\hat{c}$ are self-similar since each of these distributions at different time points (Fig. 3.15 a) and c)) collapses on a single curve (Fig. 3.15 b) and d)) when plotted against $\hat{\eta}$. In addition, the leading order solutions $\hat{\mathbf{a}}^{\mathbf{out}}$, $\hat{\mathbf{b}}^{\mathbf{out}}$ and $\hat{\mathbf{c}}^{\mathbf{out}}$ (solid black lines on Fig. 3.15 b) and d)) correspond very well to the distributions obtained via the DNS which confirms our large time asymptotic solutions.

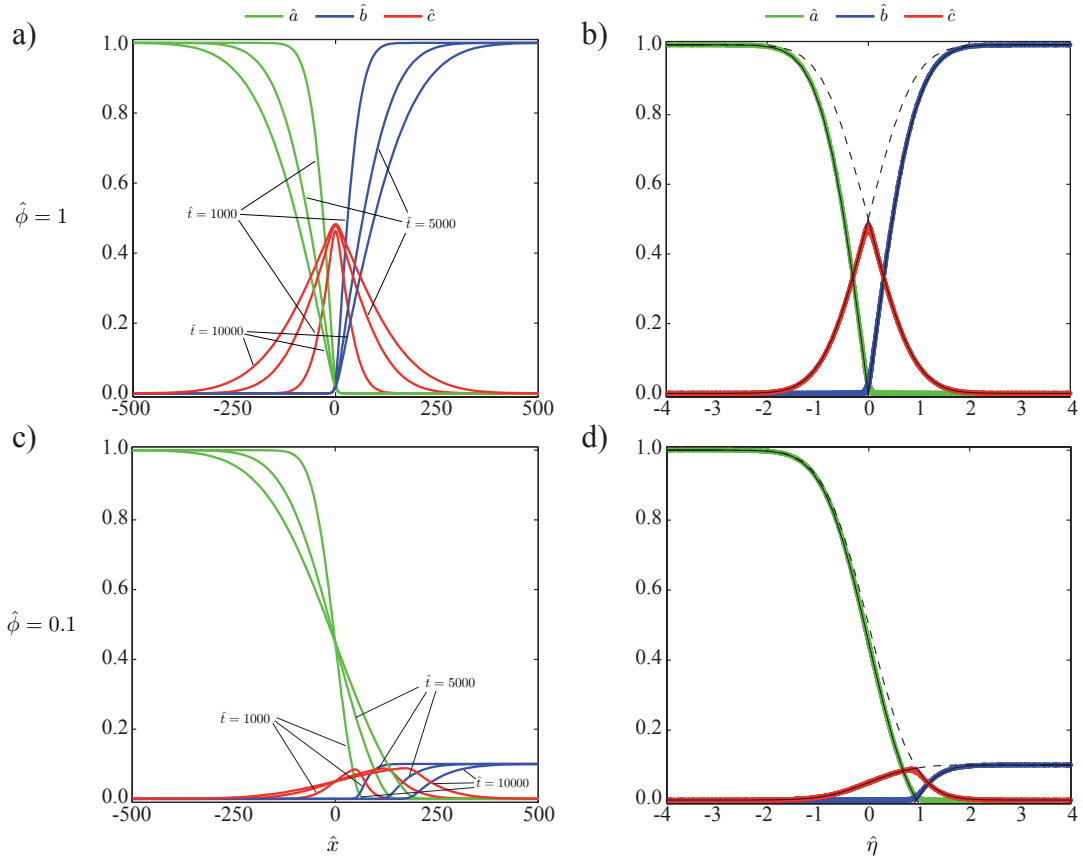

Figure 3.16: a) Profiles of $\hat{a}$ (green), $\hat{b}$ (blue) and $\hat{c}$ (red) at times $\hat{t} = 1000$, 5000 and 10000 obtained numerically when $\hat{\phi} = 1$. b) Superposition of the profiles of $\hat{a}$, $\hat{b}$ and $\hat{c}$ obtained numerically for $1000 < \hat{t} < 10000$ when $\hat{\phi} = 1$. Solid line: $\hat{\mathbf{a}}^{\mathbf{out}}$, $\hat{\mathbf{b}}^{\mathbf{out}}$ and $\hat{\mathbf{c}}^{\mathbf{out}}$ when $\hat{\phi} = 1$. c) and d) Case $\hat{\phi} = 0.1$ with the same plots as a) and b).

3.4 Transition from the early to the large times regimes

In the last section we have identified two distinct regimes in the dynamics of our RD system with initially separated reagents. In the early times regime, the chemical reaction limits product formation and hence chemical information is accessible. Conversely, in the limit of large times, the diffusion fluxes of the reagents toward the reaction zone limit product formation and chemical information is not accessible anymore. In this section, we turn our attention to the transition times from one regime to the other in order to quantify the time window over which chemical information is accessible.

The transition from the reaction-controlled to the diffusion-controlled regime is defined by a change in the reaction zone characteristics. The reaction zone is defined as a region of none zero production rate. Mathematically, the front position, width and amplitude are all defined via the reaction rate $\hat{r} = \hat{a}\hat{b}$. Here we start by defining these three quantities. Then we study each of these three quantities in both the early and the late times regimes. This allows us to measure the time points at which our RD system leaves its early times behaviour and enters its large times behaviour. To do so, we compare the exact solution of the RD problem (3.20a)-(3.20c) obtained numerically with our asymptotic solutions in the two limit cases. Consequently, we can define a time scale $\hat{t}^\star$ at which the reaction front leaves the reaction-controlled regime and a second time scale $\hat{t}_{\hat{\phi}}$ at which the reaction front enters the diffusion-controlled regime. The time window over which chemical information is accessible is then given by $\hat{t}_{\hat{\phi}}$.

3.4.1 Reaction zone characteristics

The reaction rate $\hat{r} = \hat{a}\hat{b}$ must have a bell-shaped distribution since $\hat{a}$ and $\hat{b}$ are overlapping step functions. As a result, we can define the reaction front position $\hat{x}_f$, width $\hat{w}_f$ and amplitude $\hat{h}_f$ as sketched on Fig. 3.17.

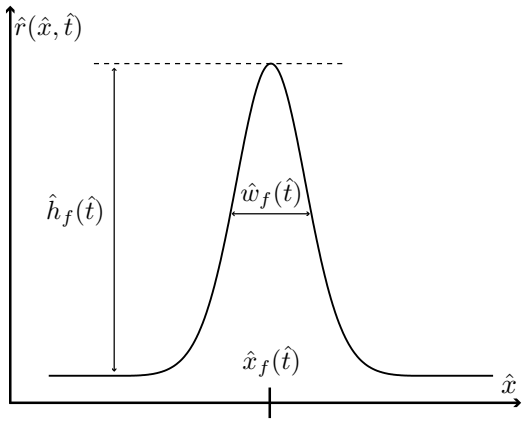

Figure 3.17: Characteristics of the reaction front $\hat{r}$: Position $\hat{x}_f$, width $\hat{w}_f$ and amplitude $\hat{h}_f$.

Following Trevelyan *et al.* [22, 125], we define the reaction front position $\hat{x}_f(\hat{t})$ as the first moment of the reaction rate $\hat{r}$:

$$\hat{x}_f(\hat{t}) = \frac{\int_{-\infty}^{+\infty} \hat{x}\hat{r}(\hat{x},\hat{t})d\hat{x}}{\int_{-\infty}^{+\infty} \hat{r}(\hat{x},\hat{t})d\hat{x}} \tag{3.36}$$

and the front width $\hat{w}_f(\hat{t})$ as the square root of the second moment of the reaction rate:

$$\hat{w}_f(\hat{t})^2 = \frac{\int_{-\infty}^{+\infty} (\hat{x}-\hat{x}_f)^2 \hat{r}(\hat{x},\hat{t})d\hat{x}}{\int_{-\infty}^{+\infty} \hat{r}(\hat{x},\hat{t})d\hat{x}} \tag{3.37}$$

Lastly, the front amplitude (or height) of the front $\hat{h}_f(\hat{t})$ is defined as the value of $\hat{r}$ at $\hat{x}_f$:

$$\hat{h}_f(\hat{t}) = \hat{r}\left(\hat{x}_f(\hat{t}),\hat{t}\right) \tag{3.38}$$

Thanks to these definitions, we can look for asymptotics solutions of $\hat{x}_f$, $\hat{w}_f$ and $\hat{h}_f$ in both the reaction-controlled and the diffusion-controlled regimes.

3.4.2 Reaction front in the small times limit

In the early times regimes we know both $\hat{a}$ and $\hat{b}$, hence we know $\hat{r} = \hat{a}\hat{b}$. As we have expanded $\hat{a}$ and $\hat{b}$ in powers of $\hat{t}$, we can also do it for $\hat{r}$:

$$\hat{r}(\hat{x},\hat{t}) = \hat{\mathbf{a}}_0(\hat{\eta})\hat{\mathbf{b}}_0(\hat{\eta}) + \hat{t}\left(\hat{\mathbf{a}}_0(\hat{\eta})\hat{\mathbf{b}}_1(\hat{\eta}) + \hat{\mathbf{a}}_1(\hat{\eta})\hat{\mathbf{b}}_0(\hat{\eta})\right) + ... \tag{3.39}$$

Position of the reaction front

The leading order of the reaction rate is:

$$\hat{r}(\hat{x},\hat{t}) = \hat{\mathbf{a}}_0(\hat{\eta})\hat{\mathbf{b}}_0(\hat{\eta}) = \frac{\hat{\phi}}{4}\mathrm{erfc}(\hat{\eta})\mathrm{erfc}(-\hat{\eta}) \tag{3.40}$$

It yields $\hat{x}_f = 0$. This is consistent with the case $\hat{\phi} = 1$ for which the problem is symmetric and thus we do not expect the reaction front to move. Hence:

$$\text{for } \hat{\phi} = 1: \quad \hat{x}_f(\hat{t}) = 0 \tag{3.41}$$

However, setting $\hat{x}_f = 0$ is not consistent with the case $\hat{\phi} < 1$ for which we expect the front to move [124]. We thus need to go to $\mathcal{O}(\hat{t}^1)$ and compute $\hat{\mathbf{a}}_1$ and $\hat{\mathbf{b}}_1$. This is done

in detail in appendix C. We do not find an analytical solution for $\hat{\mathbf{a}}_1$ and $\hat{\mathbf{b}}_1$. Instead, we obtain numerically:

$$\text{for all } \hat{\phi} < 1: \qquad \hat{x}_f(\hat{t}) \;=\; 2\,\hat{t}^{3/2}\,\frac{\displaystyle\int_{-\infty}^{+\infty}\left(\hat{\mathbf{a}}_0(\hat{\eta})\hat{\mathbf{b}}_1(\hat{\eta})+\hat{\mathbf{a}}_1(\hat{\eta})\hat{\mathbf{b}}_0(\hat{\eta})\right)\,\hat{\eta}d\hat{\eta}}{\displaystyle\int_{-\infty}^{+\infty}\hat{\mathbf{a}}_0(\hat{\eta})\hat{\mathbf{b}}_0(\hat{\eta})d\hat{\eta}} \;=\; 0.51\,\hat{t}^{3/2} \tag{3.42}$$

Width of the reaction front

Once $\hat{x}_f$ is known, the width of the front is obtained via its definition (3.37) and the leading order of the reaction rate $\hat{r} \approx \hat{\mathbf{a}}_0\hat{\mathbf{b}}_0$ to yield:

$$\hat{w}_f^2(\hat{t}) \;=\; 4\,\hat{t}\,\frac{\displaystyle\int_{-\infty}^{+\infty}(\hat{\eta}-\hat{\eta}_f)\,\hat{\mathbf{a}}_0(\hat{\eta})\hat{\mathbf{b}}_0(\hat{\eta})d\hat{\eta}}{\displaystyle\int_{-\infty}^{+\infty}\hat{\mathbf{a}}_0(\hat{\eta})\hat{\mathbf{b}}_0(\hat{\eta}))d\hat{\eta}} \;=\; 8.82\,\hat{t} \tag{3.43}$$

Amplitude of the reaction front

Finally the height of the reaction front is straightforward from the leading orders $\hat{r}(\hat{x},\hat{t}) = \frac{\hat{\phi}}{4}\text{erfc}(\hat{\eta})\text{erfc}(-\hat{\eta})$ and $\hat{x}_f(\hat{t}) = 0$:

$$\hat{h}_f \;=\; \frac{\hat{\phi}}{4} \tag{3.44}$$

We now turn our attention to the large times limit. The comparison of the asymptotics with the DNS is done in the subsection 3.4.4.

3.4.3 Reaction front in the large times limit

In the large times limit we only know $\hat{a}$ and $\hat{b}$ in the depletion zone where they do not overlap except at $\hat{x} = \hat{x}_f$. We thus need to solve the problem in the the reaction zone in order to find $\hat{r} = \hat{a}\hat{b}$. However, this does not yield analytical solutions. Here we mostly derive power laws for $\hat{x}_f$, $\hat{w}_f$ and $\hat{h}_f$ in the large times limit. The exact prefactors are then obtained numerically for each $\hat{\phi}$.

Scalings of the reaction zone

In the reaction zone, the reagents A and B are consumed by the chemical reaction so that we cannot infer any scalings for them. Instead, we look for:

$$\hat{w}_f \sim \hat{t}^{\sigma} \qquad \hat{a} \sim \hat{t}^{\alpha} \qquad \hat{b} \sim \hat{t}^{\beta} \tag{3.45}$$

Relations between the unknown exponents σ, α and β come from matching conditions between the depletion and the reaction zone. Matching the concentration fields at the border of the reaction zone does not yield any information on $\hat{a}$ and $\hat{b}$. The next condition to try is the continuity of the diffusive fluxes at the edge of the reaction zone. As the inner and outer fluxes must match, we have for the reagent A:

$$\left.\begin{array}{lccc} \text{In the depletion zone:} & \frac{\partial \hat{a}}{\partial \hat{x}} & \sim & \hat{t}^{-1/2} \\ \text{In the reaction zone:} & \frac{\partial \hat{a}}{\partial \hat{x}} & \sim & \frac{\hat{a}}{\hat{w}_f} \end{array}\right\} \quad \Rightarrow \quad -\frac{1}{2} = \alpha - \sigma \tag{3.46}$$

A similar relation holds for B which yields:

$$\alpha = \beta \tag{3.47}$$

The last relation, closing the problem, comes from the balance of diffusion and reaction in the reaction zone:

$$\frac{\partial^2 \hat{a}}{\partial \hat{x}^2} \sim \hat{a}\hat{b} \qquad \Rightarrow \qquad \frac{1}{\hat{w}_f^2} \sim \hat{b} \qquad \Rightarrow \qquad -2\sigma = \beta \tag{3.48}$$

Thus the three equations (3.46), (3.47) and (3.48) leads to:

$$\hat{w}_f \sim \hat{t}^{1/6} \qquad \hat{a} \sim \hat{t}^{-1/3} \qquad \hat{b} \sim \hat{t}^{-1/3} \tag{3.49}$$

Similarity solution in the reaction zone

We can use the linear combination (3.29a) to decouple the equation on $\hat{a}$ and $\hat{b}$. Noting $\hat{u} = \hat{a} - \hat{b} = 1/2 \operatorname{erfc}(\hat{\eta}) - \hat{\phi}/2 \operatorname{erfc}(-\hat{\eta})$, we obtain an equation on $\hat{a}$ only:

$$\frac{\partial \hat{a}}{\partial \hat{t}} = \frac{\partial^2 \hat{a}}{\partial \hat{x}^2} - \hat{a}(\hat{a} - \hat{u}) \tag{3.50a}$$

Then, we define a coordinate $\hat{\zeta}$ adapted to the reaction zone as we know that $\hat{w}_f \sim \hat{t}^{1/6}$:

$$\hat{\zeta} = \frac{\hat{x} - \hat{x}_f}{\hat{t}^{1/6}} \tag{3.51}$$

which allows us to look for:

$$\hat{a}(\hat{x}, \hat{t}) = \hat{t}^{-1/3} \hat{\mathbf{a}}^{\mathbf{in}}(\hat{\zeta}) \tag{3.52}$$

As $\hat{w}_f \ll \hat{W}_d$, we can also develop $\hat{u}$ around $\hat{x}_f$:

$$\hat{u}(\hat{x}, \hat{t}) = \hat{u}(\hat{x}_f, \hat{t}) + (\hat{x} - \hat{x}_f) \frac{\partial \hat{u}}{\partial \hat{x}}(\hat{x}_f, \hat{t}) + \mathcal{O}(\hat{x} - \hat{x}_f) \tag{3.53}$$

which yields to leading order:

$$\hat{u}(\hat{x}, \hat{t}) = -\hat{K} \frac{\hat{x} - \hat{x}_f}{\hat{t}^{1/2}} = -\hat{K} \hat{t}^{-1/3} \hat{\zeta} \tag{3.54}$$

with:

$$\hat{u}(\hat{x}_f,\hat{t})=0 \quad \text{and} \quad \hat{K}=\frac{1+\hat{\phi}}{2\sqrt{\pi}}e^{-\hat{\eta}_f^2} \quad \text{and} \quad \hat{\eta}_f=\text{erf}^{-1}\left(\frac{1-\hat{\phi}}{1+\hat{\phi}}\right) \tag{3.55}$$

As a result the equation on $\hat{\mathbf{a}}^{\mathbf{in}}(\hat{\zeta})$ is:

$$\begin{aligned} -\frac{1}{\hat{t}^{4/3}}\left(\frac{1}{3}\hat{\mathbf{a}}^{\mathbf{in}}(\hat{\zeta})+\frac{1}{6}\hat{\zeta}\hat{\mathbf{a}}^{\mathbf{in}}(\hat{\zeta})'\right) & \\ +\frac{1}{\hat{t}}\hat{\mathbf{a}}^{\mathbf{in}}(\hat{\zeta})' &= \frac{1}{\hat{t}^{2/3}}\left(\hat{\mathbf{a}}^{\mathbf{in}}(\hat{\zeta})''-\hat{\mathbf{a}}^{\mathbf{in}}(\hat{\zeta})^2-\hat{K}\hat{\zeta}\hat{\mathbf{a}}^{\mathbf{in}}(\hat{\zeta})\right) \end{aligned} \tag{3.56}$$

In the limit $\hat{t}\to+\infty$ the left hand side, becomes negligible compared to the right hand side of (3.56). Thus the equation on $\hat{\mathbf{a}}^{\mathbf{in}}$ becomes:

$$\hat{\mathbf{a}}^{\mathbf{in}}(\hat{\zeta})''-\hat{\mathbf{a}}^{\mathbf{in}}(\hat{\zeta})^2-\hat{K}\hat{\zeta}\hat{\mathbf{a}}^{\mathbf{in}}(\hat{\zeta}) = 0 \tag{3.57a}$$

$$\text{with} \quad \hat{\mathbf{a}}^{\mathbf{in}}(\hat{\zeta}) \underset{-\infty}{\to} -\hat{K}\hat{\zeta} \tag{3.57b}$$

$$\text{and} \quad \hat{\mathbf{a}}^{\mathbf{in}}(\hat{\zeta}) \underset{+\infty}{\to} 0 \tag{3.57c}$$

The boundary condition at $\hat{\zeta}\to+\infty$ is natural as the concentration of A molecules must vanish as we approach the reservoir of fresh B molecules. On the left hand side of the reaction zone, there is very little B which yields $\hat{u}=\hat{a}-\hat{b}\approx\hat{a}$. This gives the boundary condition on $\hat{\mathbf{a}}^{\mathbf{in}}(\hat{\zeta})$ for $\hat{\zeta}\to-\infty$. Again, this non linear ODE cannot be solved analytically. We used Broyden's method to solve it. Once $\hat{\mathbf{a}}^{\mathbf{in}}(\hat{\zeta})$ is known, we obtain $\hat{\mathbf{b}}^{\mathbf{in}}(\hat{\zeta})$ via $\hat{u}=\hat{a}-\hat{b}$, or equivalently $-\hat{K}\hat{\zeta}=\hat{\mathbf{a}}^{\mathbf{in}}(\hat{\zeta})-\hat{\mathbf{b}}^{\mathbf{in}}(\hat{\zeta})$.

The resulting concentration profiles $\hat{\mathbf{a}}^{\mathbf{in}}(\hat{\zeta})$ and $\hat{\mathbf{b}}^{\mathbf{in}}(\hat{\zeta})$ are shown on Fig. 3.18 a) with black lines and the superposition of $\hat{t}^{1/3}\hat{a}$ and $\hat{t}^{1/3}\hat{b}$ at different time points with colored dots. Self-similarity is confirmed by the collapse of the points from the DNS onto a single curve when plotted against $\hat{\zeta}$. In addition, good agreement between these curves and the asymptotic solutions validates our analytical treatment of our RD problem. In addition, we obtain the reaction rate $\hat{r}=\hat{a}\hat{b}\approx\hat{t}^{-2/3}\hat{\mathbf{a}}^{\mathbf{in}}\hat{\mathbf{b}}^{\mathbf{in}}$ as shown on Fig. 3.18 b). This allows us to compute numerically the different characteristics of the reaction rate.

Reaction front characteristics

The reaction front location is directly obtained by setting $\hat{u}=\hat{a}-\hat{b}$ to zero. This yields:

$$\hat{x}_f(\hat{t}) = 2\left(\text{erf}^{-1}\left(\frac{1-\hat{\phi}}{1+\hat{\phi}}\right)\right)^{1/2}\hat{t}^{1/2} \tag{3.58}$$

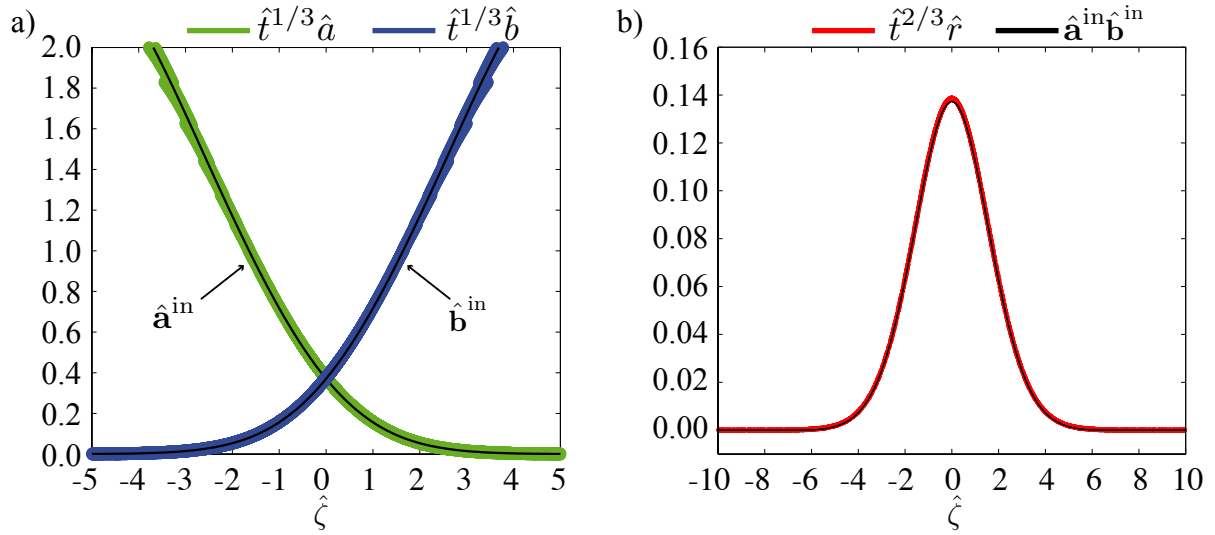

Figure 3.18: a) Large times inner solution of $\hat{a}$ and $\hat{b}$ rescaled by the scaling of their amplitude $\hat{t}^{-1/3}$ at the front. Solid black line: Asymptotic inner solutions $\hat{\mathbf{a}}^{\mathbf{in}}$ and $\hat{\mathbf{b}}^{\mathbf{in}}$. b) Corresponding reaction rate function $\hat{r} = \hat{a}\hat{b}$ rescaled by the scaling of its amplitude $\hat{t}^{-2/3}$ at the front. Solid black line: Asymptotic inner solution $\hat{\mathbf{a}}^{\mathbf{in}}\hat{\mathbf{b}}^{\mathbf{in}}$ of the normalized reaction rate. These two plots correspond to the case $\hat{\phi} = 1$.

On the other hand, the width and the height of the reaction rate are obtained numerically:

$$\hat{w}_f(\hat{t})^2 = \frac{\displaystyle\int_{-\infty}^{+\infty} \hat{\zeta}^2 \hat{\mathbf{a}}^{\mathbf{in}}(\hat{\zeta})\hat{\mathbf{b}}^{\mathbf{in}}(\hat{\zeta})d\hat{\zeta}}{\displaystyle\int_{-\infty}^{+\infty} \hat{\mathbf{a}}^{\mathbf{in}}(\hat{\zeta})\hat{\mathbf{b}}^{\mathbf{in}}(\hat{\zeta})d\hat{\zeta}}\,\hat{t}^{1/3} \tag{3.59}$$

$$\hat{h}_f(\hat{t}) = \frac{\hat{\mathbf{a}}^{\mathbf{in}}(\mathbf{0})\hat{\mathbf{b}}^{\mathbf{in}}(\mathbf{0})}{\hat{t}^{2/3}} \tag{3.60}$$

3.4.4 Crossover times $\hat{t}^\star$ and $\hat{t}_{\hat{\phi}}$

Now that we have derived asymptotic solutions for the three quantities $\hat{x}_f$, $\hat{w}_f$ and $\hat{h}_f$ in the two asymptotic regimes, we can compare these asymptotic behaviors with the results from DNS. This is done on Fig. 3.19 where one can see that the asymptotics (solid black lines) compare well with the results from DNS (colored dots) for different values of $\hat{\phi}$ from 1 down to 0.001.

The impact of $\hat{\phi}$ on the characteristics of the reaction front is manifolds. While it only affects the amplitude $\hat{h}_f$ in the reaction-controlled regime, $\hat{\phi}$ affects the three quantities $\hat{x}_f$, $\hat{w}_f$ and $\hat{h}_f$ in the diffusion-controlled regime as shown on Fig. 3.19.

Furthermore, when $\hat{\phi} = 1$, the three characteristics $\hat{x}_f$, $\hat{w}_f$ and $\hat{h}_f$ pass from the reaction-controlled to the diffusion-controlled regimes at a time $\hat{t}^\star \sim 1$. On the other hand, when $\hat{\phi} < 1$, the three characteristics $\hat{x}_f$, $\hat{w}_f$ and $\hat{h}_f$ leave the reaction-controlled regime on a time scale $\hat{t}^\star \sim 1$ and enter the diffusion-controlled regime later, on a time scale $\hat{t}_{\hat{\phi}}$ which increases as $\hat{\phi}$ is decreased. As a result, there is a mixed-regime separating the early and the large times regimes, in which reaction and diffusion are fully coupled. In addition, the duration of this mixed regime is increasing as $\hat{\phi}$ is decreased since $\hat{t}^\star \sim 1$ for all $\hat{\phi}$ while $\hat{t}_{\hat{\phi}}$ increases as $\hat{\phi}$ is decreased.

In dimensional terms, this means that (i) the reaction-controlled regime ends on a time scale $t^\star \sim 1/kA_0$ and that (ii) the diffusion-controlled regime starts on a time scale $t_{\hat{\phi}}$ increasing with the relative excess of A_0 compared to B_0. The observation (i) shows that the reaction-controlled regime ends when B molecules (the limiting reagent) are significantly consumed by the chemical reaction near the front location. This is consistent as the reaction-controlled regime assumes that the distributions of A and B molecules are not affected by the chemical reaction to leading order. On the other hand, the observation (ii) confirms that both A and B need to be exhausted at the front location for the diffusion-controlled regime to onset. Hence we expect the diffusion-controlled regime to start when A molecules are exhausted at the front location which takes place on a time scale $\sim 1/kB_0$.

Overall, having kept the reagents A and B initially separated allows us to tune the time window over which chemical information is accessible. The shortest time window is obtained for equimolar proportions ($A_0 = B_0$) and is comparable to the time window $1/kA_0$ that would be obtained in a well mixed tank. However, larger time windows are obtained by imposing an excess of A_0 compared to B_0. Then, the diffusion-controlled regime onsets on a time scale $1/kB_0$ up to which chemical information is accessible. This shows that chemical information is accessible long after $1/kA_0 = k_{\text{obs}}^{-1}$ when $A_0 \gg B_0$ and that the size of the time window over which chemical information is accessible can be chosen by adjusting $\hat{\phi} = B_0/A_0$. These two conclusions confirm the experimental observations of section 3.2.

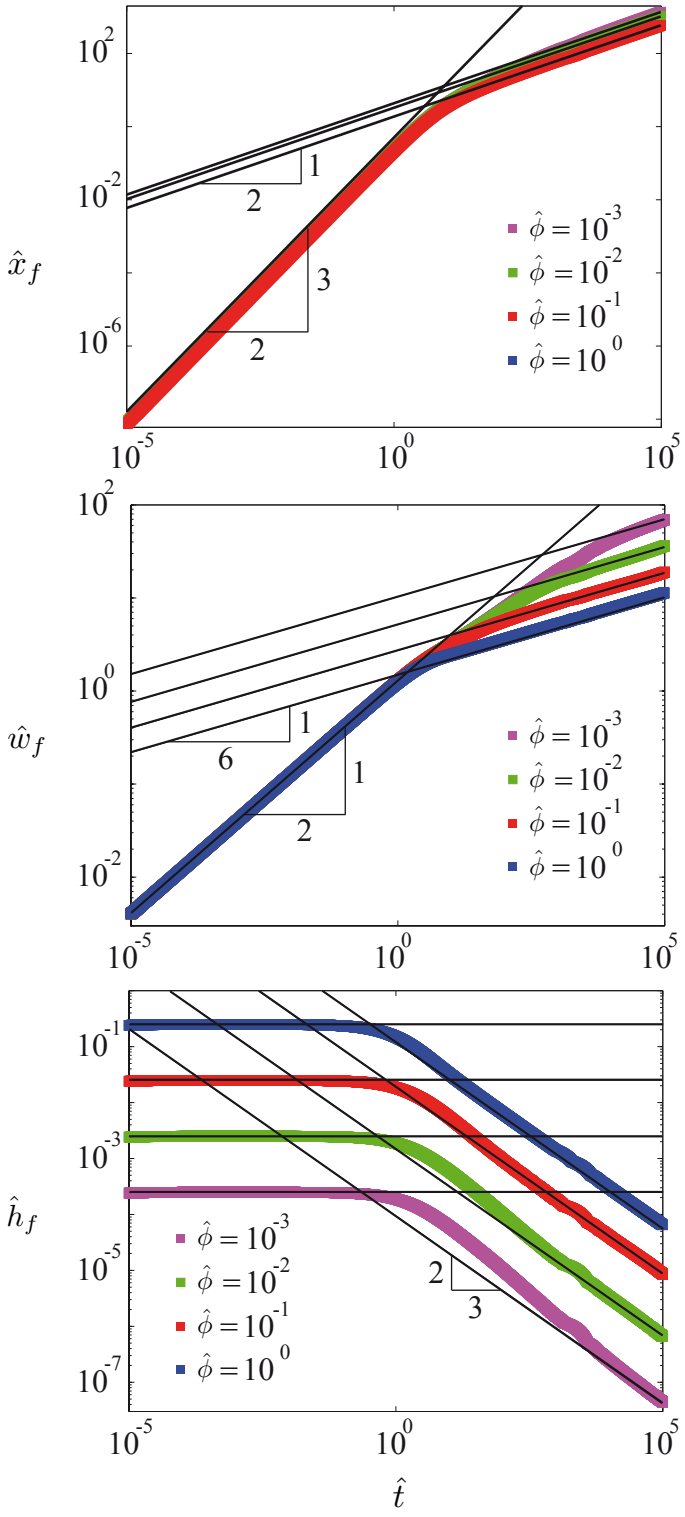

Figure 3.19: Reaction zone characteristics. a) Front position $\hat{x}_f$. b) Front width $\hat{w}_f$. c) Front height $\hat{h}_f$. Coloured dots correspond to $\hat{x}_f$, $\hat{w}_f$ and $\hat{h}_f$ extracted from DNS for different values of $\hat{\phi}$. The solid black lines are the corresponding asymptotic solutions.

3.4.5 Summary of asymptotic results

The important asymptotic results are summarized in the next table. Only the leading outer solutions are presented as these are the profiles experimentally accessible.

$\hat{t} \ll 1$			$\hat{t} \gg 1$		
Concentration fields					
$\hat{a}(\hat{x},\hat{t})$	$=$	$\frac{1}{2}\,\mathrm{erfc}(\hat{\eta})$	$\hat{a}(\hat{x},\hat{t})$	$=$	$1-\frac{\mathrm{erfc}(-\hat{\eta})}{\mathrm{erfc}\left(-\hat{\eta}_f\right)}$ for $\hat{\eta}\le\hat{\eta}_f$
$\hat{b}(\hat{x},\hat{t})$	$=$	$\frac{\hat{\phi}}{2}\,\mathrm{erfc}(-\hat{\eta})$	$\hat{b}(\hat{x},\hat{t})$	$=$	$\hat{\phi}\left(1-\frac{\mathrm{erfc}(\hat{\eta})}{\mathrm{erfc}\left(\hat{\eta}_f\right)}\right)$ for $\hat{\eta}\ge\hat{\eta}_f$
$\hat{c}(\hat{x},\hat{t})$	$=$	$\hat{t}\;\hat{\mathbf{c}}_1(\hat{\eta})$	$\hat{c}(\hat{x},\hat{t})$	$=$	$\begin{cases}\frac{\hat{\phi}}{2}\mathrm{erfc}\,(-\hat{\eta}) & \text{for } \hat{\eta}\le\hat{\eta}_f\\ \frac{1}{2}\mathrm{erfc}\,(\hat{\eta}) & \text{for } \hat{\eta}\ge\hat{\eta}_f\end{cases}$
Reaction zone					
$\hat{h}_f(\hat{t})$	$=$	$\frac{\hat{\phi}}{4}$	$\hat{h}_f(\hat{t})$	$\sim$	$\hat{t}^{-2/3}$
$\hat{w}_f(\hat{t})$	$=$	$2.97\;\hat{t}^{1/2}$	$\hat{w}_f(\hat{t})$	$\sim$	$\hat{t}^{1/6}$
$\hat{x}_f(\hat{t})$	$=$	$\begin{cases}0 & \text{when } \hat{\phi}=1\\ 0.51\;\hat{t}^{3/2} & \text{when } \hat{\phi}<1\end{cases}$	$\hat{x}_f(\hat{t})$	$=$	$2\sqrt{D_s\hat{t}}$

3.5 Monitoring the transition between the early and the large times regimes

Several experimental works have validated the asymptotic profiles derived in section 3.2. The first experiments were held in capillary tubes filled with gel to make sure that transport is purely diffusive, A and B being brought from each side of the tube [124, 126, 127]. Another experiment was concerned with the diffusion-limited corrosion of a copper deposit grown by electrolysis beforehand. This is the case of one reagent being stationary. The asymptotic analysis is similar to the one performed in the last section [128] and was validated experimentally [129]. More recently, a T-shaped microchannel was used to study one step reactions in RD and has further confirmed these RD scalings [130, 131].

The transition time to the diffusion-controlled regime can indeed be tuned to show up at a reasonable dimensional time, which therefore render the large times asymptotic regime experimentally observable [132]. For instance, the diffusion-limited dynamics is observed already after 20 min in the experiment of Koo *et al.* [126], while it takes 4 h for the slow reaction ($k \sim 10^{-1}$ $\mathrm{M}^{-1}\mathrm{s}$) studied by Taitelbaum *et al.* [124]. On the other hand, the diffusion-controlled regimes starts only after 0.1 s in the case of fast reactions ($k \sim 10^6$ $\mathrm{M}^{-1}\mathrm{s}$) studied by Baroud *et al.* in microchannel.

In this section, we tune the transition time from the reaction-controlled to the diffusion-controlled regime for it to fit in the 50 s long time window for observation of our merging device. This allows us to monitor both asymptotic regimes as well as the transition from one regime to the other, and to confirm experimentally our asymptotic solutions in each regime.

3.5.1 Distribution of B in the two asymptotic regimes

We have used the same setup as in section 3.2 and have recorded profiles of DCPIP (denoted B) over space and time. As we know that $k \sim 80$ $\mathrm{M}^{-1}\mathrm{s}^{-1}$, we can choose A_0 and B_0 so as to be able to monitor both the reaction-controlled and the diffusion-controlled regimes. We choose A_0=B_0= 2.5 mM to have a static reaction front ($x_f(t) = 0$ μm) and a transition time $t^\star \sim 1/kA_0$ around 5 s which fits well in our 50 s long time window for observation.

In the early times regime, the dimensional distributions of $A(x,t)$ and $B(x,t)$ read as, again assuming $D_A = D_B = D$:

$$A(x,t) \;=\; \frac{A_0}{2}\mathrm{erfc}\left(\frac{x}{\sqrt{4Dt}}\right) \quad \text{and} \quad B(x,t) \;=\; \frac{B_0}{2}\mathrm{erfc}\left(-\frac{x}{\sqrt{4Dt}}\right) \tag{3.61}$$

As shown on Fig. 3.20 a), the experimental profiles of $B(x,t)$ collapse on a single curve when plotted against $\hat{\eta} = x/\sqrt{4Dt}$ which confirms self-similarity. In addition, this curve

fits well with the theoretical prediction (solid black line on Fig. 3.20 a)) for $B(x,t)$ in the early times regime.

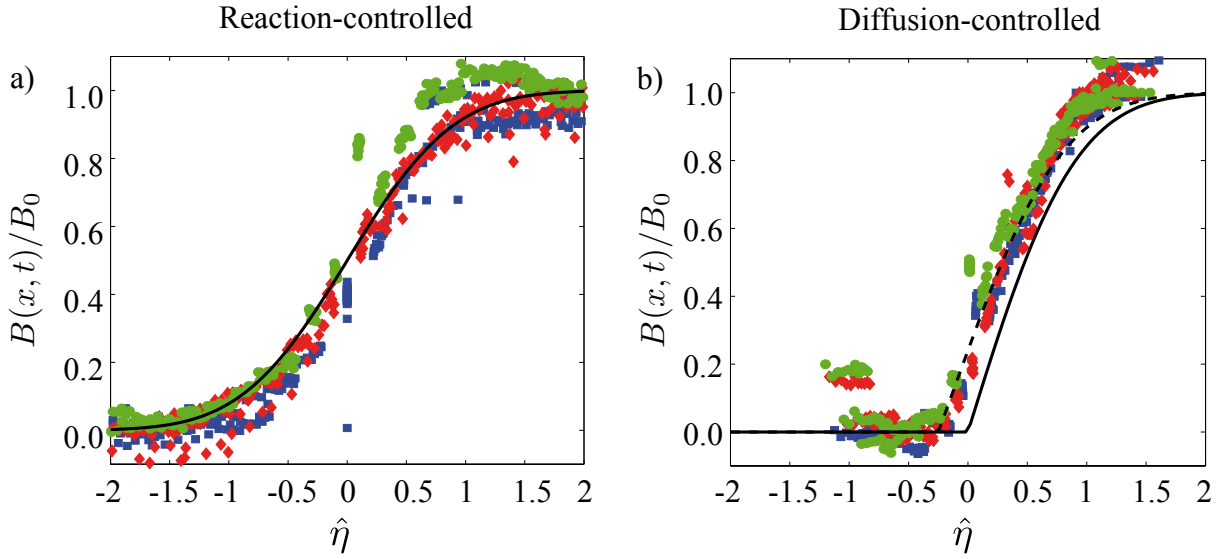

Figure 3.20: The different colored symbols correspond to different experiments, all with $A_0 = B_0 = 2.5$ mM. a) Superposed distributions of B for t between 20 ms and 400 ms normalized by B_0. Solid line: $y = 0.5\,\mathrm{erfc}(-\hat{\eta})$. b) Superposed distributions of B for t between 10 s and 50 s normalized by B_0. Solid line: $y = \mathrm{erf}(\hat{\eta})$ for $\hat{\eta} > 0$. Dashed line: $y = 1 - \mathrm{erfc}(\hat{\eta})/\mathrm{erfc}(\hat{\eta}_f)$ for $\hat{\eta} > \hat{\eta}_f$ and $\hat{\eta}_f = 0.15$. The similarity coordinate $\hat{\eta}$ is defined as $\hat{\eta} = x/\sqrt{4Dt}$ with $D = 1.1{\times}10^9\mathrm{m}^2/\mathrm{s}$.

Similarly, in the large times regime, the dimensional distributions of $A(x,t)$ and $B(x,t)$ in the depletion layer read as:

$$A(x,t) = A_0\mathrm{erf}\left(-\frac{x}{\sqrt{4Dt}}\right) \quad \text{and} \quad B(x,t) = B_0\mathrm{erf}\left(\frac{x}{\sqrt{4Dt}}\right) \tag{3.62}$$

Again, as shown on Fig. 3.20 b), the experimental profiles of $B(x,t)$ collapse on a single curve when plotted against $\hat{\eta} = x/\sqrt{4Dt}$ which confirms the self-similar evolution of $B(x,t)$. However, there is a shift between the experimental data (colored symbols) and the prediction obtained in the case with $A_0 = B_0$ and $D_A = D_B$ (solid black line). This shift can be corrected by allowing the reaction front to move. We find that fixing $\hat{\eta}_f = 0.15$ (dashed black line) yields a good agreement. The front can move for two reasons. First the initial concentrations could actually not be the same: $A_0 \neq B_0$. In the last section, we have found that $\mathrm{erf}(\hat{\eta}_f) = (1-\hat{\phi})/(1+\hat{\phi})$ in the case $D_A = D_B$. Fixing $\hat{\eta}_f = 0.15$ yields $\hat{\phi} = 1.4$ which means that we would have done a 40 % error on the initial concentrations. This is probably not the case. The second reason for the front to move is that $D_A \neq D_B$. This is consistent with the fact that A and B have different molar weights ($M_A = 176$ g/mol,

$M_B = 268$ g/mol), hence different diffusion coefficients according to the Stokes-Einstein relation. In addition, the relation $D_A/D_B = (M_B/M_A)^{1/3}$ yields $D_A \approx 1.15 D_B$ hence $D_A > D_B$. As a result, we expect the front to move toward the B rich region as A diffuses faster than B which is in agreement with the sign of $\hat{\eta_f} > 0$. Nonetheless, we do not have an explanation for the particular value of $\hat{\eta_f} = 0.15$.

3.5.2 Space-averaged concentration of B in the two asymptotic regimes

The transition from the reaction-controlled to the diffusion-controlled regime is observed on the space-averaged concentration of B. The local study of the distributions in space and time of A, B and C allows us to derive a model for the time variations of the space-averaged amount of A, B and C. Here we note with a bar space-averaged quantities. For instance, for the species B that we observe in our experiment, the space-averaged concentration is defined as:

$$\overline{B} \quad = \quad \frac{1}{2l} \int_{-l}^{l} B(x,t) dx \tag{3.63}$$

From this definition, we obtain a model for $\overline{B}$ by averaging the local conservation law (3.9b) over space. For the species B this yields:

$$\frac{d\overline{B}}{dt} \quad = \quad - \, k\overline{AB} \tag{3.64a}$$

where the diffusion term has vanished because of the no-flux boundary conditions at $x = \pm l$. As we know the reaction rate $R = kAB$ in both the reaction-controlled and the diffusion controlled regimes, we can derive asymptotes of $\overline{B}$ in these two regimes.

In the early times regime, the solutions (3.61) yields directly:

$$k\overline{AB} \quad \approx \quad \frac{kA_0B_0}{4l} \sqrt{Dt} \underbrace{\int_{-\infty}^{+\infty} \mathrm{erfc}(\hat{\eta})\mathrm{erfc}(-\hat{\eta}) d\hat{\eta}}_{\approx 1.60} \tag{3.65}$$

where the bounds of the integral $\pm l/\sqrt{4Dt}$ have been approximated to infinity. Hence we obtain:

$$\overline{B}(0) - \overline{B}(t) \quad \approx \quad 0.18 \, \frac{kA_0B_0\sqrt{D}}{l} \, t^{3/2} \tag{3.66}$$

In the large times regime, we need to go back to the solutions of $A(x,t)$ and $B(x,t)$ in the reaction zone. In dimensional form, these yield:

$$k\overline{AB} \quad = \quad \frac{kA_0B_0}{2l} \int_{-l}^{+l} \hat{\mathbf{a}}^{\mathbf{in}}(\hat{\zeta}) \hat{\mathbf{b}}^{\mathbf{in}}(\hat{\zeta}) dx \quad = \quad B_0 \sqrt{\frac{D}{t}} \underbrace{\int_{-\infty}^{+\infty} \hat{\mathbf{a}}^{\mathbf{in}}(\hat{\zeta}) \hat{\mathbf{b}}^{\mathbf{in}}(\hat{\zeta}) d\hat{\zeta}}_{\approx 0.46} \tag{3.67}$$

Hence we obtain:

$$\overline{B}(0) - \overline{B}(t) \quad \approx \quad 0.46\ B_0\ \sqrt{Dt} \tag{3.68}$$

These asymptotic solutions (3.66) and (3.68) of $\overline{B}(t)$ are compared to experimental data on Fig. 3.21. The first instants of the experiment $t \leq 1$ s are not shown on Fig. 3.21 because $\overline{B}(0) - \overline{B}(t)$ is nearly 0 then. The transition from the early to the large times behaviour is observed at $t^\star \approx 8.5$ s. The experimental data are in good agreement with the two asymptotes $\overline{B}(0) - \overline{B}(t) \sim t^{3/2}$ at early times and $\overline{B}(0) - \overline{B}(t) \sim t^{1/2}$ at large times. A shift is observed at large times between the experimental data and the asymptote which shows that we overestimate the actual space-averaged concentration $\overline{B}$. Again, this overestimation could be attributed to D_A being not the same as D_B.

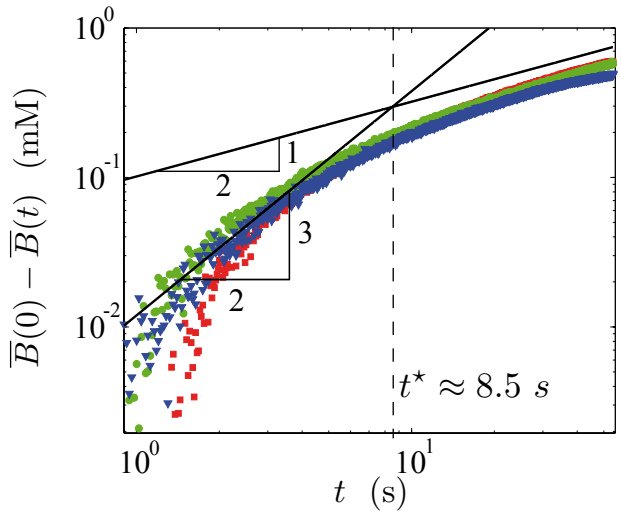

Figure 3.21: $\overline{B}(0) - \overline{B}(t)$ as a function of time t. Coloured symbols corresponds to three repeats with $A_0 = B_0 = 2.5$ mM. The solid black lines are the two asymptotes (3.66) and (3.68) with D $= 1.1 \times 10^{-9}$ m^2/s and $k = 87$ M^{-1}s^{-1}.

This set of experiments, as well as the theoretical predictions for $\overline{B}(0) - \overline{B}(t)$, validates our analytical treatment of the RD model with initially separated reagents in the case of a one step reaction. In addition, we demonstrate that the space-averaged concentration of B shows a sharp change of dynamics at $t = t^\star$ with $t^\star \sim 1/kA_0$. As a result, we could measure $t^\star$ to estimate k which requires to know A_0 only and hence makes the estimation of k very simple and efficient.

3.6 Discussion of Chapter 3

In this chapter, we studied both theoretically and experimentally the reaction-diffusion problem of two species A and B being initially kept separated and reacting via a second order rate law. We first showed that we can measure the reaction constant k by fitting the experimental profiles of $B(x,t)$ with simulated profiles from a 1D reaction-diffusion model. This procedure was further extended to a global fit on the space-averaged concentration $\overline{B}$. Our measurements of k using either fitting protocols were also shown to be in good agreement with measurements performed in a stopped-flow machine. A key observation from these experiments where $A_0 \gg B_0$ is that the precision of our measurements is enhanced by fitting on a longer period of time. We thus showed that chemical information was accessible long after the characteristic time scale $k_{\text{obs}}^{-1} = 1/kA_0$ which makes our RD approach ideal for the study of fast chemical reactions.

In order to have a better understanding of this observation, we studied in more detail the dynamics of our RD model. Two asymptotic regimes were highlighted separated by well characterized transition times. At early times, a reaction-controlled takes place in which chemical information is accessible. At large times, a diffusion-controlled regime takes place in which chemical information is not accessible anymore. As a result, measuring reaction rate constants with our RD approach looks like a race against the clock. However, the time over which chemical information is accessible was shown to vary greatly with the ratio of the initial concentrations $\hat{\phi} = B_0/A_0$ and to increase as $\hat{\phi}$ is decreased. The dynamics of the reaction front was indeed shown to leave its early time behaviour on a time scale $t^\star \sim 1/kA_0$, and to enter its large times behaviour on a time scale $t_{\hat{\phi}}$ which increase with the excess of one reagent compared to the other. Chemical information is therefore accessible up to $\hat{t}_{\hat{\phi}}$.

Lastly, we compared our theoretical predictions for the distribution of B to experiments performed in equimolar proportions. Both the reaction-controlled and the diffusion-controlled regimes were monitored in a single experiment by an adapted choice of the initial concentrations of the reagents. A good agreement between the experiments and the theory was found for both the local distribution $B(x,t)$ and the space-averaged concentration $\overline{B}(t)$.

The two conclusions of this chapter are the following:

- Keeping the reagents initially separated yields a large time regime in which product formation is solely driven by diffusion. Reaction rates cannot be measured once the diffusion-controlled regime is onset.
- The transition to the diffusion-controlled regime can be delayed by working with an excess of one reagent.

Nomenclature of Chapter 3

N.B. Dimensionless quantities wear a hat

Dimensional quantities

x, t	Space and time coordinates
A, B, C	Concentrations of A, B and C
A_0, B_0	Initial concentrations of A and B
B^{exp}, B^{sim}	Experimental and simulated concentrations of B
$\overline{B}$	Space-averaged concentration of B
$\overline{B}^{\text{exp}}$, $\overline{B}^{\text{sim}}$	Experimental and simulated space-averaged concentrations of B
D_A, D_B, D_C	Diffusion coefficients of A, B and C
D	Diffusion coefficient of A, B and C in the case of equally diffusing species
k, k_{obs}, Δk_{obs}	Reaction rate constant, observed rate and confidence interval on k_{obs}
l	Size of the domain *i.e.* Droplet diameter
$t_{1/2}$	Half-life of the reaction in a well-mixed reactor
$t^\star$	Transition time from the reaction-controlled to the mixed regime
$t_{\hat{\phi}}$	Transition time from the mixed to the diffusion-controlled regime

Dimensionless quantities

$\hat{x}$, $\hat{t}$	Space and time coordinates
$\hat{\eta}$	Self-similar coordinate adapted to the diffusive layer
$\hat{\zeta}$	Self-similar coordinate adapted to the large times reaction zone
$\hat{a}$, $\hat{b}$, $\hat{c}$	Dimensionless concentration of A, B and C

$\hat{\mathbf{a}}_\mathbf{0}$, $\hat{\mathbf{b}}_\mathbf{0}$, $\hat{\mathbf{c}}_\mathbf{0}$	Early times solutions of $\hat{a}$, $\hat{b}$ and $\hat{c}$ at $\mathcal{O}(\hat{t}^0)$
$\hat{\mathbf{a}}_\mathbf{1}$, $\hat{\mathbf{b}}_\mathbf{1}$, $\hat{\mathbf{c}}_\mathbf{1}$	Early times solutions of $\hat{a}$, $\hat{b}$ and $\hat{c}$ at $\mathcal{O}(\hat{t}^1)$
$\hat{\mathbf{a}^{\mathbf{out}}}$, $\hat{\mathbf{b}}^{\mathbf{out}}$, $\hat{\mathbf{c}}^{\mathbf{out}}$	Large times outer solutions of $\hat{a}$, $\hat{b}$ and $\hat{c}$
$\hat{\mathbf{a}^{\mathbf{in}}}$, $\hat{\mathbf{b}}^{\mathbf{in}}$	Large times inner solutions of $\hat{a}$ and $\hat{b}$
$\hat{t}^\star$	Transition time from the reaction-controlled to the mixed regime
$\hat{t}_{\hat{\phi}}$	Transition time from the mixed to the diffusion-controlled regime
$\hat{W}_d$	Width of the depletion zone in the large times limit
$\hat{r}$	Dimensionless reaction rate
$\hat{x_f}$, $\hat{w_f}$, $\hat{h_f}$	Position, width and height of the reaction rate $\hat{r}$
$\hat{\eta_f}$	Self-similar coordinate associated to $\hat{x}_f$
$\hat{\phi}$	Concentration ratio
Da	Damköhler number
$\hat{u}$	$\hat{a} - \hat{b}$
H	Heaviside function

Chapter 4

Enzymatic reactions

In this last chapter, we turn our attention to the study of enzymatic reactions in our merging chamber. Enzymes are the catalysts of the biological processes taking place in cells. As a result, enzyme catalyzed reactions can generally be thought as the conversion of a substrate S in a product P in the presence of an enzyme E:

$$\mathrm{S} \quad \xrightarrow{\mathrm{E}} \quad \mathrm{P} \tag{4.1}$$

Like any other catalyst, enzymes bring the reaction catalyzed to its equilibrium position more quickly than would occur otherwise. The rate enhancement is then given by the turnover number k_{cat} which corresponds to the number of substrate molecules an enzyme molecule can catalyze per unit time. Nonetheless, enzymes are not only remarkable for the increase in reaction rate they achieve, but also for their high degree of specifity toward certain substrates. As a result, enzymes can selectively convert a given substrate from a heterogeneous population of substrates. This selective conversion (4.1) plays a major role in cell regulation, and hence takes place on a very large range of time scales depending on the actual task to be performed, thereby setting different paces in the cell machinery. Consequently, k_{cat} varies on many orders of magnitude, from 10^{-5} s^{-1} for molecular switches up to 10^{7} s^{-1} for metabolic enzymes as shown on Fig. 4.1.

The complete measurement and description of all time-dependent properties of enzymes then requires instruments and techniques that have a variety of recording speeds and sensitivities. Amongst these, classic examples include microtiter plates for slow kinetics with time scales above 1 s, and stopped- or quenched-flow devices for fast kinetics with time scales below 1 s down to a few ms. More recently, droplet microfluidics has emerged as a powerful tool to measure both slow and fast kinetics using the same device while achieving drastic savings of reagents. Ismagilov *et al.* have measured single turnover kinetics of RNase by flowing droplets containing the reacting mixture down a winding channel [133]. Turnover numbers between 1 and 1000 s^{-1} were resolved by adjusting the flow rate of the carrier fluid and the channel geometry, while different substrate concentrations could

be tested by adjusting the flow rates ratio of the enzyme and substrate solutions. This approach was further confirmed with the study of rapid binding kinetics of stepravin and biotin [134], and the kinetics of alkaline phosphatase [135] and luciferase [136]. On the other hand, Wheeler *et al.* used a digital microfluidic platform that allows much more conditions to be tested on chip in parallel [137]. In Wheeler's device, droplets are actuated using dielectric forces which allows droplets from many different sources to be combined on a single chip, but limited kinetics to be monitored as droplets have to be mixed before the reaction can be monitored.

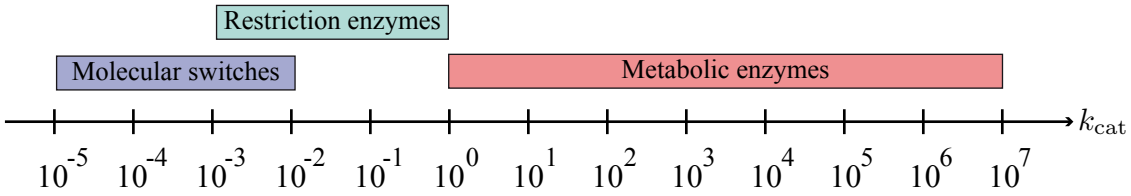

Figure 4.1: Turnover number of three classes of enzymes. Molecular switches are used in the cell signaling system. Their slow rate allows the chemical signal to remain long enough in the cell for it to be transmitted. Restriction enzymes are in charge of detecting foreign DNA in cells that must be cut. Therefore they require a very high specificity which is achieve by greater slowness. Metabolic enzymes ensure the cell survival by ensuring the cell nutrient uptake and the cell fast response to changes in its environment. They have to be rapid to overcome fast aggretions such as UV light. From Traut *et al.* [138].

The current challenge of droplet based platforms for enzyme kinetics is thus twofolds: (i) Push the time resolution below the millisecond, and (ii) provide a simple microfluidic tool to combine many reagents in parallel. Our approach has great promises in these regards as the droplet handling technique on which it relies is highly parallelizable, while the droplet fusion technique at play has no flow induced dead time.

In this chapter, we study both fast and slow enzyme kinetics using our merging device. We start by presenting Michaelis-Menten theory in section 4.1. Slow reactions are then performed in droplets using our parallelized chip, and analyzed using Michaelis-Menten theory in section 4.2. On the other hand, fast reactions must be analyzed with a RD model when held in our merging chamber. In section 4.3, we study the different regimes arising in a one dimensional RD problem with the reagents kept initially separated and following a Michaelis-Menten like reaction scheme. This yields a model to study the steady state kinetics of fast enzymatic reactions in RD. Finally, we compare our model to experiments held in a coflow microchannel in section 4.4, and in droplets using our device in section 4.5.

4.1 Michaelis-Menten theory

Michaelis-Menten theory is the gold standard to analyze enzymatic assays routinely performed in microtiter plates. It predicts the initial linear increase in product usually observed and allows us to characterize both the enzyme activity and affinity toward a given substrate. Hereafter we describe the different assumptions under which Michaelis-Menten theory applies and use it in the case of competitive inhibition.

4.1.1 Evidence for the existence of an intermediate complex

As catalysts, enzymes are not altered through the chemical reaction at play, and hence must somehow bind the substrate, and unbind the product in a subsequent step. As a result, enzyme-catalyzed reactions cannot proceed in one single step as suggested by the overall conversion (4.1), but rather in two successive steps: (i) Tthe enzyme and the substrate bind covalently to form an intermediate complex ES, which (ii) degrades into the product P and the free enzyme E. The overall conversion of S into P can thus be written as:

$$\mathrm{E} + \mathrm{S} \leftrightarrow \mathrm{ES} \leftrightarrow \mathrm{E} + \mathrm{P} \tag{4.2}$$

At the molecular level, the formation of an intermediate complex is key in the understanding of enzyme specificity toward certain substrates. Indeed, enzymes are large protein, with molar weights of few hundreds of kDa, which process much smaller substrate molecules, with molar weights of few hundreds of Da. As proteins, enzymes also have a 3D structure which greatly defines their function [139]. This was first postulated by Fischer [140] who suggested a *lock and key mechanism* to explain enzyme specificity as depicted on Fig. 4.2. Fisher's idea is that enzymes possess small active regions that are complementary in shape, size and chemical nature to certain molecules. As a result, only these molecules can fit into the enzyme active pockets in order to react. An enzyme-substrate intermediate complex has thus to form for the reaction to take place as shown on Fig. 4.2.

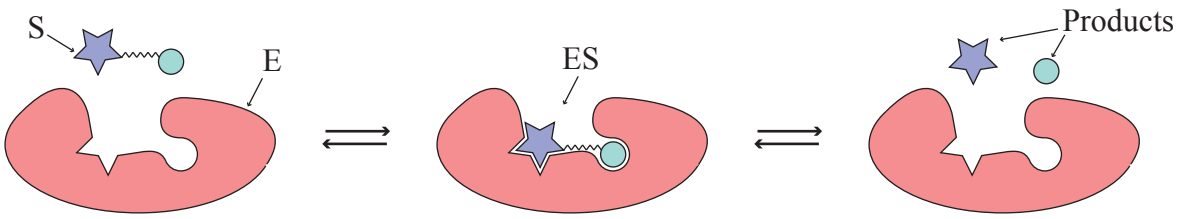

Figure 4.2: Fischer's *lock and key mechanism*. The enzyme has a 3D geometry with localized active sites which allows it to bind to complementary substrate molecules only. From Dawson [141].

On the kinetic side, experiments show that the rate of enzyme-catalyzed reactions departs from a standard second order rate law, generally valid for bimolecular reactions, and saturates at large substrate concentrations. In the one step conversion scenario (4.1), the enzyme is always in its unbound active state E. As a result, the corresponding rate keeps on increasing with the substrate concentration as the likelihood of enzyme/substrate collisions is increased with a larger substrate concentration. In the two steps conversion scenario (4.2), the enzyme divides up between an unbound active state E and a bound inactive state ES. As the substrate concentration is increased, most enzyme molecules end up in the bound inactive state as the speed of the enzyme/substrate binding step overcomes the speed of the intermediate complex degradation. As a result, the initial enzyme concentration becomes the limiting factor, and adding more substrate molecules does not increase the reaction rate anymore. A two steps reaction scheme is therefore required to take the reaction rate saturation at large substrate concentrations into account.

4.1.2 Model for product formation

Based on the reaction scheme (4.2), Michaelis and Menten [142], followed by Briggs and Haldane [143], derived a model for the product formation under several key assumptions:

1. The limiting step of an enzyme catalyzed reaction is the break down of the intermediate complex. Focusing on the first instant of the chemical reaction, they thus neglected the back reaction of the second step, so that the reaction scheme simplifies into:

$$\mathrm{E} + \mathrm{S} \underset{k_{\mathrm{off}}}{\overset{k_{\mathrm{on}}}{\rightleftarrows}} \mathrm{ES} \overset{k_{\mathrm{cat}}}{\rightarrow} \mathrm{E} + \mathrm{P} \tag{4.3}$$

   with k_{on}, k_{off} and k_{cat} the rate constants of the each unit step.

2. The enzyme does not inactivate over time. The initial amount of enzyme $[E]_0$ thus divides up between the amount of free enzyme $[E]$ and the amount of bound enzyme $[ES]$ at all times:

$$[E]_0 \;=\; [E] \;+\; [ES] \tag{4.4}$$

3. After a small induction time, the distribution of the enzyme between its free and bound states is stationary: Both the amount of free enzyme $[E]$ and bound enzyme $[ES]$ are constant over time. We say that intermediate is stationary, or has reached a steady-state. As a result, the speed at which the intermediate forms $k_{\mathrm{on}}\,[E]\,[S]$ must balance the speed at which it breaks down $(k_{\mathrm{off}} + k_{\mathrm{cat}})\,[ES]$ to yield an overall constant concentration of intermediate. As a result:

$$[E]\,[S] \;=\; K_{\mathrm{M}}\,[ES] \quad \text{with} \quad K_{\mathrm{M}} \;=\; \frac{k_{\mathrm{off}} + k_{\mathrm{cat}}}{k_{\mathrm{on}}} \tag{4.5}$$

4. Lastly, they considered the case of S being initially placed in excess compared to E: $[S]_0 \gg [E]_0$. Hence, the substrate concentration does not significantly change in the first instants of the reaction:

$$[S](t) \approx [S]_0 \tag{4.6}$$

Then, the reaction scheme (4.3) yields the initial increase in product P via the mass balance $d[P]/dt = k_{\text{cat}}[ES]$ which integrates into:

$$[P] \approx V_0\, t \qquad \text{with} \qquad V_0 = k_{\text{cat}}[E]_0 \, \frac{[S]_0}{K_{\text{M}} + [S]_0} \tag{4.7}$$

This model equation (4.7) for product formation is the gold standard of enzyme kinetics as it accurately catches the saturation of the reaction speed V_0 at high substrate concentrations. As shown on Fig. 4.3, it yields two parameters to characterize enzymes: (i) The Michaelis constant K_{M} and (ii) the turnover number k_{cat}.

Measuring K_{M} and k_{cat} is the first step of the characterization of an enzyme. The Michaelis-Menten constant is the substrate concentration (in M) at which V_0 reaches half its maximum value. The relation $[E][S] = K_{\text{M}}[ES]$ also shows that $S_0/K_{\text{M}} \sim [ES]/[E]$. As a result, the enzyme is mostly unbound when $[S]_0 \ll K_{\text{M}}$, and mostly bound to the substrate when $[S]_0 \gg K_{\text{M}}$, which shows that K_{M} is also a measure of the enzyme affinity toward a given substrate: The lower the K_{M}, the higher the affinity. On the other hand, the turnover number is a rate (in s^{-1}), corresponding to the number of substrate molecules an enzyme molecule can process per unit time. A typical measurement of K_{M} and k_{cat} thus consists of measuring V_0 at fixed enzyme concentration $[E]_0$ for varying initial substrate concentrations $[S]_0$ which yields a sigmoid curve as shown on Fig. 4.3 from which K_{M} and k_{cat} are extracted.

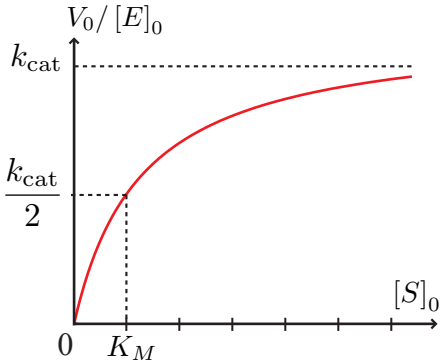

Figure 4.3: Theoretical sigmoid curve for $V_0/[E]_0$ against $[S]_0$ on which k_{cat} and K_{M} can be graphically extracted.

The strength of this model lies on its simplicity and the large time window over which it applies. On the down side, this model does not yield each unit rate k_{on}, k_{off} and k_{cat}, but

only K_{M} and k_{cat}. As a result, the actual enzyme/substrate binding constant $K_D = k_{\mathrm{off}}/k_{\mathrm{on}}$ cannot be obtained via this model.

The key assumption underlying this model is the steady-state of the intermediate complex: $[E]\,[S] = K_{\mathrm{M}}\,[ES]$. Hereafter, we solve numerically a more general model based on the mass balance equations for each species E, S, I and P in order to test the limits of this assumption and quantify the time window over which it applies.

4.1.3 The steady state assumption

A more general model can be derived using a mass balance for each species E, S, I and P:

$$\frac{d\,[E]}{dt} = -\,k_{\mathrm{on}}\,[E]\,[S] + k_{\mathrm{off}}\,[ES] + k_{\mathrm{cat}}\,[ES] \quad \text{with} \quad [E]\,(0) = [E]_0 \tag{4.8a}$$

$$\frac{d\,[S]}{dt} = -\,k_{\mathrm{on}}\,[E]\,[S] + k_{\mathrm{off}}\,[ES] \quad \text{with} \quad [S]\,(0) = [S]_0 \tag{4.8b}$$

$$\frac{d\,[ES]}{dt} = +\,k_{\mathrm{on}}\,[E]\,[S] - k_{\mathrm{off}}\,[ES] - k_{\mathrm{cat}}\,[ES] \quad \text{with} \quad [ES]\,(0) = 0 \tag{4.8c}$$

$$\frac{d\,[P]}{dt} = +\,k_{\mathrm{cat}}\,[ES] \quad \text{with} \quad [P]\,(0) = 0 \tag{4.8d}$$

This model (4.8a)-(4.8d) is readily solved using Matlab for representative values of the rate constants and the initial concentrations given by Ristenpart *et al.* [144] in the case of luciferase. These values are shown on Table 4.1.

$[E]_0$ (μM)	$[S]_0$ (mM)	k_{on} ($\mathrm{M^{-1}s^{-1}}$)	k_{off} ($\mathrm{s^{-1}}$)	k_{cat} ($\mathrm{s^{-1}}$)
1	10	10^4	1	10

Table 4.1: Values of the different parameters used to solve the set of equations (4.8a)-(4.8d). From Ristenpart *et al.* [144].

The resulting concentrations are shown on Fig. 4.4 a). When plotted on a log-log scale, as shown on Fig. 4.4 b), the time window over which the intermediate complex concentration is constant appears to be bounded by two well defined time scales t_{M} and $t^{\star}$. These two time scales have been extensively studied by Segel *et al.* [145, 146] and yield a necessary condition for the simplified model of Michaelis and Menten to hold true.

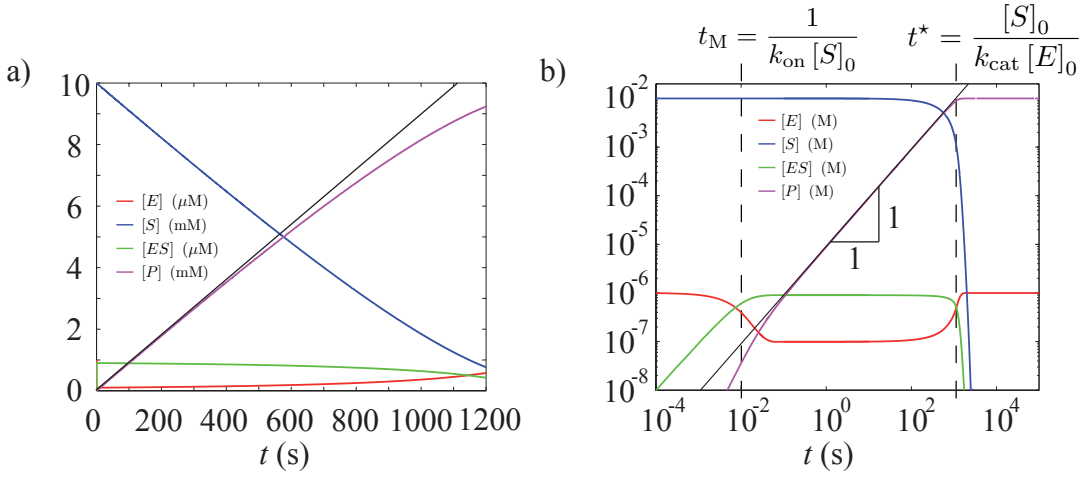

Figure 4.4: Time courses of the different species obtained by solving numerically the equations (4.8a)-(4.8d) with the input values shown on Table 4.1. a) Lin-lin-scale. b) Log-log scale, two time scales t_M and $t^\star$ defining the time window over which the increase in product is linear with time. Solid black line: Michaelis-Menten model $[P](t) = V_0 t$.

The first (or fast) time scale t_M corresponds to the time required by the intermediate complex $[ES]$ to reach its steady-state. In the case where $[S]_0 \gg [E]_0$, the substrate is roughly constant $[S] \approx [S]_0$, so that the mass balance of the intermediate (4.8b) simplifies into:

$$\begin{aligned} \text{for } t \leq t_M: \quad \frac{d[ES]}{dt} &\approx k_{on}[E]_0[S]_0 - (k_{on}[S]_0 + k_{off} + k_{cat})[ES] \\ \Rightarrow \quad [ES](t) &\approx \frac{[E]_0[S]_0}{K_M + [S]_0}\left(1 - e^{-k_{on}([S]_0 + K_M)t}\right) \end{aligned} \tag{4.9}$$

with the enzyme concentration having been written as $[E] = [E]_0 - [ES]$. Hence we have:

$$t_M = \frac{1}{k_{on}([S]_0 + K_M)} \sim \frac{1}{k_{on}[S]_0} \tag{4.10}$$

The second (or slow) time scale $t^\star$ corresponds to the time at which the substrate has been significantly depleted. Once the steady state is reached $t \geq t_M$, the conservation of the substrate (4.8b) reads as:

$$\text{for } t_M \leq t: \quad \frac{d[S]}{dt} \approx -k_{cat}\frac{[E]_0[S]}{K_M + [S]} \tag{4.11}$$

Hence the slow time scale is given by:

$$t^\star = \frac{K_M + [S]_0}{k_{cat}[E]_0} \sim \frac{[S]_0}{k_{cat}[E]_0} \tag{4.12}$$

Our two estimates of t_{M} and $t^\star$ are marked with dashed lines on Fig. 4.4 b) where one can see that they bound accurately the time window in which the intermediate is constant. These two time scales also yield a simple criterion for the Michaelis-Menten model (4.7) to apply: The fast time scale t_{M} has to be smaller than the slow time scale $t^\star$. This yields:

$$t_{\mathrm{M}} \leq t^\star \quad \Rightarrow \quad \frac{k_{\mathrm{cat}}}{k_{\mathrm{on}}\left(K_{\mathrm{M}} + [S]_0\right)} \frac{[E]_0}{K_{\mathrm{M}} + [S]_0} \leq 1 \tag{4.13}$$

This criterion is met when $[S]_0 \gg [E]_0$. When the ratio $[E]_0 \,/\, [S]_0$ gets closer to one, or even much smaller than one, the intermediate does not reach the steady state and tends to the limit case of single turnover kinetics [23] which we will not treat here. As a result:

In a well-mixed reactor with $[S]_0 \gg [E]_0$, the intermediate complex ES is said to be stationary, or in steady state, when it forms as fast as it degrades. This takes place after an induction time $t_M \sim 1/k_{on}[S]_0$. Then:

$$[E](t)[S](t) \;=\; K_M[ES](t) \quad \textit{for all } t \textit{ between } t \geq t_M$$

On the other hand, the assumption $[S] \approx [S]_0$ fails after a time $t^\star \sim [S]_0/k_{cat}[E]_0$. Hence:

$$[P](t) \;=\; \frac{[E]_0[S]_0}{K_M + [S]_0}\, t \quad \textit{for all } t \textit{ between } t_M \textit{ and } t^\star$$

4.1.4 Competitive inhibition

Once an enzyme is characterized by having measured its K_{M} and k_{cat} using the Michaelis-Menten model, a common interest lies in studying species that promote or inhibit its catalytic activity. The inhibition of enzymes is indeed of prime importance for drug discovery. Many drugs are in fact enzyme inhibitors, and thus heal patients by preventing an enzymatic reaction from taking place. There are different ways for a drug to inhibit an enzyme activity. Here we present a competitive mechanism where both the substrate S and the drug I bind the same active site on the enzyme. Inhibition occurs when the enzyme E mostly binds the drug which can be summarized by:

$$\mathrm{EI} \overset{K_{\mathrm{I}}}{\rightleftarrows} \mathrm{E} + \mathrm{S} + \mathrm{I} \underset{k_{\mathrm{off}}}{\overset{k_{\mathrm{on}}}{\rightleftarrows}} \mathrm{ES} \overset{k_{\mathrm{cat}}}{\to} \mathrm{E} + \mathrm{P} \tag{4.14}$$

where K_{I} is the equilibrium constant between the enzyme and the enzyme-inhibitor complex.

The total amount of enzyme $[E]_0$ thus divides up between the amount of free enzyme $[E]$, the amount of enzyme-substrate complex $[ES]$ and the amount of enzyme-inhibitor complex $[EI]$:

$$[ES]_0 \;=\; [E] + [ES] + [EI] \tag{4.15}$$

which yields under the assumptions of the Michaelis-Menten model:

$$V_0 = k_{\text{cat}} [E]_0 \frac{[S]_0}{K_{\text{M}}(1 + \frac{[I]_0}{K_{\text{I}}}) + [S]_0} \tag{4.16}$$

with $[I]_0$ the initial amount of inhibitor. Thus, inhibition results in an increase in K_{M}, which is a signature of a lowered affinity of the enzyme for the substrate. Measurements of K_{I} are thus performed as dose response assays of K_{M} to increasing amounts of inhibitor.

In the next section we apply both steady state and enzyme inhibition kinetics to experiments held in well-mixed droplets.

4.2 Experiments in droplets: On-chip Michaelis-Menten and inhibition kinetics

In this section we aim at replicating on chip standard enzyme assays routinely performed with microtiter plates. To this end, we used our parallelized chip to test six different conditions in parallel on the same chip.

4.2.1 Well-mixed assays using our parallelized chip

We have chosen to study the hydrolysis of 4-nitrophenyl β-D-glucopyranoside catalyzed by β-D-glucosidase from sweet almond as it has been recently studied in droplets by Gielen *et al.* [75] which gives us a reference. We have thus performed two assays using our parallelized chip: (i) Measurement of the steady state parameters K_{M} and k_{cat} and (ii) Measurement of the inhibition constant K_{I} of β-D-glucopyranoside in the presence of 1-deoxynojirimycin hydrochloride (denoted I).

Each assay consists in measuring the dose response of the initial rate of the reaction with increasing concentrations of either the substrate or the inhibitor. To measure K_{M} and k_{cat}, six droplets of increasing $[S]_0$ were first produced from six different inlets. Then, droplet at a fixed enzyme concentration $[E]_0$ were produced and pushed to the remaining empty traps using an outer flow of oil. This outer flow was kept on to mix the droplets once they have been merged within a few seconds. After a few minutes a clear difference between the drops was observable as shown on Fig. 4.5 a). Similar procedure was followed to measure K_{I}. Instead of increasing the initial substrate concentration, $[S]_0$ was kept constant and $[I]_0$ was increased. Here again, a clear difference between the drops was observable after a few minutes as shown on Fig. 4.5 b). The resulting gradients obtained in each case are in opposite direction as shown on Fig. 4.5: While an increase in $[S]_0$ yields larger reaction rates, an increase in $[I]_0$ yields lower reaction rates.

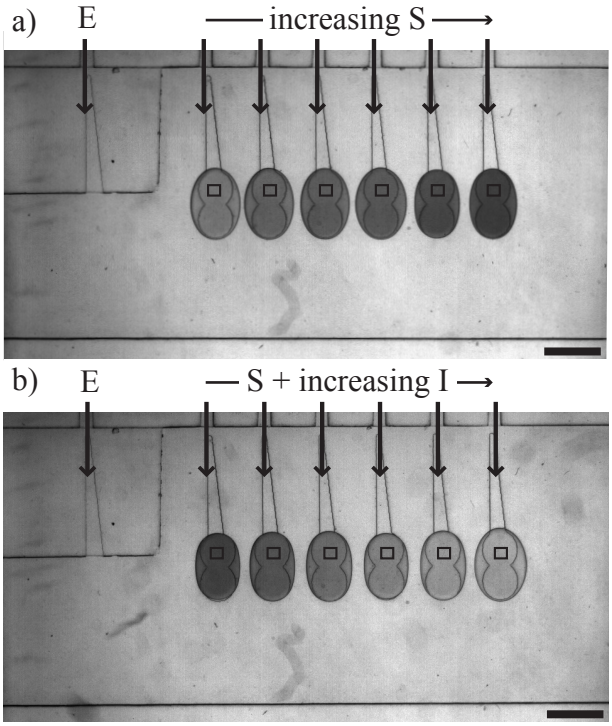

Figure 4.5: Parallelized chip in two different well-mixed assays. The buffer is PBS at pH = 7.4 and the initial enzyme concentration is $[E]_0 = 5$ μM in both cases. a) Steady-state kinetics. The substrate concentration increased from left to right $[S]_0 = 1$, 3, 7, 13, 23 and 31 mM. b) Inhibition kinetics. The substrate concentration is fixed $[S]_0 = 23$ mM and the inhibitor concentration is increased from left to right $[I]_0 = 0$, 90, 250, 750 and 1500 nM. These are the concentrations once the droplets are merged and mixed. Stock solution are thus twice as concentrated. The black box inside the drops correspond to the windows in which gray levels were read. Scale bars are 500 μm.

4.2.2 Determination of $K_{\mathbf{M}}$ and $k_{\mathbf{cat}}$

Droplets of an enzyme solution at 10 μM were paired with droplets of different substrate solutions at 2, 6, 14, 26, 46 and 62 mM. Once merged the initial concentrations in the drops were therefore $[E]_0 = 5$ μM and $[S]_0 = 1$, 3, 7, 13, 23 and 31 mM. The increase in absorbance was recorded for 10 min and this experiment was repeated three times in a row. This increase is linear in time as shown on Fig. 4.6 a). We can thus extract the slope V_0 of the traces we monitored which yields the sigmoid curve shown on Fig. 4.6 b) when the different slopes are plotted against the corresponding initial substrate concentrations. Fitting the six experimental initial rates with (4.7) then yields $K_{\mathrm{M}} = 9.3 \pm 3.1$ mM and $k_{\mathrm{cat}} = 0.7 \pm 0.09$ s^{-1}. These values are in good agreement with our reference measurements $K_{\mathrm{M}} = 9.0 \pm 1.0$ mM and $k_{\mathrm{cat}} = 0.50 \pm 0.02$ s^{-1} done in a plate reader (see appendix A.2 for details), as well as with other measurements by Gielen *et al.* who obtained $K_{\mathrm{M}} = 11.4 \pm 2$ mM and $k_{\mathrm{cat}} = 0.9 \pm 0.2$ s^{-1}.

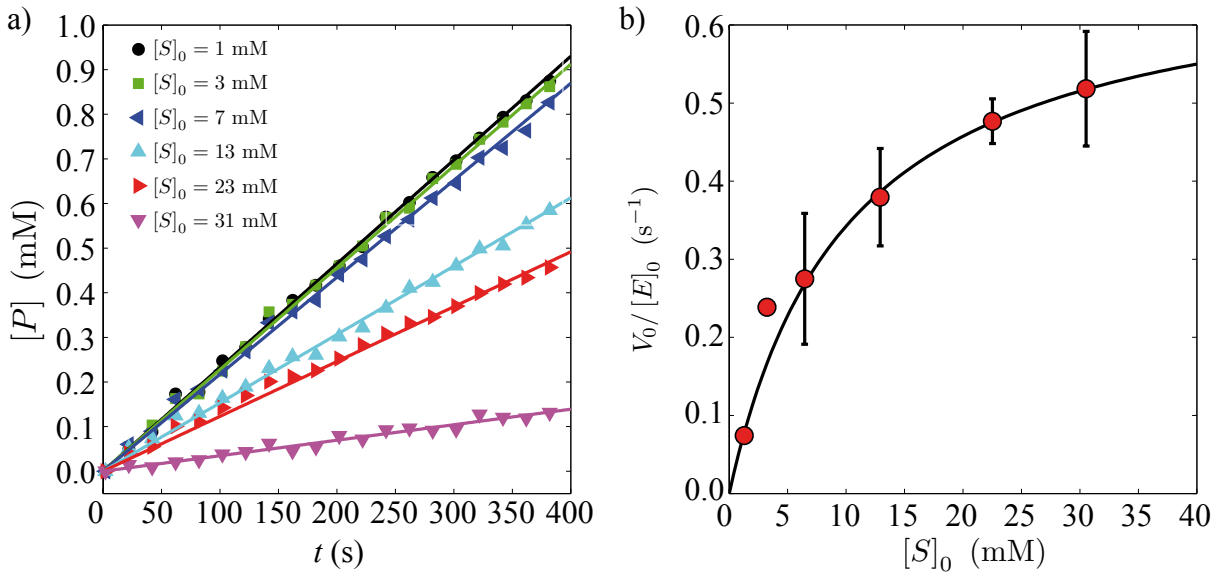

Figure 4.6: a) Time courses $[P](t)$ for six different $[S]_0$. Solid lines: Best fits with $[P](t) = V_0 t$. b) Initial slope of $[P](t)$ against the initial substrate concentration $[S]$. Solid line: Best fit with $V_0/[E]_0 = [S]_0/(K_M + [S]_0)$. The second point at $[S]_0 = 3$ mM has been ignored to get a better fit.

4.2.3 Determination of K_I

In the second round of experiments, we aimed at measuring K_I. Here again, droplets of an enzyme solution at 10 μM were produced and paired with droplets of different solutions, all at $[S]_0 = 46$ mM, and containing an increasing amount of inhibitor $[I]_0 = 0$, 180, 500, 1500 and 3000 nM. The increase in absorbance was measured for 10 min and the experiment repeated three times. The resulting time courses are linearly increasing with time as shown on Fig. 4.7 a) and we can measure their initial slope V_0. Then, we can extract K_I by fitting the normalized reaction rates V_0/V_0^{max} against the initial inhibitor concentration $[I]_0$ via the Cheng-Prusoff relation [147]:

$$\frac{V_0}{V_0^{max}} = \frac{1}{1 + \frac{[I]_0}{IC50}} \qquad \text{with} \qquad IC50 = \left(1 + \frac{[S]_0}{K_M}\right) K_I \tag{4.17}$$

Our fit is shown on Fig. 4.7 b). It yields IC50 = 182 ± 58 nM and K_I =51 ± 16 nM while our reference measurement in the plate reader yields IC50 = 238 ± 13 nM and K_I =67 ± 4 nM (see appendix A.2 for details). Besides, Gielen *et al.* have found IC50 = 108 ± 40 μM and K_I =36 ± 13 nM.

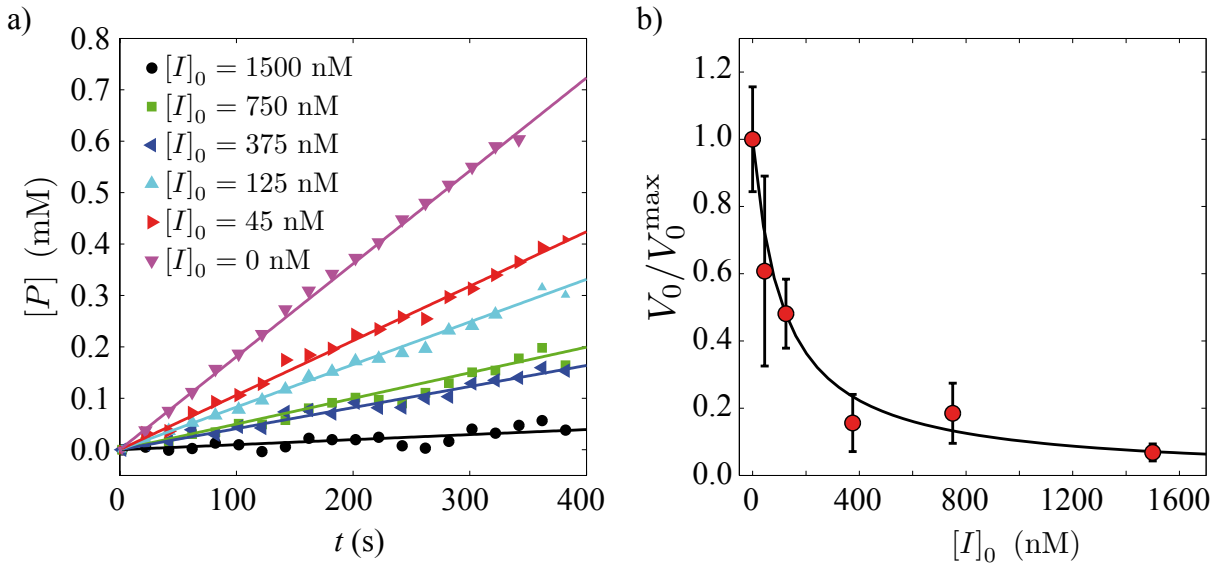

Figure 4.7: a) Time courses $[P](t)$ for six different $[I]_0$. Solid lines: Best fits with $[P](t) = V_0 t$. b) Normalized initial velocity against the initial inhibitor concentration. Solid line: Best fit with $V_0/V_0^{\max} = 1/(1 + [I]_0/\mathrm{IC50})$.

4.2.4 Perspectives

The 2D format of our parallelized chip allows us to test many different conditions on a single chip, and thereby to mimic the microtiter plate format. Our chip currently achieves six different conditions only, which is not enough to yield very good estimates of K_M, k_cat and K_I.

Indeed, precise measurements of these parameters requires more points on the rate dose response curve. For instance, for steady state kinetics, the rule of thumb is that the substrate concentration should vary from 0.2 K_M up to 5 K_M, with three measurement points per K_M. To be achieved soundly on chip, this requires dilution of the substrate to be performed on chip.

4.3 Reaction-diffusion with initially separated reagents

We now turn our attention to the study of fast enzymatic reactions in our device. For such reactions, the reaction starts just after the droplet fusion. Therefore, the diffusion of the reagents toward each other must be taken into account in the product formation dynamics. Hereafter we derive a one dimensional RD model with Michaelis-Menten kinetics:

$$\mathrm{E} + \mathrm{S} \underset{k_\mathrm{off}}{\overset{k_\mathrm{on}}{\rightleftarrows}} \mathrm{I} \overset{k_\mathrm{cat}}{\rightarrow} \mathrm{E} + \mathrm{P} \tag{4.18}$$

where the concentration of the species E, S, I and P are denoted E, S, I and P respectively. In addition, we focus on the practical case where the initial amount of substrate S_0 is much larger than the initial amount of enzyme E_0:

$$S_0 \gg E_0 \quad \text{in all this section}$$

IMPORTANT NOTE We make a change of notation for simplicity. Concentrations are not between brackets anymore, but simply in italic. The intermediate complex is denoted I and not ES anymore.

We start by formulating a one dimensional RD problem with initially separated reagents. Then we discuss the steady state approximation when the reagents are not well mixed. This allows us to distinguish different asymptotic regimes in which we can simplify our RD problem: (i) The pre-steady-state regime, (ii) the steady state regime and (iii) the diffusion-controlled regime. We choose to focus on the steady state regime and derive an analytical solution for the product concentration in this case. Finally, we validate our analytical solution by comparing it to direct numerical simulations.

4.3.1 Problem formulation

We consider the experiment shown on Fig. 4.8. A droplet containing an enzyme solution at a concentration E_0 is merged with another droplet containing a substrate solution at a concentration S_0. These droplets are treated as two 1D reservoirs of fresh reagents. At t = 0 s, a laser pulse merges the droplets and a reaction following the Michaelis-Menten scheme (4.18) takes place at the interface separating the fresh reagents as shown on Fig. 4.8 b) to d).

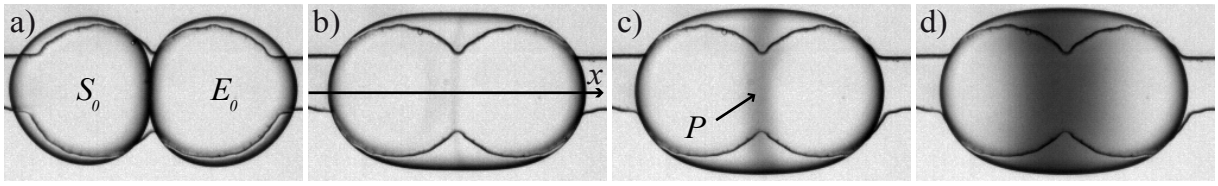

Figure 4.8: Test experiment with the hydrolysis of 4-nitrophenyl phosphate catalyzed by alkaline phosphatase from bovine intestinal mucosa. The product 4-nitrophenol is observed by absorption at 405 nm. The enzyme concentration is 16 μM, the substrate concentration is 20 mM, the buffer is at pH = 8 with 100 mM Tris and 500 mM NaCl.

Conservation laws

As enzymes have molar weights in the kDa range while substrates have molar weights in the Da range, E and S molecules have very different sizes. As a result, the substrate will

not change the enzyme size when it binds to it, and we expect the intermediate complex to have the same size as the free enzyme E. On the other hand, the product P is expected to have a size close to that of the substrate S. Then, the Stokes-Einstein equation [119] allows us to divide the species E, S, I and P in two groups of similar diffusion coefficients, the small molecules S and P having a diffusion coefficient D_{SP}, and the large molecules E and I having a diffusion coefficient D_{EI}.

Thus, the conservation equations for the species E, S, I and P take the form of diffusion equations coupled by three chemical source terms:

$$\frac{\partial E}{\partial t} = D_{EI}\,\frac{\partial^2 E}{\partial x^2} - k_{\text{on}} ES + k_{\text{off}} I + k_{\text{cat}} I \tag{4.19a}$$

$$\frac{\partial S}{\partial t} = D_{SP}\,\frac{\partial^2 S}{\partial x^2} - k_{\text{on}} ES + k_{\text{off}} I \tag{4.19b}$$

$$\frac{\partial I}{\partial t} = D_{EI}\,\frac{\partial^2 I}{\partial x^2} + k_{\text{on}} ES - k_{\text{off}} I - k_{\text{cat}} I \tag{4.19c}$$

$$\frac{\partial P}{\partial t} = D_{SP}\,\frac{\partial^2 P}{\partial x^2} + k_{\text{cat}} I \tag{4.19d}$$

Initial conditions

We note the Heaviside function $\hat{H}$. We model the initial concentrations of E and S by two touching Heaviside functions, while the intermediate I and the product P are not formed initially. Thus, the initial conditions on E, S, I and P read as:

$$E = E_0\ \hat{H}(x \geq 0) \qquad S = S_0\ \hat{H}(x \leq 0) \qquad I = 0 \qquad P = 0 \tag{4.20}$$

Boundary conditions

Our domain is bounded by the interface of the daughter droplet, which is non-permeable. As a result, we apply no-flux boundary conditions at the edges of the domain $x = \pm$ l:

$$\frac{\partial E}{\partial x} = \frac{\partial S}{\partial x} = \frac{\partial I}{\partial x} = \frac{\partial P}{\partial x} = 0 \quad \text{at } x = \pm\, l \tag{4.21}$$

4.3.2 The steady state assumption in RD

In section 4.1 we showed that in a well mixed reactor, the Michealis-Menten scheme (4.18) with $S_0 \gg E_0$ yields a regime where the intermediate complex I forms as fast as it degrades, thereby reaching a steady state defined by the equilibrium $ES = K_{\text{M}} I$. This regime was also shown to apply after an induction time t_{M} defined as:

$$t_{\text{M}} = \frac{1}{k_{\text{on}} S_0} \tag{4.22}$$

In this regime, the model of Michaelis-Menten shows that the product formation depends on K_{M} and k_{cat} only which are the two parameters usually measurable using microtiter

plates, the individual unit rates k_{on} and k_{off} being not measurable anymore when the equilibrium $ES = K_{\text{M}}I$ is established.

A similar situation can take place locally at each x position when the reagents are not well mixed. Then, the intermediate I forms as fast as it degrades at each x position leading to a local relation between the concentrations of E, S and I. Consequently, the steady state assumption in our reaction-diffusion problem reads as follows.

In RD, we say that the intermediate complex is stationary, or in steady state, when it forms as fast as it degrades at each x position, leading to the local equilibrium relation:

$$E(x,t)S(x,t) \;=\; K_M I(x,t) \quad \textit{for all } x \textit{ and } t$$

The local equilibrium $ES = K_{\text{M}}I$ is effectively found to establish using DNS of the general RD problem (4.19a)-(4.19d) with the representative values of the input parameters suggested by Ristenpart *et al.* [144]. These values are shown in Table 4.2.

E_0 (μM)	S_0 (mM)	k_{on} ($\text{M}^{-1}\text{s}^{-1}$)	k_{off} (s^{-1})	k_{cat} (s^{-1})	D_{EI} (m^2/s)	D_{SP} (m^2/s)
1	10	10^4	1	10	10^{-10}	10^{-9}

Table 4.2: Values of the different parameters used to solve the set of equations (4.19a)-(4.19d). From Ristenpart *et al.* [144].

As shown on Fig. 4.9, the distributions of both ES and $K_{\text{M}}I$ have a bell shape with non zero values where the distributions of E and S overlap. At early times (t from $t_{\text{M}}/4$ up to $10t_{\text{M}}$), the intermediate formation ES overcomes the intermediate break down $K_{\text{M}}I$ at every x positions (Fig. 4.9 a) to e)). At larger times (t from $50t_{\text{M}}$ up to $500t_{\text{M}}$), the intermediate complex I gets uniformly stationary as the distributions of ES and $K_{\text{M}}I$ coincide everywhere (Fig. 4.9 e) to h)).

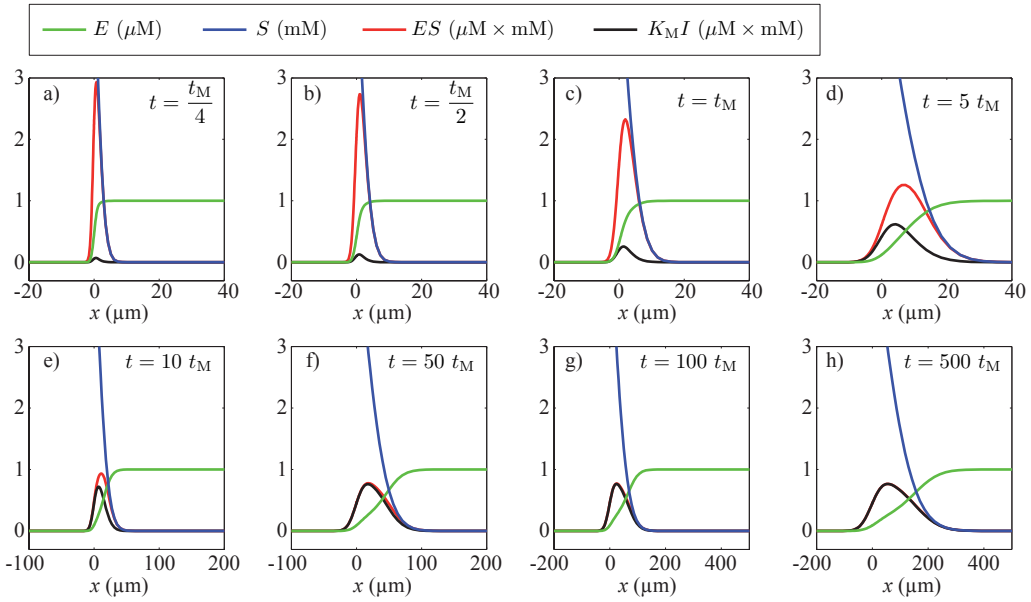

Figure 4.9: Profiles of E, S, ES and $K_{\mathrm{M}}I$ obtained numerically with the values of the input parameters shown on Table 4.2. The characteristic time t_{M} is $1/k_{\mathrm{on}}S_0$.

Two different phases are thus to be taken into account in the dynamics of the intermediate complex distribution $I(x,t)$:

- At early times, the intermediate formation speed $k_{\mathrm{on}}ES$ overcomes the intermediate speed of break down $(k_{\mathrm{off}}+k_{\mathrm{cat}})I$. Hence the main balance driving the evolution of the amplitude of $I(x,t)$ is $\partial I/\partial t = k_{\mathrm{on}}ES$ which yields the scaling $I \sim k_{\mathrm{on}}E_0S_0t$. This is the pre-steady state regime.

- At larger times, the intermediate gets stationary and $ES = K_{\mathrm{M}}I$ everywhere. This equilibrium yields the new scaling $I \sim E_0S_0/K_{\mathrm{M}}$ which shows that we expect the amplitude of $I(x,t)$ to not vary with time in this regime. This is the steady-state regime.

These two scaling laws on the amplitude of $I(x,t)$ are also verified numerically. The amplitude of ES and K_MI, denoted h^+ and h^- respectively, are defined on Fig. 4.10 a) and plotted over time on Fig. 4.10 b). The amplitude of $K_{\mathrm{M}}I$ (in blue) first increases linearly with time up to $t \approx 50\ t_{\mathrm{M}}$ where it saturates and coincides with the amplitude of ES as expected by our scaling analysis. Conversely, the amplitude of ES is constant in both the pre-steady and the steady state regimes, but changes value between the two regimes. At very large times, the amplitude of both ES and $K_{\mathrm{M}}I$ start decreasing. This is the onset of the diffusion-controlled regime. Indeed, as the reagents are initially separated, a diffusion-controlled regime must take place at very large time as discussed in the last chapter and the product formation has to be eventually limited by the diffusive supplies in fresh reagents. As the enzyme is not overall consumed by the chemical reaction, the

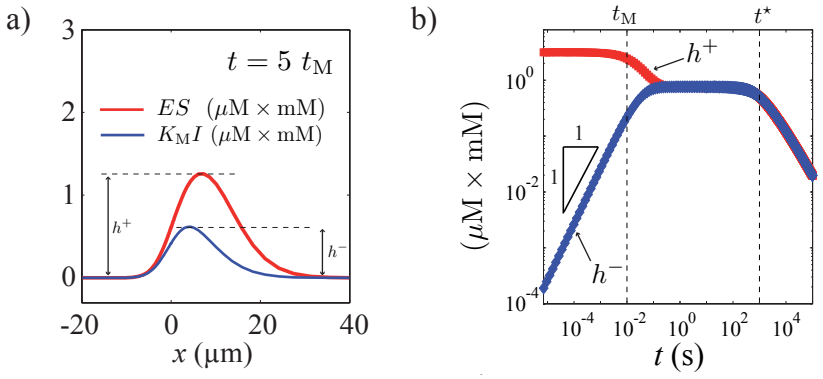

Figure 4.10: a) Definition of the amplitudes of ES (denoted h^+) and $K_M I$ (denoted h^-). b) Amplitudes h^+ and h^- over time. Dashed lines are the transition times t_M and $t^\star$.

transition time $t^\star$ from the reaction-controlled to the diffusion-controlled regime is set by the time required to turnover the initial excess of substrate near the reaction front. This takes place at most at the maximum reaction speed $k_{cat}E_0$ which yields the time required to deplete significantly the initial amount S_0 of substrate:

$$t^\star = \frac{S_0}{k_{cat}E_0} \tag{4.23}$$

This estimate of $t^\star$ corresponds effectively to the time at which the amplitudes of both $K_M I$ and ES start to decrease while keeping on coinciding as shown on Fig. 4.10 b). Hence, the steady-state assumption remains valid in the diffusion-controlled regime.

As a result, we obtain a sequence of three different regimes in the dynamics of $I(x,t)$ separated by two time scales t_M and $t^\star$. As shown on Fig. 4.11, these different regimes arise from the combination of the intermediate complex state, which can be stationary or not, with the state of the reaction zone, which can be reaction- or diffusion controlled. In addition, using the representative values proposed by Ristenpart *et al.* [144], we get $t_M = 10$ ms and $t^\star = 1000$ s. As a result, we expect to mostly observe the reaction-controlled regime with the intermediate being stationary (labels Regime II on Fig. 4.11) in our experimental 50 s long time window for observation. Hereafter, we thus focus on Regime II and use the steady state approximation to derive a reduced RD model which depends on K_M and k_{cat} only. The steady state approximation also allows us to derive an analytical solution of this problem. As shown on Fig. 4.11, while the pre-steady state has been studied by Ristenpart *et al.* [144], the regimes II and III have not been studied which also motivates our investigation of the regime II.

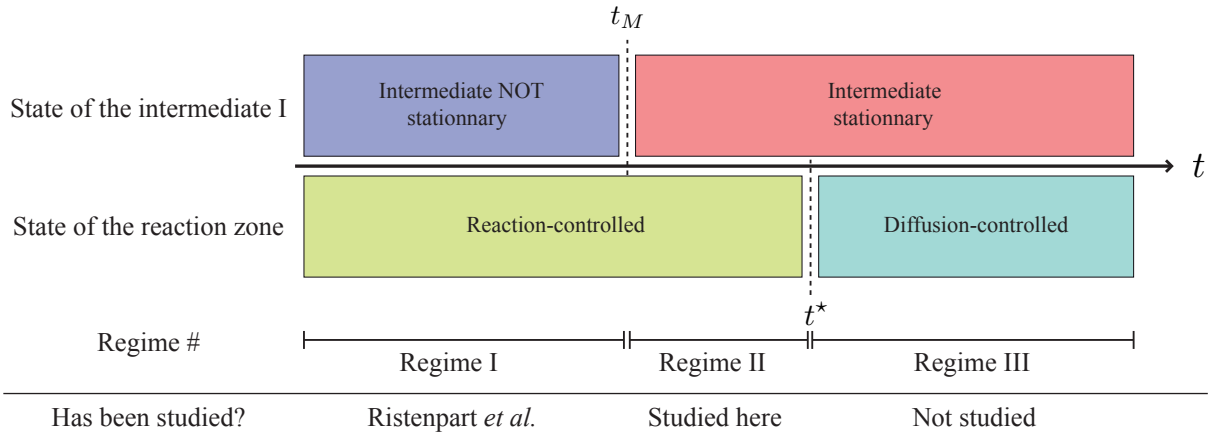

Figure 4.11: Three different regimes in the time course of our RD system with $S_0 \gg E_0$ depending on the state of both the intermediate complex I and the reaction zone. These regimes are separated by two times scale t_{M} and $t^\star$ that we have identified.

4.3.3 Steady state kinetics in RD

Here we reduce the general four species problem (4.19a)-(4.19d) on E, S, I and P to a two species problem on S and P which depends on K_{M} and k_{cat} only. To this end, we revisit two assumptions of the Michaelis-Menten model in our RD framework: (i) The global conservation of the enzyme and (ii) the steady state assumption.

Global enzyme conservation

The enzyme being globally not consumed by the chemical reaction, its total amount is conserved over time. As a result, the initial amount of enzyme divides up between its free state E and its bond state I. This distribution must hold true at every x positions which yields:

$$E(x,t) + I(x,t) \;=\; E_{\mathrm{tot}}(x,t) \quad \text{for all } x \text{ and } t \tag{4.24}$$

In addition, as we assume that E and I have the same diffusion coefficient D_{EI}, the enzyme global conservation (4.19a)+(4.19c) yields:

$$\frac{\partial E_{\mathrm{tot}}}{\partial t} \;=\; D_{EI}\,\frac{\partial^2 E_{\mathrm{tot}}}{\partial x^2} \tag{4.25}$$

which readily integrates into:

$$E_{\mathrm{tot}}(x,t) \;=\; \frac{E_0}{2}\,\mathrm{erfc}\left(-\frac{x}{\sqrt{4D_{EI}t}}\right) \tag{4.26}$$

As a result, we know exactly E_{tot} which allows us to simplify the general four species problem (4.19a)-(4.19d) to a three species problem on S, P and E.

Reduced RD model

When the intermediate is stationary, we can combine the relations $ES = K_M I$ and $E_{\text{tot}} = E + I$ to yield the intermediate complex concentration:

$$I(x,t) = \frac{E_{\text{tot}}(x,t)S(x,t)}{K_{\text{M}} + S(x,t)} \quad \text{for all } x \text{ and } t \tag{4.27}$$

Then, the four species problem (4.19a)-(4.19d) reduces to a two species problem on S and P:

$$\frac{\partial S}{\partial t} = D_{SP}\frac{\partial^2 S}{\partial x^2} - k_{\text{cat}}\frac{E_{\text{tot}}S}{K_M + S} \tag{4.28a}$$

$$\frac{\partial P}{\partial t} = D_{SP}\frac{\partial^2 P}{\partial x^2} + k_{\text{cat}}\frac{E_{\text{tot}}S}{K_M + S} \tag{4.28b}$$

This simplified version of our RD model is readily solved with Matlab which allows us to compare our reduced RD model (4.28a)-(4.28b) to the full model (4.19a)-(4.19d).

Comparison of the reduced and the full model

We first looked at the product profiles $P(x,t)$ obtained by each model. As shown on Fig. 4.12, the reduced model overestimates the actual product concentration at early time up $t \approx 50\ t_{\text{M}}$ at which point the reduced and the full model yield similar product profiles.

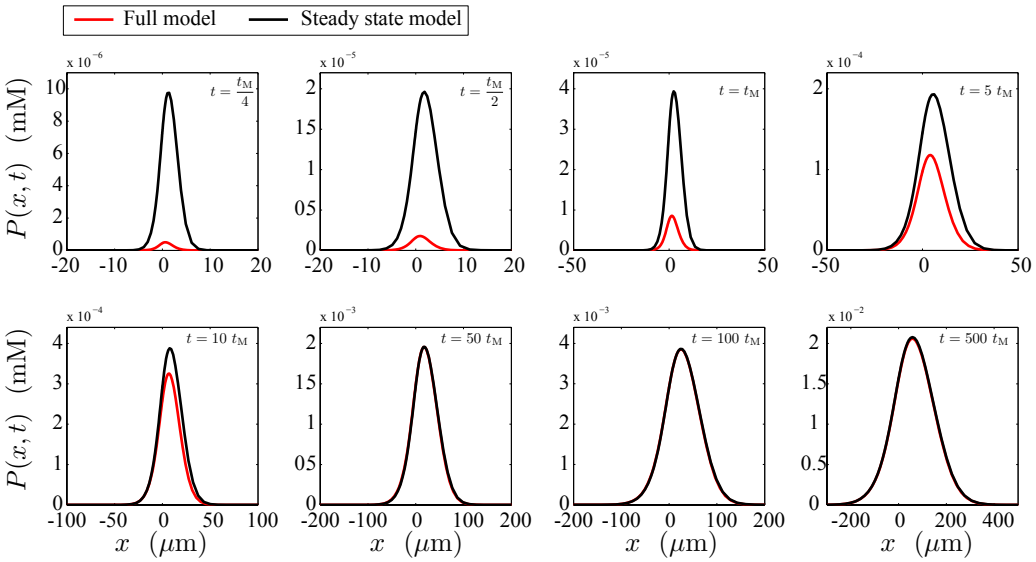

Figure 4.12: Product profiles $P(x,t)$ at different time points obtained with the reduced (black) and the full (red) RD models.

We confirm this first observation by measuring at each time point the amplitude h_p, the width w_p and the position x_p of the product distribution as sketched on Fig. 4.13 a).

Here again, the different characteristics of the product profile coincide for $t \gg t_{\mathrm{M}}$.

As shown on Fig. 4.13 b), the product amplitude h_p predicted by the full model passes from a t^2 behaviour before t_{M} to a t^1 behaviour after t_{M}. This change of dynamics can be explained by the change of dynamics that $I(x,t)$ encounters over t_{M}. Indeed, as I degrades into P, changes in the dynamics of $I(x,t)$ induces changes in the dynamics of $P(x,t)$. The relation $\partial P/\partial t \sim k_{\mathrm{cat}} I$ then yields $P \sim k_{\mathrm{cat}} I t$ which relates the scalings of the amplitude of $I(x,t)$ to the scaling of the amplitude of $P(x,t)$. As a result:

- For $t \leq t_{\mathrm{M}}$, the intermediate is not stationary and we know that the amplitude of $I(x,t)$ scales like $k_{\mathrm{on}} E_0 S_0 t$. Hence we expect $h_p \sim k_{\mathrm{cat}} k_{\mathrm{on}} E S t^2$.

- For $t_{\mathrm{M}} \leq t \leq t^\star$, we know that the amplitude of $I(x,t)$ scales like $E_0 S_0 / K_{\mathrm{M}}$. Hence we expect $h_p \sim E_0 S_0 t / K_{\mathrm{M}}$.

On the other hand, the product amplitude obtained with the reduced model does not exhibit any change of dynamics over t_{M} and keeps on increasing linearly with time. This t^1 behaviour of the product amplitude is therefore a signature of the steady state regime.

Besides, as shown on Fig. 4.13 c) the width w_p of the product distribution $P(x,t)$ is found to be the same using both models. It increases as $t^{1/2}$ and does not change behaviour over t_{M} and $t^\star$ which suggests that w_p is mostly driven by diffusion. Finally, the product position, defined as the location where $P(x,t)$ is maximum, is also found to increase as $t^{1/2}$ as shown on Fig. 4.13 d). A sharp change in the dynamics of x_p is observed at $t^\star$. This is because x_p changes direction. For $t \ll t^\star$, the product position moves toward the enzyme rich side with the excess of substrate diffusively entering the enzyme rich region. At larger times $t \gg t^\star$, the substrate is depleted around the reaction front so that the reaction front starts to move toward the substrate rich region. As a result, the product position displaces toward the substrate rich side of the domain in the large times limit.

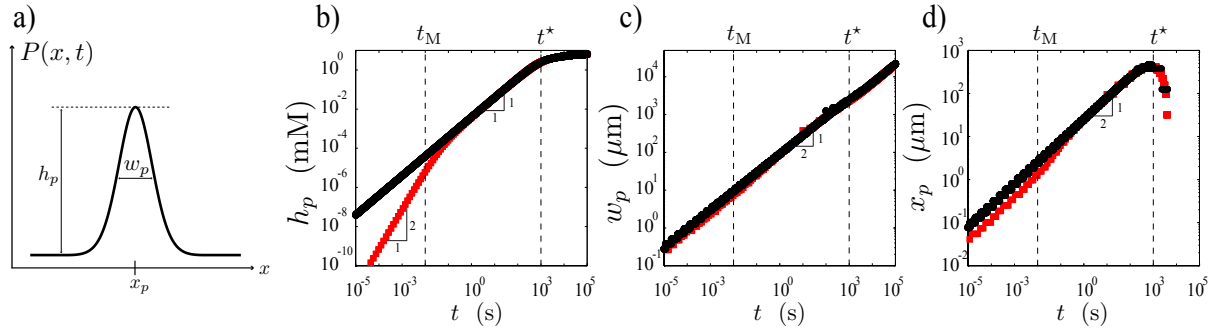

Figure 4.13: a) Sketch of the product distribution with the different characteristic h_p, w_p and x_p begin graphically defined. b) Product amplitude h_p over time. c) Product width w_p over time. d) Product position x_p over time.

Amongst the three characteristics h_p, w_p and x_p, the product amplitude seems the more promissing when aiming at measuring $K_{\rm M}$ and $k_{\rm cat}$. Hereafter, we focus on h_p and derive a model for it in the steady state regime.

4.3.4 Self-similar solution in the steady state regime

In order to derive an analytical solution for the product amplitude h_p, we need to approximate the source term $k_{\rm cat}I$ in the product conservation law. To this end, we use the steady state approximation and the initial condition $S_0 \gg E_0$. Then, we look for $P(x,t)$ as a self-similar function of the variable $\hat{\eta} = x/\sqrt{4D_{SP}t}$ which yields a model for h_p which depends on $K_{\rm M}$ and $k_{\rm cat}$ only.

Substrate profiles

The assumption $S_0 \gg E_0$ allows us to consider that the substrate is not much affected by the chemical reaction for time $t \ll t^\star$ which transforms the substrate conservation equation (4.19b) into:

$$\frac{\partial S}{\partial t} = D_{SP}\,\frac{\partial^2 S}{\partial x^2} \tag{4.29}$$

The equation (4.29) again readily integrates into:

$$S(x,t) = \frac{S_0}{2}\,\mathrm{erfc}\left(\frac{x}{\sqrt{4D_{SP}t}}\right) \tag{4.30}$$

As a result, we can use the substrate profile (4.30) instead of solving numerically of for $S(x,t)$ which transforms the two species problem (4.28a)-(4.28b) into a problem on $P(x,t)$ only.

Self-similar solution in the steady state regime

In the steady state regime, we can now combine the relations $ES = K_{\rm M}I$ and $E + I = E_{\rm tot}$ with our analytical estimate of $S(x,t)$ to yield:

$$I(x,t) = \frac{E_0}{2}\,\frac{\mathrm{erfc}\left(-\frac{x}{\sqrt{4D_{EI}t}}\right)\mathrm{erfc}\left(\frac{x}{\sqrt{4D_{SP}t}}\right)}{\frac{2K_M}{S_0} + \mathrm{erfc}\left(\frac{x}{\sqrt{4D_{SP}t}}\right)} \tag{4.31}$$

Consequently, we obtain the source term in the product conservation equation (4.19d). This source term is a function of the self-similar variable $\hat{\eta} = x/\sqrt{D_{SP}t}$ which invites us to look for $P(x,t)$ as a function $\hat{\eta}$. In addition, we showed in the last subsection that the product amplitude is linear for $t_{\rm M} \ll t \ll t^\star$. Hence, in this period of time, we can look for $P(x,t)$ in the form:

$$P(x,t) = k_{\rm cat}E_0\; t\; \hat{p}(\hat{\eta}) \tag{4.32}$$

Injecting (4.32) into (4.19d) then yields an equation for $\hat{p}(\hat{\eta})$:

$$\hat{p}'' \; + \; 2\,\hat{\eta}\,\hat{p}' \; - \; 4\,\hat{p} \; + \; 2\,\frac{\operatorname{erfc}\left(-\hat{\eta}/\hat{\rho}^{1/2}\right)\operatorname{erfc}\left(\hat{\eta}\right)}{2\hat{k}+\operatorname{erfc}\left(\hat{\eta}\right)} \;\; = \;\; 0 \tag{4.33}$$

where two new parameters $\hat{k}$ arise:

$$\hat{\rho} \;=\; \frac{D_{EI}}{D_{SP}} \qquad \text{and} \qquad \hat{k} \;=\; \frac{K_M}{S_0} \tag{4.34}$$

The equation (4.33) on $\hat{p}(\hat{\eta})$ can be solved numerically using Broyden's method. This yields a bell shape function with a maximum value denoted $\hat{p}_m$ which is a function of both $\hat{\rho}$ and $\hat{k}$. As a result, we obtain a model for the amplitude $h_p(t)$ of $P(x,t)$ in the steady state regime which is very similar to the well-mixed model of Micahelis and Menten:

$$h_p(t) \;=\; V_0^{RD}\,t \qquad \text{with} \qquad V_0^{RD} \;=\; k_{\text{cat}}E_0\;\hat{p}_m(\hat{\rho},\hat{k}) \tag{4.35}$$

The variations of $\hat{p}_m$ with $1/\hat{k} = S_0/K_{\text{M}}$ are shown on Fig. 4.14 a). Similarly to the well-mixed Michaelis-Menten model, the reaction speed increases linearly with S_0 when $S_0 \ll K_{\text{M}}$ and saturates when $S_0 \gg K_{\text{M}}$. Nonetheless, in practice, enzymatic assays are usually performed for S_0 around K_M and as shown Fig. 4.14 a), $\hat{p}_m$ does not have a simple scaling when $S_0 \approx K_{\text{M}}$ which prevents us from further simplification of $\hat{p}_m$. As a result, when aiming at fitting experimental data with this model for h_p, we will have to solve numerically for different values of $\hat{k}$ ($\hat{\rho}$ being fixed) in order to find K_{M}. The variations of $\hat{p}_m$ with $\hat{\rho} = D_{EI}/D_{SP}$ are shown on Fig. 4.14 b) where we see that the magnitude of $\hat{p}_m$ is much less affected by the variations of $\hat{\rho}$ than it is by the variations of $\hat{k}$.

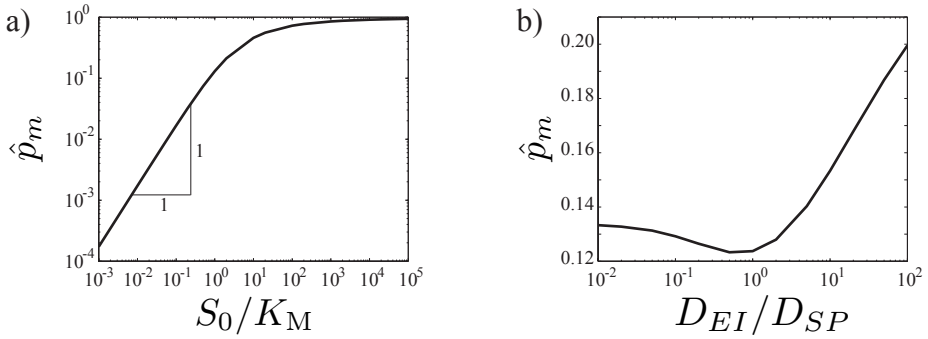

Figure 4.14: a) Variations of $\hat{p}_m$ with $1/\hat{k}$, $\hat{\rho}$ being fixed at 0.1 according to the values suggested by Ristenpart *et al.* [144]. b) Variations of $\hat{p}_m$ with $\hat{\rho}$, $\hat{k}$ being fixed at 1.

Comparison to DNS

In order to validate our model for $h_p(t)$, we compare our predictions for the amplitude $h_p(t)$ and the normalized shape $\hat{p}(\hat{\eta})/\hat{p}_m$ of the product distribution $P(x,t)$ using both

the self-similar solution and the full RD model. The corresponding amplitude and shape functions are shown on Fig. 4.15. The amplitude h_p obtained with our self-similar model corresponds to the solution of the full RD model for $t_{\mathrm{M}} \ll t \ll t^\star$ as shown on Fig. 4.15 a). On the other hand, there is a discrepancy in the product shape functions between the DNS and the self-similar solution. There are two reasons for this discrepancy. First, we overestimate the substrate concentration on the enzyme rich side by using the expression (4.30). Second, we neglect the displacement of the front x_p in our self-similar function. Looking for $P(x,t)$ as a function of $(x - x_p(t))/\sqrt{4D_{SP}t}$ should yield a better agreement between the product shape functions, but it requires a model for $x_p(t)$ to which we did not have any attempt.

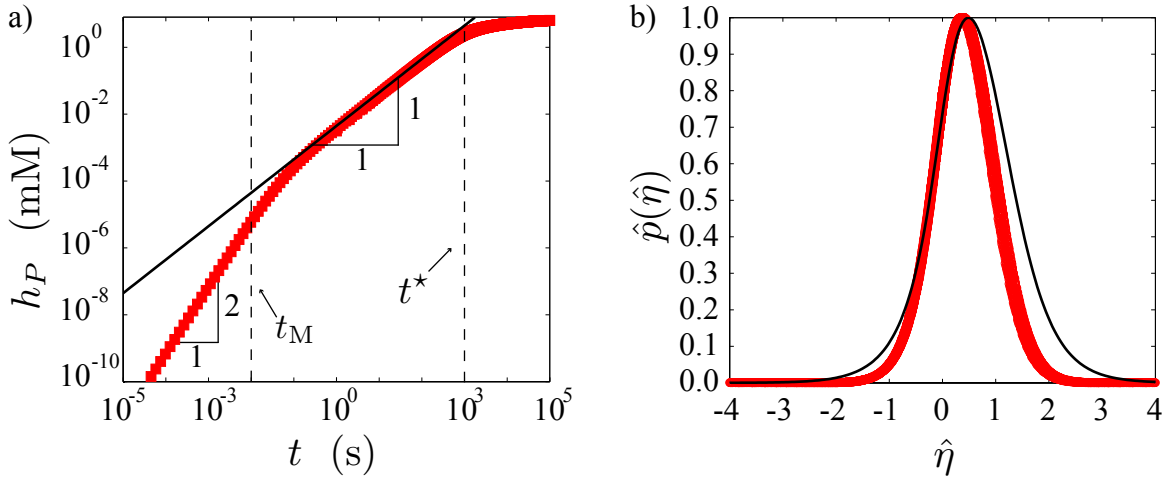

Figure 4.15: a) Product amplitude h_p versus time. Red dots is the DNS obtained with the input parameters of Table 4.2. The solid line is the corresponding solution of $h_p = V_0^{RD}t$. b) Product shape function in the steady state regime. Red dots: Superposition of product shapes obtained with the full RD model for 1 $s \leq t \leq 500$ s and plotted against $x/\sqrt{4D_{SP}t}$. Black line: $\hat{p}(\hat{\eta})$ for the corresponding values of $\hat{\rho}$ and $\hat{k}$.

We can draw three conclusions from the work presented in this section:

(i) In RD, when $S_0 \gg E_0$, the product formation present a long reaction-controlled regime with the intermediate being stationary. This regime last for times between $t_M = 1/k_{on}S_0$ and $t^\star = S_0/k_{cat}E_0$.

(ii) In this regime, the RD model reduces to:

$$\begin{aligned} \frac{\partial S}{\partial t} &= D_{SP}\,\frac{\partial^2 S}{\partial x^2} - k_{cat}\frac{E_{tot}S}{K_M+S} \\ \frac{\partial P}{\partial t} &= D_{SP}\,\frac{\partial^2 P}{\partial x^2} + k_{cat}\frac{E_{tot}S}{K_M+S} \end{aligned}$$

for all x and $t_M \ll t \ll t^\star$. This allows us to measure K_M and k_{cat}.

(iii) We can also measure the amplitude $h_p(t)$ of $P(x,t)$ in order to measure K_M and k_{cat} and use the following model for h_p:

$$h_p(t) = V_0^{RD}\,t \qquad with \qquad V_0^{RD} = k_{cat}E_0\,\hat{p}_m(\hat{\rho},\hat{k})$$

4.4 Comparison with experiments in a T-channel

In this section, we study experimentally the steady state kinetics of an enzyme following the Michaelis-Menten scheme (4.18) in reaction-diffusion. Before going into droplets, we benchmark our RD model for steady state kinetics using a well described microfluidic technique: The T or Y shaped microchannel. This technique has indeed been already used in RD to study forward one step reactions [101, 130], immunoassays [148], equilibrated one step reactions [131, 149], enzymatic reactions in pre-steady state [144], and interdiffusion dynamics [150, 151].

Here we start by presenting the experimental setup and then we use two fitting protocols to extract the steady state parameters K_M and k_cat. First we compare the concentration maps of product obtained experimentally and numerically to yield measurements of K_M and k_cat. Second, we fit directly on the amplitude of $P(x,t)$ and use our model for h_p to extract K_M and k_cat.

4.4.1 Experiments in a coflow geometry

The experiment consists in flowing two streams of reagents next to each other in a Y shaped channel as shown on Fig. 4.16. Our channel is 2 cm long, 1.5 mm wide, and 185 μm high.

Hence there is a good separation of length scales $h \ll w \ll l$ which ensures that the Hele-Shaw approximation holds true. As a result, we expect the velocity field to be along the channel (y direction on Fig. 4.16), Poiseuille like along the height of the channel (z direction on Fig. 4.16), and constant along the width of the channel a distance h apart from the side walls (x direction on Fig. 4.16). Besides, we choose to inject each species at a rate $Q = 0.5$ μL/min which induces a mean velocity $U = 60$ μm/s in the test section and which was found to yield well resolved concentration maps.

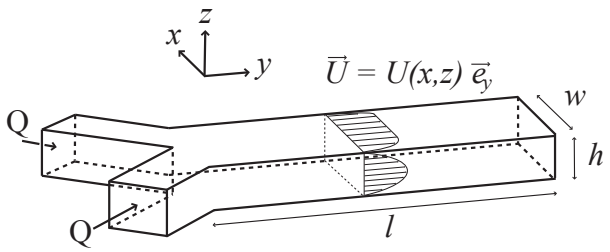

Figure 4.16: Channel geometry and flow field. In our geometry $l = 2$ cm, $w = 1.5$ mm and $h = 185$ μm. This is a Hele-Shaw cell where the flow is Poiseuille like along the z direction and nearly constant along the x and y directions.

We also choose to study the same reaction since in section 4.1 as it is well calibrated. The reaction is the hydrolysis of 4-nitrophenyl β-D-glucopyranoside catalyzed by β-D-glucosidase from sweet almond, which yields 4-nitrophenol that we observe by absorption at 405 nm. A typical concentration map of 4-nitrophenol is shown on Fig. 4.17.

In section 4.1 we measured $K_{\mathrm{M}} = 9.3 \pm 3.1$ mM and $k_{\mathrm{cat}} = 0.7 \pm 0.09$ s^{-1} for this reaction which allows us to choose the working concentrations of both the enzyme E and the substrate S. Two rounds of experiments were done to vary both the substrate and the enzyme concentrations. In the first round, the substrate concentration is kept constant at $S_0 = 30$ mM and the enzyme initial concentration is varied from 10 to 100 μM. In the second round of experiments, the enzyme concentration is fixed at $E_0 = 82$ μM and the substrate concentration is varied from 2 to 50 mM.

In addition, the relatively large channel height $h = 185$ μm and a bandpass filter centered at 405 ± 2 nm allows us to detect as low as 0.1 mM of 4-nitrophenol (see appendix A.2 for calibration curves), which is far below the reaction K_{M}, already measured around 10 mM in section 4.1. On the other hand, the limit of solubility of the substrate was found to be around 70 mM. As a result, this reaction is ideal to test our RD model as it allows us to perform experiments on a wide range of substrate concentrations around K_{M}.

The next step of our approach consists in fitting our experimental maps of 4-nitrophenol (Fig. 4.17) with concentration maps from our RD model for steady state kinetics. Hereafter we discuss the equivalence of our RD model and the advection-diffusion-reaction model

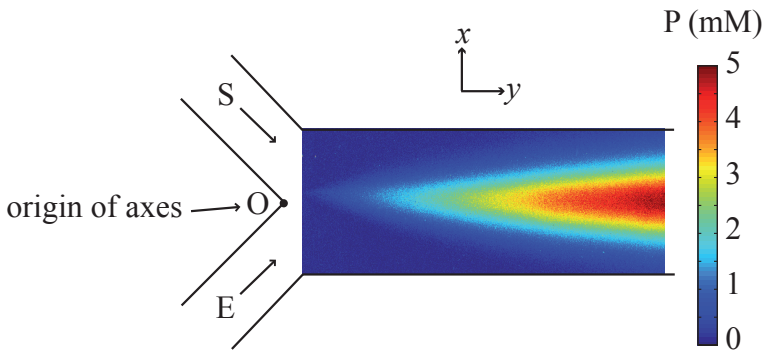

Figure 4.17: Experimental maps of 4-nitrophenol obtained by flowing a solution of β-D-glucosidase at 82 μM next to a solution of 4-nitrophenyl β-D-glucopyranoside at 50 mM. The buffer is PBS at pH = 7.4. The calibration curve to transform optical densities into product concentrations in shown in appendix A.2.

conventionally used in coflow microchannels.

4.4.2 From an advection-diffusion-reaction model to a RD model

As the reagents are flowed next to each other in our channel geometry, they meet through diffusion across the interface separating the two streams of reagents while being advected down the channel by the mean flow. As a result, when an enzyme E is flowed next to its substrate S, the product P forms a triangular layer along the channel as shown on Fig. 4.17. This stationary pattern can be modeled by a 2D reaction-advection-diffusion model of the form:

$$\vec{U}.\nabla P \quad = \quad D_{SP}\,\nabla^2 P \quad + \quad R \tag{4.37}$$

where R is the source term for product formation.

This equation (4.37) is analogous to our RD model under several key assumptions:

- First, the flow must be along the y direction $\vec{U} = U\ \vec{e}_y$ which reduces the advection term $\vec{U}.\nabla P$ to $U\partial P/\partial y$. This a fair assumption owing to the good separation of length scale of our channel geometry $h \ll w \ll l$.

- Second, we assume that the flow velocity U is constant and equal to the height averaged velocity. Then, with the space-time relation $y = Ut$ induced by the flow, the advection term can also be written as $\vec{U}.\nabla P = \partial P/\partial t$. This assumption consists in neglecting near wall effects such as hydrodynamic dispersion [99], and entrance effects [131] for which the 3D velocity profile must be taken into account. This assumption holds true near the central line of the channel on which we focus.

- Third, we consider depth averaged concentration maps of species. As a result, diffusion has not to be taken into account along the z direction.

- Fourth, advection dominates diffusion along the y direction. This is verified when $Pe \gg 1$ with Pe the Péclet number based on h defined as $Pe = Uh/D_{SP}$. In our experiment, we measured $D_{SP} = 0.7\times 10^{-9}$ m^2/s and we have $h = 185$ μm and U = 60 μm/s. This yields Pe = 93 which validates this assumption.

While the first three assumptions rely mostly on the channel high aspect ratio, the last assumption relies on the flow velocity we impose. Special care must thus be taken in the choice of the flow rate at which experiments are performed. Under these four assumptions, the model (4.37) reduces to:

$$\frac{\partial P}{\partial t} \;=\; D_{SP}\,\frac{\partial P}{\partial x^2} \;+\; R \tag{4.38}$$

with $t = U/y$ and R the source term from the Michealis-Menten scheme (4.18). In addition, no flux boundary conditions can be applied at the walls of the channel and the reagent are initially separated as we choose the origin of axes to be at the Y junction as shown on Fig. 4.17. This allows us to use all the results from the last section.

4.4.3 Direct fit using DNS

With the values of $K_{\rm M}$ and $k_{\rm cat}$ from section 4.1 and the initial concentrations, we can estimate the transition times t_M and $t^\star$ in order to identify the asymptotic regime that we observe in our experiment. The first transition time $t_M = 1/k_{\rm on}S_0$ can be estimated by $t_M \sim K_M/k_{\rm cat}S_0$ with $k_{\rm on} = (k_{\rm off} + k_{\rm cat})/K_{\rm M} \sim k_{\rm cat}/K_{\rm M}$. This yields $t_M \approx 0.4$ s. The second transition time $t^\star = S_0/k_{\rm cat}E_0$ is calculated to be $t^\star = 265$ s. In addition, our 2 cm long channel translates into a 300 s long time window for observation with a mean velocity $U = 60$ μm/s. As a result, we mostly observe the reaction-controlled asymptotic regime with the intermediate being stationary.

We can thus look for $K_{\rm M}$ and $k_{\rm cat}$ by fitting our experimental concentration maps with the following model:

$$\frac{\partial S}{\partial t} \;=\; D_{SP}\,\frac{\partial^2 S}{\partial x^2} \;-\; k_{\rm cat}\frac{E_{\rm tot}S}{K_M+S} \quad \text{with} \quad S(x,0) \;=\; S_0\;\hat{H}(x\le 0) \tag{4.39a}$$

$$\frac{\partial P}{\partial t} \;=\; D_{SP}\,\frac{\partial^2 P}{\partial x^2} \;+\; k_{\rm cat}\frac{E_{\rm tot}S}{K_M+S} \quad \text{with} \quad P(x,0) \;=\; 0 \tag{4.39b}$$

which is derived from the general model (4.19a)-(4.19d) by assuming the global conservation of the enzyme (4.27), and that the intermediate is stationary. Best fit profiles are shown on Fig. 4.18 for $t_{\rm M} \ll t \ll t^\star$. There is a very good agreement between our simulations and our experiments as both the amplitude, the width and the position of the numerical and experimental product distributions match. This fit was obtained with our choice of D_{EI} to match the width of the distributions.

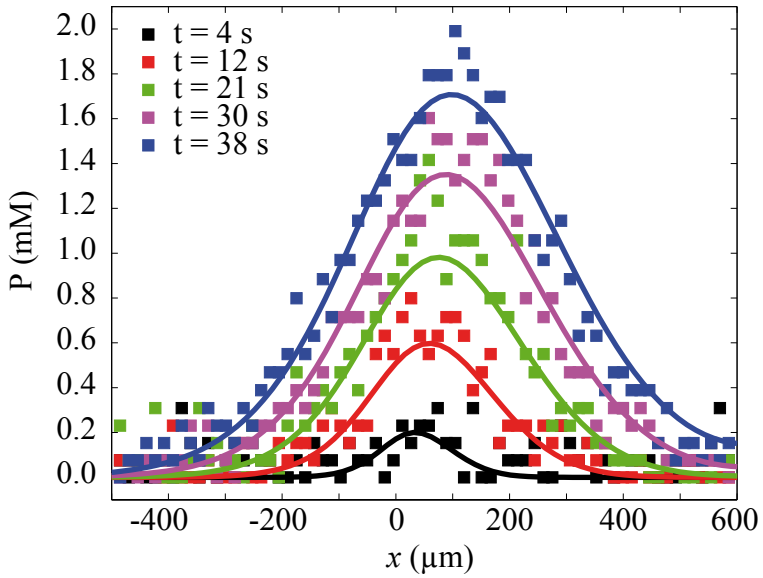

Figure 4.18: Experimental product profiles and best fit profiles in the case $E_0 = 82$ μM, $S_0 = 30$ mM, $D_{SP} = 0.7 \times 10^{-9}$ m^2/s, $D_{EI} = 1.2\times 10^{-9}$ m^2/s, $k_{\rm cat} = 1$ s^{-1}, $K_{\rm M} = 6$ mM. With these values we have $t_{\rm M} \approx 0.4$ s and $t^\star \approx 300$ s. Here we focus on the time window $t_{\rm M} \ll t \ll t^\star$. The value of D_{EI} has been chosen so as to fit the width of the distributions.

Best fit profiles are found by solving the problem (4.39a)-(4.39b) for different values of $K_{\rm M}$ and $k_{\rm cat}$ and minimizing the error:

$$\text{error} \quad = \quad \frac{||P^{\rm sim}(x,t) - P^{\rm exp}(x,t)||}{||P^{\rm sim}(x,t)||} \tag{4.40}$$

where $P^{\rm sim}$ and $P^{\rm exp}$ are the simulated and the experimental product space-time diagrams respectively. This yields the error map shown on Fig. 4.19 a), and the measurements $K_{\rm M}$ = 6.1 $\pm$ 0.2 mM and $k_{\rm cat}$ = 1.0 $\pm$ 0.1 s^{-1} which compare well with our other measurements done in the well-mixed case in the section 4.1. The margin of error on $K_{\rm M}$ and $k_{\rm cat}$ are calculated by taking the value of either $K_{\rm M}$ or $k_{\rm cat}$ at which the residue, shown on Fig. 4.19 b) for $K_{\rm M}$ and Fig. 4.19 c) for $k_{\rm cat}$, increases by 1% from the miminum value.

This first fitting protocol yields $K_{\rm M}$ and $k_{\rm cat}$ in a single experiment which transposes standard multiple dose response experiments in a much more simpler format. However, it requires to resolve the full space-time diagrams $P(x,t)$. Hereafter we use another fitting protocol which consists in fitting on the product amplitude only.

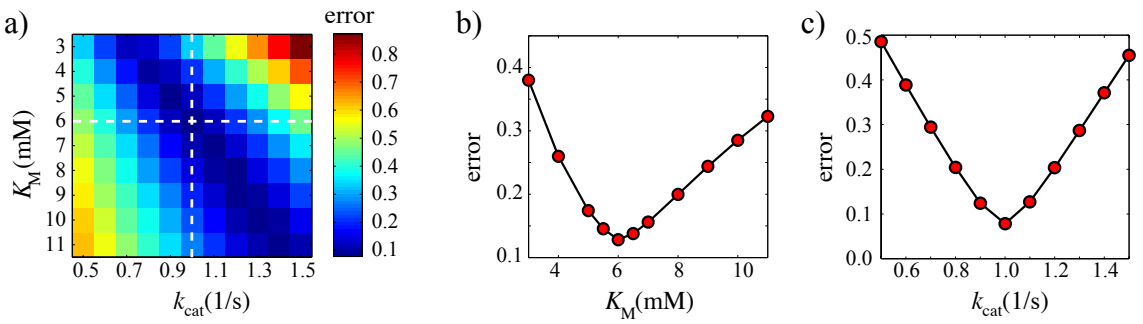

Figure 4.19: a) Error map against K_{M} and k_{cat}. b) Error against K_{M} with k_{cat} fixed at its best fit value $k_{\mathrm{cat}} = 1.0$. c) Error against k_{cat} with K_{M} fixed at its best fit value $K_{\mathrm{M}} = 6.1$.

4.4.4 Fit on the product amplitude

We can also use our benchmark experiment to validate experimentally our self-similar model for $P(x,t)$:

$$P(x,t) \;=\; k_{\mathrm{cat}} E_0 \; t \; \hat{p}(\hat{\eta}) \tag{4.41}$$

where $\hat{p}$ is the solution of:

$$\hat{p}'' + 2\hat{\eta}\hat{p}' - 4\hat{p} + 2\frac{\mathrm{erfc}\left(-\eta/\hat{\rho}\right)\mathrm{erfc}\left(\eta\right)}{2\hat{k} + \mathrm{erfc}\left(\hat{\eta}\right)} \;=\; 0 \tag{4.42a}$$

$$\text{with} \;\; \hat{p}(0) \;=\; 0 \;\; \text{and} \;\; \hat{\eta} \;=\; \frac{x}{\sqrt{4D_{SP}t}} \tag{4.42b}$$

To this end, we compare both the amplitude (denoted h_p) and the shape function (denoted $\hat{p}/\hat{p}_m$ with $\hat{p}_m$ the maximum value of $\hat{p}$) that we obtain experimentally with the solution of our model. Denoting h_p the product amplitude, we have shown in section 4.1 that:

$$h_p(t) \;=\; V_0^{\mathrm{RD}} \; t \tag{4.43a}$$

$$\text{with} \;\; V_0^{\mathrm{RD}} \;=\; k_{\mathrm{cat}} E_0 \hat{p}_m \tag{4.43b}$$

where $\hat{p}_m$ was shown to depend on S_0/K_{M} and D_{EI}/D_{SP} in section 4.1. As a result, the product amplitude depends on both K_{M} and k_{cat} while the product shape function depends on K_{M} only.

We use the values of K_{M} and k_{cat} obtained in the last subsection by fitting the full product profile, namely $K_{\mathrm{M}} = 6.1 \pm 0.2$ mM and $k_{\mathrm{cat}} = 1.0 \pm 0.1$ s^{-1}, in order to compute the product amplitude and shape functions. The comparison between our predictions and our measurements of h_p is shown on Fig. 4.20 a) for different values of S_0. The product amplitude increases effectively linearly with time in the first instants after the reaction start and our model proves successful to represent this initial linear increase at the different substrate concentrations. We also compare the product shape functions obtained

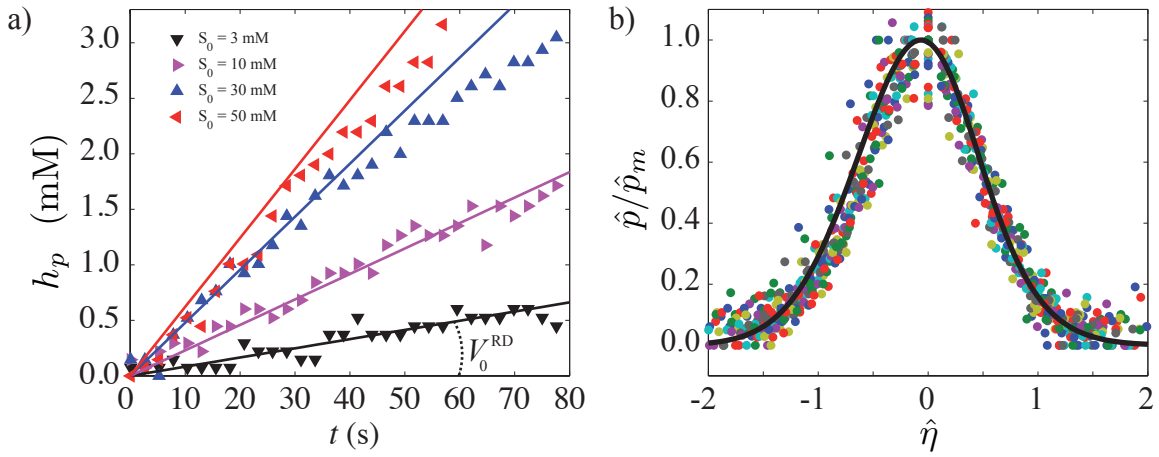

Figure 4.20: Self-similar solution for product formation. a) Product amplitude. Coloured dots are experiments at varying S_0 and fixed $E_0 = 82$ μM. Solid lines are corresponding product amplitude $h_p = k_{\text{cat}} E_0 \, \hat{p}_m \, t$ calculated with $D_{SP} = 0.7 \times 10^{-9}$ m^2/s, $D_{EI} = 1.2 \times 10^{-9}$ m^2/s, $K_{\text{M}} = 6.1$ mM and $k_{\text{cat}} = 0.8$ s^{-1}. b) Product shape function. Coloured dots: Superposition of 40 product shape functions between t = 0.2 s and t = 40 s in the case S_0 = 30 mM. Solid line: Corresponding shape function from the model.

experimentally and via our model. As shown on Fig. 4.20 b), the experimental product distribution is indeed self-similar as the product shapes obtained at different time points collapse on a single curve when plotted against $\hat{\eta} = x/\sqrt{4D_{SP}t}$. In addition, this curve is found to compare well with our prediction for $\hat{p}/\hat{p}_m$. This confirms the validity of our model in the first instants after the reaction start.

Our self-similar model for the product amplitude $h_p(t) = V_0^{\text{RD}} \, t$ is further confirmed by comparing the dependency of V_0^{RD} with varying S_0 and E_0. The corresponding curves with the values of K_{M} and k_{cat} obtained in the last subsection are shown on Fig. 4.21 a) and Fig. 4.21 b) with dashed lines. The sigmoid shape of V_0^{RD} with S_0 (Fig. 4.21 a)) as well as the linear increase of V_0^{RD} with E_0 (Fig. 4.21 b)) are well captured. However, the slope of V_0^{RD} with E_0 (dashed line) is badly represented and setting $K_{\text{M}} = 5.1$ and $k_{\text{cat}} = 1.30$ yields the best fit (solid black line on Fig. 4.21 b)). As the results presented on Fig. 4.21 b) correspond to a second round of experiments, this difference in K_{M} and k_{cat} is presumably due to varying degrees of enzyme viability from one batch to another.

This shows that our self-similar model for product formation allows us to extract K_{M} and k_{cat} by fitting on V_0^{RD} only. By doing so, we follow a very similar approach to standard protocols used for well-mixed assays and much simpler than studying the full space time diagram $P(x,t)$.

Another concern is the time window over which our model applies. Indeed, the product

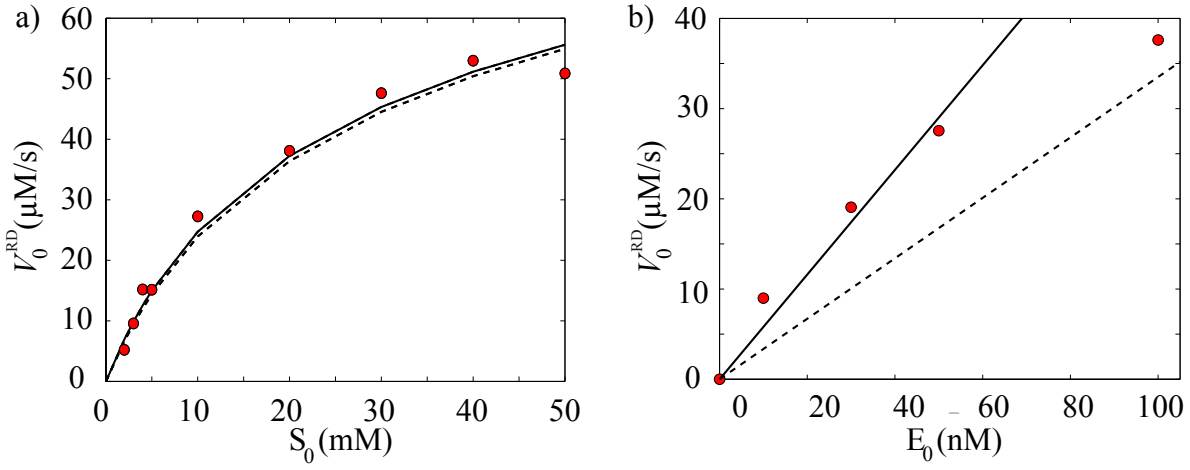

Figure 4.21: a) Initial slope V_0^{RD} against S_0. b) Initial slope V_0^{RD} against E_0. In both graphs, red dots correspond to experiments, dashed lines to predicitions from the model with $K_{\mathrm{M}} = 6.1$ mM and $k_{\mathrm{cat}} = 0.8$ s^{-1}, and solid lines to best fits with the model which yield $K_{\mathrm{M}} = 5.7 \pm 0.1$ mM and $k_{\mathrm{cat}} = 0.79 \pm 0.01$ s^{-1} in a), and $K_{\mathrm{M}} = 5.1 \pm 0.3$ mM and $k_{\mathrm{cat}} = 1.3 \pm 0.02$ s^{-1} in b).

amplitude becomes sublinear at large times as shown on Fig. 4.20 a). The initial linear increase of h_p is also measured to last shorter as the reaction speed is increased by working with higher substrate concentrations: h_p is linear for the first 80 s when $S_0 = 3$ mM and only up to 30 s when $S_0 = 50$ mM. This observation is in contradiction with our theoretical estimate for the ending time of the linear phase $t^\star = S_0/k_{\mathrm{cat}}E_0$ in two respects. First we observe that the actual ending time of the linear phase decreases with increasing substrate concentrations which should be the other way around according to $t^\star = S_0/k_{\mathrm{cat}}E_0$. Second, the experimental and predicted order of magnitudes of $t^\star$ do not match. For $S_0 = 50$ mM, we observe an actual ending time of the linear phase around 30 s while it should be around 600 s according to $t^\star = S_0/k_{\mathrm{cat}}E_0$ with $E_0 = 82$ μM and k_{cat} around 1 s^{-1}.

This discrepancy between the observed and predicted time scale $t^\star$ highlights the limits of our model at large times. Amongst the good candidates to explain the premature leveling off of h_p, we can think of the onset of the back reaction $E + P \to I$ which implies a departure of the reaction from a pure Michaelis-Menten scheme [144], or a significant adsorption of the enzyme to the PDMS channel walls so that the actual enzyme concentration available in solution gradually decreases along the downstream direction y [152, 153].

As a result, we expect our model to apply in the very first instants after the reaction start only. This is a strong constraint that we have faced when aiming at fast reactions in droplets since the time window over which our model applies gets shorter and shorter as the reaction speed is increased. This is discussed in the next section.

4.5 Comparison with experiments in droplets

In this section, we use our merging chamber to study fast enzymatic reactions in droplets. To this end, we use our RD model for steady state kinetics which allows us to extract K_{M} and k_{cat} from the reaction front that takes place once the droplets are merged.

We start by presenting our experiments and the raw data we extract. Then, we use our RD model as well as our model for the linear increase of the product amplitude in order to analyze the first instants of the reactions. This allows us to extract measurements for K_{M} and k_{cat} that we compare to reference measurements performed with a plate reader.

4.5.1 Experiments

With our merging device, the time window for observation in the RD regime is 50 s, time during which the detection limit has to be passed for some signal to be detected. Two reactions were tested, both being hydrolyses catalyzed by alkaline phosphatase (AP) which is known to be a fast enzyme [154, 155] with K_{M} in the μM range and k_{cat} in the 100 s^{-1}. The first reaction is the hydrolysis of 4-nitrophenyl phosphate to yield 4-nitrophenol. It is followed by absorption at 405 nm and we achieved a detection limit of 0.1 mM in our device (see the appendix A.2 for the calibration curve) which is well above the expected K_{M}. The second reaction is the hydrolysis of 4-methylumbelliferyl phosphate (denoted MUP) to yield the fluorescent product 4-methylumbelliferone. The detection limit is then around 1 μM which is below the expected K_{M}. We did not have solubility issues at large substrate concentrations $S_0 \gg K_{\mathrm{M}}$ in both cases. To be able to work with initial substrate concentrations around K_{M} we have thus chosen to work with the fluorescent substrate MUP.

A basic experiment consists in merging two droplets using our reaction chamber, one droplet containing the substrate MUP, the other droplet containing the enzyme AP. The buffer is TBS with a pH fixed at 8.0. The formation of the fluorescent product 4-methylumbelliferone is then monitored along the daughter droplet for 50 s. To this end, the fluorophores were continuously excited at 360 nm and their fluorescent signal read at 450 nm using a standard UV lamp and DAPI filters. No shutter was used to limit the exposition of the fluorophores to UV. Three frames were taken per second with an exposure time of 200 ms. This yields experimental pictures as shown on Fig. 4.22 a) with the fluorescent product forming at the interface between the two reservoirs of fresh reagents. Once the intensity is read along the x axis and transposed into a concentration of 4-nitrophenol (see appendix A.3 for the calibration curve), we obtain a space-time diagram of the product concentration as on Fig. 4.22 b).

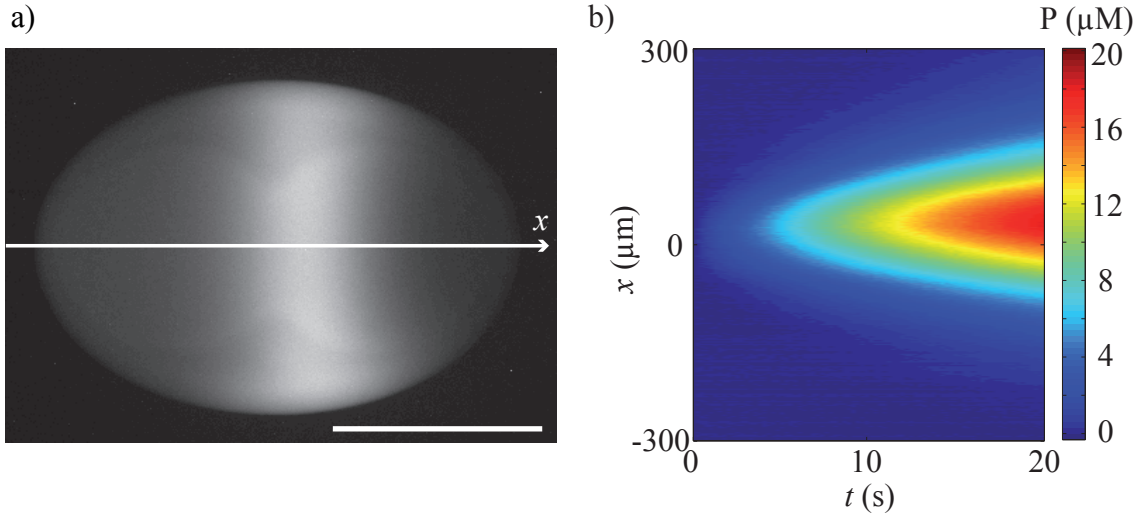

Figure 4.22: a) A droplet containing a solution of MUP at 100 μM (left hand side) has been merged with a droplet containing a solution of AP at 25 nM (right hand side). The photograph is taken at $t = 16$ s. Scale bar is 500 μm. b) The fluorescent signal is read along the x axis to yield a space time diagram. The corresponding calibration curve is shown in the appendix A.3.

4.5.2 Direct fit using DNS

Fitting on K_{M} and k_{cat} using DNS of (4.39a)-(4.39b) was achieved for fairly low reaction speeds, *i.e.* at a low enzyme concentration, and by focusing on the initial instant where the product amplitude is fairly linear. An example of best fit is shown on Fig. 4.23 for which we fixed $E_0 = 25$ nM, $S_0 = 100$ μM, $D_{SP} = 0.6\times 10^{-9}$ m^2/s, $D_{EI} = 0.5\times 10^{-9}$ m^2/s and a time window for fitting of 6.4 s. This fit yields $K_{\mathrm{M}} = 4$ μM and $k_{\mathrm{cat}} = 85$ s^{-1}. The values of the diffusion coefficients have been chosen so that the simulated and the experimental widths of the product profiles fit. Here again, there is a good agreement between experiment and theory for both the product height, width and position, although the model under estimates the width of the product distribution during the first seconds after fusion.

At large times, the experiment and the model stop coinciding mostly because the measured product amplitude becomes sublinear. For instance, in the case with $E_0 = 25$ nM and $S_0 = 100$ μM, we measure that the product amplitude starts leveling off after 7 s (Fig. 4.24). On the other hand, with $K_{\mathrm{M}} = 4$ μM and $k_{\mathrm{cat}} = 85$ s^{-1}, we can estimate $t_M = 0.5$ ms and $t^\star = 48$ s. This observation confirms our observations of the last section of this premature saturation of the product amplitude. Amongst the good candidates that could explain this effect, we can think of:

- A departure of the reaction from the pure Michaelis-Menten scheme. Alkaline phosphatase is indeed inhibited by the free phosphate released as a coproduct of the

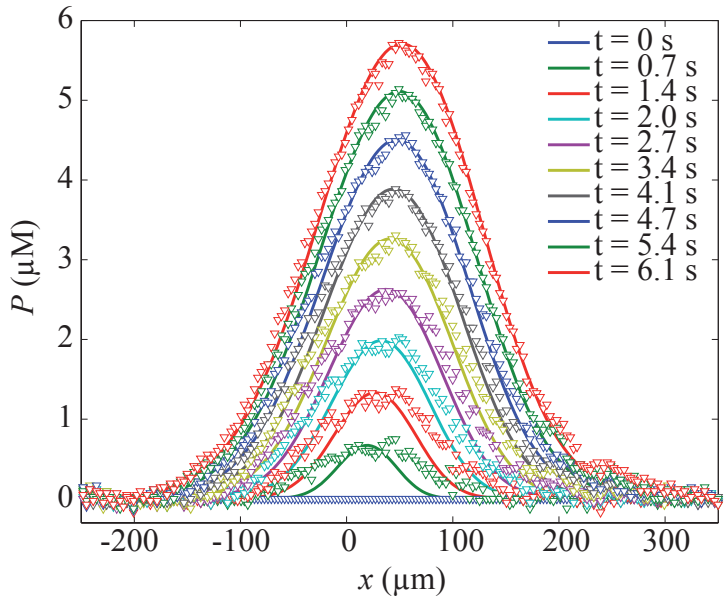

Figure 4.23: Comparison of product profiles measured in droplets with product profiles obtained via DNS of our RD model with $E_0 = 25$ nM, $S_0 = 100$ μM, $D_{SP} = 0.6\times 10^{-9}$ m^2/s, $D_{EI} = 0.5\times 10^{-9}$ m^2/s, $K_\mathrm{M} = 4$ μM and $k_\mathrm{cat} = 85$ s^{-1}.

reaction [156]. As a result, the larger the amount of free phosphates, the lower the amount of free active enzymes, and hence the reaction slows down.

- The decrease in the amount of enzyme molecules available in solution could also be induced by the adsorption of the enzyme onto the droplet interface. Ismagilov *et al.* have ruled out this option by showing that AP does not adsorb onto a water/FC40 interface covered with a perfluorinated OEG based surfactant (using a pendant drop experiment and a steady state kinetics assay). In my opinion, this option could still apply in our experiments as we did not use the exact same surfactant (we used a perfluorinated PEG based surfactant) at a very low concentration of 0.1 % (w:w) so that the coverage of the interface by the surfactant molecules might be imperfect.

- Photobleaching of the fluorophores could also be invoked. Indeed, the fluorescent product 4-methylumbelliferone is prone to photobleaching. We measured its time constant to be around 300 s (see appendix A.3 for the curves). This issue is also readily addressed by developing a time sharing unit to limit the time exposition of the fluorophores to UV.

Anyhow, we decided to focus on the very first instants after reaction start during which our model applies, and to avoid the complications arising at large times. However, as the reaction speed is increased, by increasing the enzyme or the substrate concentration, the linear phase gets shorter and shorter so that fitting the whole space-time diagram of $P(x,t)$ is not amenable anymore. Instead, we can extract the initial slope of the product

amplitude and use our model for h_p to measure K_{M} and k_{cat} at varying E_0 and S_0.

Hereafter, we start by confirming our self-similar model for $P(x,t)$ and use to extract K_{M} and k_{cat} from initial slope measurements.

4.5.3 Fit on the product amplitude

In the first place, we use the values of K_{M} and k_{cat} obtained from our fit on the full product profile shown on Fig. 4.23 in order to confirm our self-similar model for $P(x,t)$ in the case of enzymatic reactions held in droplets. We thus fix $K_{\mathrm{M}} = 4$ μM, $k_{\mathrm{cat}} = 85$ s^{-1} and $S_0 = 100$ μM as well as $D_{SP} = 0.6\times 10^{-9}$ m^2/s and $D_{EI} = 0.5\times 10^{-9}$ m^2/s. As shown on Fig. 4.24 a), our predictions for the amplitude of the product compare well with the actual initial slopes of the amplitudes we measured at varying enzyme concentration E_0. In addition, the product shape functions are also in good agreement as shown on Fig. 4.24 b) in the case $E_0 = 25$ nM and $S_0 = 100$ μM. This confirms the validity of our model during the first seconds after the reaction starts in droplets.

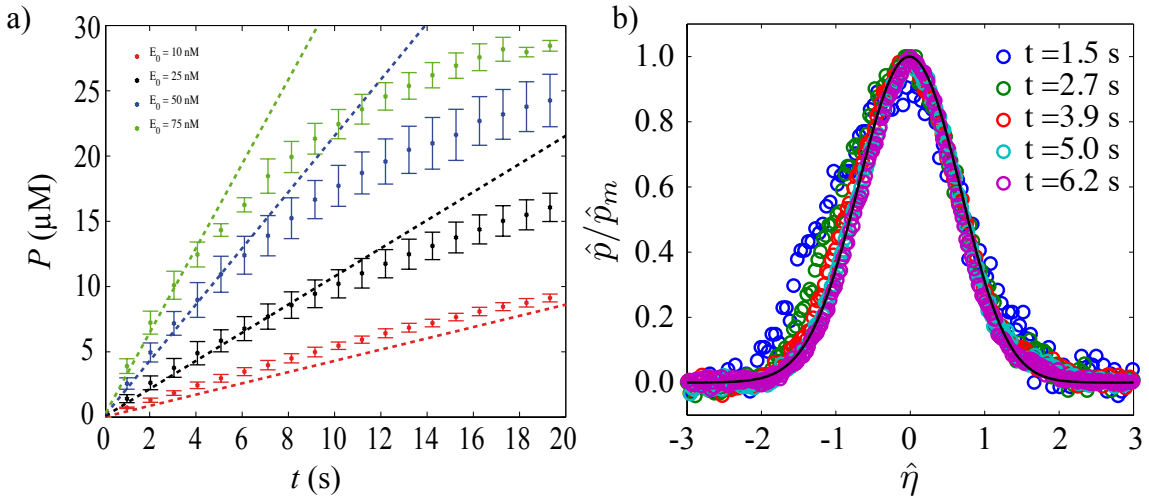

Figure 4.24: Reduced model. $E_0 = 25$ nM, $S_0 = 100$ μM, $D_{SP} = 0.6\times 10^{-9}$ m^2/s, $D_{EI} = 0.5\times 10^{-9}$ m^2/s, $K_{\mathrm{M}} = 4$ μM, $k_{\mathrm{cat}} = 85$ s^{-1}

Nonetheless, best fits of the product amplitude are achieved for different values of the steady state parameters K_{M} and k_{cat} which highlights the dispersion of our measurement of K_{M} and k_{cat} when using our merging device.

To extract a good measurement of these two parameters *i.e.* representative of our complete set of experiments, we choose to first extract the initial slope for each experiment, and fit this set of slopes against S_0 and E_0 using our model for V_0^{RD} in a second time:

$$V_0^{\mathrm{RD}} = k_{\mathrm{cat}} E_0 \hat{p}_m \tag{4.44}$$

with $\hat{p}$ the solution of (4.42a) and $\hat{p}_m$ the maximum value of $\hat{p}$. Two sets of experiments were performed, one with E_0 fixed at 100 nM and S_0 varied from 1 μM up to 100 μM, the other with S_0 fixed at 100 μM and E_0 varied from 10 nM up to 100 nM.

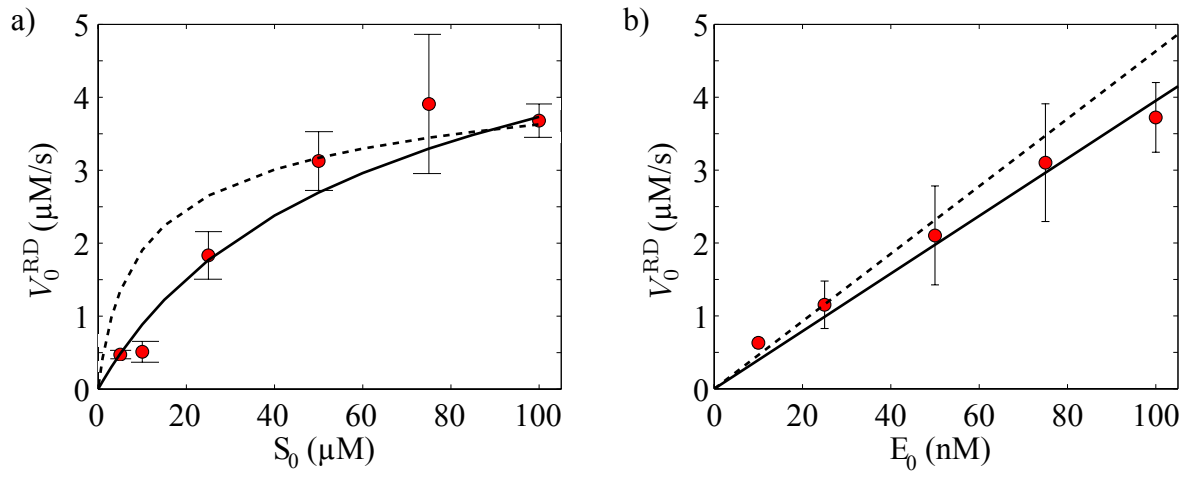

Figure 4.25: Evolution of the initial slope of the product amplitude against a) the initial enzyme concentration and b) the initial substrate concentration.

Resulting measurements of the initial slope of the product amplitude V_0^{RD} are shown on Fig. 4.25 with red dots. On this figure, the dashed lines correspond to the prediction of V_0^{RD} using our model (4.44) with the values $K_\mathrm{M} = 4$ μM, $k_\mathrm{cat} = 85$ s^{-1} obtained in the last subsection. On the other hand, the solid lines correspond to best fits of V_0^{RD} against S_0 (Fig. 4.25 a)) or E_0 (Fig. 4.25 b)) with our self-similar model. These fits yield $K_\mathrm{M} = 34 \pm 0.28$ mM and $k_\mathrm{cat} = 150 \pm 1$ s^{-1} in the case of V_0^{RD} against S_0, and $K_\mathrm{M} = 4.14 \pm 0.28$ mM and $k_\mathrm{cat} = 70 \pm 1$ s^{-1} in the case of V_0^{RD} against E_0. Here again, margin of error on our measurements are obtained by taking the value of either K_M or k_cat at which the residue increases by 1% from its miminum value. We also performed a reference measurement in the plate reader which yields $K_\mathrm{M} = 3.84 \pm 0.02$ mM and $k_\mathrm{cat} = 10.8 \pm 0.1$ s^{-1} (see appendix A.3).

All these measurements of K_M and k_cat are not in full agreement. They correspond to different rounds of experiments performed with different solutions of reagents, at different working concentrations (this is especially true for the plate reader experiment for which E_0 is in the pM range) and on different days. The difference between the values of K_M and k_cat we obtained is presumably due to varying degrees of enzyme viability from one batch to another, as well as the lack of precise temperature control for both the on chip and the plate reader experiments. To confirm this assumption, a control experiment at a fixed temperature that uses the exact same solutions in both the reference method and droplets should be designed.

4.6 Discussion of Chapter 4

In this last chapter we used our device that pairs droplets on demand to study enzyme kinetics on different time scales. Slow enzymatic reactions are studied using standard steady state kinetics. To this end, we used our parallelized chip which allows us to test six different conditions on a single chip. Once merged, the drops are mixed either using an outer flow of oil, or passively by diffusion. The product formation is then monitored and we have demonstrated that standard Michaelis-Menten theory allows us to measure accurately kinetics parameters such as K_{M}, k_{cat} or K_{I}. In its present form, our chip is nonetheless complex as it is connected to eight different inputs. Increasing the number of conditions to be tested therefore requires to generate the different formulations on chip which is a current topic of research in our group.

On the fast reactions side, we have derived a RD model for steady state kinetics. The steady state assumption for the intermediate complex was shown numerically to apply at every positions along the daughter droplet for times between $t_{\mathrm{M}} = 1/k_{\mathrm{on}}S_0$ and $t^\star = S_0/k_{\mathrm{cat}}E_0$. This allows us to reduce our general four species problem on E, S, I and P, to a two species problem on S and P only. In the limit of $S_0 \gg E_0$ we also found a self-similar solution for $P(x,t)$ which allows us to derive a model for the amplitude of $P(x,t)$. Then, we have performed two sets of experiments to which we compared our theoretical predictions. As a benchmark, we started with the study of a slow reaction in a T-shaped channel for which we showed that our RD model yields accurate measurements of K_{M} and k_{cat}. In addition, we have demonstrated that monitoring the product amplitude over time is sufficient to extract both K_{M} and k_{cat}. This has proven very useful when we turned our attention to the study of a fast enzymatic reaction in droplets using our merging device. Working within droplets has indeed proved more challenging. Fitting on the full space-time diagram $P(x,t)$ was demonstrated for relatively slow reactions. In order to take into account the dispersion of our measurements in droplets, we have chosen to fit on the initial slope of the product amplitude against either E_0 or S_0. This protocol yields values of K_{M} and k_{cat} in partial agreement.

Overall, we have validated experimentally our RD model for steady state kinetics using a T shaped channel. Within droplets we have faced further complications as the reaction speed was increased. These complications can be addressed by changing our detection technique. Indeed, a lower detection limit would allow us to decrease the working concentrations of both the substrate and the enzyme which has two great advantages. First, as the reaction speed is decreased the linear increase of the product amplitude should last longer. Second, we could use the exact same solutions in droplets and in the plate reader in order to test a reaction in the same conditions using both our merging chamber and the plate reader. However, the trade off between space-time resolution and the sensitivity of the detection technique would certainly have to be reconsidered. Indeed, sub-μM detection limit are usually achieved by a long time integration and by increasing the light density at the measurement site using a tight focused laser or a high magnification objective [157].

While the time resolution can be preserved, the space resolution is lost as most of this technique rely on point measurements. An integrated model based on a space-averaging of our local model should thus be derived when aiming at a sub-μM detection.

Conclusion

The purpose of my PhD project was the study of biochemical reactions using droplet microfluidics with a close focus on enzyme kinetics. In my opinion, the main achievements of this work are threefolds.

First, we have developed different strategies to build addressable arrays of droplets. This has been achieved through the combination of two techniques to manipulate droplets, namely the rails and anchors to passively guide and trap droplets [42] and a mobile laser spot to actively select a drop within an array [34]. We have demonstrated the strength of this approach on three examples by selectively extracting drops from an array, selectively placing droplets in an array and selectively triggering a chemical reaction in an array of paired droplets.

Second, we designed an innovative platform to pair droplets without the need to continuously flow the outer phase. Instead, we used gradients of confinements only to produce, propel and trap droplets. Thus, different inner phases can be connected in parallel to the same 2D microchannel and injected sequentially to build well organized arrays of distinct pairs of droplets where each droplet has been addressed to a trap. As a result, many different reactions under varying conditions can be tested on a single chip. In addition, holding droplets stationary allows us to monitor them precisely, thereby extracting high quality data from the evolution over time of the drops content. Experimentally, we used our parallelized chip to reproduce standard enzymatic assays on chip by measuring steady state parameters K_{M} and k_{cat} as well as an inhibition constant K_{I}.

Third, we developed a reaction-diffusion framework to analyze the reaction front that takes place when two droplets are merged in our device. This work is built on the pioneer work of Gálfi and Rácz [21] which focused on the case of a one step bimolecular reaction. After having investigated, both theoretically and experimentally, the different regimes of product formation that arise in the later case, we turned our attention to the case of enzyme catalyzed reactions following a Michaelis-Menten scheme. Here again, different regimes of product formation arise. We chose to focus our analyses on the case where the intermediate complex is stationary and confirmed our theoretical findings experimentally. This allowed us to measure steady state kinetics parameters K_{M} and k_{cat} of fast enzymatic reactions using minute amounts of reagents.

This work has been achieved through a close interplay between experimental, numerical and experimental investigations. Further developments can be done for each of these three investigations.

On the theoretical side, the case of enzymatic reactions has great promises. To my knowledge, the diffusion limited regime, when the reaction follows a Michaelis-Menten scheme, has indeed not been studied yet, while more complex reaction schemes, involving product inhibition or burst kinetics for instance, should be investigated in order to cope with more realistic enzymatic reactions.

On the numerical side, improvements of our finite differences code can be done by implementing an adaptive mesh [158] and a more efficient time stepping method [159]. The former improvement would allow us to refine the mesh at the front location at all times as it displaces, while the later would allow us to decrease the computation time.

On the experimental side, our parallelized chip has a great potential to perform many different reactions on a single chip. To this end, I believe that dilution should be embeded on chip in order to limit the number of connecting points to the chip. A very nice approach was suggested by Miller *et al.* to this end which makes use of Taylor-Aris dispersion to create a gradient of concentration and "freezes" this gradient into droplets using a flow focuser. When using gradients of confinement to generate drops as sketched on Fig. 4.26, we could make a pulse of substrate in a long thread of a buffer solution, create a gradient using Taylor-Aris dispersion, and atomize the gradient into droplets using many side channels ending in a large reservoir. Thereby, a few hundreds of different substrate concentrations could be tested on chip in parallel.

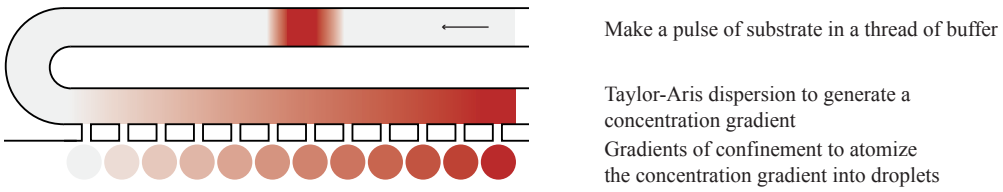

Figure 4.26: Gradients of confinements to store a concentration gradient within droplets

Finally, gradients of confinement could also be used to formulate highly precisely the content of a drop which is of prime interest to test the dose response of the activity of an enzyme in a complex environment with different substrates and inhibitors. As sketched on Fig. 4.27, this could be achieved by routing small droplets from different inlets toward an anchoring site, merge the bunch of small droplets once the desired formulation is obtained, and pair the resulting larger droplet with a drop containing the enzyme.

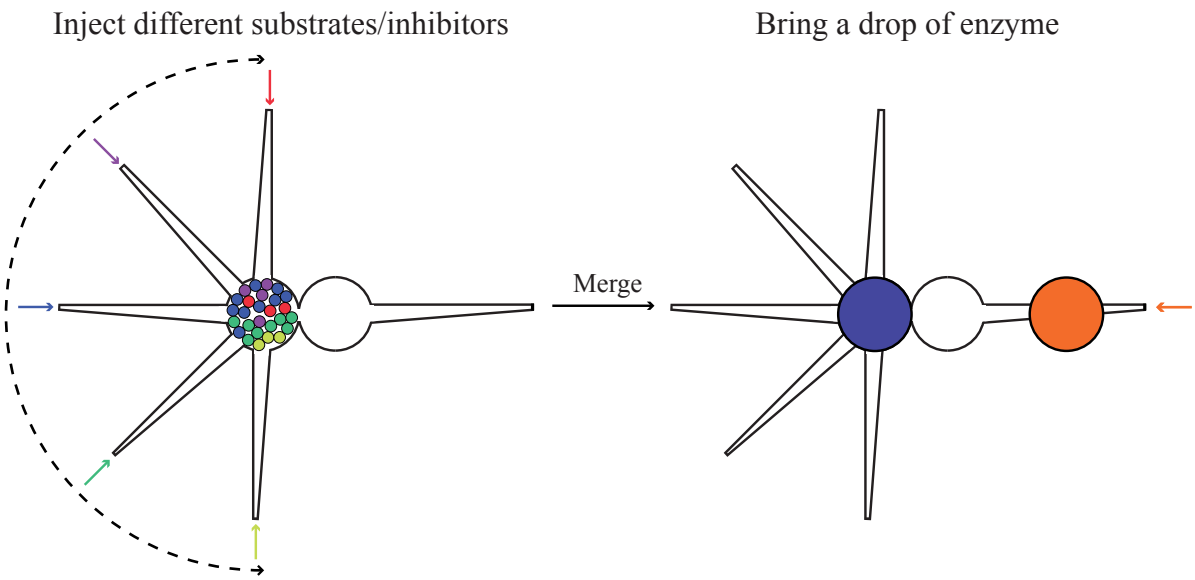

Figure 4.27: Gradients of confinement to precisely formulate the content of a drop with many species.

In conclusion, we are confident that the different tools to handle droplets and monitor chemical reactions presented in this manuscript can lead to numerous applications in biochemistry in the near future.

Appendix A

Calibration curves and plate experiments

In this appendix we present the different reference measurements we performed, either in the plate reader to get values of kinetic parameters, or in microchannels to calibrate the gray levels or the fluorescent intensities we were recording.

A.1 Reduction of DCPIP by L-ascorbic acid

This reaction is studied in Chapter 3. We verified that Beer's law applies for this reaction in order to convert the gray levels into concentrations of DCPIP. We thus measured the absorbance (OD stands for optical density) across a 185 μm thick microchannel (*i.e* with the same height as our test section) using our detection setup at varying concentrations of DCPIP.

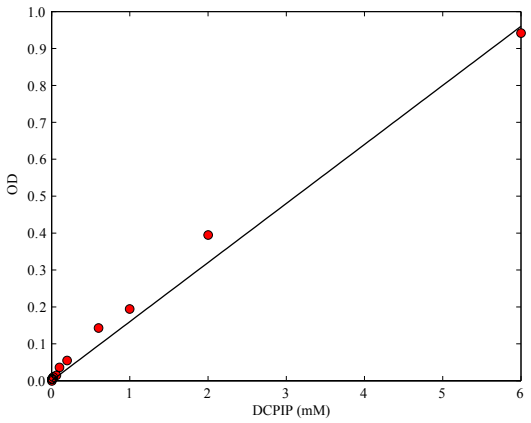

Figure A.1: Absorbance as a function of the concentration of DCPIP which is varied from 1 μM up to 6 mM. The solid line is $y = 0.16x + 0.03$.

As shown on Fig. A.1, the absorbance is effectively linear with the concentration of DCPIP in agreement with Beer's law. From the slope we can also extract the molar extinction coefficient $\epsilon = 8378$ $M^{-1}cm^{-1}$ of DCPIP in our conditions.

A.2 Hydrolysis of 4-nitrophenyl β-D-glucopyranoside

This reaction is studied in Chapter 4. The measurements below have been done with Christopher Bayer. We performed reference measurements of K_M, k_{cat} and the IC50 of the inhibitor DNM (1-deoxynojirimycin hydrochloride) using a plate reader. As shown on Fig. A.2 a), the measured OD is linear with the concentration of 4-nitrophenol for concentrations in the hundreds of μM range. This calibration curve yields an extinction coefficient of 4-nitrophenol $\epsilon = 16400$ $M^{-1}cm^{-1}$ with a path length of 0.5 cm. With this calibration, we measured the initial slope of the product formation traces with $E_0 = 0.1$ μM and S_0 varying between 1 and 30 mM in the plate reader. This yields the Michaelis-Menten curve shown on Fig. A.2 b) where the dashed line corresponds to the best fit obtained for $K_M = 8.26 \pm 0.06$ μM and $k_{cat} = 0.241 \pm 0.002$ s^{-1}. Then, we turned our attention to the inhibition of β-D-glucosidase by DNM. We fixed $E_0 = 0.1$ μM and $S_0 = 23$ mM and varied the initial concentration of inhibitor from 0 up to 1500 nM. This yields the inhibition curve shown on Fig. A.2 c) from which we measured IC50 = 238 $\pm$ 1 nM.

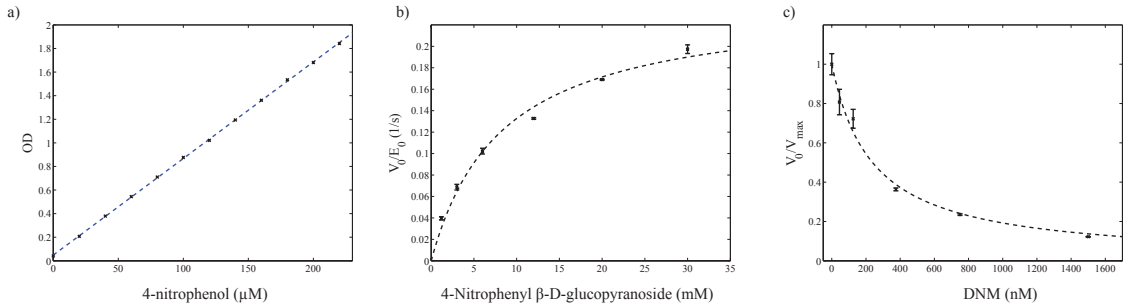

Figure A.2: a) Calibration curve. Dashed line: $y = 0.0082x + 0.0483$. b) Michaelis-Menten curve. The dashed line is $y = k_{cat}x/(K_M + x)$ which yields $K_M = 8.26 \pm 0.06$ μM and $k_{cat} = 0.241 \pm 0.002$ s^{-1}. c) Inhibtion curve. The dashed line is $y = 1/(1 + x/IC50)$ which yields IC50 = 238$\pm$1 nM

We also calibrated the gray levels of our camera in a 185 μm thick microchannel. As shown on Fig. A.3, Beer's law does not applies at relatively large substrate concentration. Instead, we have fitted our experimental points with $y = a(1 - e^{-bx})$.

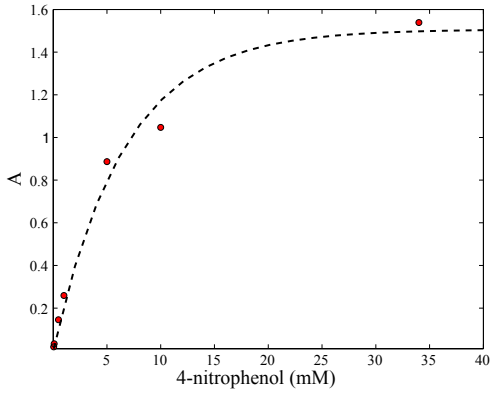

Figure A.3: Calibration curve in a 185 μm thick microchannel. OD versus concentration of 4-nitrophenol. The dashed line is $y = 1.5\,(1 - e^{-0.15x})$.

A.3 Hydrolysis of 4-Methylumbelliferyl phosphate

This reaction is studied in Chapter 4. We first performed reference measurements of K_{M} and k_{cat} using a plate reader. Our calibration curve shown on Fig. A.2 yields the extinction coefficient of 4-methylumbelliferone $\epsilon = 4800\ \mathrm{M}^{-1}\mathrm{cm}^{-1}$. Next, we measured the steady state kinetic parameter of our reaction as shown on Fig A.2 b). We obtain $K_{\mathrm{M}} = 3.84 \pm 0.02\ \mu\mathrm{M}$ and $k_{\mathrm{cat}} = 10.78 \pm 0.05\ \mathrm{s}^{-1}$.

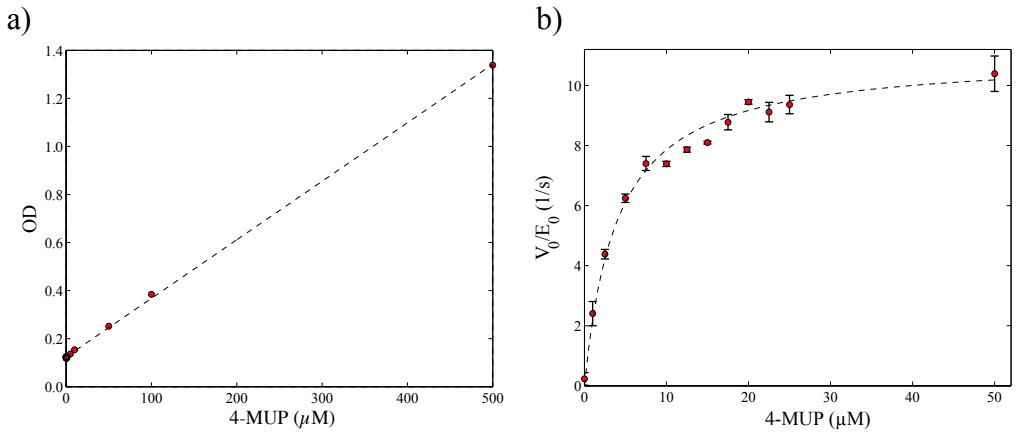

Figure A.4: a) Calibration curve of 4-methylumbelliferone in the plate reader. The dashed line is $y = 0.0024x + 0.1241$. b) Michaelis-Menten curve. The dashed line is $y = k_{\mathrm{cat}}x/(K_{\mathrm{M}} + x)$ which yields $K_{\mathrm{M}} = 3.84 \pm 0.02\ \mu\mathrm{M}$ and $k_{\mathrm{cat}} = 10.78 \pm 0.05\ \mathrm{s}^{-1}$

Next, we have calibrated the fluorescent levels using our detection setup in microchannel as shown on Fig. A.6.

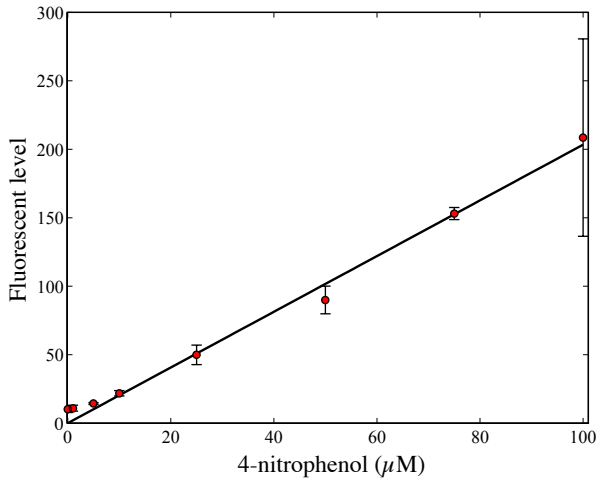

Figure A.5: Calibration curve in a 185 μm thick microchannel. Fluorescent intensity versus concentration of 4-methylumbelliferone. The solid line is $y = 2x$

Finally, we estimated the photobleaching constant of 4-methylumbelliferone by recording over time the decrease in fluorescence of a drop containing 4-methylumbelliferyl phosphate at 100 μM. Once fitted with $y = e^{-t/\tau}$, the photobleaching constant is found to be $\tau \approx 300$ s which is well above our 50 s long time window for observation in RD.

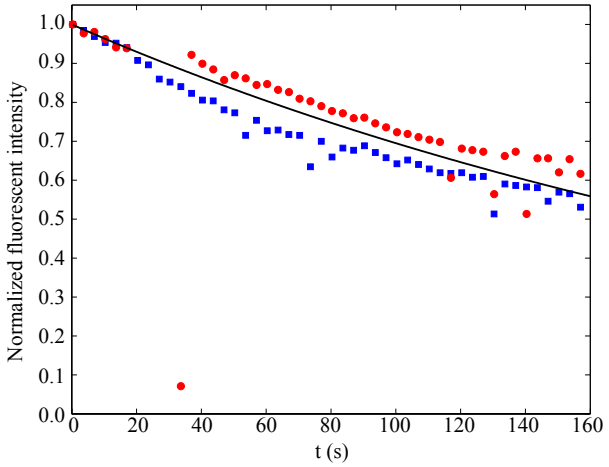

Figure A.6: Normalized fluorescent levels over time of a drop of 4-methylumbelliferyl phosphate at 100 μM. The colored dots correspond to two repeats of the same experiment. The solid line is $y = e^{-t/275}$.

Appendix B

Numerical methods

Here we describe the two numerical methods we used to analyze RD fronts. The finite differences code has been written with Xavier Garnaud. The code for Broyden's method has been written with Sébastien Michelin.

B.1 Finite differences code

We want to solve numerically our RD problem with the reagent initially separated. We consider here the case of a one step reaction. For enzymatic reactions, the source term only changes. In dimensionless form, the problem to be solved is:

$$\frac{\partial \hat{a}}{\partial \hat{t}} = \frac{\partial^2 \hat{a}}{\partial \hat{x}^2} - \hat{a}\hat{b} \tag{B.1a}$$

$$\frac{\partial \hat{b}}{\partial \hat{t}} = \frac{\partial^2 \hat{b}}{\partial \hat{x}^2} - \hat{a}\hat{b} \tag{B.1b}$$

$$\frac{\partial \hat{c}}{\partial \hat{t}} = \frac{\partial^2 \hat{c}}{\partial \hat{x}^2} + \hat{a}\hat{b} \tag{B.1c}$$

with $\hat{a}$, $\hat{b}$, $\hat{c}$ subjected to the following initial and boundary conditions:

$$\hat{a} = \hat{H}(\hat{x} \leq 0) \qquad \hat{b} = \hat{\phi}\ \hat{H}(\hat{x} \geq 0) \qquad \hat{c} = 0 \tag{B.2}$$

and

$$\frac{\partial \hat{a}}{\partial \hat{x}} = \frac{\partial \hat{b}}{\partial \hat{x}} = \frac{\partial \hat{c}}{\partial \hat{x}} = 0 \quad \text{at } \hat{x} = \pm\ \sqrt{\mathrm{Da}} \tag{B.3}$$

Matrix formulation and non-uniform mesh

We start by writing the set of equations (B.1a)-(B.1c) using matrices and we distinguish the linear part coming from the diffusion operator $\hat{L}$ and the non linear part $\hat{G}(\hat{q})$ coming

from the chemical source and sink terms:

$$\frac{\partial \hat{q}}{\partial \hat{t}} \;=\; \hat{L}\hat{q} \;+\; \hat{G}(\hat{q}) \tag{B.4}$$

with:

$$\hat{q} = \begin{bmatrix} \hat{a} \\ \hat{b} \\ \hat{c} \end{bmatrix} \qquad \hat{L} = \begin{bmatrix} \frac{\partial^2}{\partial \hat{x}^2} & 0 & 0 \\ 0 & \frac{\partial^2}{\partial \hat{x}^2} & 0 \\ 0 & 0 & \frac{\partial^2}{\partial \hat{x}^2} \end{bmatrix} \qquad \hat{G}(\hat{q}) = \begin{bmatrix} -\hat{a}\hat{b} \\ -\hat{a}\hat{b} \\ \hat{a}\hat{b} \end{bmatrix}, \tag{B.5}$$

The equation (B.4) is parabolic and can thus be solved iteratively. We now need to discretize it, define a numerical scheme yielding a recurrence relation, and a time stepping procedure. As we impose that the reagents are initially separated, sharp gradients of concentrations form near the front, especially at early times. As a result, resolving these gradients requires a high mesh density near the reaction front, while the mesh density can be lowered away from the front, where profiles are flat. Fortunately, we know that the front is at $\hat{x} = 0$ at early times. Hence we just need to increase the mesh density in this region.

Mesh refinement consists in mapping a physical space $(\hat{x}, \hat{t})$ where mesh points are oddly distributed, with a computing space $(\hat{\xi}, \hat{\tau})$ where mesh points are evenly distributed. Mathematically, this is a change of variable:

$$\hat{x} \;=\; f(\hat{\xi}) \tag{B.6a}$$
$$\hat{t} \;=\; \hat{\tau} \tag{B.6b}$$

where f can be chosen so that it concentrates mesh points in the physical space around the reaction front. The equation (B.4) is a formulation of the problem (B.1a)-(B.1c) in the physical space $(\hat{x}, \hat{t})$. We need to rewrite this equation in the computing space $(\hat{\xi}, \hat{\tau})$ by expressing $\hat{D}_{\hat{x}} = \partial/\partial\hat{x}$ in terms of $\hat{D}_{\hat{\xi}} = \partial/\partial\hat{\xi}$. This is done by the chain rules:

$$\frac{\partial \hat{s}}{\partial \hat{x}} \;=\; \frac{\partial \hat{\xi}}{\partial \hat{x}}\frac{\partial \hat{s}}{\partial \hat{\xi}} \;=\; \frac{1}{f'(\hat{\xi})}\frac{\partial \hat{s}}{\partial \hat{\xi}} \;\Rightarrow\; \hat{D}_{\hat{x}} \;=\; \frac{1}{f'(\hat{\xi})}\hat{D}_{\hat{\xi}} \tag{B.7a}$$

$$\frac{\partial^2 \hat{s}}{\partial \hat{x}^2} \;=\; \frac{\partial}{\partial \hat{x}}\left(\frac{1}{f'(\hat{\xi})}\frac{\partial \hat{s}}{\partial \hat{\xi}}\right) \;\Rightarrow\; \hat{D}^2_{\hat{x}} \;=\; -\frac{f''(\hat{\xi})}{f'(\hat{\xi})^3}\hat{D}^2_{\hat{\xi}} \;+\; \frac{1}{f'(\hat{\xi})^2}\hat{D}_{\hat{x}} \tag{B.7b}$$

In practice, we worked with:

$$f(\hat{x}) \;=\; \sqrt{\mathrm{Da}}\left(\left(-\frac{3}{2} + \frac{b}{2} + a\right)\hat{\eta}^5 + \left(\frac{5}{2} - \frac{b}{2} - 2a\right)\hat{\eta}^3 + a\hat{\eta}\right); \tag{B.8a}$$

which allows us to choose the values of f and its first derivatives at the edge of the domain and at $\hat{x} = 0$ (see Fig. B.1).

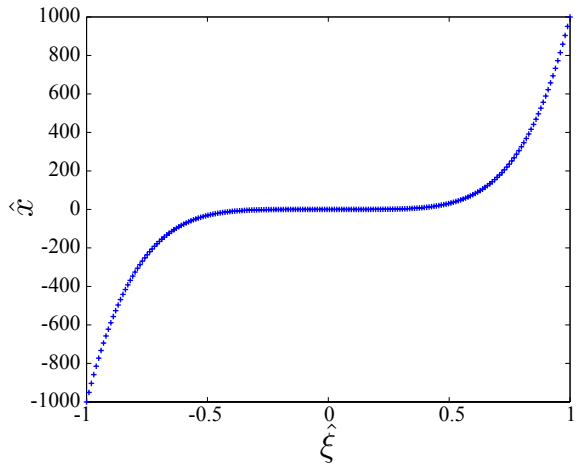

Figure B.1: Refined mesh used to resolve the reaction zone at early time. Here $a = 10^{-4}$, $b = 5$ and $\mathrm{Da} = 10^6$

IMEX scheme

Next, we need to choose a numerical scheme to discretize the equation (B.1a)-(B.1c). Sharp gradients of concentrations, present especially at early times, make the linear term $\hat{L}\hat{q}$ stiff. When treated explicitly, stiff terms require the use of small time steps, limited by the space increment size through the CFL condition. This invites us to treat this term implicitly as linear terms can be inverted efficiently. On the other hand, we do not want to treat the non linear part $\hat{G}(\hat{q})$ implicitly as its non linearity makes it inefficient to invert. We thus treat $\hat{G}(\hat{q})$ explicitly which yields an overall IMEX scheme (IMplicit-EXplicit scheme).

We want to estimate (B.4) at the time $n + 1/2$ with a second order accuracy in both space and time. The linear part $\hat{L}\hat{q}$ of the right hand side of (B.4) is estimated using a Crank-Nicolson approximation:

$$[\hat{L}\hat{q}]^{n+1/2} \approx \frac{\hat{L}\hat{q}^{n+1} + \hat{L}\hat{q}^{n}}{2} + o(\Delta\hat{t}^2) \tag{B.9}$$

where centered finite differences are used for the discretization of the operator $\hat{L}$ in the computing space. The non linear part $\hat{G}(\hat{q})$ of the right hand side of (B.4) is computed explicitly by interpolation of G at $n-1$, n and $n+1/2$. This is the Adams-Brashford method:

$$[\hat{G}(\hat{q})]^{n+1/2} \approx \frac{3}{2}\hat{G}(\hat{q}^n) - \frac{1}{2}\hat{G}(\hat{q}^{n-1}) + o(\Delta\hat{t}^2) \tag{B.10}$$

From that we obtain a relation between $\hat{q}^{n-1}$, $\hat{q}^n$ and $\hat{q}^{n+1}$:

$$\frac{\hat{q}^{n+1} - \hat{q}^n}{\Delta\hat{t}} = \frac{\hat{L}\hat{q}^{n/1} + \hat{L}\hat{q}^{n}}{2} + \frac{3}{2}\hat{G}(\hat{q}^n) - \frac{1}{2}\hat{G}(\hat{q}^{n-1}) \tag{B.11}$$

which yields the recurrence relation:

$$\hat{q}^{n+1} = \hat{A}^{-1}\hat{B}\hat{q}^n + \frac{3}{2}\hat{A}^{-1}\hat{G}(\hat{q}^n) - \frac{1}{2}\hat{A}^{-1}\hat{G}(\hat{q}^{n-1}) \tag{B.12}$$

with:

$$\hat{A} = (\frac{1}{\Delta\hat{t}} - \frac{1}{2}\hat{L}) \qquad \hat{B} = (\frac{1}{\Delta\hat{t}} + \frac{1}{2}\hat{L}) \tag{B.13}$$

Thanks to this recurrence relation, we can start from the initial conditions we impose and walk in time to deduce later times.

Adaptive time stepping

By treating the stiff term $\hat{L}\hat{q}$ implicitly, we can adapt the time step $\Delta\hat{t}$ to the actual stiffness of the problem at a given time point, and thus increase $\Delta\hat{t}$ once the initial sharp gradients have been smoothed out by diffusion. The time stepping procedure consists in comparing the value of $\hat{q}^{n+1}$ given by the recurrence relation (B.12) to an estimation $\hat{q}^\star$ of $\hat{q}^{n+1}$ based on an interpolation of $\hat{q}^n$ and $\hat{q}^{n-1}$. When these two estimations of $\hat{q}^{n+1}$ are not too far from each other, the time step is increased, while if their distance δ exceeds a given threshold the time step is decreased. Fig. B.2 shows a cartoon of the time stepping procedure.

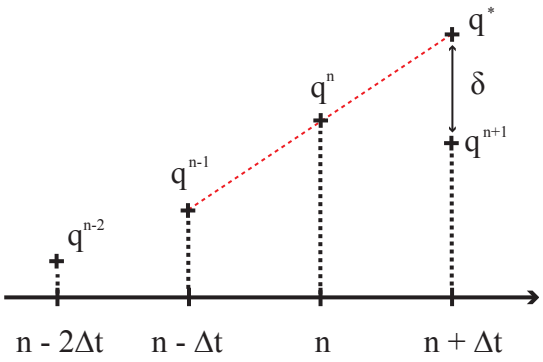

Figure B.2: Time stepping procedure

B.2 Broyden's method for non linear ODEs

Here after we explain Broyden's method on an example extract from the paper by Gálfi and Rácz [21]. The problem to be solved is:

$$G''(z) - G^2(z) - KzG(z) = 0 \tag{B.14}$$

$$G(z \to -\infty) \to -Kz \tag{B.15}$$

$$G(z \to -\infty) \to 0 \tag{B.16}$$

Once discretized, this problem becomes a set of N algebraic equations, N being the number of points of the mesh. Formally, this can be written as:

$$F(G) = 0 \tag{B.17}$$

where F is a discretized version of the ODE (B.14) with the boundary conditions being included in the conditions on g_1 and g_N:

$$F(G) = \begin{cases} \dfrac{g_2 - g_1}{h} + K \\ \dfrac{g_3 + g_1 - 2g_2}{h^2} - K z_2 g_2 - g_2^2 \\ ... \\ \dfrac{g_N + g_{N-2} - 2g_{N-1}}{h^2} - K z_{N-1} g_{N-1} - g_{N-1}^2 \\ g_N \end{cases} \tag{B.18}$$

The next step consists in finding the value $G^\star$ of $G = (g_1, ..., g_N)$ which minimizes $F(G)$.

1D case

When $G = g_1$, the problem is simple. We look for $G^\star$ so that:

$$F(G^\star) = 0 \tag{B.19}$$

Starting from an initial guess for G, denoted G_0, we can develop F around G_0:

$$F(G_0 + dG) = F(G_0) + dG \cdot F'(G_0) \tag{B.20}$$

This gives a second value of G, denoted $G_1 = G_0 + dG$, closer to $G^\star$:

$$G_1 = G_0 - \frac{F(G_0)}{F'(G_0)} \tag{B.21}$$

Then, successive iterations yield a better estimation of $G^\star$.

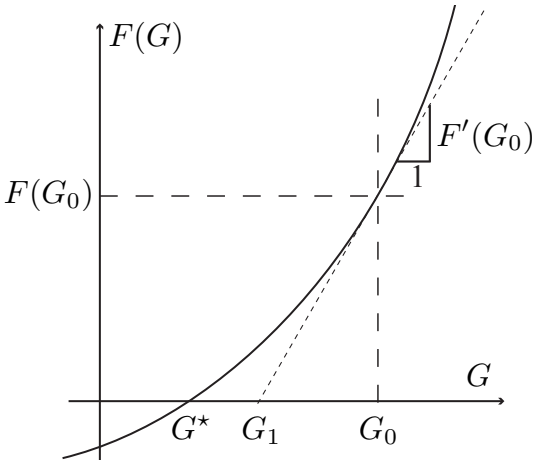

Figure B.3: Descent method in 1D.

ND case

When $G = (g_1, ..., g_N)$, the approach remains the same but Jacobian matrices must be used instead of standard derivatives. This reads as:

$$G_1 \;=\; G_0 - \boldsymbol{J_0^{-1}} F(G_0) \tag{B.22}$$

As the number of mesh points N increases, the rank of the Jacobian matrix $\boldsymbol{J}$ increases and inverting $\boldsymbol{J}$ becomes time consuming.

Broyden's method

Instead of inverting $\boldsymbol{J}$ at each iteration, Broyden's method suggests to invert it once at the first iteration, and then deduce the later values of $\boldsymbol{J^{-1}}$ by interpolation through the Broyden's formula:

$$\boldsymbol{J_1^{-1}} \;=\; \boldsymbol{J_0^{-1}} + \frac{(G_1 - G_0) - \boldsymbol{J_0^{-1}}\,(F(G_1) - F(G_0))}{(G_1 - G_0)\,\boldsymbol{J_0^{-1}}\,(F(G_1) - F(G_0))}\,(F(G_1) - F(G_0)) \tag{B.23}$$

Again, successive iterations then yield $G^\star$.

Appendix C

Early times reaction front position for one step reactions

In this appendix, we detail the derivation for the expression of the reaction front position in the early times limit described in section 3.4. The reaction front position is defined as the first moment of the reaction rate $\hat{r} = \hat{a}\hat{b}$ with $\hat{a}$ and $\hat{b}$ the dimensionless concentrations of A and B:

$$\hat{x}_f \;=\; \frac{\displaystyle\int_{-\infty}^{+\infty} \hat{x}\hat{r}d\hat{x}}{\displaystyle\int_{-\infty}^{+\infty} \hat{r}d\hat{x}} \tag{C.1}$$

In the early times limit, $\hat{a}$ and $\hat{b}$ are also expanded in powers of $\hat{t}$:

$$\hat{a}(\hat{x},\hat{t}) \;=\; \hat{\mathbf{a}}_0(\hat{\eta}) \;+\; \hat{t}\;\hat{\mathbf{a}}_1(\hat{\eta}) \;+\; t^2\;\hat{\mathbf{a}}_2(\hat{\eta}) \;+\; ... \tag{C.2a}$$

$$\hat{b}(\hat{x},\hat{t}) \;=\; \hat{\mathbf{b}}_0(\hat{\eta}) \;+\; \hat{t}\;\hat{\mathbf{b}}_1(\hat{\eta}) \;+\; t^2\;\hat{\mathbf{b}}_2(\hat{\eta}) \;+\; ... \tag{C.2b}$$

Hence $\hat{r}$ has also an expansion in powers of $\hat{t}$:

$$\hat{r} \;=\; \hat{\mathbf{a}}_0\hat{\mathbf{b}}_0\;\hat{t}^0 \;+\; \left(\hat{\mathbf{a}}_0\hat{\mathbf{b}}_1 + \hat{\mathbf{a}}_1\hat{\mathbf{b}}_0\right)\;\hat{t}^1 \;+\; ... \tag{C.3}$$

where we showed in section 3.3 that:

$$\hat{\mathbf{a}}_0 \;=\; \frac{1}{2}\mathrm{erfc}\left(\hat{\eta}\right) \;\text{ and }\; \hat{\mathbf{b}}_0 \;=\; \frac{\hat{\phi}}{2}\mathrm{erfc}\left(-\hat{\eta}\right) \tag{C.4}$$

Then, injecting (C.3) into (C.1) yields:

$$\hat{x}_f \;=\; 2\,\frac{\displaystyle\int_{-\infty}^{+\infty} \hat{\mathbf{a}}_0\hat{\mathbf{b}}_0\;\hat{\eta}d\hat{\eta}}{\displaystyle\int_{-\infty}^{+\infty} \hat{\mathbf{a}}_0\hat{\mathbf{b}}_0 d\hat{\eta}}\;\hat{t}^{1/2} \;+\; 2\,\frac{\displaystyle\int_{-\infty}^{+\infty} \left(\hat{\mathbf{a}}_0\hat{\mathbf{b}}_1 + \hat{\mathbf{a}}_0\hat{\mathbf{b}}_1\right)\;\hat{\eta}d\hat{\eta}}{\displaystyle\int_{-\infty}^{+\infty} \hat{\mathbf{a}}_0\hat{\mathbf{b}}_0 d\hat{\eta}}\;\hat{t}^{3/2} \;+\; \mathcal{O}(\hat{t}^{5/2}) \tag{C.5}$$

The first term of the right hand side of (C.5) is always 0 since $\hat{\mathbf{a}}_0\hat{\mathbf{b}}_0\ \hat{\eta}$ is an odd function of $\hat{\eta}$. This is consistent with the symmetric case $\hat{\phi} = 1$ but not with the case $\hat{\phi} \neq 1$. As a result, we need to estimate the second term of the right hand side of (C.5). To this end, we inject the expansion of $\hat{a}$ and $\hat{b}$ into the conservation laws:

$$\frac{\partial \hat{a}}{\partial \hat{t}} = \frac{\partial^2 \hat{a}}{\partial \hat{x}^2} - \hat{a}\hat{b} \tag{C.6a}$$

$$\frac{\partial \hat{b}}{\partial \hat{t}} = \frac{\partial^2 \hat{b}}{\partial \hat{x}^2} - \hat{a}\hat{b} \tag{C.6b}$$

and look for $\hat{\mathbf{a}}_1$ and $\hat{\mathbf{b}}_1$. This yields:

$$\hat{\mathbf{a}}_1'' + 2\hat{\eta}\hat{\mathbf{a}}_1' - 4\hat{\mathbf{a}}_1 - 4\hat{\mathbf{a}}_0\hat{\mathbf{b}}_0 = 0 \quad \text{with} \quad \hat{\mathbf{a}}_1(\pm\hat{\eta}) = 0 \tag{C.7a}$$

$$\hat{\mathbf{b}}_1'' + 2\hat{\eta}\hat{\mathbf{b}}_1' - 4\hat{\mathbf{b}}_1 - 4\hat{\mathbf{a}}_0\hat{\mathbf{b}}_0 = 0 \quad \text{with} \quad \hat{\mathbf{b}}_1(\pm\hat{\eta}) = 0 \tag{C.7b}$$

The equations (C.7a)-(C.7b) can be solved using Broyden's method. Finally, when $\hat{\phi} < 1$, we obtain to leading order:

$$\hat{x}_f = 0.51\ \hat{t}^{3/2} \tag{C.8}$$

Appendix D

Published papers

- Etienne Fradet, Craig McDougall, Paul Abbyad, Rémi Dangla, David McGloin and Charles N. Baroud. Combining rails and anchors with laser forcing for selective manipulation within 2D droplet arrays. *Lab on a Chip*, 2011, 11, 4228-4234.
- Rémi Dangla, Etienne Fradet, Yonatan Lopez and Charles N. Baroud. The physical mechanisms of step emulsification. *J. Phys. D: Appl. Phys.*, 2013, 46, 114003.
- Etienne Fradet, Paul Abbyad, Marten H. Vos and Charles N. Baroud. Parallel measurements of reaction kinetics using ultralow-volumes. *Lab on a Chip*, 2013.

Lab on a Chip

View Online / Journal Homepage
Dynamic Article Links

Cite this: DOI: 10.1039/c1lc20541b

www.rsc.org/loc

PAPER

Combining rails and anchors with laser forcing for selective manipulation within 2D droplet arrays†

Etienne Fradet,[a] Craig McDougall,[b] Paul Abbyad,[c] Rémi Dangla,[a] David McGloin[b] and Charles N. Baroud*[a]

Received 21st June 2011, Accepted 26th September 2011
DOI: 10.1039/c1lc20541b

We demonstrate the combination of a rails and anchors microfluidic system with laser forcing to enable the creation of highly controllable 2D droplet arrays. Water droplets residing in an oil phase can be pinned to anchor holes made in the base of a microfluidic channel, enabling the creation of arrays by the appropriate patterning of such holes. The introduction of laser forcing, *via* laser induced thermocapillary forces to anchored droplets, enables the selective extraction of particular droplets from an array. We also demonstrate that such anchor arrays can be filled with multiple, in our case two, droplets each and that if such droplets have different chemical contents, the application of a laser at their interface triggers their merging and a chemical reaction to take place. Finally by adding guiding rails within the microfluidic structure we can selectively fill large scale arrays with monodisperse droplets with significant control over their contents. In this way we make a droplet array filled with 96 droplets containing different concentrations of fluorescent microparticles.

1 Introduction

Performing a set of independent reactions in a two-dimensional (2D) array format is a standard approach for implementing a large number of parallel assays. This is the case for instance in multi-well plates, DNA or protein chips, and many other genomic technologies. Droplet microfluidic techniques have aimed to replicate such a 2D format in recent years, since the ability to keep a drop stationary allows the long term observation of its contents, in addition to providing combinatorial measurements on a single image. Patterning a 2D area with different droplets is straightforward when using surface microfluidic manipulations, *e.g.* through electro-wetting[1] or surface acoustic waves.[2] More classical drop deposition techniques have also been used to produce arrays of distinct droplets for combinatorial enzymatic studies[3] or for polymerase chain reaction (PCR).[4]

Producing arrays of droplets in microchannels has proved more challenging, in part due to the standard methods for forming drops: both T-junctions and flow-focusing devices rely on the presence of a strong flow of the carrier fluid,[5] so that holding the drops in an array requires a method to stop their motion against the outer flow. This has been achieved through innovative designs of the microfluidic geometries and operating protocols, leading to different methods to array drops: quasi-2D arrays were formed by winding a linear path in the plane of the microchannel. Drops flowed in series in this microchannel and were blocked at particular locations, for example by having side pockets in the channel,[6,7] by flowing the drops into parallel dead-end microchannels,[8] or into parallel corrugated channels.[9] These devices however suffer from strong droplet interactions since the drops are tightly confined into linear motion by the channel walls, which can make their operation difficult. Some authors reduced these interactions by increasing locally the channel width and depth.[10] Real 2D arrays, in which droplet interactions are weak, were formed by placing obstacles in a wide microchannel[11] and the obstacles could be designed to hold one, two or more drops.[12,13]

More recently, Abbyad *et al.*[14] demonstrated the manipulation of drops in 2D by using *rails* and *anchors*, which correspond to grooves that are etched on the surface of the microchannel. In this approach, drops are squeezed by the top and bottom boundaries of the microchannel, which increases their surface energy. By partially entering into the grooves, the drop reduces its surface energy. This creates a gradient of surface energy at the edge of the grooves, which leads to an attractive force pulling it into the region with larger depth. This was used to guide drops along linear paths (a *rail*) or to hold them stationary in an *anchor*.[14]

The current challenge is therefore to pattern a 2D area with a heterogeneous droplet population, either by selectively placing a drop at the desired location, selectively extracting a drop, or selectively initiating a chemical reaction. To date, none of the methods for arraying drops allow for such controlled operations.

[a]*Laboratoire d'Hydrodynamique (LadHyX) and Department of Mechanics, Ecole Polytechnique, CNRS, 91128, Palaiseau, France. E-mail: baroud@ladhyx.polytechnique.fr*
[b]*Electronic Engineering and Physics Division, University of Dundee, Nethergate, Dundee, DD1 4HN, UK*
[c]*Laboratoire d'Optique et Biosciences (LOB), Ecole Polytechnique, INSERM U696, CNRS, 91128 Palaiseau, France*
† Electronic supplementary information (ESI) available. See DOI: 10.1039/c1lc20541b

Instead, random filling is used in most cases and there exists no mechanism for selectively extracting a particular drop. While random distribution of drops can yield useful information in the case of two droplet species,[13] it quickly becomes limiting when there are many species to be studied simultaneously. Here we demonstrate how the controlled filling, extraction, or reactions can be performed by combining the *rails* and *anchors* approach with the selective manipulation through laser-induced local heating:[15–17] The *rails* and *anchors* provide a passive, robust and simple 2D guidance and trapping of drops, while the mobile laser spot adds an intelligent and versatile selectivity.

After the materials and methods section (Section 2), we turn to the physical ingredients that determine the different forces in Section 3. This is followed by demonstrations of drop extraction in Section 4. Filling an array with a controlled drop population is then demonstrated by showing how to build an array of drops which displays a gradient of concentration (Section 5). Finally, we demonstrate how to trigger local reactions on demand (Section 6).

2 Materials and methods

Microfluidic device fabrication

All experiments were conducted in PDMS microchannels (Dow Corning Sylgard 184) sealed onto glass slides by plasma bonding. The fabrication procedure relies on dry film photoresist soft lithography techniques[18] which enable rapid prototyping of multi-level structures. The multilayer masters were etched in stacks of Eternal Laminar E8013 and Eternal Laminar E8020 negative films (of thickness 35 $\pm$ 2 μm and 50 $\pm$ 2 μm respectively) depending on the desired thickness of the main channel and patterns.

The successive steps were the following: (i) photoresist layers were successively laminated onto a clean glass slide using a PEAK Photo Laminator (PS320) at a temperature $T = 100\ ^{\circ}C$ until the desired height h of the main channel was reached; (ii) The photoresist stack was exposed to UV (Hamamatsu Lightningcure LC8) through a photomask of the base channel (comprising a test section, droplet generation devices and entrance and exit channels); (iii) Additional photoresist layers were laminated on top of the exposed stack until the desired depth p of the patterns (anchor holes and/or rails) was reached; (iv) The stack of photoresist films was exposed again to UV, through the second photomask featuring only the patterns to be added onto the base channel. Finally, the full structure was developed by immersion in an aqueous bath of carbonate potassium at 1% mass concentration.

Furthermore, in order to render the internal channel surface hydrophobic, a surface treatment was applied: A dilute solution of 1*H*,1*H*,2*H*,2*H*-perfluorodecyltrichlorosilane (Sigma-Aldrich) in FC40 oil (3M Fluorinert) (20 μL in 1 mL of FC40) was flowed through the microchannel for approximately 5 min. The channel was then rinsed with pure FC40 to remove the residue chemicals remaining in the bulk.

Chip design and operation

The common architecture of the microfluidic chip was a base channel with a blank 'test section' onto which rail and anchor patterns were etched. The base channel consisted of one (Sections 4–5) or two (Section 6) droplet generation devices discharging into a wide main test section. The system then emptied into a single outlet channel. The height of the base channel h was 100 μm everywhere. Channels upstream of the test section had widths ranging from 100 to 200 μm. The test section was a rectangle of dimensions 10 $\times$ 3 mm (Sections 4 and 6) or 20 $\times$ 4.5 mm (Section 5).

Various patterns of rails and anchors could then be added onto the base test section depending on the desired applications. Section 4 relied on a regular square array of small circular holes of diameter $d = 50$ μm and depth $p = 35$ μm. For Section 6, only two rows of holes with a diameter $d = 200$ μm were used. The pattern designed for Section 5 was a complex combination of rails, ranging in width from 50 μm to 200 μm, combined with square anchors of 120 μm a side.

Throughout the study, the continuous phase was FC40 oil (3M Fluorinert) of viscosity $\mu = 4.1$ cP containing fluorinated surfactants for both emulsion stabilization and improvement of the wetting conditions. Experiments described in Sections 4 and 5 used a Krytox (Dupont) ammonium salt,[19] at 0.5% mass concentration, while those in Section 6 used a PEG-based surfactant at 0.01% mass concentration.[19] Two inlets of oil were required: one at a flow rate Q_o for the droplet generation and one at a flow rate Q_e to adjust droplet entrainment in the test section independently of the droplet generation.

Different aqueous solutions were used as the dispersed phase and were injected at a flow rate Q_w: Section 4 uses pure water droplets; in Section 5 a solution of water containing fluorescent beads (Invitrogen green fluorescent beads, 1 μm) at a volume fraction of 0.4%. In Section 6, the two aqueous solutions consisted of a solution of $FeCl_3$ at 0.27 M and a solution of KSCN at 0.8 M. The interfacial tension γ between a pure water drop and the FC40 solution was measured to be $\sim$20 mN m^{-1}. We observed however that the contents of the drops, such as the chemicals of Section 6 or the fluorescent beads, could have an impact and reduce this value in some cases.

A system of computer controlled syringe pumps (Cetoni neMESYS) was used to control the different flow rates (Q_w, Q_o and Q_e) in real time.

Optical setup and laser operation

The optical arrangement employed for droplet manipulation makes use of a 1480 nm continuous wave infrared laser source (Fitel Furukawa FOL1424) and a commercial inverted microscope system (Nikon TE2000) equipped with epifluorescent illumination (Exfo X-cite 6210C). A pair of galvanometric mirrors (Cambridge Technologies 6210H) permitted beam positioning in the microchannels to be controlled by a mouse click using in-house Labview programs. Following the galvanometric mirror, the laser beam was both expanded appropriately (to overfill the back aperture of the microscope objective) and relayed to the back aperture of the objective by a 4f conjugate lens system and an appropriate dichroic mirror (OCTAX). The laser power was measured to be 200 mW in the focal plane of the microscope objective. The described system provided an approximately diffraction limited spot at the focal plane whose position was readily computer controlled by the user. A camera

was used to image the field of view *via* a sideport and record monochrome video at typical frame rates of 60 frames per second (Photron Fastcam 1024 PCI). Alternatively, a digital SLR camera (Nikon D70) was used to capture color images *via* the front camera port of the microscope. Whilst the laser spot wavelength was outside the range of both cameras, the spot location was visible as a dark shadow on the computer screen.

3 Physical ingredients

Guiding and trapping drops in our devices are based on manipulating three forces of different physical origins, as sketched in Fig. 1: The force due to the surface patterning F_γ, the entrainment force due to the flow of the outer fluid F_d, and the force due to the laser heating F_l. Below we discuss the main attributes of each of these forces.

Force due to surface patterning

The surface energy of a droplet can be written as $E_\gamma = \gamma A$, where γ is the interfacial energy and A the surface area of the droplet. While γ can be considered as nearly constant over the course of an experiment, A can vary significantly as the droplet changes its shape. An unconfined drop will take a spherical shape in order to minimize its surface area while the confinement can be used to force the drop to take a flattened "pancake" shape of height nearly equal to the microchannel height h. In the plane of the microchannel, one can describe the drop by its radius R; in the case when $R \gg h$, the main contribution to the surface area is given by the top and bottom boundaries of the droplet and we can write $A \simeq 2\pi R^2$, with a small correction due to the area around the drop in the vertical direction.

When the channel height is locally modified, for instance by etching a groove into one of the surfaces, the drop enters into the groove. This always leads to a reduction of the total surface area of the drop,[20] thus reducing its surface energy. Removing the drop from the region of low surface energy therefore requires a force F_γ, whose magnitude is given by the gradient of the energy and always pointing towards the energy minimum. Dangla *et al.*[20] estimate this anchoring force as $\gamma \Delta A/d$, where ΔA is the difference in surface area between the drop over the groove and away from it, and d is a characteristic length scale over which the energy changes. They measure forces in the range of 100–600 nN for similar geometries to the ones presented here.

For a circular groove, a geometric calculation shows that F_γ does not depend on the drop size in the case when $R \gg h$. This is not the case however in the case of a rail, where F_γ scales linearly with the drop radius R.

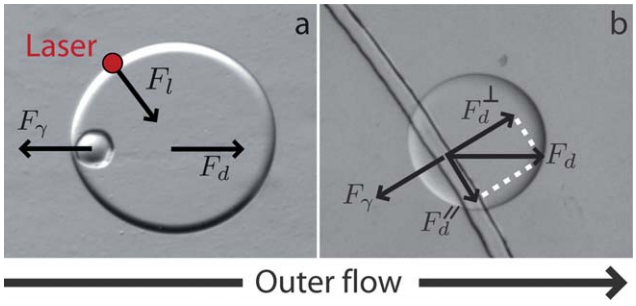

Fig. 1 Forces acting on a drop in the presence of surface patterning: The anchoring force due to the surface patterning F_γ, the drag force due to the flow of the outer fluid F_d, and the force due to the laser heating F_l. (a) The case of an anchor. (b) In the case of a rail, the unbalanced force due to the drag parallel to the rail F_d'' leads to motion along this direction.

Force due to the outer flow

The flow of the outer fluid applies a drag force F_d on the droplet through hydrodynamic drag. This force is always directed in the direction of motion of the outer fluid. Its magnitude scales as $F_d \sim \mu_o U R^2/h$, where μ_o is the outer fluid viscosity and U is the velocity of the outer fluid. F_d therefore increases with the flow velocity and depends strongly on the size of the droplet.

For given drop and channel geometries, we can measure a critical velocity beyond which $F_d > F_\gamma$ at which point the drop cannot be held anymore. For velocities below this critical velocity, a drop in an anchor is deformed from its circular shape (Fig. 1(a)). Conversely, a drop that is in a rail is pushed along the rail due to the existence of a component in the tangent direction F_d'' of the drag force (Fig. 1(b)). Once the critical velocity is reached, drops cannot be held anymore and they are de-pinned by the outer flow.[14] An important regime concerns velocities that are slightly below the critical velocity. In this regime, the anchor strength is sufficient to hold one droplet stationary but not two, since the net drag force experienced by the touching pair increases while the anchoring force remains constant. Abbyad *et al.*[14] identified a range of velocities where drops enter into a 'buffering' mode, in which an incoming drop replaces the drop that was previously anchored. This buffering regime will be used below to determine the occupation of anchor sites in the experiments.

Force due to the laser heating

The final force F_l that we must consider is due to the localized heating by a focused laser.[21] When the water–oil interface is heated locally, variations in surface tension lead to the creation of a flow along the interface, which in turn leads to flow inside and outside the droplet.[16] The net effect on the droplet is a "pushing" force, by which the laser heating forces the droplet away from the laser position. This has been used in one-dimensional (1D) microchannels to sort or buffer drops, or change the order in which they flow.[17] The magnitude of F_l was measured[21] in confined microchannels to be in the range of 100–300 nN. Verneuil *et al.* also observed that the contributions to the force are dominated by the flows along the thin films between the drop and the lateral channel walls, which implied that the force depended on the drop size in that case.[21] Finally, the direction of the force due to the laser heating is determined by the direction of the thermo-capillary flows. In the case studied by Verneuil *et al.*,[21] the presence of surfactants in the continuous phase implied that laser produced a repulsive force, by inducing anomalous thermo-capillarity. There are however no measurements of the magnitude or size dependence of F_l in the absence of lateral walls.

4 Extracting a drop from an array of holes

The force balance described above can now be used to selectively remove a drop from an anchor site, by adding the laser-induced force to the drag force from the fluid flow. An example implementation is shown in Fig. 2 and in ESI movie S1.† In this experiment, drops are initially formed in a flow-focusing geometry and flowed into the test section, which is patterned with a square lattice of holes. Some drops become anchored at the hole positions, filling the lattice in a random fashion. The water flow is then stopped and the oil flow rate is held constant at Q_o = 2 μL min^{-1}.

Once the lattice is filled (Fig. 2(a)), the laser focus is selectively positioned within the test section. If the laser is focused inside the droplet, it can remove it from the anchor. This allows the user to select a position on the computer screen and to remove the corresponding drop at that particular position. The oil flow rate then transports the drop away from the array and out of the microchannel (Fig. 2(b)). Fig. 2(c) shows an 'X' pattern formed using this method.

This device can be operated in two different regimes. In the current regime, small anchors and a weak oil flow rate are used, therefore requiring a high laser power (P_{laser} = 200 mW) to remove the drops. Alternatively, lower laser powers can be used by increasing the flow rate to work closer to the critical anchoring velocity. In that case however, extracted drops interact with their neighbours and can lead to a buffering mode, in which drops downstream of the extracted drop also get unpinned.

5 Selectively filling an array

Here, the ability to sort and subsequently fill a two-dimensional array with droplets of a uniform size is presented. The methodology is again based upon the combination of creative chip design, which combines rails and anchors of different strengths, and highly localised laser induced forcing for derailing the drops. By superimposing anchors onto rails, droplets may be guided directly to the anchor sites where they become trapped on these 'storage rails'. The presented method involves first selectively filling these storage rails and then allowing the droplets to assemble into the desired array by entering into a buffering mode through an increase of the carrier oil flow rate.

To construct an array of droplets, we use a chip test section composed of 6 rails, each of which is periodically superimposed with 16 anchor sites, producing a 96 drop array. The rail sorting portion of this test section is shown in Fig. 3(a) which demonstrates active switching of droplets between rails, achieved by employing laser-induced forces as described above. In the absence of the laser, droplets are guided along the central rail to the exit of the chip by default. The selective derailing operation is demonstrated in Fig. 3(b) and ESI movie S2.† To fill the array, rails are filled in sequence, row by row, beginning with the right-most junction to the left-most junction. Any order can be used however, even working on a drop-by-drop basis.

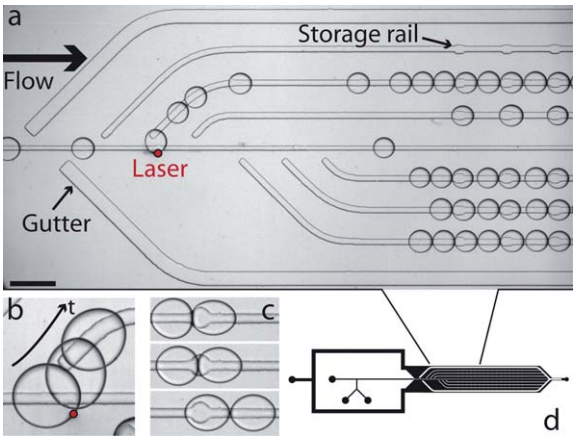

Fig. 3 (a) Test region (20 × 4.5 mm, h = 100 μm) for building an array of droplets. All rails are 50 μm deep. The central default rail is 50 μm wide. The side gutter rails used to filter out large droplets are 200 μm wide. The 6 storage rails are 75 μm wide and the anchor sites superimposed on these rails are 120 μm squares. The image shows the fifth rail being filled (see movie S2 for full sequence†). The scale bar is 600 μm. (b) Superposition of three images showing a drop leaving the default rail into a storage rail. (c) Once the storage rails are filled the entrainment flow rate Q_e is increased to initiate a buffering mode whereby the droplets self arrange into an array of one droplet trapped at each anchor site. (d) A schematic of the complete chip design illustrates the droplet formation portions of the chip relative to the test region.

Selective filling of the array, in addition to anchoring the drops in place, depends upon several key design features which are highly sensitive to droplet size. Consequently, the device geometry is constructed specifically for a given droplet size. For this experiment the chips (shown in Fig. 3(d)) are designed for droplets of a 150 μm radius.

The first of these features is designed to ensure that all droplets placed on the array are of the same size. Such steps are necessary, as droplet monodispersity is not guaranteed for transient stages of droplet production, nor for all flow rates. Droplets are only placed in the array when the laser is used to direct them there. Furthermore, droplets below the size of interest cannot be derailed from the central rail, due to the limit on the maximum deflection achievable with the employed laser power. Small

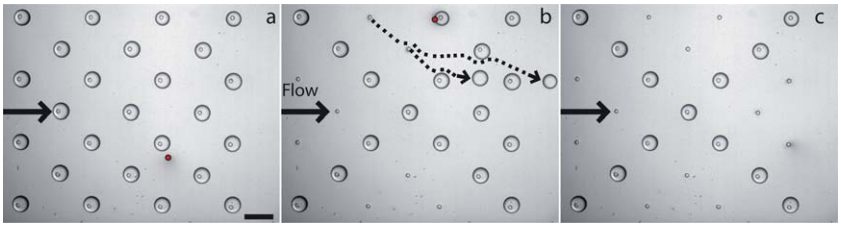

Fig. 2 Selectively extracting drops. (a) The array of holes (d = 50 μm and p = 35 μm) is initially filled with water drops. (b) The laser is focused on the water–oil interface, pushing the drops out of the anchor. (c) An X is patterned with the remaining droplets. Scale bar is 400 μm.

droplets are therefore guided out of the chip and never reach the storage rails. To ensure droplets of a size larger than those under study are also eliminated, two side gutters are placed upstream and redirect large droplets along the side of the test section. Therefore, large droplets are prevented from entering the array portion of the chip as the gutter rails provide an energetically favorable alternative route. These features ensure that only droplets of the desired size are available for active laser forcing onto the array rails.

The remaining features are concerned with filling the storage rails. Once a droplet passes the two side gutters, it enters the rail switching area and is available for sorting into the storage rails containing square anchor sites. As can be seen in Fig. 3(b), the storage rails have been designed to be wider than the central guide rail and there is a gap between the storage rails and the central default rail. This intentional gap is to avoid junction sites, where the local width reaches a maximum value. This leads to junctions behaving as anchor sites from which drops cannot be removed. Upon deflection by the laser, the droplet sees the wider side rail as an energetically favorable route and leaves the default rail as illustrated in both Fig. 3(b) and ESI movie S2.†

Once sorted onto the storage rails, the droplet encounters anchor sites and becomes trapped. The dimensions of the anchors have been chosen for the given droplet radii so that they may hold one droplet parked stationary against the mean flow. However, the anchor site is intentionally too weak to hold multiple droplets stationary. Consequently, under the correct external flow conditions the droplets will enter into a buffering regime. It is noteworthy that whilst the storage rails are being filled with droplets, the apparent channel cross section available for the oil to flow through decreases due to the stationary droplets. Such a reduction causes an increase in the velocity that must be taken into account when filling the anchor sites, to prevent all the droplets from being swept out of the array. Therefore, the entrainment oil flow rate Q_e is reduced from 40 to 20 μL min^{-1} during the filling period as the storage rails become populated, while the small oil (Q_o) and water (Q_w) flow rates are maintained at a steady 0.5 and 0.18 μL min^{-1} respectively. This ensures that all rails are completely filled with monodisperse droplets during the filling procedure. Once this procedure is completed, the entrainment flow rate Q_e is increased slowly to 70 μL min^{-1} to initiate the desired droplet buffering regime (Fig. 3 (c)). Under these conditions arrays of 96 droplets may be constructed in a controlled manner at a rate of approximately 1 min per rail for droplet sorting and a further minute for droplet buffering into a complete array.

Whilst maintaining the droplet size for a given chip design, this methodology may be extended to droplets of varying composition. An example of such a controlled filling appears in Fig. 4, where an array of 96 anchored droplets with an increasing concentration of fluorescent beads is shown. In the chip used here, a mixer was positioned before the T-junction used for droplet formation, allowing the composition of the droplets to be altered in time. To modify the composition of the droplets, a stream of pure water is mixed with a concentrated bead solution in pure water (0.4% by volume). For the various rails of the array, the ratio of pure water to bead solution is altered by varying the relative flow rates whilst maintaining an overall flow rate of 0.18 μL min^{-1} for the mixture. This ensures that the

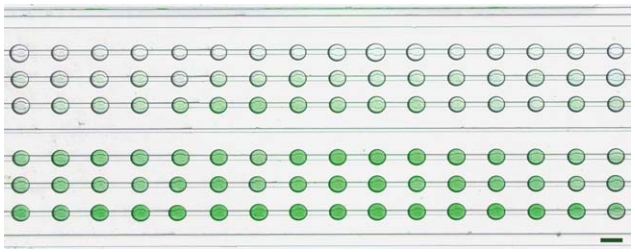

Fig. 4 A superposition of bright-field and fluorescent images of a 96 anchor array. The droplet composition has been altered from pure water to a solution of water and green fluorescent beads to create a gradient. The droplet volume is 7 nL each. The scale bar is 300 μm.

droplets are of uniform size. For the top rail, droplets are composed entirely of pure water and the flow rate of the bead solution is set to zero. For each row, moving down the array, the flow rate of the bead solution is increased in 0.005 μL min^{-1} increments whilst the water rate is decreased by the same amount.

The filling protocol begins with the top rail, which is filled with droplets containing pure water. The laser is then removed, causing all droplets to follow the default central path to the drain. The droplet composition is then altered to the concentration required for the next rail and allowed to reach a steady state before filling of that rail commences. To do so we translate the laser to the correct position for the new rail and direct droplets into the storage rail. Once the rail is filled with droplets, the laser is again removed and the droplet composition altered. The remaining storage rails are filled in this stepwise manner, changing the droplet formation specifically for each rail and using the laser to position the droplets onto the rails.

6 Controlled initiation of chemical reactions at anchor sites

Our final demonstration of the power of the technique is to carry out the loading of two droplets into the anchor sites and then use laser induced merging of droplets to enable controlled chemical reactions within selected droplet pairs. This can be done at a location predefined by the anchor position and it indicates the potential of this method as an analysis and assaying tool.

We make use of an array of anchors in the chip test section. A key point here is that the anchor holes are designed to be twice as wide as the droplet diameters, so that each can accommodate two droplets. In this situation, where the holes are larger than the droplet, an outer flow rate of 80 μL min^{-1} removes one drop per trap while in the experiment presented in Section 4, an outer flow rate of 10 μL min^{-1} detaches all the drops.

To initiate a chemical reaction we must load droplets with different contents into each hole site. We choose droplets with $FeCl_3$ and KSCN, which react to form a colored liquid from two colorless ones. We begin by generating one species of droplets from the top flow focusing junction and fill the anchor sites (Q_o^{top} = 7 μL min^{-1}, Q_w^{top} = 0.1 μL min^{-1}). Initially this leads to two droplets occupying each anchor site, since the holes are twice as big as the droplets (Fig. 5(a + b) and supplementary movie S3†). We then increase the oil flow rate (Q_o^{top} = 80 μL min^{-1}, Q_w^{top} = 0 μL min^{-1}) to wash out one of each pair, thus leaving one

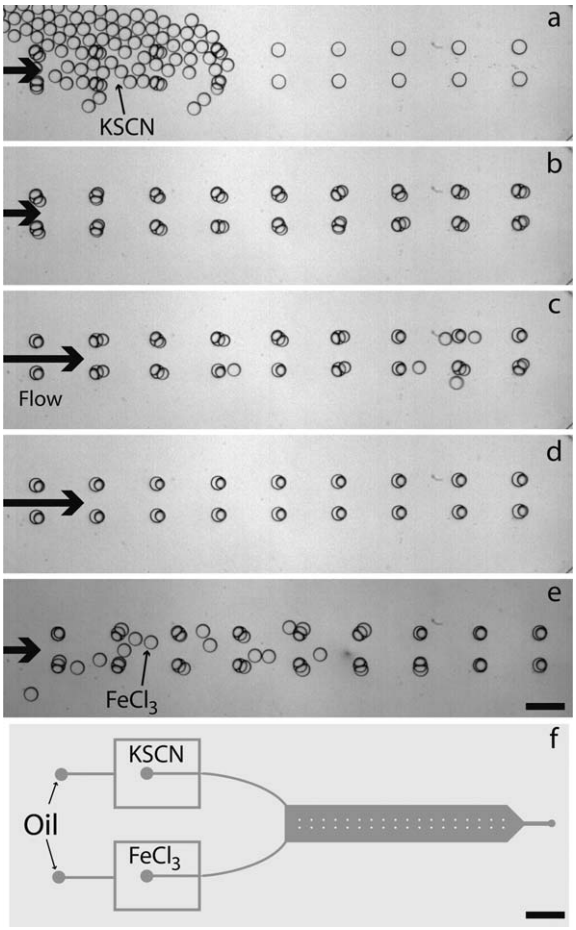

Fig. 5 (a + b) Filling first species into anchor holes. (c + d) Emptying one droplet from each trap to leave one drop per anchor site. (e) Bringing in the second species droplets to anchor holes. The scale bar is 400 μm. (f) Schematic of channel used, illustrating dual inlets for the two different chemical species. The test section (containing the anchors) is 100 μm high, 1 cm long and 3 mm wide. The anchor holes have a height of 50 μm and a diameter of 200 μm. The scale bar is 3 mm.

droplet per site (Fig. 5(c + d)). We then introduce droplets containing the second species from the bottom flow focusing device (Fig. 5(e)). Here lower flow rates than for the first droplets are used to prevent accidentally knocking any further droplet out of the holes: $Q_o^{bottom} = 5\ \mu L\ min^{-1}$, $Q_w^{bottom} = 0.05\ \mu L\ min^{-1}$. A loaded array, with two droplets per trap site, each with different contents, is shown in Fig. 6(a).

Having established the ability to fill the holes with droplets we can then use laser induced droplet merging[15] to start the chemical reaction. With the control we have over the positioning of the laser this means that we can target a specified droplet pair in the array. The power used is 200 mW, and a dwell time at the droplet interface of 100 ms is required before any fusion takes place when laser position is well placed.

The process of laser initiated droplet merging is shown in Fig. 6(b) and ESI movie S4,† where we choose to react the droplets such that they form a 'W' pattern. The track of the laser is shown by the solid and dashed lines in Fig. 6(b), which correspond to a time $t = 117$ ms after the merging of the drops at the top-center location. Fig. 6(c) shows the final state where only

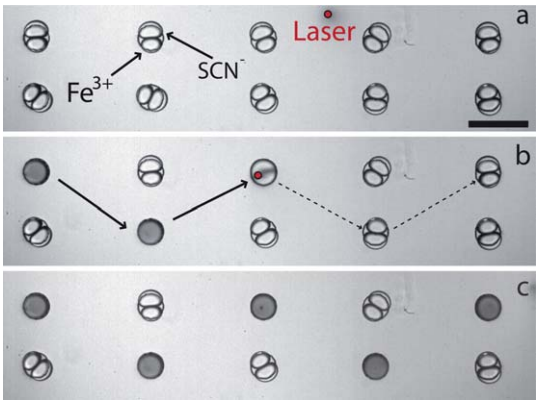

Fig. 6 Laser induced merging of droplets in anchor sites. (a) Filled droplet array. Laser spot is shown as a red dot. (b) The laser is scanned in the pattern shown. As it stops on the droplet-droplet interface it initiates fusion and a chemical reaction takes place. The solid line shows where the beam has been, the dashed line its future path. (c) The laser completes its path leaving 5 anchor points with a reaction product and all other droplets undisturbed. Scale bar is 400 μm.

the droplets illuminated by the laser have undergone the reaction.

7 Summary and discussions

In summary, we have demonstrated the first device that allows a selective patterning of a 2D array with microfluidic droplets. This is performed either through selectively filling or emptying the array, or by triggering a chemical reaction on demand. The approach relies on combining the rails and anchors approach, which provides robust passive manipulation, and the localized heating from the laser which adds selectivity and local actuation.

Both of these approaches are highly scalable, independent of the microchannel material and rely on very simple micro-fabrication: the rails and anchors are produced using lithographic techniques and can easily be densified over wide areas. The design of the test section is nearly common to all of the devices, which only differ in the pattern of rails and anchors that are designed for a specific application. This further simplifies the fabrication in large quantities for commercial applications. As for the optical heating, any number of operations can be performed with single beam by simply scanning the laser focus or by using holographic techniques to split one beam into a complex pattern.[22] The tight focus of the laser allows manipulation of individual droplets, even in very dense arrays, providing a clear advantage over electrical or acoustic methods.

The throughput of the devices presented here is appropriate for many applications that require a high level of control, since all of the experiments presented here lasted less than a few minutes using purely manual control of the flow rate and the laser position. This duration can be further reduced through use of an automated time-sharing of the laser heating, which can produce many operations simultaneously, or through optimization of the device designs. In the case of the droplet extraction for instance, a different pattern of anchors or the addition of gutter rails would allow the device to function at higher oil velocity, therefore allowing much faster sorting of the drops.

Increasing the throughput in the case of the array filling depends on the ability to derail rapidly moving drops. This will be realizable by improving the tolerance on the micro-fabrication process, which would allow the distance between the side-rails and the central rail to be better calibrated for the drop sizes. By optimizing this distance, drops can be derailed with a minimal deflection, which would allow us to work at higher flow rates.

Finally, future work will have to investigate the effect of the laser heating on the contents of the droplets, as well as ways to minimize these effects such as pulsing the laser source. While we expect that the heating can damage some proteins or sensitive biological material, it should still allow DNA or chemical manipulation without any significant artifacts.

8 Acknowledgments

Special thanks to Estelle Mayot for providing the perfluorinated surfactants used in our studies. The authors also thank Caroline Frot for microfabrication assistance. This project was partially supported by a 'Royal Society International Joint Project'. D. M. is a Royal Society University Research Fellow. The authors finally acknowledge the financial support from CNRS and Ecole Polytechnique.

References

1 S. K. Cho, H. Moon and C. J. Kim, *J. Microelectromech. Syst.*, 2003, **12**, 70–80.
2 A. Wixforth, *Superlattices Microstruct.*, 2003, **33**, 389–396.
3 L. Mugherli, O. N. Burchak, L. A. Balakireva, A. Thomas, F. Chatelain and M. Y. Balakirev, *Angew. Chem. Int. Ed.*, 2009, 1433–7851.
4 H. Kim, S. Vishniakou and G. W. Faris, *Lab Chip*, 2009, **9**, 1230–1235.
5 C. N. Baroud, F. Gallaire and R. Dangla, *Lab Chip*, 2010, **10**, 2032–2045.
6 H. Boukellal, S. Selimovic, Y. Jia, G. Cristobal and S. Fraden, *Lab Chip*, 2009, **9**, 331–338.
7 W. Shi, J. Qin, N. Ye and B. Lin, *Lab Chip*, 2008, **8**, 1432–1435.
8 P. Laval, N. Lisai, J. B. Salmon and M. Joanicot, *Lab Chip*, 2007, **7**, 829–834.
9 C. H. J. Schmitz, A. C. Rowat, S. Koester and D. A. Weitz, *Lab Chip*, 2009, **9**, 44–49.
10 J. Shim, G. Cristobal, D. R. Link, T. Thorsen, Y. Jia, K. Piattelli and S. Fraden, *J. Am. Chem. Soc.*, 2007, **129**, 8825–8835.
11 A. Huebner, D. Bratton, G. Whyte, M. Yang, A. J. deMello, C. Abell and F. Hollfelder, *Lab Chip*, 2009, **9**, 692–698.
12 Y. Bai, X. He, D. Liu, S. N. Patil, D. Bratton, A. Huebner, F. Hollfelder, C. Abell and W. T. S. Huck, *Lab Chip*, 2010, **10**, 1281–1285.
13 A. Huebner, C. Abell, W. T. S. Huck, C. N. Baroud and F. Hollfelder, *Anal. Chem.*, 2011, **83**, 1462–1468.
14 P. Abbyad, R. Dangla, A. Alexandrou and C. N. Baroud, *Lab Chip*, 2011, **11**, 813–821.
15 C. N. Baroud, M. R. de Saint Vincent and J. P. Delville, *Lab Chip*, 2007, **7**, 1029–1033.
16 C. N. Baroud, J. P. Delville, F. Gallaire and R. Wunenburger, *Phys. Rev. E*, 2007, **75**, 046302.
17 M. L. Cordero, D. R. Burnham, C. N. Baroud and D. McGloin, *Appl. Phys. Lett.*, 2008, **93**, 034107.
18 K. Stephan, P. Pittet, L. Renaud, P. Kleimann, P. Morin, N. Ouaini and R. Ferrigno, *J. Micromech. Microeng.*, 2007, **17**, N69–N74.
19 J. Clausell-Tormos, D. Lieber, J. C. Baret, A. El-Harrak, O. J. Miller, L. Frenz, J. Blouwolff, K. J. Humphry, S. Köster and H. Duan, *et al.*, *Chem. Biol.*, 2008, **15**, 427–437.
20 R. Dangla, S. Lee and C. N. Baroud, *Phys. Rev. Lett.*, 2011, **107**, 124501.
21 E. Verneuil, M. L. Cordero, F. Gallaire and C. N. Baroud, *Langmuir*, 2009, **25**, 5127–5134.
22 D. G. Grier, *Nature*, 2003, **424**, 810–816.

IOP Publishing Journal of Physics D: Applied Physics

J. Phys. D: Appl. Phys. **46** (2013) 114003 (8pp) doi:10.1088/0022-3727/46/11/114003

The physical mechanisms of step emulsification

Rémi Dangla[1], Etienne Fradet[1], Yonatan Lopez and Charles N Baroud

Ladhyx and Department of Mechanics, Ecole Polytechnique, CNRS, 91128 Palaiseau, France

E-mail: baroud@ladhyx.polytechnique.fr

Received 2 August 2012, in final form 21 November 2012
Published 22 February 2013
Online at stacks.iop.org/JPhysD/46/114003

Abstract

We revisit the physical balance that takes place when an interface between two immiscible fluids reaches a step change in the height of a microchannel. This situation leads to the production of droplets in a process known as 'step emulsification'. However, the mechanism that is responsible for the drop breakup and that determines its size has not been explained in simple terms. We propose a geometric model for drop breakup based on a quasi-static balance between the curvature of the thread inside the inlet channel and the curvature of the "bulb" downstream of the step. We find that the confinement limits the lowest values of curvature that can be adopted by the thread. In contrast, the bulb curvature decreases as its size increases, which leads to a critical bulb radius beyond which the two regions cannot be in static equilibrium. This leads to a flow which breaks the bulb into a droplet. The critical bulb radius predicted by the geometric analysis is in good agreement with experimental measurements for different step and inlet channel geometries. The radius of the drop that detaches is therefore bounded from below by this value and increases slowly with the dispersed phase flow rate.

(Some figures may appear in colour only in the online journal)

1. Introduction

The production of drops and bubbles in microfluidic devices is a well studied and widely applied problem. In this context, a few standards have emerged and gained widespread acceptance, such as T-junctions or flow-focusing junctions [1–3]. In parallel to these widespread techniques, a few other methods have also appeared. Of these, step emulsification stands out for its simplicity and robustness. In this method, the microfluidic device is initially filled with the fluid that will form the outer phase. The dispersed phase fluid is then pushed into a microchannel that leads to a step change in height. Monodisperse drops are produced at this location and transported by the flow of the outer fluid.

Such devices were developed as microfabricated equivalents of membrane emulsification systems in order to take advantage of the advances in microfabrication technologies [4]. Since then, a series of papers (e.g. [5]) have shown that this technique is widely applicable and robust and that it can be used to produce monodisperse drops over a wide range of sizes, dictated mainly by the microchannel depth. More recently, different groups have used steps in their microchannel designs in order to produce drops of a well calibrated size [6, 7], usually combining them with the classical T-junction or flow focusing junction.

Although the step emulsification technique has attracted widespread interest, there is no simple analytical expression to predict the size of drops that are produced by this technique. Instead, some phenomenological models have been suggested based on experimental measurements [8, 9]. In other cases, the dynamics of the interface has been modelled but solving these models generally requires heavy numerical solutions [5, 10–12]. A simple description for the physical mechanism that leads to the droplet detachment is still lacking.

Here we approach the problem of step emulsification from a geometric point of view, by studying the equilibrium shapes of the interface as it advances over the step in the microchannel. In a quasi-static situation, the curvature must be equilibrated everywhere in the system for the Laplace pressure jumps to be balanced. In particular, the curvature upstream of the step must adjust to the geometry of the interface downstream of the step, which is less confined and whose curvature decreases as its size grows. Yet, the strong confinement upstream of the step fixes a minimum value of the mean curvature (κ^*) of

[1] These authors contributed equally to this work.

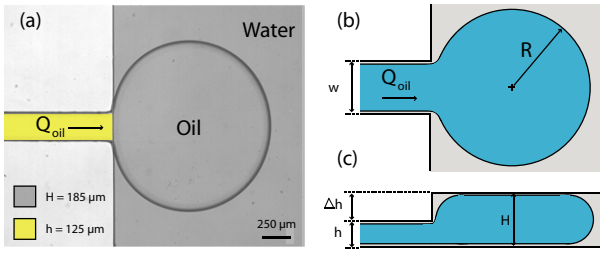

Figure 1. Problem geometry. (*a*) Top-down view: a bulb of oil injected into a water-filled reservoir. The width of the injection is $w = 250\,\mu$m and increases to $W = 5$ mm at the step, while the height increases from $h = 125\,\mu$m to $H = h + \Delta h = 185\,\mu$m in this example. (*b*) Top view sketch of the model geometry. (*c*) Side view of the same situation.

the interface below which equilibrium shapes no longer exist. We show that the curvature downstream of the step can reach values below κ^* and that the system comes out of equilibrium at this stage, leading to a drop breaking off over the step.

This droplet formation mechanism is generic to microchannel geometries with confinement asymmetries. It is detailed in section 2, where we relate the curvature criterion for the existence of equilibrium shapes to the volume of fluid downstream of the step. This yields an expression for the value of the drop radius R^* which triggers the collapse of the interface. This prediction is then tested experimentally, as explained in sections 3 and 4. Finally, these results are discussed in the context of microfluidics using confinement asymmetries in section 5.

2. A quasi-static mechanism for droplet formation

In order to address the droplet formation mechanism analytically, we consider the simplest microchannel geometry for droplet production at a step change in the channel height. It consists of a rectangular inlet channel of width w and height h ($w > h$) that leads to a wide reservoir of increased height $H = h + \Delta h$ filled with a quiescent fluid, as sketched in figure 1. Hence, the step is located at the junction between the inlet and the reservoir, in contrast with the original geometry where the change in channel height occurs some distance downstream of the inlet channel [4].

During its operation, the device is first filled with the continuous phase prior to injecting the dispersed phase at a constant flow rate. The dispersed phase forms a continuous thread in the inlet channel. At the entrance of the reservoir, the lateral confinement is suddenly released and the thread expands into a bulb of in-plane radius R, which grows as more fluid is injected.

We assume that the dispersed phase does not wet the channel walls and that a thin film of the continuous phase is always present. In this case, the interface geometry must be tangent to the wall at the point of apparent contact. This also implies that some of the continuous phase always remains in the inlet channel, in the form of corner gutters [13].

Next, we assume in our model that gravitational effects are negligible. These effects can be quantified by the Bond number $Bo = \Delta\rho g H^2/\gamma$, where $\Delta\rho$ is the difference in density between the two fluids, g is the acceleration due to gravity, H is the largest height in the device and γ is the interfacial tension. For the channel geometries we consider below, the Bond number remains in the range 10^{-2}–10^{-1}, which implies that gravitational effects may lead to corrections that are below 10% of our model predictions.

Last, provided that the injection flow rate is low, it is reasonable to assume that the system evolves in a quasi-static manner, i.e. that the interface around the thread and the bulb is in an equilibrium state at each instant. In this case, the shape of the interface must be such that its mean curvature κ is constant over the entire interface, apart from the regions where it is pressed against a channel wall and forced to follow the wall geometry.

The mean curvature κ is a local quantity defined at every point on the interface as the sum of the curvatures of the surface along its two principal directions (see [14, 15] for a detailed introduction). The Young–Laplace equation locally relates κ to the difference between the inner and outer pressures p_i and p_o, respectively, via the interfacial tension γ:

$$\gamma\kappa = p_\mathrm{i} - p_\mathrm{o}. \tag{1}$$

Hence, the quasi-static assumption also implies constant pressures in both phases, or equivalently that flow-induced pressure variations are negligible compared with the Laplace pressure jump $\gamma\kappa$. Finally, the quasi-static assumption is equivalent to requiring a small capillary number $Ca = \mu Q/\gamma H^2 \ll 1$, where μ is a typical fluid viscosity and Q is the injection flow rate of the dispersed phase. In practice, our experiments always verify this condition.

Under these assumptions, it is pertinent to ask whether there exists an equilibrium shape for a bulb of size R connected to the thread in the inlet channel. Below, we begin by studying the equilibrium shapes of the thread upstream of the step and of the bulb in the reservoir separately. Then, we consider the equilibrium of the entire system by searching for situations when the curvature of the thread can match the curvature of the bulb.

2.1. Shape and curvature of the thread

We model the dispersed phase in the inlet channel as a semi-infinite fluid thread. A possible equilibrium shape of the interface is shown in figure 2(*a*). It is obtained using Surface Evolver [16] by imposing the Laplace pressure jump $\Delta p = 4\gamma/h$ at the interface, or equivalently by imposing the mean curvature of the thread $\kappa_\mathrm{th} = 4/h$. The thread is a straight cylinder of cross-section flattened against all four channel walls. The interface only bends in the corners along circular arcs of radius $r = \kappa_\mathrm{th}^{-1}$, leaving out corner gutters of the continuous phase.

Equilibrium shapes of higher curvature are obtained by reducing the size of the gutters and thereby the radius of curvature r of the curved interface. However, the curvature of the straight cylinder geometry cannot decrease below the critical value $\kappa^* = 2/h$. When $\kappa_\mathrm{th} = \kappa^*$, the top and bottom gutters meet at mid-height in the channel as shown on figure 2(*b*). The side interface is no longer pressed against

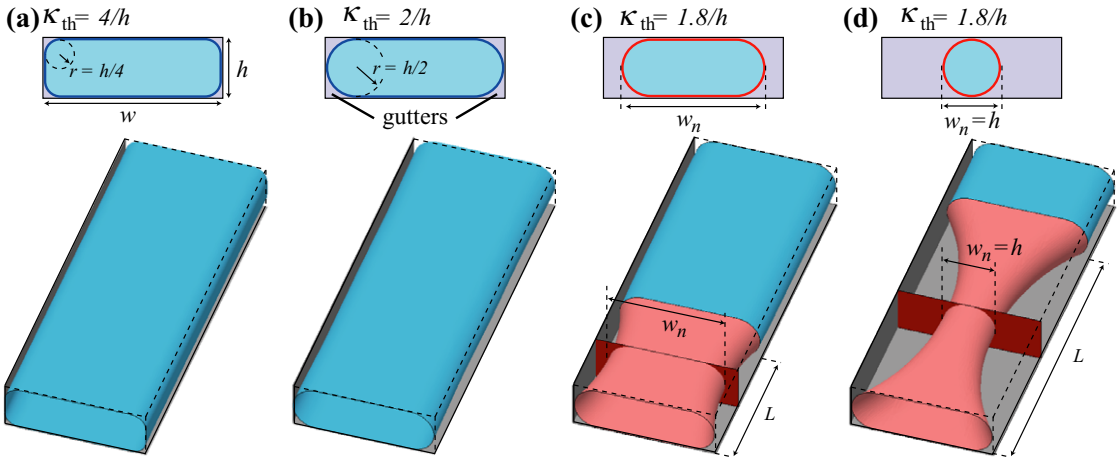

Figure 2. Shape of a confined thread in a rectangular channel (*a*) For a high curvature $\kappa_{\text{th}} = 4/h$, the thread is a straight cylinder of cross-section flattened against all four channel walls except near corners where the interface bends to form gutters. (*b*) When $\kappa_{\text{th}} = 2/h$, the gutters meet at mid-height in the channel and the lateral interfaces no longer flatten against the side walls. (*c*) Decreasing the imposed curvature to $1.8/h$ leads to the necking of the thread. This shape is not in equilibrium and the necking region grows in time. (*d*) When the necking region becomes large enough, the thread becomes unstable locally by the Rayleigh–Plateau instability.

the lateral walls and has the shape of a semicircle of radius $r = h/2$. Given that the mean curvature κ_{th} of a straight cylinder is equal to the curvature of its cross-section, decreasing κ_{th} below $2/h$ implies increasing r above $h/2$. This is impossible without violating the non-wetting boundary condition at the channel walls, which imposes that the interface intersects solid boundaries tangentially with a contact angle of π.

In fact, there are no equilibrium shapes of the interface if the imposed curvature is smaller than $\kappa^* = 2/h$. To illustrate this statement, we artificially impose $\kappa_{\text{th}} = 1.8/h$ to a section of fixed length L of the thread while maintaining a curvature $\kappa_{\text{th}} = 2/h$ over the rest of the interface using Surface Evolver. To reach the imposed curvature of $1.8/h$, the interface of the thread forms a neck as shown on figure 2(*c*). In this region, the thread maintains a transverse curvature of $2/h$ in order to intersect the channel walls tangentially while bending inwards in the plane to feature a negative in-plane curvature of $-0.2/h$. However, although the shape of the neck locally reaches a stable geometry of constant mean curvature $\kappa = 1.8/h$, the thread is not at equilibrium globally since the curvature of the neck differs from the curvature of the rest of the thread. As we progressively extend the length L of the necking region, its width w_n decreases until it eventually matches the height of the channel h. In this configuration shown in figure 2(*d*), the centre of the neck detaches from all four channel walls and resembles an unconfined fluid thread which is prone to the Rayleigh–Plateau instability [17–19]. Increasing L any further triggers the collapse of the thread.

Overall, we find that a thread of non-wetting fluid confined in a rectangular channel is at equilibrium only when its curvature is higher than $\kappa^* = 2/h$. Otherwise, the thread is necessarily out of equilibrium, forms a neck, and then breaks in two.

2.2. *Shape and curvature of the bulb*

We now consider the equilibrium shape of the bulb in the reservoir which we model as a droplet of radius R, confined between two solid plates separated by a distance H. Two limiting cases can be solved analytically.

(i) When the radius R of the drop is smaller than $H/2$, it takes a spherical shape since it is not confined. Its mean curvature is then $\kappa_{\text{b}} = 2/R$.

(ii) The limit of a very large drop was studied by Laplace [20] and more recently by Park and Homsy [21]. The drop then has a pancake shape and a curvature

$$\kappa_{\text{b}} = \frac{2}{H}\left(1 + \frac{\pi}{4}\frac{1}{\chi}\right), \tag{2}$$

where $\chi = 2R/H \gg 1$ is the aspect ratio of the drop.

In all cases, the equilibrium shape of the interface away from the plates is an axisymmetric surface of constant mean curvature whose axis of symmetry is perpendicular to the plane of the reservoir. In the unbounded case, such surfaces are called Delaunay surfaces and can be classified into three subfamilies depending on the nature of their generatrix: catenoids, unduloids and nodoids [22]. Confinement only adds boundary conditions that dictate how the interface connects to the solid plates but it does not modify the generic differential equation $\kappa = \text{cst}$ that generates the family of Delaunay surfaces. Consequently, the shape of a droplet confined between two parallel plates is a slice of a Delaunay surface.

In the case of a non-wetting droplet, the interface must intersect the plates tangentially with a contact angle π. This implies that at the walls, the tangent of the generatrix of the Delaunay surface is perpendicular to its axis of symmetry, a condition which is only met by nodoids. In a cylindrical coordinate system (ρ, θ, z) centred at the centre of mass of the droplet, nodoids are described by the set of parametric equations

$$\rho(s) = \frac{\sqrt{e^2-1}}{\kappa_{\text{b}}}\sqrt{\frac{e-\cos s}{e+\cos s}} \tag{3a}$$

$$z(s) = \frac{e^2-1}{\kappa_{\text{b}}}\int_\pi^s \frac{-\cos u}{\sqrt{e^2-\cos^2 u}(e+\cos u)}\,\mathrm{d}u. \tag{3b}$$

Here, e is a parameter that gives the nodoid shape and can vary from 1 to ∞, s is a curvilinear coordinate, and u is an integration dummy variable.

The generatrix is 2π-periodic in s and its tangent is perpendicular to the z-axis when $\mathrm{d}z/\mathrm{d}\rho = 0$, which occurs for $s = \pi/2 + n \cdot \pi$, with n an arbitrary integer. Intuitively, the interface of the squeezed drop must bend outwards and away from its axis of symmetry. This is the case for $s = [\pi/2, 3\pi/2]$. As a result, we obtain that the shape of a drop squeezed between two parallel plates is described by the set of parametric equations above with s varying between $\pi/2$ and $3\pi/2$.

In equations (3*a*) and (3*b*), the curvature κ_b of the droplet is just a scaling factor. Hence, all possible geometries are scanned by varying e from 1 to ∞. For example, we recover the spherical shape when $e \to 1$ while $e \gg 1$ yields pancake droplets. In practice, for a given drop geometry or value of e, κ_b is fixed by the height of the reservoir

$$H = \frac{e^2 - 1}{\kappa_\mathrm{b}} \int_{\pi/2}^{3\pi/2} \frac{-\cos u}{\sqrt{e^2 - \cos^2 u}(e + \cos u)} \,\mathrm{d}u \qquad (4)$$

and the radius R for the drop is obtained by taking $s = \pi$ in equation (3*a*) for $\rho(s)$:

$$R = \frac{e + 1}{\kappa_\mathrm{b}}. \qquad (5)$$

Combining these expressions for R and H, we can express the mean curvature κ_b as a function of e and χ in a compact equation

$$\kappa_\mathrm{b} = \frac{2}{H} \frac{e + 1}{\chi}, \qquad (6)$$

knowing that e is directly related to χ via

$$\frac{1}{\chi} = \frac{e - 1}{2} \int_{\pi/2}^{3\pi/2} \frac{-\cos u}{\sqrt{e^2 - \cos^2 u}(e + \cos u)} \,\mathrm{d}u. \qquad (7)$$

When the drop is spherical ($e = 1$ and $\chi = 1$), we recover $H \cdot \kappa_\mathrm{b} = 4$ as expected. In the asymptotic limit of large pancake drops ($e \gg 1$), $e = \chi + \pi/4 + \mathcal{O}(1)$ such that $H \cdot \kappa_\mathrm{b} = 2[1 + \pi/4\chi + \mathcal{O}(1/\chi)]$, in agreement with the asymptotic limit (2) found by Laplace.

Overall, we can express $H \cdot \kappa_\mathrm{b}$ from the unconfined spherical case $\chi < 1$ to the pancake droplet limit $\chi \gg 1$ in the form $H \cdot \kappa_\mathrm{b} = 2\,[1 + f(\chi)]$, with

$$\begin{aligned} f(\chi) &= \frac{2}{\chi} - 1 && \text{when } 0 < \chi < 1 \\ &= 1 && \text{for } \chi = 1 \\ &\approx \frac{\pi}{4}\frac{1}{\chi} && \text{when } \chi \gg 1 \end{aligned} \qquad (8)$$

and find a lower bound $2/H$ for the bulb curvature.

These results are shown in figure 3, where the different shapes are displayed along with the value of $f(\chi)$.

2.3. Matching curvatures: a scenario for droplet formation

The quasi-static equilibrium hypothesis implies that the mean curvature of the thread upstream of the step κ_th has to be equal to the mean curvature of the bulb in the reservoir κ_b. Yet, we showed above that the mean curvature of the thread upstream of the step has a lower bound $\kappa^* = 2/h$ below which it is out of equilibrium. By matching curvatures, this threshold curvature now also applies to the bulb. Consequently, the interface may evolve out of equilibrium and collapse to release a droplet in the reservoir when κ_b decreases below $\kappa^* = 2/h$.

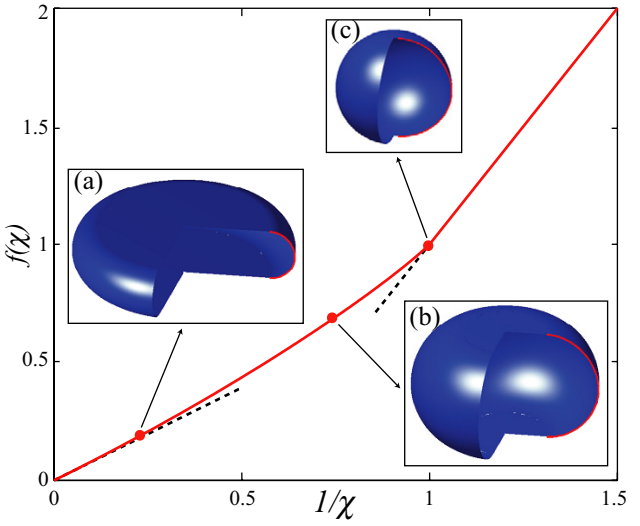

Figure 3. Plot of $f = H \cdot \kappa_\mathrm{b}/2 - 1$ versus the inverse aspect ratio of the bulb χ. Insets (a)–(c) 3D plots of nodoid droplets obtained from the parametric equations (3*a*) and (3*b*) for (a) $e = 3$, (b) $e = 1.5$ and (c) $e = 1.001$. The dashed lines represent the two analytical limits.

The proposed scenario is the following: when the bulb first enters the reservoir, it is spherical. Its mean curvature is always higher than the critical value κ^* and the thread is strongly confined, as shown in figure 2(*a*). However, as more fluid is injected into the device, the size of the bulb increases while its mean curvature κ_b decreases. In the presence of a step, the lower bound $2/H$ for the bulb curvature is lower than the critical curvature $\kappa^* = 2/h$ of the thread. Hence, for any value of $\Delta h > 0$, the radius of the bulb eventually reaches a critical value R^* for which the curvature of the bulb is equal to $\kappa^* = 2/h$. The shape of the thread is then tangent to the channel side walls (figure 2(*b*)). Beyond this critical size R^*, the mean curvature of the thread can only match the bulb curvature by taking a negative value in the plane of the channel, as shown in figure 2(*c*). As discussed above, this situation is out of equilibrium. The pressure in the gutters around the thread is lower than the pressure in the reservoir. This drives a backflow of the continuous fluid, which in turn increases the size of the necking region. Eventually, the thread breaks when $w_n = h$ and a drop of radius R^∞ detaches into the reservoir.

The critical radius R^* is defined by the equation $\kappa_\mathrm{b} = 2/h$, which translates to

$$f(\chi^*) = \frac{\Delta h}{h} \qquad (9)$$

for the critical aspect ratio χ^* of the bulb. Recalling expression (8) and figure 3 for $f(\chi)$, we can solve this equation analytically for large step heights $\Delta h/h > 1$ and numerically otherwise. When $\Delta h/h > 1$, we obtain that the

dispersed phase is out of equilibrium before the bulb becomes confined by the walls of the reservoir and the critical bulb size $R^* = h$ is independent of the step height. As the step height $\Delta h/h$ decreases, R^* increases, diverging along the asymptote $R^* = \pi hH/8\Delta h$ when $\Delta h/h \to 0$. The full results are shown in section 4, figure 5.

3. Experimental methods

3.1. Microchannel fabrication

The experiments were performed in PDMS microchannels (Dow Corning Sylgard 184). The microchannel fabrication was performed using dry film soft-lithography techniques [23], which allowed us to obtain different step heights by a successive lamination of different film types (Etertec, Eternal Laminar, thicknesses 15, 35, and 50 μm)

The process began by (1) laminating the photoresist film layers onto a glass slide using an office laminator (PEAK PS320), at a constant temperature $T = 100\,^{\circ}$C, to get the base shape with the desired height. (2) The film was then exposed to UV light (Hamamatsu Lightningcure LC8) through a printed photomask corresponding to the inlet channel and the wide reservoir. (3) After exposing this channel, additional layers of film were added to obtain the desired height of the step. (4) The stack of photoresist films was exposed again to the UV light through a mask corresponding only to the reservoir region. (5) Finally the whole device was developed by immersing it in a solution of water at 1% (w/w) of carbonate potassium, to produce the master on which the PDMS could be moulded.

Once the moulds were fabricated, they were measured using an optical profilometer (Zygo). The measured values of the deconfinement parameter were in the range $0.064 \leqslant \Delta h/h \leqslant 1.516$, in addition to the condition of zero step height as a control. The height and width of the inlet channel were kept constant at $h = 125\,\mu$m and $w = 250\,\mu$m, except for the condition $\Delta h/h = 0.064$ for which $h = 250\,\mu$m and $w = 500\,\mu$m. Once the moulds were measured, they were replicated into PDMS microchannels using the standard PDMS moulding techniques.

3.2. Fluids and experimental protocol

The experiments were performed using a fluorinated oil (FC-40, viscosity $\mu = 4$ cP) as the dispersed phase. The continuous phase was a mixture of water and sodium dodecyl sulfate (SDS) at 3% concentration by weight. The interfacial tension γ was 18 mN m^{-1}. Good wetting of the water phase on the PDMS was ensured by using the channels within a few minutes after plasma bonding.

The channel was initially manually filled with the aqueous solution through specifically fabricated side holes, while ensuring that no gas bubbles were trapped. The oil was then injected using a programmable high precision syringe pump (Cetoni NeMESYS), at flow rates ranging from $Q = 0.1$ to $20\,\mu$l min^{-1} and each experiment was repeated three times. Images of the fluid exit through the channels were captured using a high-speed camera (Photron Fastcam 1024), mounted on a Nikon TE2000-U inverted microscope, filming at 250 frames s^{-1}.

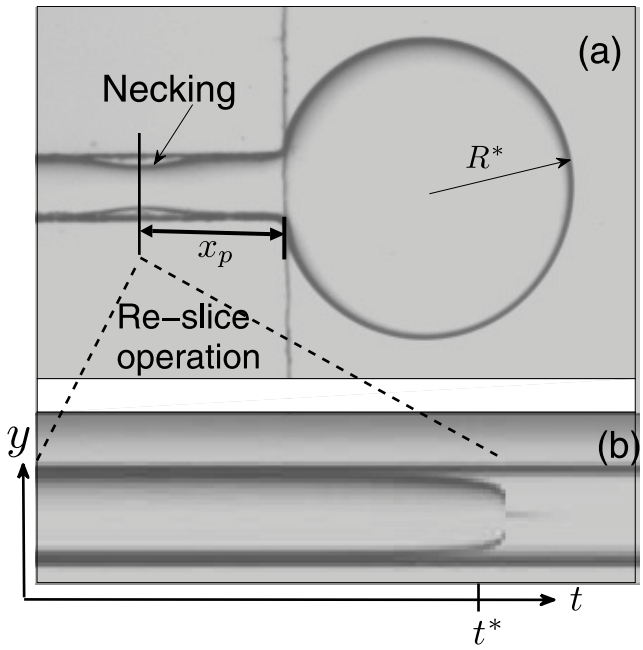

Figure 4. (a) The location of the neck formation is found from the late-time images of the drop detachment. (b) A space–time diagram is then constructed to determine the initial moments of the neck destabilization.

3.3. Image analysis

Two radii were of interest in the movies that we captured: the final radius R^∞ was measured once the drop had detached. More importantly, we identified the radius R^* at which a neck began to form upstream of the step as shown in figure 4. This was done by first locating the position (x_p) where the neck formed (figure 4(a)) and building space–time diagram of the grey values at this position (figure 4(b)). This allowed us to determine the time t^* at which the liquid interface began to separate from the walls; the bulb radius at this time was taken as the measure of R^*.

Note that the values of R^* that are reported here correspond to the smallest value of Q. Therefore, even though the criterion for stability depends on visually identifying the fluid detachment from the wall, the error on R^* is small since the drop volume changes very slowly.

4. Results

4.1. Equilibrium loss

Using this experimental protocol, we first determined the value of the bulb radius at which the drop began to detach. The values of this critical radius R^* as a function of the step height Δh are shown in figure 5, where the physical values are normalized by the height h of the inlet channel. The experimental data (solid squares) were obtained for the minimum flow rate $Q = 0.10\,\mu$l min^{-1} and the black solid line corresponds to the radius predicted by equation 9. This line is not a fit to the data as it does not contain any free parameters.

Both the model and the experiments show that the critical radius decreases with increasing deconfinement $\Delta h/h$. In fact,

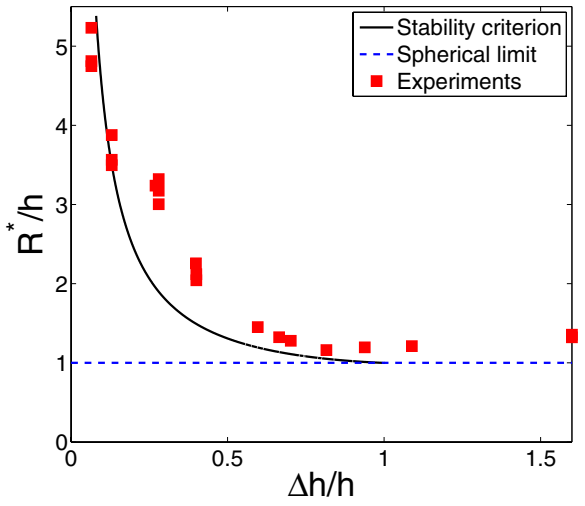

Figure 5. The evolution of R^* as a function of the step height. The points correspond to experimental measurements at a flow rate of $Q = 0.01\ \mu\mathrm{l\,min}^{-1}$. The solid line indicates the prediction from balancing the curvatures inside the inlet channel and in the deep section. The dashed line corresponds to the prediction for infinitely deep step.

the model predicts that the critical radius should diverge $R^* \to \infty$ as $\Delta h/h \to 0$, which is in agreement with the experimental observations that yield $R^* = 5h$ for $\Delta h = 0.064h$. Moreover, the control experiment with no step does not produce any drops, with the bulb remaining attached to the inlet channel. For $\Delta h/h \geqslant 1$, the model predicts that the critical radius should reach a plateau $R^* = h$. This plateau is observed in the experiments, although the measured critical radius is slightly superior to h.

The quantitative differences between the model and the measurements can be attributed to three main sources: first, gravitational effects can play a role, since FC-40 is about 85% denser than water. Second, the edge at which the inlet channel meets the reservoir may impose some corrections in order to account for the complex shape near the channel exit. Finally, slight variations in the photo-resist thickness can lead to a sloping top wall of the reservoir, which has been shown to significantly influence confined two-phase flows [24]. Nevertheless, the model and the experiments are in semi-quantitative agreement with no free adjustable parameters.

4.2. Drop radius

In practical situations, the quantity of interest is the size of the final drop that detaches from the inlet channel. This drop radius (R^∞) corresponds to the critical value of the radius, augmented by the fluid in the thread downstream of the necking, which is small compared with the drop volume in our conditions. This must also be corrected for the further inflation of the drop by the fluid that has been injected during the necking time. If the necking time is independent of the flow rate, we would therefore expect the projected drop area to increase linearly with the flow rate to leading order, which would lead to the scaling $(R^\infty - R^*) \sim Q^{1/2}$. We expect that the necking time should decrease with increasing step height, since

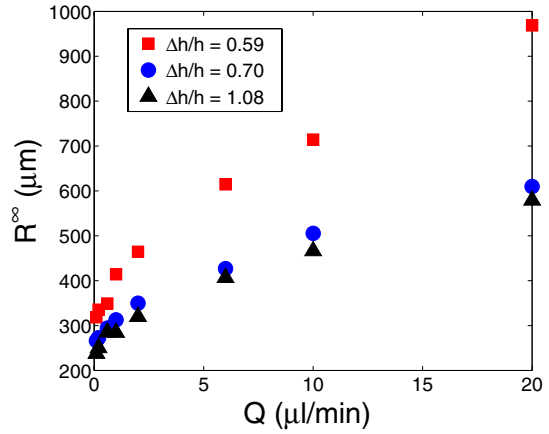

Figure 6. Final drop size (R^∞) as a function of the input flow rate (Q) ranging between 0.01 and 20 $\mu\mathrm{l\,min}^{-1}$, for three representative step heights.

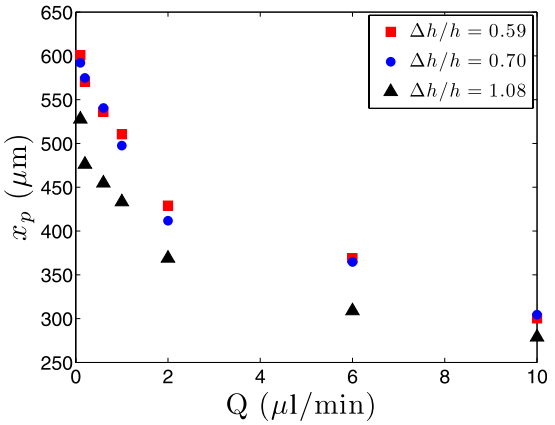

Figure 7. Position of the neck formation distance from the step as a function of the flow rate, for the same steps as figure 6.

the pressure imbalance that drives the necking of the thread increases with Δh.

We measured the drop radii (R^∞) as a function of the flow rate at which the dispersed phase is injected. As shown in figure 6, we observe that the drop size indeed increases with the flow rate, in agreement with the 'inflationary' theory. Nonetheless, the change in drop radius is small, since at most a three-fold difference in radius (9 times in volume) is observed for a two-thousand fold increase in flow rate (Q from 0.01 to 20 $\mu\mathrm{l\,min}^{-1}$). A fit of $R^\infty - R^*$ yields a power law of exponent larger than 0.5, between 0.6 and 0.7. This indicates that the necking time depends on the flow rate. Moreover, we find that the drop size decreases with increasing step height regardless of the oil flow rate. This implies that the variations in the necking time are not sufficient to modify the hierarchy of sizes dictated by the dependence of R^* on Δh.

4.3. Breakup distance

Finally, it is worth noting the location of the necking which leads to the drop breakup x_p. This position depends on the flow rate of the inner phase, as shown in figure 7. In fact, the geometric mechanism presented here provides a prediction for the critical bulb radius but it cannot predict where the neck

will form. Predicting x_p would require a dynamic model that accounts for the back flow into the inlet channel and its interactions with the fluid thread. Such a model would need to take into account the fluid properties, as well as geometric details about the inlet channel.

5. Summary and discussions

In this paper, we present a theory for step emulsification based on quasi-static geometric arguments. We argue that the growth of the bulb in the reservoir leads to a thinning of the thread in the inlet channel in order to maintain a curvature equilibrium between the two regions. We also identify a minimum value of curvature, imposed by the confinement of the thread in the inlet channel, below which equilibrium shapes of the interface cannot exist. A geometric calculation then shows that the bulb curvature always decreases below this critical value if the reservoir has a larger height than the inlet channel. This forces the system out of equilibrium: a backflow of the continuous phase is generated upstream of the step, which leads to the drop breakup.

The curvature balance model does not depend on the fluid properties. In particular, it is insensitive to the value of the interfacial tension even though the physics that we describe is dominated by surface effects. This is because the interfacial tension is acting in both regions of the microchannels and its value drops out of the balance.

However, our model does not directly predict the actual size of the drops that are formed. Instead, we provide a lower bound for the drop size, which must then be corrected for dynamical effects. Those effects do depend on the fluid properties: the back flow that is driven into the inlet channel is accelerated by the capillary pressure imbalance (which depends on γ) and slowed down by viscous effects (which depend on μ) and by the overpressure due to the driving (which depends on the flow rate Q). In order to reduce the impact of the dynamics on the drop size, one may imagine designing the inlet channel with local modulations in width or depth in order to facilitate the breakup.

Finally, note that the curvature imbalance can also be produced by a more gradual change in the channel height. We have recently shown [24] that droplets with well calibrated sizes can be produced by a sloping channel, through a similar mechanism. In the case of a sloping roof, the drop size depends on the inlet channel geometry, as in the present case, but also on the slope angle. Moreover, the slope provides a mechanism to move the droplet after its formation, since the drops feel a force that drives them towards the regions of lowest confinement [25]. When combined with local modulations of the channel height [26, 27], such an approach can lead to a new generation of droplet microfluidics that does not require any flow of the continuous phase.

Acknowledgments

The authors thank Caroline FROT for technical assistance on the project. The research leading to these results has received funding from the European Research Council under the European Union's Seventh Framework Programme (FP7/2007-2013)/ERC Grant agreement no 278248 'MULTICELL'.

References

[1] Christopher G F and Anna S L 2007 Microfluidic methods for generating continuous droplet streams *J. Phys. D: Appl. Phys.* **40** R319–36
[2] Baroud C N, Gallaire F and Dangla R 2010 Dynamics of microfluidic droplets *Lab Chip* **10** 2032–45
[3] Seemann R, Brinkmann M, Pfohl T and Herminghaus S 2012 Droplet based microfluidics *Rep. Prog. Phys.* **75** 016601
[4] Sugiura S, Nakajima M, Iwamoto S and Seki M 2001 Interfacial tension driven monodispersed droplet formation from microfabricated channel array *Langmuir* **17** 5562–6
[5] Kobayashi I, Mukataka S and Nakajima M 2005 Novel asymmetric through-hole array microfabricated on a silicon plate for formulating monodisperse emulsions *Langmuir* **21** 7629–32
[6] Priest C, Herminghaus S and Seemann R 2006 Generation of monodisperse gel emulsions in a microfluidic device *Appl. Phys. Lett.* **88** 024106
[7] Malloggi F, Pannacci N, Attia R, Monti F, Mary P, Willaime H, Tabeling P, Cabane B and Poncet P 2010 Monodisperse colloids synthesized with nanofluidic technology *Langmuir* **26** 10–1441
[8] Sugiura S, Nakajima M and Seki M 2002 Prediction of droplet diameter for microchannel emulsification *Langmuir* **18** 3854–9
[9] Stoffel M, Wahl S, Lorenceau E, Höhler R, Mercier B and Angelescu D E 2012 Bubble production mechanism in a microfluidic foam generator *Phys. Rev. Lett.* **108** 198302
[10] Christov N C, Danov K D, Danova D K and Kralchevsky P A 2008 The drop size in membrane emulsification determined from the balance of capillary and hydrodynamic forces *Langmuir* **24** 1397–410 PMID: 17963414
[11] van Dijke K C, Schroën K C P G H and Boom R M 2008 Microchannel emulsification: From computational fluid dynamics to predictive analytical model *Langmuir* **24** 10107–15 PMID: 18702473
[12] van der Zwan E, Schroën K and Boom R A 2009 geometric model for the dynamics of microchannel emulsification *Langmuir* **25** 7320–7
[13] Wong H, Morris S and Radke C J 1992 Three-dimensional menisci in polygonal capillaries *J. Colloid Interface Sci.* **148** 317–36
[14] Eggers J G and Villermaux E 2008 Physics of liquid jets *Rep. Prog. Phys.* **71** 036601
[15] Ajaev V S and Homsy G M 2006 Modeling shapes and dynamics of confined bubbles *Ann. Rev. Fluid Mech.* **38** 277–307
[16] Brakke K A 1992 The Surface Evolver *Exp. Math.* **1** 141–65
[17] Garstecki P, Stone H A and Whitesides G M 2005 Mechanism for flow-rate controlled breakup in confined geometries: a route to monodisperse emulsions *Phys. Rev. Lett.* **94** 164501
[18] Raven J P and Marmottant P 2009 Microfluidic crystals: dynamic interplay between rearrangement waves and flow *Phys. Rev. Lett.* **102** 084501
[19] van Steijn V, Kleijn C R and Kreutzer M T 2009 Flows around confined bubbles and their importance in triggering pinch-off *Phys. Rev. Lett.* **103** 214501
[20] Laplace P S 1806 Traité de mécanique céleste; supplément au dixième livre, sur l'action capillaire, Courcier, Paris
[21] Park C W and Homsy G M 1984 Two-phase displacement in Hele Shaw cells: theory *J. Fluid Mech.* **139** 291–308

[22] Delaunay C 1841 Sur la surface de revolution dont la courbure moyenne est constante *J. Math. Pures Appl.* **6** 309–15
[23] Stephan K, Pittet P, Renaud L, Kleimann P, Morin P, Ouaini N and Ferrigno R 2007 Fast prototyping using a dry film photoresist: microfabrication of soft-lithography masters for microfluidic structures *J. Micromech. Microeng.* **17** N69–74
[24] Dangla R, Kayi S C and Baroud C N 2013 Droplet microfluidics driven by gradients of confinement *Proc. Natl. Acad. Sci, USA* (in press) doi:10.1073/pnas.1209136110
[25] Dangla R, Lee S and Baroud C N 2011 Trapping microfluidic drops in wells of surface energy *Phys. Rev. Lett.* **107** 124501
[26] Abbyad P, Dangla R, Alexandrou A and Baroud C N 2011 Rails and anchors: Guiding and trapping droplet microreactors in two dimensions *Lab Chip* **11** 813–21
[27] Fradet E, McDougall C, Abbyad P, Dangla R, McGloin D and Baroud C N 2011 Combining rails and anchors with laser forcing for selective manipulation within 2D droplet arrays *Lab Chip* **11** 4228–34

Lab on a Chip

RSC Publishing

PAPER

View Article Online
View Journal

Cite this: DOI: 10.1039/c3lc50768h

Parallel measurements of reaction kinetics using ultralow-volumes†

Etienne Fradet,[a] Paul Abbyad,‡[b] Marten H. Vos[b] and Charles N. Baroud*[a]

We present a new platform for the production and manipulation of microfluidic droplets in view of measuring the evolution of a chemical reaction. Contrary to existing approaches, our device uses gradients of confinement to produce a single drop on demand and guide it to a pre-determined location. In this way, two nanoliter drops containing different reagents can be placed in contact and merged together, in order to trigger a chemical reaction. The reaction rate is extracted from an analysis of the observed reaction–diffusion front. We show that the results obtained using this platform are in excellent agreement with stopped-flow measurements, while decreasing the sample consumption 5000 fold. We also show how the device operation can be parallelized in order to react an initial sample with a range of compounds or concentrations, on a single integrated chip. This integrated chip thus further reduces sample consumption while reducing the time required for the experimental runs from hours to minutes.

Received 26th June 2013,
Accepted 28th August 2013

DOI: 10.1039/c3lc50768h

www.rsc.org/loc

Recent years have witnessed rapid progress of droplet microfluidic methods for chemical and biological analysis,[1–3] which has led to applications for DNA analysis,[4,5] cell manipulation,[6] or other biological or biochemical advances.[3,7] Most of this work has focused on high-throughput applications that require 10^3–10^6 droplets, leading to the development of many tools for the formation and transport of such drops, in addition to methods for measuring their contents. These developments have already led to a new way of thinking about biological systems, through the emergence of "digital biology" where an initial sample is separated into compartments that provide a binary (*yes* or *no*) answer.[4]

An alternative approach is to extract more detailed information from a single droplet by observing variations of its contents in time, for instance to observe the evolution of a chemical reaction[8,9] or the response of a small number of cells to a stimulus.[10,11] Tools that address this low-throughput niche have been developed in the surface-actuated microfluidics approach, either through electrowetting[12] or through surface acoustic waves,[13] but they have remained very underdeveloped in microchannels. So although the volumes required to perform the measurement are small, a large part of the sample is wasted due to fluid handling limitations. This can be an important drawback when expensive or rare samples are used or when many different reactions are required.

Part of the difficulty of working with few drops comes from the classical methods of droplet generation and transport, which rely on stable flow rates at a flow-focusing or T-junction to produce the drops.[14] This implies that the initial drop production, before the fluid flows have reached a steady state, is poorly controlled. Recently however, gradients of confinement were introduced for the production and transport of drops without the need for a flow of the outer fluid and without any transient effects.[15] Two individual drops could therefore be produced on demand and brought together to merge and react, by only relying on the channel geometry, using a technique called "rails and anchors".[11]

Here we demonstrate a robust and easy to fabricate microfluidic platform that will allow such measurements to become routine. In particular, we show how chemical kinetics can be extracted from a single fusion of two nanoliter droplets and how the device can be parallelized to perform multiple independent reactions on an integrated chip. A simplified analysis method is introduced to measure the chemical kinetics and the results compare favorably with measurements obtained from a commercial stopped-flow machine, while requiring only a tiny fraction of the reagents.

The device consists of a square test section connected to four inlet channels of smaller width and height, two for oil and two for aqueous solutions, as shown on Fig. 1a. In addition, a goggle-like pattern, of larger height, is etched on top of the test section. This multilevel structure (Fig. 1b) is micro-fabricated using simple multi-layer dry film soft lithography.[16,17] In this

[a] *Laboratoire d'Hydrodynamique (LadHyX) and Department of Mechanics, Ecole Polytechnique, CNRS, 91128, Palaiseau, France. E-mail: baroud@ladhyx.polytechnique.fr*

[b] *Laboratoire d'Optique et Biosciences (LOB), Ecole Polytechnique, INSERM U696, CNRS, 91128, Palaiseau, France*

† Electronic supplementary information (ESI) available. See DOI: 10.1039/c3lc50768h

‡ Current address: Department of Chemistry & Biochemistry, Santa Clara University, Santa Clara, California 95053, USA.

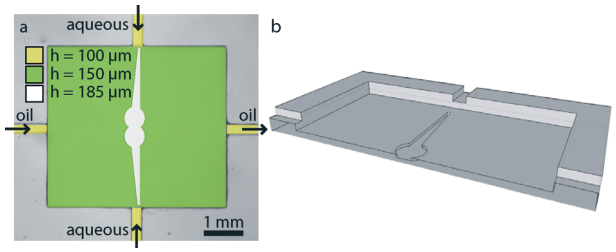

Fig. 1 (a) Top-down view of the test section. It consists of three regions of different heights h: four inlet channels, the test section in green, and the goggle pattern in white. (b) Perspective view of half the reaction chamber.

method, successive layers of solid photoresist are deposited and exposed to UV using a succession of masks that determine the features at each height. Once all layers are deposited and exposed, the complete device is developed to reveal the mold that is then used to produce PDMS devices. This procedure is rapid (few minutes) and simple to implement; it does not require a mask aligner since it relies on superposing millimeter-scale structures. The geometry that is thus defined provides the three operations that must be performed on the drops: their production, propulsion and pairing.

During operation, the device is first filled with a fully wetting oil used as the continuous phase and the oil is kept stationary for the rest of the experiment. By pushing the aqueous solutions past the step into the test section, a drop detaches when it reaches a well-calibrated size, a technique known as step emulsification.[18] The drop size is determined by the height of the step and, to a lesser extent, the injection rate of the dispersed phase.[19] As a result, injecting the aqueous solution past the step allows the production, on demand, of a single droplet of desired volume.

In the experiments reported here, the drop that detaches is large enough to remain squeezed between the top and bottom walls and this vertical confinement makes droplets sensitive to channel height modulations.[11,15] Indeed, confined droplets have a larger surface energy than spherical unconstrained drops of identical volume. Since droplets tend to minimize their surface energy, they migrate towards regions of reduced confinement. Consequently, the V-shaped grooves in our device, corresponding to the arms of the goggle, passively propel droplets toward the center of the test section by gradually releasing their confinement. Finally, droplets coming from the two inlet channels are held against each other in adjacent anchors in the center of the test region. The shape of the anchors ensures that the two drops are touching.

Typical device operation is shown in Fig. 2 and accompanying movie S1, ESI.† The device is first filled with a mixture of perfluorinated oil (FC40, 3M Fluorinated) and a PEG based fluoro-surfactant[20] at 0.1% (w:w). Next, a solution of 2,6-dichlorophenolindophenol (DCPIP) is injected from the top injection channel and a drop detaches and comes to a rest in the central trap, after which a drop of L-ascorbic acid is generated in the same way from the bottom injection channel (Fig. 2a–b).

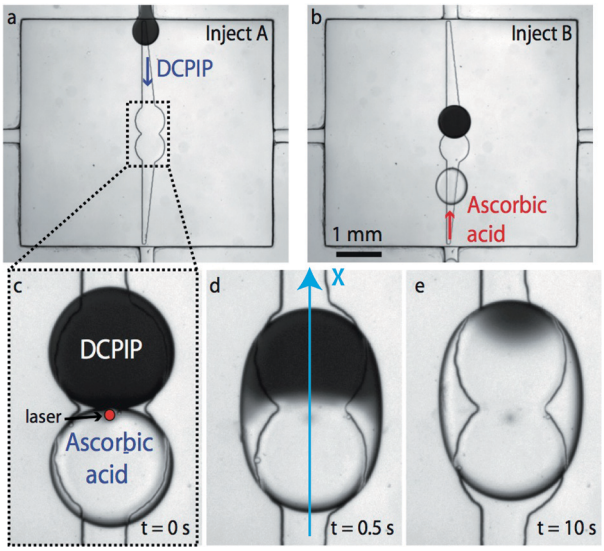

Fig. 2 Channel operation showing the reduction of DCPIP to a colorless molecule by L-ascorbic acid. (a) Injection of the DCPIP. (b) Injection of the L-ascorbic acid. (c) Static pair of touching droplets. An infrared laser pulse (wavelength λ = 1480 nm, power $P \sim$ 150 mW), lasting 200 ms, is focused near the droplet–droplet interface to trigger coalescence. The laser is removed before coalescence starts. (d–e) Reactive front propagating along the fused droplet. The arrow indicates the line over which the time evolution is measured.

The two drops do not merge, due to the presence of the surfactant (Fig. 2c). However, a laser pulse on the touching interfaces triggers their fusion, which is initiated only after the laser has been removed,[17] and the fused drop quickly relaxes to the final oblong shape imposed by the anchors. The reaction starts immediately after fusion and a reactive front propagates in the fused droplet, as shown in Fig. 2d–e, until the limiting reagent has been exhausted. Finally, once the reaction is completed, a transverse oil flux is used to remove the drop and reset the test section for another experiment.

In contrast to moving droplets where internal flows mix the reagents,[21–24] the reaction in the stationary drops takes place through a reaction–diffusion process.[9] In our devices, we match the drop sizes and interfacial tensions so that the contents remain well separated after the drop fusion. In the case when a drop of DCPIP (dark blue) is fused with a drop of buffer, the diffusion coefficient of the DCPIP can be measured (D_B = 0.77 × 10^{-9} m^2 s^{-1}) by following the spreading of the dye (see ESI† section 1 and movie S2). When the second drop contains the L-ascorbic acid, the reaction evolution can be modeled by a reaction–diffusion (R–D) set of equations with initially separated reagents.

We use the shorthand notation A for L-ascorbic acid, B for DCPIP and C for the reaction product. Since A and B are initially separated in two different droplets, they have to diffuse toward each other in order to react once the droplets merge. As a result, the local concentrations of A, B and C, noted [A], [B] and [C], are functions of both space and time. In addition, the reaction is known to follow second order kinetics[25] so the reaction rate is $R = k[A][B]$, which is also a function of space

and time. As a result, conservation laws for the three species yield:

$$\partial_t[\mathrm{A}] = D_\mathrm{A}\partial_{xx}[\mathrm{A}] - k[\mathrm{A}][\mathrm{B}] \quad (1)$$

$$\partial_t[\mathrm{B}] = D_\mathrm{B}\partial_{xx}[\mathrm{B}] - k[\mathrm{A}][\mathrm{B}] \quad (2)$$

$$\partial_t[\mathrm{C}] = D_\mathrm{C}\partial_{xx}[\mathrm{C}] + k[\mathrm{A}][\mathrm{B}] \quad (3)$$

where D_A, D_B and D_C are the diffusion coefficients of A, B and C, respectively (the model details are given in the ESI† section 2).

A and C being colorless, we are not able to measure their diffusion coefficients using brightfield images. Instead, we estimate them by comparing the molar weights of the molecules with B (see ESI† section 1). Then, the rate constant k is the only unknown parameter left in our model, which we therefore treat as a fitting parameter.

Eqn (1)–(3) are solved numerically for different reaction rate constants k and the numerical solution is compared with the measured profiles of B along the central axis of the daughter droplet (sketched by the x axis on Fig. 2d). The comparison is then used to obtain the value of k which makes the experimental and simulated profiles of B fit best for different times. A typical example is shown in Fig. 3a, where experimental profiles of DCPIP are superposed with their numerical best fits at four time points. Repeating the experiment for five initial concentrations A_0 yields k = 83 ± 4 $\mathrm{M^{-1}\ s^{-1}}$.

While this method yields a value of the reaction rate, it relies on image fitting techniques. A simpler approach is to monitor the total amount of B in the fused droplet over time ($\bar{B}$). This reduces the problem to fitting a time series of a single variable whose evolution integrates the effects of both diffusion and reaction. Three representative fits are shown in Fig. 3b, where the solid line is a fit to the experimental data based on the integrated R–D model. Again, the model captures well the evolution of the experimental measurements over the whole course of the experiment.

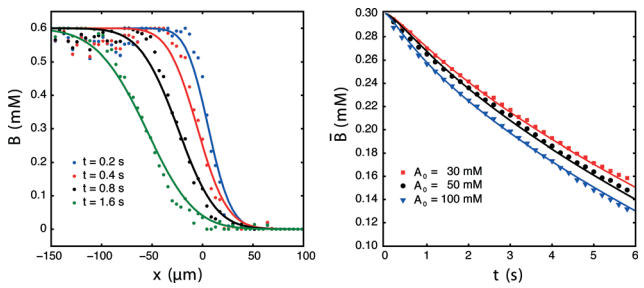

Fig. 3 (a) Spatial distribution of B and corresponding simulated best fits at different time points. t = 0 s is the time of droplet fusion; x = 0 μm is the initial position of the fused interface. The initial concentrations are A_0 = 100 mM and B_0 = 0.6 mM. The solutions are at pH = 6. (b) Evolution of the total amount of B ($\bar{B}$) over time, for three different values of A_0. The solid lines are the best fits obtained from the R–D model.

The values of the kinetic constant from the two R–D fitting methods are compared, in Fig. 4, with measurements done in a commercial stopped-flow spectrometer (Biologic Science Instruments) using the same solutions. Since we keep $A_0 \gg B_0$ in our experiments, the process in the well-mixed case behaves as a pseudo-first order reaction[25] and the DCPIP decreases exponentially with time. The characteristic rate of the decay $k_\mathrm{obs} = kA_0$ is provided directly by the stopped flow apparatus. In the droplet experiments however, the pseudo-first order approximation does not hold since the concentrations of A and B vary in space and time. Instead, the fits with the R–D model yield the value of k. Nonetheless, the measurements in droplets and using the stopped-flow are in very good agreement, as shown in Fig. 4. Indeed, the three methods yield values of k between 80 and 87 $\mathrm{M^{-1}\ s^{-1}}$, in agreement with previously reported values.[26]

In both the local and integral fitting protocols, k is obtained by finding the minimum of the residual error between the simulations and the experiments (see ESI† sections 3 and 4). The selectivity of these measurements can then be evaluated by observing the behavior of the residual as k departs from the optimal value, particularly while varying the time window in which the fits are performed. We find that a reliable measure of k can be obtained for time windows larger than around 1 s, independently of k_obs, and that the selectivity improves for longer windows (ESI† Fig. S3 & S4). This result implies that chemical information can be extracted from the R–D front even at times $t \gg k_\mathrm{obs}^{-1}$. This contrasts strongly with most approaches in which fast kinetics require a very high time resolution of the measurement method. So while techniques that rely on mixing the species cannot resolve reactions whose typical time is shorter than the mixing time, the droplet-based measurement relies on long observations even for fast kinetics.

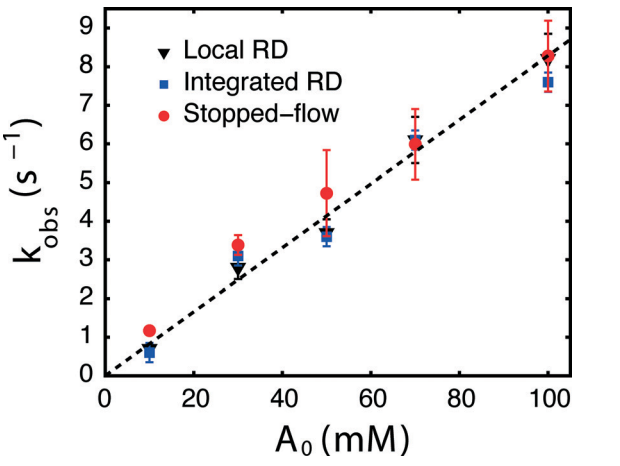

Fig. 4 Comparison between on-chip measurements of k, obtained from spatial and integrated fits, with measurements of $k_\mathrm{obs} = kA_0$ performed in a stopped-flow spectrometer. B_0 = 0.6 mM for all experiments. The error bars on the stopped flow measurement correspond to variations between different runs. The error bars on the reaction–diffusion measurements correspond to the selectivity of the fitting procedure by taking the value of k_obs at which the residue increases by 1% from the minimum value.

In practical terms, the results shown here demonstrate that the microfluidic approach can yield equivalent results to the stopped flow apparatus, while using 20 nL of reagents per measurement, compared with typically 100 μL of each reagent per run in the stopped flow. The effective sample consumption is therefore decreased more than 5000 fold. The time required to run these reactions is similar in an automated stopped flow and in the microfluidic system described above. This time can however be greatly reduced by working in a parallelized chip that allows all five conditions of Fig. 4 to be tested on an integrated device. Such a design is shown in Fig. 5 (and ESI† movie S3), where the rail and anchor pattern has been reproduced in order to allow six independent conditions to be tested on a single chip (see ESI† section 5 for chip dimensions).

In this parallel chip, the top row of traps is filled with a single drop of each of the six independent reagents, which originate from different syringes outside the chip (Fig. 5a). Once those positions are occupied (Fig. 5b), six drops of the common reagent are produced on the left hand side, before a gentle flux of oil is used to direct them to the empty trapping sites. It is also possible to use the laser to guide individual droplets into the desired anchors.[17] This leads to all six positions being occupied by six different pairs of drops (Fig. 5c) and the independent reactions can again be triggered, when desired, by the laser.

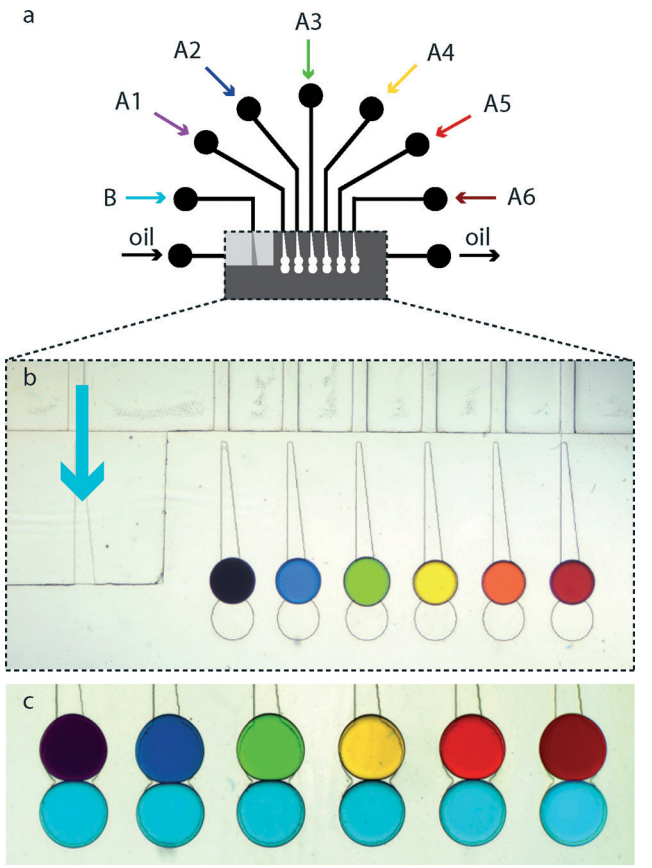

Fig. 5 A parallel chip that serves to test a solution *via* six independent reactions. (a) A sketch of the chip that shows the different inlets. (b) The chip is initially filled with a single droplet of the six test conditions, before the test solution (light blue) is injected from the left-most inlet. (c) After filling, each trap contains a different pair of droplets that can be fused at will by using the focused laser.

In conclusion, the method presented here relies on integrating different capabilities on a single chip (drop production and transport, active merging, analysis of the R–D front) to provide a system for measuring fast chemical kinetics while using ultra-low volumes. The fluids are mostly stationary but the geometry and the external flows can be combined to implement temporary movements. Combinatorial assays can thus be obtained by pairing droplets that originate from many different inlets through a pre-programmed sequence of operations. In practice, a few μL of sample are sufficient to run a series of reactions with different substrates in a few minutes. This performance yields significant gains in cost and time, motivating the use of such a device in the screening of molecular interactions or for measuring the kinetics of precious enzymes.

Acknowledgements

The authors acknowledge the help of Caroline Frot with microfabrication, useful discussions with Christopher Bayer and other members of the Florian Hollfelder group of Cambridge University. The research leading to these results received funding from the European Research Council (ERC) Grant Agreement 278248 Multicell.

References

1 H. Song, D. Chen and R. F. Ismagilov, *Angew. Chem., Int. Ed.*, 2006, **45**, 7336–7356.
2 S.-Y. Teh, R. Lin, L.-H. Hung and A. Lee, *Lab Chip*, 2008, **8**, 198–220.
3 A. B. Theberge, F. Courtois, Y. Schaerli, M. Fischlechner, C. Abell, F. Hollfelder and W. T. S. Huck, *Angew. Chem., Int. Ed.*, 2010, **49**, 5846–5868.
4 N. R. Beer, B. J. Hindson, E. K. Wheeler, S. B. Hall, K. A. Rose, I. M. Kennedy and B. W. Colston, *Anal. Chem.*, 2007, **79**, 8471–8475.
5 A. Hatch, J. Fisher, A. Tovar, A. Hsieh, R. Lin, S. Pentoney, D. Yang and A. Lee, *Lab Chip*, 2011, **11**, 3838–3845.
6 H. N. Joensson and H. Andersson Svahn, *Angew. Chem., Int. Ed.*, 2012, **51**, 12176–12192.
7 D. Chiu, R. Lorenz and G. Jeffries, *Anal. Chem.*, 2009, **81**, 5111–5118.
8 B. Sun, D. Lim, J. Kuo, C. Kuyper and D. Chiu, *Langmuir*, 2004, **20**, 9437–9440.
9 A. Huebner, C. Abell, W. T. S. Huck, C. N. Baroud and F. Hollfelder, *Anal. Chem.*, 2011, **83**, 1462–1468.
10 C. Sims and N. Allbritton, *Lab Chip*, 2007, **7**, 423–440.
11 P. Abbyad, R. Dangla, A. Alexandrou and C. N. Baroud, *Lab Chip*, 2011, **11**, 813–821.
12 K. Choi, A. H. Ng, R. Fobel and A. R. Wheeler, *Annu. Rev. Anal. Chem.*, 2012, **5**, 413–440.

13 Y. Bourquin, J. Reboud, R. Wilson, Y. Zhang and J. M. Cooper, *Lab Chip*, 2011, **11**, 2725–2730.
14 C. N. Baroud, F. Gallaire and R. Dangla, *Lab Chip*, 2010, **10**, 2032–2045.
15 R. Dangla, S. Kayi and C. Baroud, *Proc. Natl. Acad. Sci. U. S. A.*, 2013, **110**, 853–858.
16 K. Stephan, P. Pittet, L. Renaud, P. Kleimann, P. Morin, N. Ouaini and R. Ferrigno, *J. Micromech. Microeng.*, 2007, **17**, N69.
17 E. Fradet, C. McDougall, P. Abbyad, R. Dangla, D. McGloin and C. N. Baroud, *Lab Chip*, 2011, **11**, 4228–4234.
18 S. Sugiura, M. Nakajima, S. Iwamoto and M. Seki, *Langmuir*, 2001, **17**, 5562–5566.
19 R. Dangla, E. Fradet, Y. Lopez and C. N. Baroud, *J. Phys. D: Appl. Phys.*, 2013, **46**, 114003.
20 C. Holtze, A. Rowat, J. Agresti, J. Hutchison, F. Angile, C. Schmitz, S. Köster, H. Duan, K. Humphry and R. Scanga, *et al., Lab Chip*, 2008, **8**, 1632–1639.
21 H. Song, J. Tice and R. F. Ismagilov, *Angew. Chem., Int. Ed.*, 2003, **42**, 768–772.
22 X. Niu, S. Gulati, J. Edel and A. de Mello, *Lab Chip*, 2008, **8**, 1837–1841.
23 M. Zagnoni, C. N. Baroud and J. M. Cooper, *Phys. Rev. E*, 2009, **80**, 046303.
24 L. Mazutis and A. D. Griffiths, *Lab Chip*, 2012, **12**, 1800–1806.
25 K. Matsumura, Y. Enoki, H. Kohzuki and S. Sakata, *Jpn. J. Physiol.*, 1990, **40**, 567–571.
26 B. Tonomura, H. Nakatani, M. Ohnishi, J. Yamaguchi-Ito and K. Hiromi, *Anal. Biochem.*, 1978, **84**, 370–383.

Bibliography

[1] Lorenz M Mayr and Dejan Bojanic. Novel trends in high-throughput screening. *Current opinion in pharmacology*, 9(5):580–588, 2009.

[2] Adam Smith. Screening for drug discovery: the leading question. *Nature*, 418(6896):453–459, 2002.

[3] Rémi Dangla. 2D droplet microfluidics driven by confinement gradients. *PhD thesis*, 2012.

[4] Jonathan J Burbaum. Miniaturization technologies in hts: how fast, how small, how soon? *Drug Discovery Today*, 3(7):313–322, 1998.

[5] `http://www.fishersci.com/ecomm/servlet/fsproductdetail_10652_7105764/`. [Online; accessed 20-July-2013].

[6] `http://research.ncl.ac.uk/bioHT/`. [Online; accessed 20-July-2013].

[7] `http://www.clontech.com/US/Products/Fluorescent_Proteins_and_Reporters/Chemiluminescent_Reporters/Luciferase_Assay/xxclt_displayImage.jsp?imgCntId=20757&sitex`. [Online; accessed 20-July-2013].

[8] `http://newsroom.ucr.edu/1351/`. [Online; accessed 20-July-2013].

[9] Robert Hołyst and Marek Litniewski. Heat transfer at the nanoscale: evaporation of nanodroplets. *Physical review letters*, 100(5):055701, 2008.

[10] Pierre-Gilles De Gennes. Wetting: statics and dynamics. *Reviews of modern physics*, 57(3):827, 1985.

[11] Joshua Lederberg. A simple method for isolating individual microbes. *Journal of Bacteriology*, 68(2):258, 1954.

[12] Dan S Tawfik and Andrew D Griffiths. Man-made cell-like compartments for molecular evolution. *Nature biotechnology*, 16(7):652–656, 1998.

[13] Michael G Pollack, Richard B Fair, and Alexander D Shenderov. Electrowetting-based actuation of liquid droplets for microfluidic applications. *Applied Physics Letters*, 77(11):1725–1726, 2000.

[14] Sung Kwon Cho, Hyejin Moon, and Chang-Jin Kim. Creating, transporting, cutting, and merging liquid droplets by electrowetting-based actuation for digital microfluidic circuits. *Microelectromechanical Systems, Journal of*, 12(1):70–80, 2003.

[15] Achim Wixforth. Acoustically driven planar microfluidics. *Superlattices and Microstructures*, 33(5):389–396, 2003.

[16] Paul Calvert. Inkjet printing for materials and devices. *Chemistry of Materials*, 13(10):3299–3305, 2001.

[17] Charles N Baroud, Francois Gallaire, and Rémi Dangla. Dynamics of microfluidic droplets. *Lab on a Chip*, 10(16):2032–2045, 2010.

[18] Todd Thorsen, Richard W Roberts, Frances H Arnold, and Stephen R Quake. Dynamic pattern formation in a vesicle-generating microfluidic device. *Physical review letters*, 86(18):4163, 2001.

[19] Shelley L Anna, Nathalie Bontoux, and Howard A Stone. Formation of dispersions using Òflow focusingÓ in microchannels. *Applied physics letters*, 82:364, 2003.

[20] Rémi Dangla, S Cagri Kayi, and Charles N Baroud. Droplet microfluidics driven by gradients of confinement. *Proceedings of the National Academy of Sciences*, 110(3):853–858, 2013.

[21] L Gálfi and Z Rácz. Properties of the reaction front in an A+B→C type reaction-diffusion process. *Physical Review A*, 38(6):3151, 1988.

[22] PMJ Trevelyan. Analytical small-time asymptotic properties of A+B→C fronts. *Physical Review E*, 80(4):046118, 2009.

[23] H. Song, J.D. Tice, and R.F. Ismagilov. A microfluidic system for controlling reaction networks in time. *Angewandte Chemie*, 115(7):792–796, 2003.

[24] Lucas Frenz, Joshua Blouwolff, Andrew D Griffiths, and Jean-Christophe Baret. Microfluidic production of droplet pairs. *Langmuir*, 24(20):12073–12076, 2008.

[25] Nicolas Bremond, Abdou R Thiam, and Jérôme Bibette. Decompressing emulsion droplets favors coalescence. *Physical review letters*, 100(2):024501, 2008.

[26] Linas Mazutis, Jean-Christophe Baret, Patrick Treacy, Yousr Skhiri, Ali Fallah Araghi, Michael Ryckelynck, Valérie Taly, and Andrew D Griffiths. Multi-step microfluidic droplet processing: kinetic analysis of an in vitro translated enzyme. *Lab on a Chip*, 9(20):2902–2908, 2009.

[27] Xize Niu, Shelly Gulati, Joshua B Edel, et al. Pillar-induced droplet merging in microfluidic circuits. *Lab on a Chip*, 8(11):1837–1841, 2008.

[28] Yung-Chieh Tan, Jeffrey S Fisher, Alan I Lee, Vittorio Cristini, and Abraham Phillip Lee. Design of microfluidic channel geometries for the control of droplet volume, chemical concentration, and sorting. *Lab on a Chip*, 4(4):292–298, 2004.

[29] Fabien Jousse, Robert Farr, Darren R Link, Michael J Fuerstman, and Piotr Garstecki. Bifurcation of droplet flows within capillaries. *Physical Review E*, 74(3):036311, 2006.

[30] Michael J Fuerstman, Piotr Garstecki, and George M Whitesides. Coding/decoding and reversibility of droplet trains in microfluidic networks. *Science*, 315(5813):828–832, 2007.

[31] Manu Prakash and Neil Gershenfeld. Microfluidic bubble logic. *Science*, 315(5813):832–835, 2007.

[32] Michael Schindler and Armand Ajdari. Droplet traffic in microfluidic networks: A simple model for understanding and designing. *Physical review letters*, 100(4):044501, 2008.

[33] Jongin Hong, Minsuk Choi, Joshua B Edel, et al. Passive self-synchronized two-droplet generation. *Lab on a Chip*, 10(20):2702–2709, 2010.

[34] C.N. Baroud, M.R. de Saint Vincent, and J.P. Delville. An optical toolbox for total control of droplet microfluidics. *Lab Chip*, 7(8):1029–1033, 2007.

[35] Wei-Heong Tan and Shoji Takeuchi. A trap-and-release integrated microfluidic system for dynamic microarray applications. *Proceedings of the National Academy of Sciences*, 104(4):1146–1151, 2007.

[36] W. Shi, J. Qin, N. Ye, and B. Lin. Droplet-based microfluidic system for individual Caenorhabditis elegans assay. *Lab Chip*, 8(9):1432–1435, 2008.

[37] Hakim Boukellal, Šeila Selimović, Yanwei Jia, Galder Cristobal, and Seth Fraden. Simple, robust storage of drops and fluids in a microfluidic device. *Lab on a Chip*, 9(2):331–338, 2009.

[38] Jung-uk Shim, Galder Cristobal, Darren R Link, Todd Thorsen, Yanwei Jia, Katie Piattelli, and Seth Fraden. Control and measurement of the phase behavior of aqueous solutions using microfluidics. *Journal of the American Chemical Society*, 129(28):8825–8835, 2007.

[39] Christian HJ Schmitz, Amy C Rowat, Sarah Köster, and David A Weitz. Dropspots: a picoliter array in a microfluidic device. *Lab on a Chip*, 9(1):44–49, 2009.

[40] Jon F Edd, Katherine J Humphry, Daniel Irimia, David A Weitz, and Mehmet Toner. Nucleation and solidification in static arrays of monodisperse drops. *Lab on a Chip*, 9(13):1859–1865, 2009.

[41] A. Huebner, D. Bratton, G. Whyte, M. Yang, A. J. deMello, C. Abell, and F. Hollfelder. Static microdroplet arrays: a microfluidic device for droplet trapping, incubation and release for enzymatic and cell-based assays. *Lab Chip*, 9(5):692–698, 2009.

[42] Paul Abbyad, Rémi Dangla, Antigoni Alexandrou, and Charles N Baroud. Rails and anchors: guiding and trapping droplet microreactors in two dimensions. *Lab on a Chip*, 11(5):813–821, 2011.

[43] Dino Di Carlo, Nima Aghdam, and Luke P Lee. Single-cell enzyme concentrations, kinetics, and inhibition analysis using high-density hydrodynamic cell isolation arrays. *Analytical chemistry*, 78(14):4925–4930, 2006.

[44] A.M. Huebner, C. Abell, W.T.S. Huck, C.N. Baroud, and F. Hollfelder. Monitoring a reaction at submillisecond resolution in picoliter volumes. *Analytical Chemistry-Columbus*, 83(4):1462, 2011.

[45] Su Eun Chung, Wook Park, Sunghwan Shin, Seung Ah Lee, and Sunghoon Kwon. Guided and fluidic self-assembly of microstructures using railed microfluidic channels. *Nature materials*, 7(7):581–587, 2008.

[46] Fr Hauksbee. An account of an experiment touching the direction of a drop of oil of oranges, between two glass planes, towards any side of them that is nearest press'd together. by mr. fr. hauksbee, frs. *Philosophical Transactions*, 27(325-336):395–396, 1710.

[47] Gaspard Monge. *Mémoire sur quelques effets d'attraction ou de répulsion apparente entre les molécules de matière*. De l'Imprimerie Royale, 1787.

[48] Thomas Young. An essay on the cohesion of fluids. *Philosophical Transactions of the Royal Society of London*, 95:65–87, 1805.

[49] Pierre Simon de Laplace. *Traité De Mécanique Céleste: Supplément au dixième livre du traité de méchanique céleste sur l'action capillaire*, volume 6. Duprat, 1808.

[50] Pierre-Gilles De Gennes, Françoise Brochard-Wyart, and David Quéré. *Capillarity and wetting phenomena: drops, bubbles, pearls, waves*. Springer, 2004.

[51] Eric Lauga, Abraham D Stroock, and Howard A Stone. Three-dimensional flows in slowly varying planar geometries. *Physics of fluids*, 16:3051, 2004.

[52] Geoffrey Taylor and PG Saffman. A note on the motion of bubbles in a hele-shaw cell and porous medium. *The Quarterly Journal of Mechanics and Applied Mathematics*, 12(3):265–279, 1959.

[53] Rémi Dangla, François Gallaire, and Charles N Baroud. Microchannel deformations due to solvent-induced PDMS. *Lab on a Chip*, 10(21):2972–2978, 2010.

[54] George Keith Batchelor. *An introduction to fluid dynamics*. Cambridge university press, 2000.

[55] SRK Maruvada and C-W Park. Retarded motion of bubbles in hele–shaw cells. *Physics of fluids*, 8:3229, 1996.

[56] JS Lee and YC Fung. Stokes flow around a circular cylindrical post confined between two parallel plates. *J. Fluid Mech*, 37(657-670):16, 1969.

[57] R. Dangla, S. Lee, and C.N. Baroud. Trapping microfluidic drops in wells of surface energy. *Physical Review Letters*, 107(12):124501, 2011.

[58] Jean-Christophe Baret, Oliver J Miller, Valerie Taly, Michaël Ryckelynck, Abdeslam El-Harrak, Lucas Frenz, Christian Rick, Michael L Samuels, J Brian Hutchison, Jeremy J Agresti, et al. Fluorescence-activated droplet sorting (fads): efficient microfluidic cell sorting based on enzymatic activity. *Lab on a Chip*, 9(13):1850–1858, 2009.

[59] Leonard A Herzenberg, Richard G Sweet, and Leonore A Herzenberg. Fluorescence-activated cell sorting. *Sci Am*, 234(3):108–117, 1976.

[60] Mack J Fulwyler. Electronic separation of biological cells by volume. *Science*, 150(3698):910–911, 1965.

[61] K. Ahn, J. Agresti, H. Chong, M. Marquez, and DA Weitz. Electrocoalescence of drops synchronized by size-dependent flow in microfluidic channels. *Applied Physics Letters*, 88(26):264105–264105, 2006.

[62] M. L. Cordero, D. R. Burnham, C. N. Baroud, and D. McGloin. Thermocapillary manipulation of droplets using holographic beam shaping: Microfluidic pin ball. *Appl. Phys. Lett.*, 93(3):034107, 2008.

[63] Kai Zhang, Qionglin Liang, Sai Ma, Xuan Mu, Ping Hu, Yiming Wang, and Guoan Luo. On-chip manipulation of continuous picoliter-volume superparamagnetic droplets using a magnetic force. *Lab on a Chip*, 9(20):2992–2999, 2009.

[64] Thomas Franke, Adam R Abate, David A Weitz, and Achim Wixforth. Surface acoustic wave (saw) directed droplet flow in microfluidics for PDMS devices. *Lab on a Chip*, 9(18):2625–2627, 2009.

[65] X. Niu, F. Gielen, A.J. demello, and J.B. Edel. Electro-coalescence of digitally controlled droplets. *Analytical chemistry*, 81(17):7321–7325, 2009.

[66] Pierre-Gilles de Gennes. Guidage d'une microgoutte par un faisceau laser. *Comptes Rendus Physique*, 6(10):1149–1152, 2005.

[67] C. N. Baroud, J. P. Delville, F. Gallaire, and R. Wunenburger. Thermocapillary valve for droplet production and sorting. *Phys. Rev. E*, 75(4):046302, 2007.

[68] D. G. Grier. A revolution in optical manipulation. *Nature*, 424(6950):810–816, 2003.

[69] I Perch-Nielsen, Peter John Rodrigo, Carlo Amadeo Alonzo, and Jesper Glückstad. Autonomous and 3D real-time multi-beam manipulation in a microfluidic environment. *Optics express*, 14(25):12199–12205, 2006.

[70] María Luisa Cordero, Emilie Verneuil, François Gallaire, and Charles N Baroud. Time-resolved temperature rise in a thin liquid film due to laser absorption. *Physical Review E*, 79(1):011201, 2009.

[71] Emilie Verneuil, ìa Luisa Cordero, François Gallaire, and Charles N Baroud. Laser-induced force on a microfluidic drop: origin and magnitude. *Langmuir*, 25(9):5127–5134, 2009.

[72] C Holtze, AC Rowat, JJ Agresti, JB Hutchison, FE Angile, CHJ Schmitz, S Köster, H Duan, KJ Humphry, RA Scanga, et al. Biocompatible surfactants for water-in-fluorocarbon emulsions. *Lab on a Chip*, 8(10):1632–1639, 2008.

[73] Jean-Christophe Baret. Surfactants in droplet-based microfluidics. *Lab on a Chip*, 12(3):422–433, 2012.

[74] Oliver J Miller, Abdeslam El Harrak, Thomas Mangeat, Jean-Christophe Baret, Lucas Frenz, Bachir El Debs, Estelle Mayot, Michael L Samuels, Eamonn K Rooney, Pierre Dieu, et al. High-resolution dose–response screening using droplet-based microfluidics. *Proceedings of the National Academy of Sciences*, 109(2):378–383, 2012.

[75] Fabrice Gielen, Liisa van Vliet, Bartosz T Koprowski, Sean RA Devenish, Martin Fischlechner, Joshua B Edel, Xize Niu, Andrew J deMello, and Florian Hollfelder. A fully unsupervised compartment-on-demand platform for precise nanoliter assays of time-dependent steady-state enzyme kinetics and inhibition. *Analytical chemistry*, 85(9):4761–4769, 2013.

[76] V Barbier, H Willaime, P Tabeling, and F Jousse. Producing droplets in parallel microfluidic systems. *Physical Review E*, 74(4):046306, 2006.

[77] Takasi Nisisako and Toru Torii. Microfluidic large-scale integration on a chip for mass production of monodisperse droplets and particles. *Lab on a Chip*, 8(2):287–293, 2008.

[78] Michinao Hashimoto, Sergey S Shevkoplyas, Beata Zasońska, Tomasz Szymborski, Piotr Garstecki, and George M Whitesides. Formation of bubbles and droplets in parallel, coupled flow-focusing geometries. *Small*, 4(10):1795–1805, 2008.

[79] S. Sugiura, M. Nakajima, S. Iwamoto, and M. Seki. Interfacial tension driven monodispersed droplet formation from microfabricated channel array. *Langmuir*, 17(18):5562–5566, 2001.

[80] Isao Kobayashi, Kunihiko Uemura, and Mitsutoshi Nakajima. Controlled generation of monodisperse discoid droplets using microchannel arrays. *Langmuir*, 22(26):10893–10897, 2006.

[81] Rémi Dangla, Etienne Fradet, Yonatan Lopez, and Charles N Baroud. The physical mechanisms of step emulsification. *Journal of Physics D: Applied Physics*, 46(11):114003, 2013.

[82] Seung-Yong Jung, Scott T Retterer, and C Patrick Collier. On-demand generation of monodisperse femtolitre droplets by shape-induced shear. *Lab on a Chip*, 10(20):2688–2694, 2010.

[83] Marc A Unger, Hou-Pu Chou, Todd Thorsen, Axel Scherer, and Stephen R Quake. Monolithic microfabricated valves and pumps by multilayer soft lithography. *Science*, 288(5463):113–116, 2000.

[84] Tom R Reid. *The chip: How two Americans invented the microchip and launched a revolution*. Random House Digital, Inc., 2007.

[85] Todd Thorsen, Sebastian J Maerkl, and Stephen R Quake. Microfluidic large-scale integration. *Science*, 298(5593):580–584, 2002.

[86] Seung-Yong Jung, Scott T Retterer, and C Patrick Collier. Interfacial tension controlled fusion of individual femtolitre droplets and triggering of confined chemical reactions on demand. *Lab on a Chip*, 10(24):3373–3376, 2010.

[87] A. Huebner, C. Abell, W. T. S. Huck, C. N. Baroud, and F. Hollfelder. Monitoring a reaction at submillisecond resolution in picoliter volumes. *Anal. Chem.*, 83:1462–1468, 2011.

[88] C. N. Baroud, M. R. de Saint Vincent, and J. P. Delville. An optical toolbox for total control of droplet microfluidics. *Lab Chip*, 7:1029–1033, July 2007.

[89] E. Fradet, C. McDougall, P. Abbyad, R. Dangla, D. McGloin, and C.N. Baroud. Combining rails and anchors with laser forcing for selective manipulation within 2D droplet arrays. *Lab on a Chip*, 11(24):4228–4234, 2011.

[90] E. Fradet, P. Abbyad, M.H. Vos, and C.N. Baroud. Parallel measurements of reaction kinetics using ultralow-volumes. *Lab on a Chip*, 2013.

[91] David C Duffy, J Cooper McDonald, Olivier JA Schueller, and George M Whitesides. Rapid prototyping of microfluidic systems in poly (dimethylsiloxane). *Analytical chemistry*, 70(23):4974–4984, 1998.

[92] Janelle R Anderson, Daniel T Chiu, Rebecca J Jackman, Oksana Cherniavskaya, J Cooper McDonald, Hongkai Wu, Sue H Whitesides, and George M Whitesides. Fabrication of topologically complex three-dimensional microfluidic systems in PDMS by rapid prototyping. *Analytical Chemistry*, 72(14):3158–3164, 2000.

[93] Jenifer Clausell-Tormos, Diana Lieber, Jean-Christophe Baret, Abdeslam El-Harrak, Oliver J Miller, Lucas Frenz, Joshua Blouwolff, Katherine J Humphry, Sarah Köster, Honey Duan, et al. Droplet-based microfluidic platforms for the encapsulation and screening of mammalian cells and multicellular organisms. *Chemistry & biology*, 15(5):427–437, 2008.

[94] Eric Brouzes, Martina Medkova, Neal Savenelli, Dave Marran, Mariusz Twardowski, J Brian Hutchison, Jonathan M Rothberg, Darren R Link, Norbert Perrimon, and Michael L Samuels. Droplet microfluidic technology for single-cell high-throughput screening. *Proceedings of the National Academy of Sciences*, 106(34):14195–14200, 2009.

[95] Mingyan He, J Scott Edgar, Gavin DM Jeffries, Robert M Lorenz, J Patrick Shelby, and Daniel T Chiu. Selective encapsulation of single cells and subcellular organelles into picoliter-and femtoliter-volume droplets. *Analytical Chemistry*, 77(6):1539–1544, 2005.

[96] Linas Mazutis, Ali Fallah Araghi, Oliver J Miller, Jean-Christophe Baret, Lucas Frenz, Agnes Janoshazi, Valérie Taly, Benjamin J Miller, J Brian Hutchison, Darren Link, et al. Droplet-based microfluidic systems for high-throughput single dna molecule isothermal amplification and analysis. *Analytical chemistry*, 81(12):4813–4821, 2009.

[97] Xize Niu, Fabrice Gielen, Joshua B Edel, et al. A microdroplet dilutor for high-throughput screening. *Nature chemistry*, 3(6):437–442, 2011.

[98] PV Danckwerts. The definition and measurement of some characteristics of mixtures. *Applied Scientific Research, Section A*, 3(4):279–296, 1952.

[99] Howard A Stone, Abraham D Stroock, and Armand Ajdari. Engineering flows in small devices: microfluidics toward a lab-on-a-chip. *Annu. Rev. Fluid Mech.*, 36:381–411, 2004.

[100] Michelle R Bringer, Cory J Gerdts, Helen Song, Joshua D Tice, and Rustem F Ismagilov. Microfluidic systems for chemical kinetics that rely on chaotic mixing in droplets. *Philosophical Transactions of the Royal Society of London. Series A: Mathematical, Physical and Engineering Sciences*, 362(1818):1087–1104, 2004.

[101] Andrew Evan Kamholz, Bernhard H Weigl, Bruce A Finlayson, and Paul Yager. Quantitative analysis of molecular interaction in a microfluidic channel: the T-sensor. *Analytical Chemistry*, 71(23):5340–5347, 1999.

[102] P. Curie. Sur la symétrie dans les phénomènes physiques, symétrie d'un champ électrique et d'un champ magnétique. *J. Phys. Theor. Appl.*, 3(1):393–415, 1894.

[103] O. Tresse, T. Jouenne, and GA Junter. Antibacterial efficacy of tobramycin against anaerobic Escherichia coli cultures in the presence of electron acceptors. *Journal of Antimicrobial Chemotherapy*, 40(3):419–421, 1997.

[104] Roger Y Tsien. The green fluorescent protein. *Annual review of biochemistry*, 67(1):509–544, 1998.

[105] Stephen A Rice. *Diffusion-limited reactions*. Elsevier, 1985.

[106] Kenneth A Connors. *Chemical kinetics: the study of reaction rates in solution*. Wiley. com, 1990.

[107] M von Smoluchowski. Versuch einer mathematischen Theorie der Koagulationskinetik kolloider Lösungen. *Z. phys. Chem*, 92(129-168):9, 1917.

[108] RS Berry, SA Rice, and J Ross. *Physical Chemistry. 2nd*. New York: Oxford University Press, 2000.

[109] Peter Waage and CM Gulberg. Studies concerning affinity. *Journal of chemical education*, 63(12):1044, 1986.

[110] H Gutfreund. Rapid-flow techniques and their contributions to enzymology. *Trends in biochemical sciences*, 24(11):457–460, 1999.

[111] H Hartridge and FJW Roughton. A method of measuring the velocity of very rapid chemical reactions. *Proceedings of the Royal Society of London. Series A, Containing Papers of a Mathematical and Physical Character*, 104(726):376–394, 1923.

[112] Delafield DuBois. An apparatus for the study of rapid chemical reactions. *Journal of Biological Chemistry*, 137(1):123–138, 1941.

[113] Q H_ Gibson and L Milnes. Apparatus for rapid and sensitive spectrophotometry. *Biochemical Journal*, 91(1):161, 1964.

[114] Britton Chance. The kinetics of the enzyme-substrate compound of peroxidase. *Journal of Biological Chemistry*, 151(2):553–577, 1943.

[115] Mo Eigen. Fast elementary steps in chemical reaction mechansims. *Pure and Applied Chemistry (England)*, 6, 1963.

[116] H Gutfreund. Transients and relaxation kinetics of enzyme reactions. *Annual Review of Biochemistry*, 40(1):315–344, 1971.

[117] Ben'ichiro Tonomura, Hiroshi Nakatani, Masatake Ohnishi, Junko Yamaguchi-Ito, and Keitaro Hiromi. Test reactions for a stopped-flow apparatus: Reduction of 2, 6-dichlorophenolindophenol and potassium ferricyanide by l-ascorbic acid. *Analytical biochemistry*, 84(2):370–383, 1978.

[118] Kazuhito Matsumura, Yasunori Enoki, Hisaharu Kohzuki, and Susumu Sakata. A simple procedure for determination of the dead time of a stopped-flow instrument. *The Japanese journal of physiology*, 40(4):567–571, 1990.

[119] Albert Einstein. *Investigations on the Theory of the Brownian Movement*. Dover-Publications. com, 1956.

[120] Alan Mathison Turing. The chemical basis of morphogenesis. *Bulletin of mathematical biology*, 52(1):153–197, 1990.

[121] Kyoung-Jin Lee, William D McCormick, John E Pearson, and Harry L Swinney. Experimental observation of self-replicating spots in a reaction-diffusion system. *Nature*, 369(6477):215–218, 1994.

[122] S Nettesheim, A Von Oertzen, HH Rotermund, and G Ertl. Reaction diffusion patterns in the catalytic CO-oxidation on Pt (110): Front propagation and spiral waves. *The Journal of chemical physics*, 98:9977, 1993.

[123] Grigory Isaakovich Barenblatt. *Scaling, self-similarity, and intermediate asymptotics: dimensional analysis and intermediate asymptotics*, volume 14. Cambridge University Press, 1996.

[124] Haim Taitelbaum, Yong-Eun Lee Koo, Shlomo Havlin, Raoul Kopelman, and George H Weiss. Exotic behavior of the reaction front in the A+B→C reaction-diffusion system. *Physical Review A*, 46(4):2151, 1992.

[125] PMJ Trevelyan. Higher-order large-time asymptotics for a reaction of the form nA+mB→C. *Physical Review E*, 79(1):016105, 2009.

[126] Yong-Eun Lee Koo and Raoul Kopelman. Space-and time-resolved diffusion-limited binary reaction kinetics in capillaries: experimental observation of segregation, anomalous exponents, and depletion zone. *Journal of statistical physics*, 65(5-6):893–918, 1991.

[127] Andrew Yen and Raoul Kopelman. Experimental study of a ternary A+2B→C reaction-diffusion system with a propagating reaction front: Scaling exponents. *Physical Review E*, 56(3):3694, 1997.

[128] Martin Z Bazant and Howard A Stone. Asymptotics of reaction–diffusion fronts with one static and one diffusing reactant. *Physica D: Nonlinear Phenomena*, 147(1):95–121, 2000.

[129] Christophe Léger, Françoise Argoul, and Martin Z Bazant. Front dynamics during diffusion-limited corrosion of ramified electrodeposits. *The Journal of Physical Chemistry B*, 103(28):5841–5851, 1999.

[130] Charles N Baroud, Fridolin Okkels, Laure Ménétrier, and Patrick Tabeling. Reaction-diffusion dynamics: Confrontation between theory and experiment in a microfluidic reactor. *Physical Review E*, 67(6):060104, 2003.

[131] Jean-Baptiste Salmon, Claire Dubrocq, Patrick Tabeling, Sandrine Charier, Damien Alcor, Ludovic Jullien, and Fabien Ferrage. An approach to extract rate constants from reaction-diffusion dynamics in a microchannel. *Analytical chemistry*, 77(11):3417–3424, 2005.

[132] Laurence Rongy. Influence of Marangoni and buoyancy convection on the propagation of reaction-diffusion fronts. *PhD thesis*, 2008.

[133] Helen Song and Rustem F Ismagilov. Millisecond kinetics on a microfluidic chip using nanoliters of reagents. *Journal of the American Chemical Society*, 125(47):14613–14619, 2003.

[134] Monpichar Srisa-Art, Emily C Dyson, Andrew J deMello, and Joshua B Edel. Monitoring of real-time streptavidin- biotin binding kinetics using droplet microfluidics. *Analytical chemistry*, 80(18):7063–7067, 2008.

[135] L Spencer Roach, Helen Song, and Rustem F Ismagilov. Controlling nonspecific protein adsorption in a plug-based microfluidic system by controlling interfacial chemistry using fluorous-phase surfactants. *Analytical chemistry*, 77(3):785–796, 2005.

[136] Albert Liau, Rohit Karnik, Arun Majumdar, and Jamie H Doudna Cate. Mixing crowded biological solutions in milliseconds. *Analytical chemistry*, 77(23):7618–7625, 2005.

[137] Elizabeth M Miller and Aaron R Wheeler. A digital microfluidic approach to homogeneous enzyme assays. *Analytical chemistry*, 80(5):1614–1619, 2008.

[138] Thomas Traut. *Allosteric regulatory enzymes*. springer, 2008.

[139] John H Dawson. Probing structure-function relations in heme-containing oxygenases and peroxidases. *Science*, 240(4851):433–439, 1988.

[140] Emil Fischer. Einfluss der configuration auf die wirkung der enzyme. *Berichte der deutschen chemischen Gesellschaft*, 27(3):2985–2993, 1894.

[141] DE Koshland Jr. Application of a theory of enzyme specificity to protein synthesis. *Proceedings of the National Academy of Sciences of the United States of America*, 44(2):98, 1958.

[142] Leonor Michaelis and Maud L Menten. Die kinetik der invertinwirkung. *Biochem. z*, 49(333-369):352, 1913.

[143] George Edward Briggs and John Burdon Sanderson Haldane. A note on the kinetics of enzyme action. *Biochemical journal*, 19(2):338, 1925.

[144] William D Ristenpart, Jiandi Wan, and Howard A Stone. Enzymatic reactions in microfluidic devices: Michaelis-Menten kinetics. *Analytical chemistry*, 80(9):3270–3276, 2008.

[145] Lee A Segel. On the validity of the steady state assumption of enzyme kinetics. *Bulletin of mathematical biology*, 50(6):579–593, 1988.

[146] Lee A Segel and Marshall Slemrod. The quasi-steady-state assumption: a case study in perturbation. *SIAM review*, 31(3):446–477, 1989.

[147] Cheng Yung-Chi and William H Prusoff. Relationship between the inhibition constant (K_{I}) and the concentration of inhibitor which causes 50 per cent inhibition (I_{50}) of an enzymatic reaction. *Biochemical pharmacology*, 22(23):3099–3108, 1973.

[148] Anson Hatch, Andrew Evan Kamholz, Kenneth R Hawkins, Matthew S Munson, Eric A Schilling, Bernhard H Weigl, and Paul Yager. A rapid diffusion immunoassay in a T-sensor. *Nature Biotechnology*, 19(5):461–465, 2001.

[149] Flavie Sarrazin, Jean-Baptiste Salmon, David Talaga, and Laurent Servant. Chemical reaction imaging within microfluidic devices using confocal raman spectroscopy: the case of water and deuterium oxide as a model system. *Analytical chemistry*, 80(5):1689–1695, 2008.

[150] Jean-Baptiste Salmon and Armand Ajdari. Transverse transport of solutes between co-flowing pressure-driven streams for microfluidic studies of diffusion/reaction processes. *Journal of applied physics*, 101(7):074902–074902, 2007.

[151] J Dambrine, B Géraud, and JB Salmon. Interdiffusion of liquids of different viscosities in a microchannel. *New Journal of Physics*, 11(7):075015, 2009.

[152] E Eteshola and D Leckband. Development and characterization of an ELISA assay in PDMS microfluidic channels. *Sensors and Actuators B: Chemical*, 72(2):129–133, 2001.

[153] Young Shik Shin, Keunchang Cho, Sun Hee Lim, Seok Chung, Sung-Jin Park, Chanil Chung, Dong-Chul Han, and Jun Keun Chang. PDMS-based micro pcr chip with parylene coating. *Journal of Micromechanics and Microengineering*, 13(5):768, 2003.

[154] Joseph E Coleman. Structure and mechanism of alkaline phosphatase. *Annual review of biophysics and biomolecular structure*, 21(1):441–483, 1992.

[155] HN Fernley and PG Walker. Kinetic behaviour of calf-intestinal alkaline phosphatase with 4-methylumbelliferyl phosphate. *Biochem. J*, 97:95–103, 1965.

[156] George N Bowers and Robert B McComb. A continuous spectrophotometric method for measuring the activity of serum alkaline phosphatase. *Clinical Chemistry*, 12(2):70–89, 1966.

[157] Klaus B Mogensen, Henning Klank, and Jörg P Kutter. Recent developments in detection for microfluidic systems. *Electrophoresis*, 25(21-22):3498–3512, 2004.

[158] Weizhang Huang, Yuhe Ren, and Robert D Russell. Moving mesh partial differential equations (MMPDES) based on the equidistribution principle. *SIAM Journal on Numerical Analysis*, 31(3):709–730, 1994.

[159] Stéphane Descombes, Max Duarte, Thierry Dumont, Violaine Louvet, and Marc Massot. Adaptive time splitting method for multi-scale evolutionary partial differential equations. *Confluentes Mathematici*, 3(03):413–443, 2011.

Résumé

La microfluidique de gouttes - *i.e.* l'emploi de gouttelettes comme microréacteurs - offre de nombreux avantages pour l'étude des systèmes biologiques. Dans ce travail de thèse, nous présentons une nouvelle approche pour la production et la manipulation de gouttelettes au sein de microcanaux afin de suivre l'avancement de réactions biochimiques au cours du temps. Contrairement aux approches existantes, notre dispositif utilise des gradients de confinement afin de produire et guider une unique goutte vers son lieu de stockage. Ce faisant, deux gouttes de contenus différents peuvent être appariées et fusionnées afin de déclencher une réaction chimique. Les réactifs n'étant pas activement mélangés, un front de réaction se propage alors le long de la goutte fille duquel on peut extraire la cinétique de la réaction. Nous commençons par l'étude de réactions simples ayant lieu en une étape. Un modèle 1D de réaction-diffusion permet de représenter la dynamique du front de réaction ce qui est vérifié en confrontant les solutions de ce modèle, obtenues numériquement ou analytiquement, à des mesures effectuées en gouttes. Puis, nous nous intéressons au cas des réactions enzymatiques. Nous démontrons d'abord la parallélisation de notre technique d'appariement de gouttes afin de reproduire en microcanal différents tests enzymatiques usuellement effectués en plaque multipuits. Finalement, nous étudions le cas des réactions enzymatiques rapides à l'aide de notre modèle de réaction-diffusion. Là encore, la comparaison d'expériences tenues en gouttes et de prédiction issues de notre modèle nous permet d'extraire une mesure des paramètres cinétiques de la réaction mise en jeu.

Mots clefs: Goutte, microfluidique, gradient de confinement, laser, réaction-diffusion, raccordement asymptotique, enzyme

Abstract

Droplet microfluidics - *i.e.* the use of droplets as microreactors - offers significant advantages for the study of biological systems. In this work, we present a new platform for the production and manipulation of microfluidic droplets in view of measuring the evolution of biochemical reactions. Contrary to existing approaches, our device uses gradients of confinement to produce a single drop on demand and guide it to a pre-determined location. In this way, two nanoliter drops containing different reagents can be placed in contact and merged together in order to trigger a chemical reaction. Then, an analysis of the observed reaction front yields the reaction rate. We start with the case of one step reactions. We derive a one dimensional reaction-diffusion model for the reaction front and compare numerical and analytical solutions of our model to experiments held in our microsystem. Then, we turn our attention to the case of enzymatic reactions. First, we show how the device operation can be parallelized in order to react an initial sample with a range of compounds or concentrations and we perform standard well-mixed enzyme assays with our parallelized chip, thereby mimicking titer plate assays in droplets. Second, we build onto our reaction-diffusion model to predict the rate of fast enzymatic reactions held in our device. Again, numerical and analytical solutions of our model are compared to experiments done in droplets which yields measurements of the kinetic parameters of the reaction at play.

Key words: Droplet, microfluidics, gradient of confinement, laser, reaction-diffusion, asymptotics, enzyme